



Valsts pētījumu programma  
„INOVATĪVO DAUDZFUNKCIONĀLO MATERIĀLU,  
SIGNĀLAPSTRĀDES UN INFORMĀTIKAS TEHNOLOĢIJU IZSTRĀDE  
KONKURĒTSPĒJĪGIEM ZINĀTŅU IETILPĪGIEM PRODUKTIEM”

## Projekts Nr. 2 „Inovatīvas signālapstrādes tehnoloģijas viedu un efektīvu elektronisko sistēmu radīšanai”

**vadītājs Dr. M. Greitāns**

INFORMATĪVĀ ATSKAITE PAR PROJEKTA TREŠĀ ETAPA REALIZĀCIJU  
(2012. gada janvāris - decembris)

**PASŪTĪTĀJA** līguma uzskaites Nr. 2012.-10-4/VPP

**Programmas vadītājs:** Dr.habil.phys. A. Šternbergs, LU Cietvielu fizikas institūts

**Projekta vadītājs:** Dr. sc. comp. M. Greitāns, Elektronikas un datorzinātņu institūts

# Saturs

Saturs	2
1. Laika notikumu mērīšanas sistēmas prototipu izveide, lai demonstrētu iespējas nodrošināt pikosekunžu precizitāti dažādos pielietojumos (satelītlāzerlokācijā, fluorescences raksturojošo laiku mērījumu spektroskopijā, <i>time-of-flight</i> masas spektroskopijā u.c.)	6
1.1. Event timing precision enhancement	6
1.1.1. Determination of correction function for DSP-based event timers	6
1.1.2. Precision stability enhancement by using a PLL for the calibrating	12
1.1.3. Event timing using the Time Position Estimation of the Gravity Centre	14
1.2. Performance estimation of the Event Timing System	18
1.2.1. Stability Test - evaluation of the offset drift	19
1.2.2. Linearity Test - evaluation of non-linearity errors	20
1.2.3. Resolution Test - evaluation of random errors	22
1.2.4. Conclusion	24
1.3. Event Timing System prototype for Sattelite Lazer Ranging	24
1.3.1. Principles of operation	24
1.3.2. The RTS hardware	25
1.3.3. The RTS software	27
1.3.4. Conclusion	28
1.4. Network Timing System on the base of the A033-ET	28
1.4.1. Architecture	29
1.4.2. Principles of operation	29
1.4.3. Controlling the Event Timer	33
1.4.4. Measurements in Continuous mode	35
1.4.5. Measurements in Cyclical mode	37
1.4.6. Conclusions	39
1.5. Measurement signal digitizing based on timing operation providing for complexity-reduced digital filtering	39
1.5.1. Timing of signal-reference crossing events	40
1.5.2. Basics of complexity-reduced filtering	41
1.5.3. Involved filtering procedures	42
1.5.4. Filter implementation specifics	43
1.5.5. Conclusion	45
References	45
2. Superplatjoslas tuvdarbības impulsu radara vairākantenu prototipa izstrāde un tā iegūto signālu efektīvas apstrādes optimizācija	48
2.1. Saskaņojošas iekārtas	48
2.2. Experiments with the 2D and 3D through wall imaging systems	48
2.2.1. Antenna system with 2D imaging possibility	49
2.2.2. Antenna system with 3D imaging possibility	51
2.2.3. Antenna system with 3D extended imaging possibility	55
2.2.4. The accuracy of establishing of target coordinates	57
2.2.5. Multiple signals in one channel	63
2.2.6. Computer user interface	64
2.2.7. Data transfer between device and the computer	64
2.2.8. Adjustable reflector setting	65
2.2.9. Further plans for 2D localisation model	66
References	66

3. Viedo transporta sensoru tīklu, tai skaitā, auto mezglpunktu un satiksmē iesaistīto objektu ārpus auto, izstrāde, iekļaujot iegultu sistēmu pielietošanu un energo-efektīvas programmatūras izveidi	67
3.1. Experimental IEEE 802.11p network .....	67
3.2. Experimental vehicular wireless sensor node .....	69
3.2.1. Related work .....	69
3.2.2. Approach .....	70
3.2.2.1. Hardware .....	70
3.2.2.2. Software .....	71
3.2.3. Evaluation .....	73
3.3. Stereo vision for smart vehicle with cooperative cruise control.....	73
3.3.1. Passive stereo machine vision.....	73
3.3.2. Passive stereo machine vision applications .....	74
3.3.3. Previous work in intelligent car systems using 3D vision .....	75
3.3.4. Hardware .....	75
3.3.5. Software .....	76
3.4. Smart road studs for dangerous road situation warnings .....	78
3.4.1. Related work .....	78
3.4.2. Approach.....	79
3.4.2.1. Hardware.....	80
3.4.2.2. Solar power supply .....	81
3.4.2.3. Packaging .....	81
References.....	82
4. Biomedicīnas signālu reģistrācijas iekārtu prototipu izstrāde, iesaistot sensoru tīkla tehnoloģijas un attīstīto signālapstrādes algoritmu adaptāciju konkrētiem pielietojumiem	86
4.1. Electroencephalographic helmet for analysis, interpretation and processing of cortical EEG signal .....	86
4.1.1. Experimental EEG data gathering and processing.....	87
4.1.2. Studies of evoked potentials related to visual stimuli and brain rhythms	89
4.2. Smart solutions in diagnostics and hindering the development of scoliosis based on biofeedback generated by sensor networks .....	90
4.2.1. Device prototype improvements .....	90
4.2.2. Data processing improvements .....	92
4.2.3. Smartphone (Android) application .....	94
4.2.4. Published results .....	94
4.3. Biometric person recognition system based on palm vein patterns.....	95
References.....	95
5. Uz rotācijas leņķiem balstītas vispārinātas signālu analīzes metožu attīstība un algoritmu modelēšana	97
5.1. Vispārinātās Jakobi matricas (EGURM) faktORIZĀCIJA .....	97
5.1.1. EGURM kā triju kompleksu matricu reizinājums .....	97
5.1.2. Reālu vērtību EGURM ekvivalenta faktORIZĀCIJA .....	98
5.1.3. EGURM daudzveidība un precizitāte .....	98
5.2. Doplera radara (DR) signālu ciparapstrāde.....	99
5.2.1. DR signāla ciparapstrādes algoritmi .....	99
5.2.1.1. Viena atstarojošā punkta modelis .....	99
5.2.1.2. Minimālo kvadrātu metode .....	99
5.2.1.3. Vairāku atstarojošo punktu modelis.....	100
5.2.1.4. Perspektīva - uz rotācijas leņķiem balstītu funkciju modelis.....	101

5.3.	Uz rotācijas leņķiem balstītu signālu ciparapstrādes ierīču moduļu izstrāde un mikrominiaturizācija (ASIC/FPGA).....	101
5.3.1.	EGU-rotatora arhitektūra balstīta uz reālu vērtību rotatoriem.....	101
5.3.1.1.	EGU-rotatora VHDL koda sintēze.....	102
5.3.1.2.	Sintezētā rotatora resursu patēriņa salīdzinājums.....	103
5.3.1.3.	Perspektīva.....	103
5.3.2.	DR signālu ciparapstrādes modulis.....	103
5.4.	Uz Vispārinātās Ortogonālās Nesinusoidālās Frekvenčdales balstītas datu pārraides sistēmas pilnveidošana.....	104
5.4.1.	Kanāla izlīdzināšana.....	104
5.4.2.	Bloku sinhronizācija.....	105
5.4.3.	Frekvences sinhronizācija.....	106
5.5.	Izstrādātie funkciju/programmu moduļi MATLAB/Simulink bibliotekām "Phi-FunctionsToolbox/Blockset".....	106
5.5.1.	DR DSP moduļa izstrādes-prototipēšanas vide.....	106
5.5.2.	Perspektīva.....	107
	References.....	108
6.	Radioviļņu daudzceļu izplatīšanās modeļu uzlabošana izplatīšanās apstākļos ar gariem koridoriem un dzelzsbetona griestu pārsegumiem.....	110
6.1.	Ranged models for fast fading environment.....	110
6.2.	Doppler frequency shift estimation.....	111
	References.....	112
7.	Starpautomobiļu komunikācijas sistēmas modeļa izstrāde un mobilo objektu vietas noteikšanas pētījumi, izmantojot satelītu reāllaika kinemātikas datu apstrādi, un transporta līdzekļa pārvietošanās modeļa izstrāde, lai noteiktu zudumus, kas rodas bāzes stacijām pārslēdzoties.....	113
7.1.	Starpautomobiļu datu pārraides sistēmas izpēte, kustības drošības paaugstināšanai.....	113
7.1.1.	Vadības sistēmas uz V2V bāzes.....	113
7.1.2.	Mobilo objektu vietas noteikšanas pētījumi ar augstas precizitātes GPS aparatūru dažādos mērījumu režīmos.....	116
7.2.	Transporta līdzekļa pārvietošanās modeļa izveide, sasaistot to ar datu pārraides ātrumu starp kustīgā objekta iekārtām un bāzes stacijām.....	124
7.2.1.	Cikliskais bezvadu tīkls.....	124
7.2.2.	Wlan veiktspēja autotransporta vidē.....	130
7.2.2.1.	Results of practical measurement.....	130
7.2.2.2.	Results of the mathematical models.....	133
7.2.2.3.	Results of Simulation software NCTUns7.0.....	134
	References.....	135
8.	Efektivitātes paaugstināšana daudzu ceļu datplūsmu sadarbības scenārijiem mobilos bezvadu ad-hoc tīklos (MANET) izmantojot OSI starp-līmeņu saites un video (cognitive) radio tīklu tehnoloģijas.....	136
8.1.	Introduction.....	136
8.2.	Survey of multiple path video transmission.....	136
8.2.1.	Coding methods.....	136
8.2.2.	Optimal number of streams.....	137
8.2.3.	Video data rate.....	138
8.2.4.	Multi-path routing.....	138
8.3.	An Algorithm to select optimal parameters.....	139
8.4.	Video transmission quality metrics.....	140

8.4.1.	Basic network characteristics.....	141
8.4.1.1.	Performance of the network devices.....	141
8.4.1.2.	Protocols deployed.....	142
8.4.1.3.	Network structure.....	142
8.4.1.4.	Radio channel.....	142
8.4.1.5.	Network dynamics .....	143
8.4.1.6.	Network load.....	144
8.4.2.	Path selection .....	144
8.4.2.1.	Path disjointness.....	145
8.4.2.2.	Hop count.....	145
8.4.2.3.	Interference .....	146
8.4.3.	Interdependence graph of the network characteristics.....	146
8.4.4.	Techniques to improve transmission quality metrics.....	147
8.5.	Smart antennas for interference mitigation.....	147
8.5.1.	Directivity control mechanism.....	148
8.5.2.	Elaborated model .....	149
8.6.	Conclusions.....	150
	References.....	151
Pielikums #1		153

# **1. Laika notikumu mērīšanas sistēmas prototipu izveide, lai demonstrētu iespējas nodrošināt pikosekunžu precizitāti dažādos pielietojumos (satelītlāzerlokācijā, fluorescences raksturojošo laiku mērījumu spektroskopijā, *time-of-flight* masas spektroskopijā u.c.)**

The main object of this year activity is the event timing system development with improving of timing technologies and providing the picoseconds precision in different applications.

During this period the following problems were researched:

- determination of correction function for reducing integral non-linearity;
- precision stability enhancement by using a dual PLL for the calibrating signal generation;
- precision improvement on the basis of the Gravity Center Estimation of the secondary signal;
- performance estimation of the event timing system;
- development of an event timing system prototype for Sattelite Lazer Ranging;
- implementing of a network timing system for time interval measurement;
- signal digitizing based on timing operation providing for complexity-reduced digital filtering.

The first problem solving allows defining the nonlinearity correction function minimizing expenditure of time and computing resources. The correction function stability means that external environment variation in time and temperature has minimal influence on the measurement precision. Solving of the third problem would allowed to get the same results, but with another method. The forth problem solving is dedicated to evaluate the performance parameters with sufficient reliability. The fifth and sixth problem decisions show the system prototypes for some applications. And the last problem is related to the effective filtration algorithm of an analog signal by the special timing presentation.

## **1.1. *Event timing precision enhancement***

### **1.1.1. *Determination of correction function for DSP-based event timers***

Event timers perform precise digital timing of specific events such as leading and/or trailing edges of asynchronous pulses. Note that these devices are known also under other names, e.g. as time digitisers, time-to-digital converters, event-time recorders, etc.

DSP-based event timers use a method for high-precision event timing (called EET-method), which is based on digital processing of bell-shaped analog signals generated in response to input events [1.1]. Practical implementation of this method has allowed achieving performance characteristics that are close to the parameters of the currently available best event timers in the world. Specifically, the event timers based on this method offer picosecond precision of time measurements performed at event rate up to tens of MHz [1.2]. In addition, using of DSP tools for replacing the usually intricate analog circuits has led to significantly simplified timer hardware and reduced unit costs. In [1.3] one of the key problems in increasing the event timer precision through more effective correction of non-linearity errors is considered.

The event timers based on the EET-method contain a particular Time-to-Digital Converter (TDC) responsible for the time measurement within the period  $T_R$  of the master clock. For any event that occurs at the instant  $t_j$ , the interpolator converts the value  $\tau_j = t_j \bmod T_R$  to its digital estimate  $D_j = F(t_j)$ . Conversion of all possible  $\tau_j$  values is based on a particular stair-step transfer function. Actual deviations of the stair steps from the linear approximation characterise the integral non-linearity of this function [1.4].

According to EET-method, the non-linearity correction is based on experimentally determined correction function  $\tau_j^* = F_C(D_j)$  the shape of which is the mirror-image of the actual TDC transfer function (Fig.1.1).

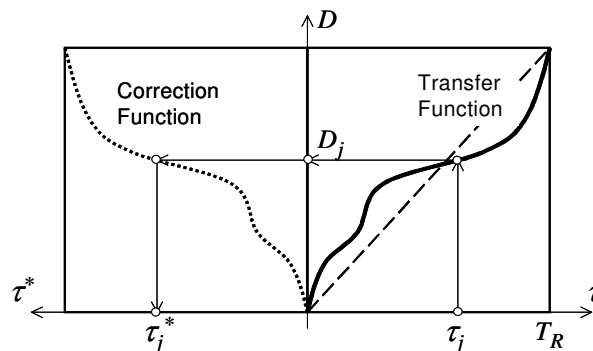


**Figure 1.1 The TDC transfer function and nonlinearity correction function**

Using this function, each intermediate estimate  $D_j$  is converted to the final estimate  $\tau_j^*$  and the initial non-linearity error can be considerably (many times) reduced in this way. However effective correction of the initial TDC non-linearity is possible only when the correction function is precisely determined in strict conformity with the actual TDC transfer function. Any errors in determining the correction function (further referred to as TDC calibration) lead to uncorrected residual non-linearity in time measurements and that significantly increases their total error.

To support the 2-3 ps precision in the event timer A033-ET [1.2] the TDC calibration should be performed with essentially better precision (<1 ps RMS). In addition, taking into account possible variations in time of the TDC transfer function, the TDC calibration should be performed relatively rapidly to trace such variations as necessary. Thus the problem to be solved is to find the best technique for precise and fast TDC calibration.

There are various approaches to TDC calibration, including the well-proved approach based on generating special sequences of test pulses [1.4]. In this case it is assumed that the modular values  $\{\tau_j = t_j \bmod T_R\}$  of the test pulse occurrence instants  $\{t_j\}$  are uniformly distributed within the interpolation interval  $T_R$  and the number  $M$  of these values  $\{\tau_j\}$  is so large that intervals between any adjacent values in the ordered distribution are significantly less than the stair step size of the transfer function.

Under this condition the histogram of ordered digital values  $\{D_j\}$  reflects so-called differential TDC non-linearity [1.4]. Next, the correction function values  $F_C(D_j)$  (reflecting the integral TDC non-linearity) can be calculated by cumulative summing of normalised frequencies  $\{f_i\}$  of the  $\{D_j\}$  realisations:

$$F_C(D_j) = T_R \sum_{i=1}^j f_i$$

The achievable precision of such TDC calibration evidently depends mainly on the proper distribution of the test events, i.e. on its similarity to the continuous uniform distribution. In [1.3] two widely known techniques for test pulse generation are analysed:

- a) time scanning technique and
- b) statistic technique.

The restrictions of first technique are caused by accumulative component of the random jitter [1.5]. The accumulative jitter can lead to considerable non-linearity of TDC calibration even if the mentioned jitter component is extremely small (Fig.1.2).

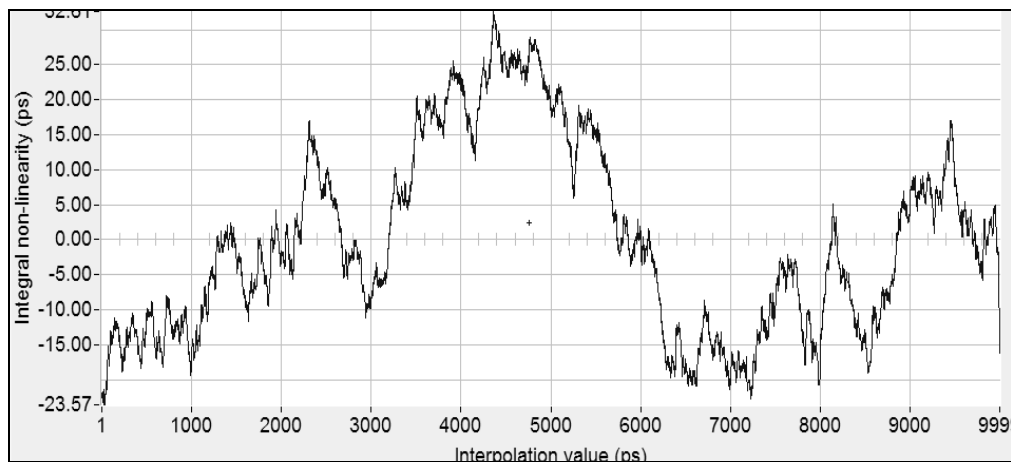


**Figure 1.2 Example of non-linearity errors in TDC calibration caused by accumulative jitter (M=70000)**

In addition, the process of jitter accumulation is random and that leads to considerable instability of TDC calibration.

The drawback of the statistic technique is in too long time for gathering of sufficient statistics. As can be seen from the simulation results, more than  $10^7$  test events are needed to achieve residual non-linearity less than 1 ps (Fig.1.3). These data conform to the theoretical predictions given in [1.4].

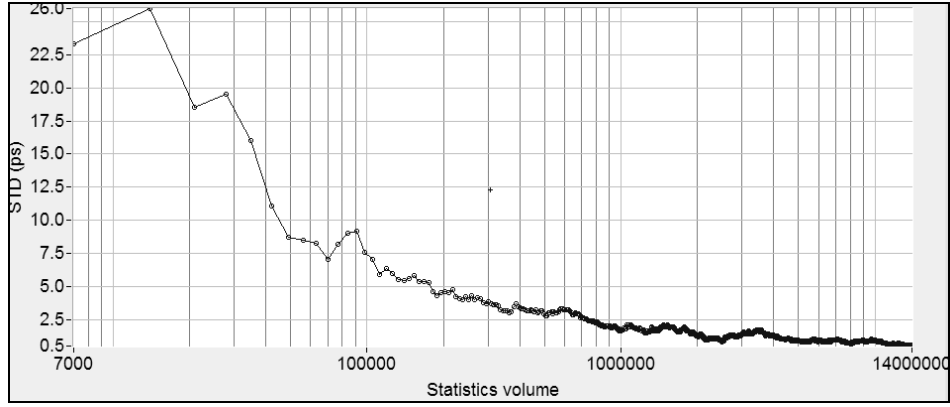


**Figure 1.3 Non-linearity (RMS) TDC calibration versus statistics volume**

Under real operating conditions the time required for accumulating such statistics is within the range of 15-20 minutes and this time interval evidently is too long for really fast TDC calibration.

Thus the practical application of the above-mentioned techniques for TDC calibration cannot support the required quality in view of either insufficient precision or speed. To find an acceptable compromise between these conventional techniques, we have developed so-called pseudo-random technique for TDC calibration.

Let us consider a test pulse sequence with constant period  $T_C$  aliquant to the  $T_R$ . Such sequence provides a set of some random remainders  $\{\tau_j = jT_C \bmod T_R\}$  and an appearance of these values  $\{\tau_j\}$  frequently looks like random. Taking that into account, it could be supposed that, like the statistic technique of TDC calibration, the distribution of the values  $\{\tau_j\}$  may approximate the required ones for a number of particular  $T_C$  values. On the other hand, such approximation could be performed much faster than that for the true statistic technique. To confirm or reject this hypothesis we have used both computer simulation and real experiments.

The model of randomly jittered oscillator, described in [1.5], and some experimental data concerning typical parameters of the model were used for computer simulation of the considered test pulse sequence. In addition, it was assumed that the test pulses are generated as a limited number of separate trains so that the period  $T_C$  in every pulse train could slightly differ, reflecting long-term instability of the test pulse sequence. Taking all that into account, the time instant  $t_{jk}$  of every  $jk$ -event occurring in the  $j$ -th train of the test pulses can be expressed for simulation as follows:

$$t_{jk} = k(T_C + \Delta_j^D) + \sum_{i=1}^k \Delta_i^A + \Delta_k^S,$$

where  $\Delta_j^D$  - random value of period  $T_C$  variation for  $j$ -th train of the test pulses,

$\Delta_i^A$  - random value of accumulative jitter component,

$\Delta_k^S$  - random value of superimposed jitter component.

All these random values are considered as uncorrelated and characterised by standard deviations  $SD^D$ ,  $SD^A$  and  $SD^S$  respectively.

To simplify computer simulations, the TDC transfer function was assumed to be linear. In this case the integral non-linearity of the evaluated correction function directly reflects the residual non-linearity in event time measurements caused by the imperfectness of TDC calibration. To be specific, in conformity with typical performance characteristics of the event timer A033-ET, we assume that  $TR = 10$  ns and the number of stair-steps of the transfer function is equal to 7000. The length of single train is limited down to 16K pulses by the size of internal FIFO memory of this event timer.

At first we checked the similarity of the proposed technique to the statistic techniques in terms of the robustness properties. In this case the simulation results indicate presence of some “bad”  $T_C$  values which cannot provide for acceptable quality of TDC calibration (Fig.1.4a) in view of spurious bursts in distribution of  $\{\tau_j\}$  values. Nevertheless, there is a much larger set of the values  $T_C$  that provide for quite acceptable level of non-linearity.

To confirm the simulation results, we have checked them experimentally under the conditions where period  $T_C$  for calibration of the specific event timer was finely altered in the same range (Fig.1.4b). In both cases the total number of test pulses was 160K. As can be seen, the results of “bad” period detection are similar in both cases.

Thus, keeping in mind a possible long-term instability of the test pulse period, it is preferable to choose its nominal value in a widest area of  $T_C$  variation where overgrown level of non-linearity is absent. For example, as Figure 1.4 suggests, this is in the area  $T_C = 7470 \pm 25$  ps. At first glance such requirement to the stability of the test pulses oscillator ( $10^{-5}$  approx) is not too rigid.

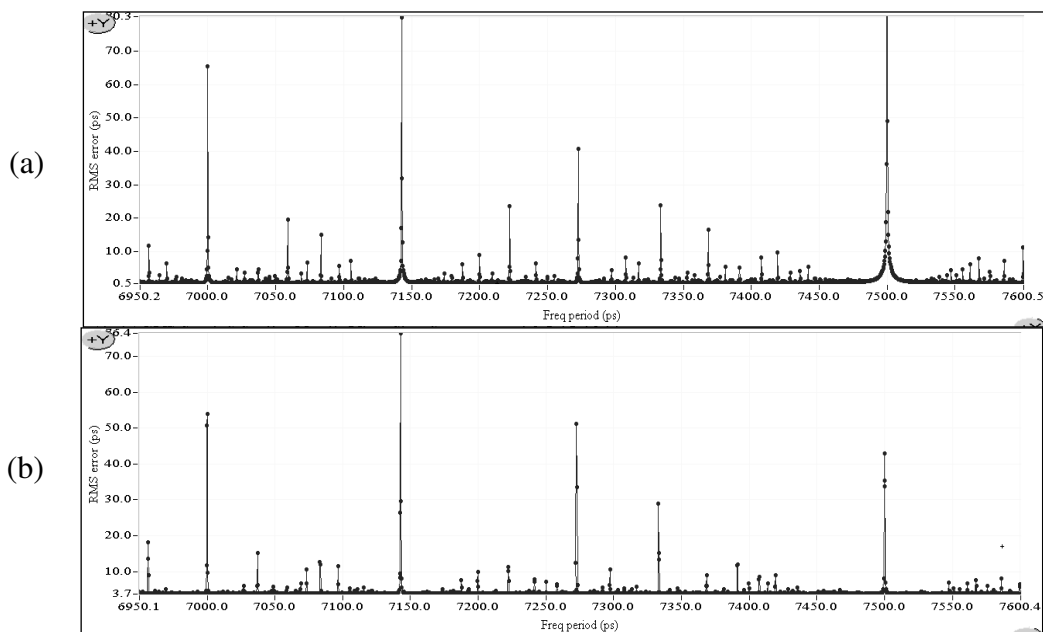


**Fig.1.4 The estimation of the integral non-linearity vs. period  $T_C$  :  
computer simulation and (b) real experiments.**

However when usual crystal clock oscillators are used for these purposes in a wide temperature range, realisation of “bad”  $T_C$  values is not excluded completely.

There are few different approaches to resolve this problem, including special synthesis of the test pulse sequences strictly related to the clock period [1.6].

To compare the pseudo-random techniques of TDC calibration with the statistic technique, the dependence of integral non-linearity TDC calibration from the length of test pulse sequence is evaluated. As simulation results show, the acceptable level of such non-linearity (at least, less than 1 ps) is achievable for the sequence length beginning from 48K pulses (Fig.1.5).

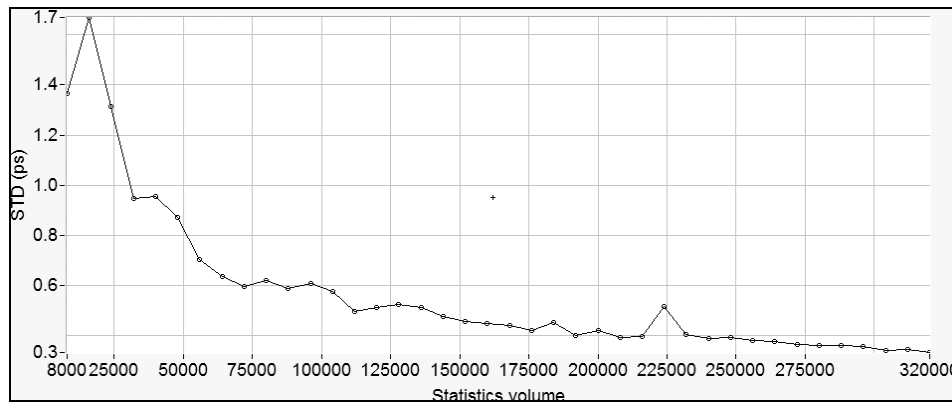


**Fig.1.5 Integral non-linearity vs. sequence length**

That is in many times less than results obtainable when the true statistic technique is used. In particular, application of the pseudo-random technique with the test sequence containing 160K pulses has provided for achievement of TDC calibration precision of about 0.61 ps (Fig.1.6).

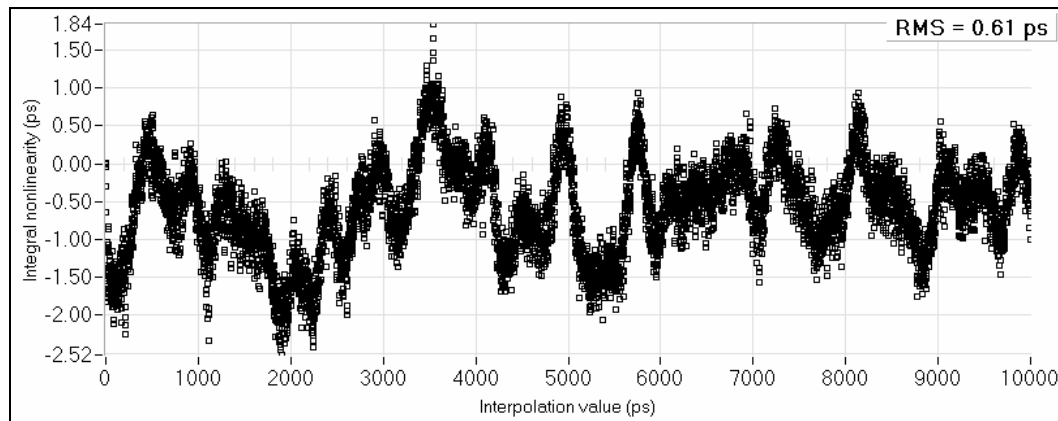


**Fig.1.6 Non-linearity error over interpolation interval TR**

In this case the calibration time normally does not exceed 10-15 seconds.

The offered pseudo-random technique of TDC calibration really provides acceptable compromise between its precision and time-consumption, to some extent reducing the main drawbacks of the conventional time scanning technique and the statistic technique. In particular, unlike the time scanning technique, the pseudo-random technique allows scattering of the cumulative jitter within the interpolation

interval, significantly increasing the calibration precision. In addition, the offered technique, in comparison with the statistic technique, can provide comparable precision of TDC calibration by using much smaller data volume.

Practical effectiveness of the offered technique has been tested experimentally in a number of developed and custom-made event timers. Specifically, the event timers employing such calibration have provided the timing RMS precision in the range 2.5-3.0 ps where the fraction of the error due to the TDC calibration procedure does not exceed 15%.

Taking into account the well-proved high potential of the offered pseudo-random technique, investigations concerning its improvement (in terms of reliability enhancement) will be continued.

### **1.1.2. Precision stability enhancement by using a PLL for the calibrating**

However, as mentioned above, using of a stand-alone crystal oscillator for calibration signal generation sometimes results in necessity to overly repeat the calibration procedure, which leads to the excess of the acceptable time of calibration. Basically, this drawback is caused by temperature instability of the standalone calibration signal source. In [1.6] a practical way to avoid this drawback is considered.

The approach to find the best values of calibration signal frequency is given in [1.3]. These values are defined relative to the master clock frequency, which means that the calibration signal should be derived from the master clock frequency. There are well known methods to do that such as direct synthesis and indirect one. The latter is done by the frequency locked loop and phase locked loop (PLL) technique.

Generally the choice of the best technique depends on the availability of technical means for its implementation. In particular, we have investigated application of dual PLL circuit for such purposes.

The calibration signal generation and the covering of the interpolation interval with small steps can be done by using a single PLL (with a frequency offset with respect to the master clock frequency), which is equipped a voltage controlled crystal oscillator (VCXO), to guarantee high stability of interpolation interval covering. Typical frequency tuning range of VCXOs is 50...100 ppm. So, the frequency offset of only 20...30 ppm could be provided. The PLL frequency divider coefficients  $A$  and  $B$  are calculated according to the equation:  $T_{VCXO} = T_R \cdot A/B$ , where  $T_R$  – master clock period,  $T_{VCXO}$  – VCXO period,  $A$  and  $B$  – frequency division coefficients. Let us assume that the VCXO is the source of the calibration signal with almost the same frequency as the master clock's one. To provide the offset of 25 ppm the coefficients 40000 and 40001 are needed. For longer VCXO periods the coefficient  $B$  is correspondingly greater. Although such offset provide a very small step of covering the interpolation interval (0.25 picoseconds for the typical master clock frequency of 100 MHz), the numbers of division coefficients are too big for synthesizing a quality pulse signal – the delays between the charge pump actions are too long. This step is preserved if longer periods of the calibrating signal are required by the proper choice of division coefficient. For example division coefficients of  $10 \cdot n + 1$  ( $n$  – integer) provide this step.

To improve the quality of the synthesis an additional PLL based on very high frequency voltage controlled oscillator VCO (GHz range) can be employed. The synthesizer consists of the two PLL stages (referred as PLL<sub>1</sub> and PLL<sub>2</sub>), each of them containing phase-frequency detectors with charge pump (PFD/CP), passive low pass filters (LF), integrated VCOs and frequency dividers (Fig.1.7).

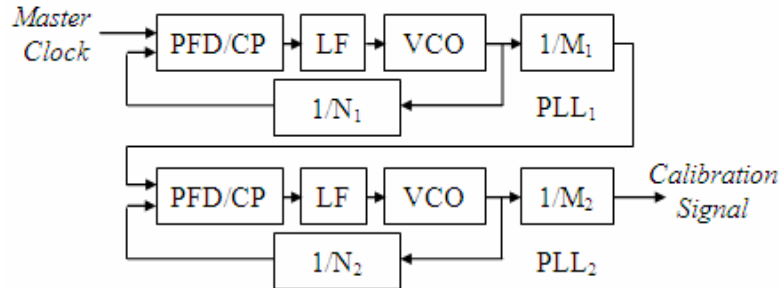


**Fig.1.7 Block diagram of time base and calibration signal synthesizer**

It was assumed that using prime numbers for coefficients of frequency dividers could allow synthesizing frequencies, which would result in desired small steps of covering the interpolation interval. The period of the calibration signal  $T_C$ , obtained by a dual PLL scheme (PLL<sub>1</sub> and PLL<sub>2</sub>), is expressed as:

$$T_C = T_R \cdot \frac{M_1 \cdot M_2}{N_1 \cdot N_2},$$

where  $T_R$  – master clock period,  $N_1$  – PLL<sub>1</sub> feedback frequency divider,  $M_1$  – PLL<sub>1</sub> output frequency divider,  $N_2$  – PLL<sub>2</sub> feedback frequency divider,  $M_2$  – PLL<sub>2</sub> output frequency divider. The calculated step of interpolation interval covering for particular values of parameters of the above described dual PLL ( $T_R=10\text{ns}$ ,  $N_1=40$ ,  $M_1=4\cdot\underline{67}$ ,  $N_2=251$ ,  $M_2=\underline{11}\cdot 1023$  – key prime numbers are underlined) is approximately 4 ps.

Two PLL chips AD9524 (from Analog Devices) have been employed in an experimental calibration signal synthesizer. The experimental studies have been carried out on the base of the existing event timer A033-ET [1.2]. The results of the test measurements performed over a considerable temperature range with regular recalibration are given in Fig.1.8a. These results can be compared with the measurement results obtained by using a stand-alone crystal oscillator as a calibration signal source. As can be seen, there are evident inappropriate spikes of obtained RMS precision among measurement results (Fig. 1.8b) for the case of the stand-alone calibration signal generator. In the case of using the experimental synthesizer the spikes are excluded.

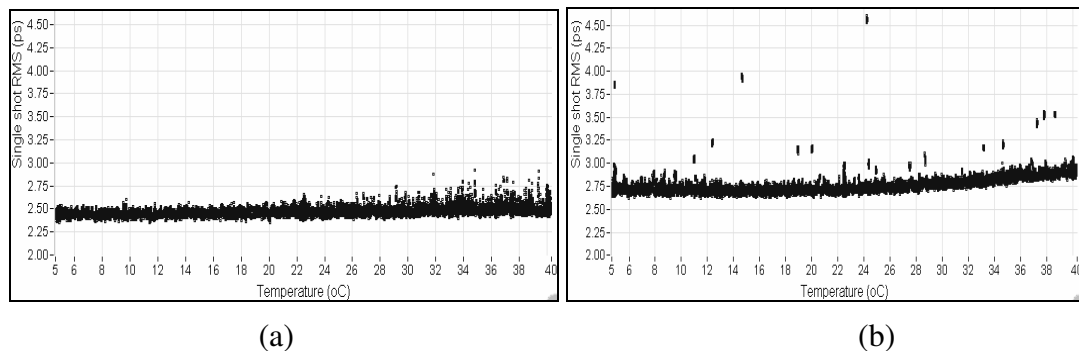


**Fig. 1.8 Single-shot RMS precision vs temperature for calibration generators: (a) on the base of the PLL circuit; (b) on the base of the stand-alone oscillator.**

The proposed technique of the event timer calibration, which is based on using a dual PLL for the calibrating signal generation, proved to be effective. Experimental tests have shown that this technique reliably supports maximum nonlinearity error about 0.5ps (RMS). The expected timer precision is maintained irrespective of the ambient temperature variations. This technique has a good potential to calibrate time measurement instruments with adequate precision.

### **1.1.3. Event timing using the Time Position Estimation of the Gravity Centre**

The problem of the accurate estimation of the time position of the gravity centre of an analog signal arises when conducting interpolation measurements of the time instants of an event's occurrence (the event timing problem) [1.7]. In interpolators based on methods of digital signal processing, when an event occurs, a unipolar analog signal is generated that is then digitized with a sampling rate of  $f_R = 1/T_R$  where  $T_R$  - is the sampling period. The time position of the analog signal within the  $n$ -th sampling interval  $[nT_R, (n+1)T_R]$  is calculated by discrete samples, where  $n$  is the number of periods of the reference frequency recorded by the counter.

Once the analog signal  $u(t)$  is sampled by ADC with frequency  $f_R$  it is transformed into a sequence of samples taken at the time instants  $\{kT_R\}_{k=1}^N$ , where  $N$  is the number of signal samples. In this case the position of the gravity centre of the sequence of samples over time is described by:

$$\hat{\gamma} = T_R \frac{\sum_{k=1}^N k u[kT_R]}{\sum_{k=1}^N u[kT_R]}.$$

In [1.8, 1.9] it has been shown that, when estimating the gravity center of an analog signal by samples, a systematic error arises. The error depends on the modular remainder of the time of the event occurrence  $t$ :

$$\tau = t \bmod T_R.$$

Since the analog signal is generated at the time of the event occurrence this modular remainder is equal to the signal's time shift. The signal's time shift  $\tau$  is measured from the beginning of the sampling period and can vary from zero up to  $T_R$ , i.e.  $\tau \in [0, T_R)$ .

Depending on the time shift systematic errors lead to the appearance of nonlinearity in the interpolation dimensions [1.4]. Therefore, to compensate the effect of systematic errors, it is necessary to carry out an additional correction of the estimates of the time position of the gravity centre by a special correction function, which is calculated in the calibration process [1.3].

New method to improve the estimation accuracy without additional correction of the results is considered in [1.10]. The method is based on the estimation of the gravity centre of a bell-shaped unipolar signal by spectral coefficients.

As shown in [1.10] the problem of estimating the phase delay time can be solved as the problem of approximating a finite unipolar analog signal in the interval  $[\tau, T_u + \tau]$  by means of the finite trigonometric series function

$$g(t; \lambda) = c_0 + \sum_{n=1}^m (a_n \cos n\omega_c t + b_n \sin n\omega_c t)$$

Where  $\omega_c = \frac{2\pi}{T_u}$  and  $\lambda = [c_0, a_1, b_1, \dots, a_m, b_m]^T$  is the vector of the spectral coefficients of the approximating function, which are given by

$$a_n = A_n \cos \varphi_u(n\omega_c),$$

$$b_n = -A_n \sin \varphi_u(n\omega_c).$$

Here and below, the superscript  $T$  denotes the transposition vector of a vector or matrix. The phase delay time through the spectral coefficients is given by

$$\tau_\varphi(n\omega_c) = \frac{1}{n\omega_c} \operatorname{arctg}\left(\frac{b_n}{a_n}\right).$$

The value of the phase delay time at  $n=1$  at the frequency  $\omega_c$  can be taken for the estimate of the time position of the gravity centre.

For the discrete time  $\{kT_s\}_{k=1}^N$  the approximating function  $g(t; \lambda)$  can be rewritten as

$$g[kT_s; \lambda] = c_0 + \sum_{n=1}^m [a_n \cos(nk\omega_c T_s) + b_n \sin(nk\omega_c T_s)],$$

where  $k = 1, 2, \dots, N$ . The estimation  $\hat{\lambda}$  of the vector of the parameters (spectral coefficients) of the approximating trigonometric regression function  $g(t; \lambda)$  is determined on the basis of the minimum condition of the error functionals (least-squares method):

$$\hat{\lambda} = \arg \min_{\lambda} \sum_{k=1}^N \{u[kT_s] - g[kT_s; \lambda]\}^2,$$

where  $\hat{\lambda} = [\hat{c}_0, \hat{a}_1, \hat{b}_1, \dots, \hat{a}_m, \hat{b}_m]^T$  is the column vector of the estimates of the regression coefficients (spectral coefficients). The estimation of the phase delay time by estimates of the spectral coefficients at the frequency  $\omega_c = 2\pi/T_u$  is given by

$$\hat{\tau}_\varphi(\omega_c) = \frac{1}{\omega_c} \operatorname{arctg}\left(\frac{\hat{b}_1}{\hat{a}_1}\right) = \frac{T_u}{2\pi} \operatorname{arctg}\left(\frac{\hat{b}_1}{\hat{a}_1}\right).$$

For a symmetric analog signal this expression is an estimate of the gravity centre's position; i.e.,

$$\hat{\gamma} = \hat{\tau}_\varphi(\omega_c).$$

When using the least squares method, the number of the processed signal  $N$  samples should not be less than the total number of estimated regression coefficients

$$M = 2m + 1.$$

To meet these conditions with a small number of samples ( $3 \leq N \leq 7$ ) the generated analog signal should be such that the approximating function in the form of the trigonometric series will contain the minimum required number of frequency components  $m$ . This is possible if the shape of the analog signal is described by a smooth function, i.e., by a function with a continuous derivative for all the finite interval of the signal's detection  $[\tau, T_u + \tau]$ . These functions include the bell-shaped functions.

The bell-shaped signal in the form of a Gaussian curve is not a finite signal; hence, it is physically unrealizable. To approximate the shape of finite bell-shaped signals, it is convenient to use half-sinusoid power functions:

$$s(x) = \begin{cases} \sin^p(x), & \forall x \in [0, \pi] \\ 0, & \forall x \notin [0, \pi] \end{cases},$$

where, in the general case, the exponent  $p$  can be a non-integer.

The effect of the interpolation measurements on the systematic errors and the values of the difference between the values of the duration of the regression function and the bell-shaped analog signal were studied numerically using a model. In the computer simulation, the duration of the bell-shaped analog signal ("fourth order sine")  $T_u = 49.689$  ns, the number of samples  $N = 5$ , and the sampling frequency was 100 MHz (sampling period  $T_s = 10$  ns). In the study of the systematic errors, the sample quantization errors were not taken into account; i.e., it was assumed that at the sampling points the sample values were exactly equal to the instantaneous values of the analog signal.

The simulation shows that, when the durations of the regression function and the analog signal do not coincide, a systematic error occurs of the interpolation measurement nonlinearly depending on the time of the event occurrence  $\tau \in [0, T_s)$ . However, the magnitude of this error is sufficiently small compared with the magnitude of the difference between the durations. As shown in Fig. 1.9 the nonlinear interpolation measurement error does not exceed  $\pm 1.5$  ps with a difference of the durations of  $\pm 300$  ps.

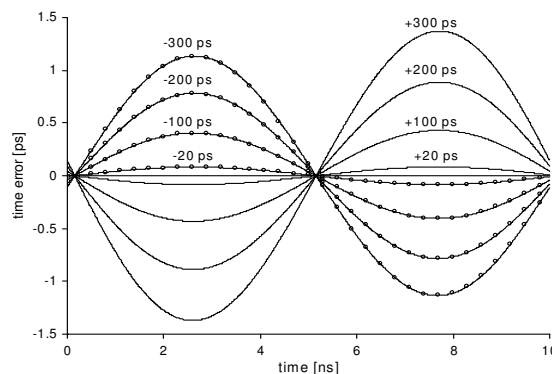


**Fig. 1.9. The systematic error dependence on the difference between the duration values of the regression function and the bell-shaped analog signal**

The effectiveness of the method of the interpolation measurement based on the estimation of the gravity centre's position of the bell-shaped signal can be illustrated by the computer simulation results of the measurement of the time intervals between the events of a periodic flow. In the simulation, the duration of the bell-shaped signal was set in the range from 50 to 300 ns; thus, at the sampling frequency of 100 MHz, the signal samples used in the processing varied from 5 to 30. The duration of the interval between the events of the periodic flow was selected to be 37.87251131377  $\mu$ s with the total number of events being 1000. To digitize the analog signals, a program model of 12, 14, and 16 bit analog to digital converters was used. The estimation of the time gravity centre position of the bell-shaped signal was carried for two methods:

- a) direct gravity centre's position calculation through the samples;
- b) gravity centre's position estimation through the spectral coefficients.

The obtained results for the first method (upper curve) and for the second method (bottom curve) are shown in Figure 1.10 for the "second order sine" and in Figure 1.11 for the "fourth order sine" approximation of the bell-shaped signal.

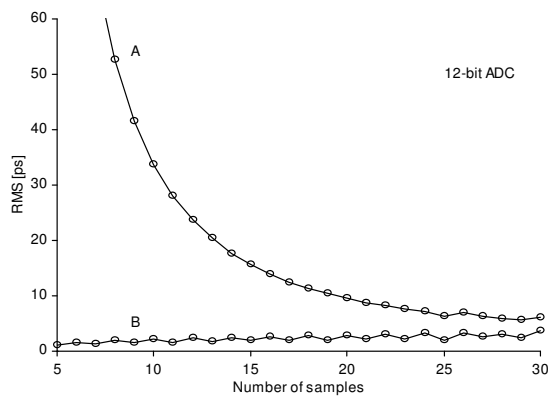


**Fig. 1.10. Time interval measurement error dependence on the number of samples of the bell-shaped signal of the "second order sine"**

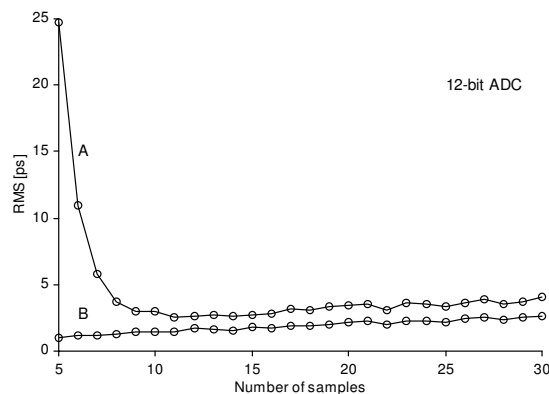


**Fig. 1.11. Time interval measurement error dependence on the number of samples of the bell-shaped signal of the "fourth order sine"**

The dependence of the mean root square error of the time interval measurement on the number of ADC bits was numerically investigated, too. The results (Fig. 1.12) suggest that the use of the 14-bit ADC to digitize the analog bell-shaped signal approximated by the “fourth order sine” makes it possible to obtain a mean root square error less than 0.5 ps in the processing of 5–10 samples when measuring intervals.

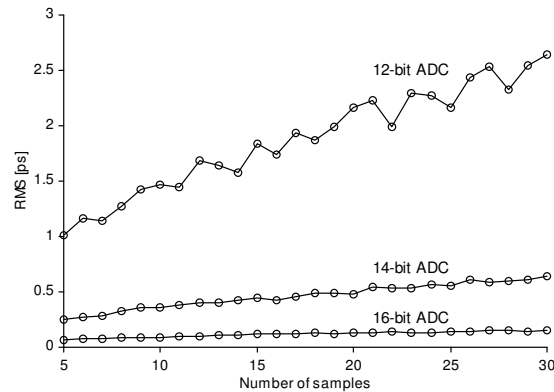


Fig. 1.12. Time interval measurement error dependence on the number of bits of the ADC.

## 1.2. Performance estimation of the Event Timing System

Event Timer A033-ET provides an extreme precision [1.2]. Therefore exact determination of its characteristics in a commonly accepted way is impossible or, at least, very difficult. For example, the widely used comparison method needs a certified reference instrument with a much higher precision than the A033-ET. There are only a few such instruments in the world and they are accessible only in exceptional cases. For this reason proper methods have been developed for reliable precision testing of each manufactured A033-ET device.

Although, in fact, the A033-ET measures separate events, its precision is specified for a time interval between two measured events. A total measurement error  $\Delta T_j$  of a time interval  $T_j$  between any two measured input events can be expressed as follows:

$$\Delta T_j = B(t) + E(T_j) + \xi_j,$$

where:  $B(t)$  – time-varying measurement offset;

$E(T_j)$  – non-linearity error depending on the value of the measured time interval;

$\xi_j$  – unbiased random error.

Specific values of these error components completely specify the precision of the A033-ET device for most applications. Particular methods and means considered below are intended for the experimental evaluation and specification of each mentioned error component of the measurement error.

The errors caused by instability of the clock frequency and trigger errors are beyond the consideration because the A033-ET usually uses an external reference frequency source and measures events presented by normalised pulses.

### 1.2.1. Stability Test - evaluation of the offset drift

Event Timer A033-ET has a single-channel configuration and measures all events coming at either input of the ET-device sequentially in the same manner and by the same means. As result the offset, as a systematic error in time interval between two events, can occur if and only if these events arrive at the different inputs of the ET-device. This offset is caused by the difference between internal propagation delays of input signals before they reach the common measurement node. The difference of these delays and their variation with the change of ambient temperature is the only reason for the offset drift. Typically the temperature stability of the offset drift is well under  $1 \text{ ps}^{\circ\text{C}}$  and depends on particularities of the electronic chips used for specific ET-device.

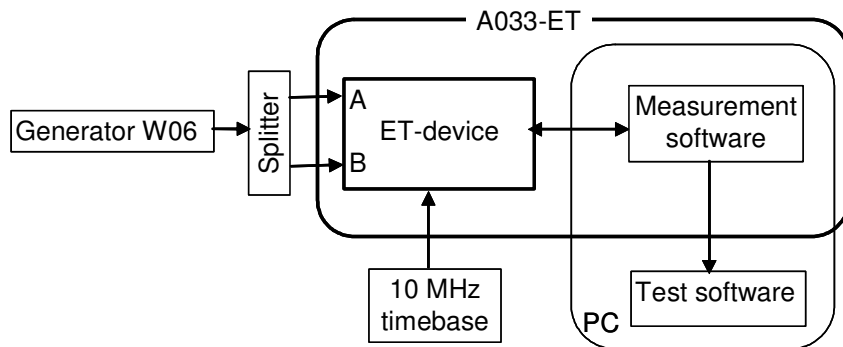


Fig.1.13. Test setup for offset drift evaluation

The test setup (Fig.1.13) contains a self-made Test Signal Generator W06, which generates a low-jittered periodic pulse signal. To estimate the generator W06 jitter the special method was used [1.11]. The deviation of the generated period was estimated about 0.8 ps RMS. This signal is symmetrically split into two inputs of the ET-device providing minimal and equal propagation delays and almost identical test signals. As in the case of other tests considered earlier, the ET-device under test is housed in an incubator which provides the ambient conditions in accordance with a carried out test.

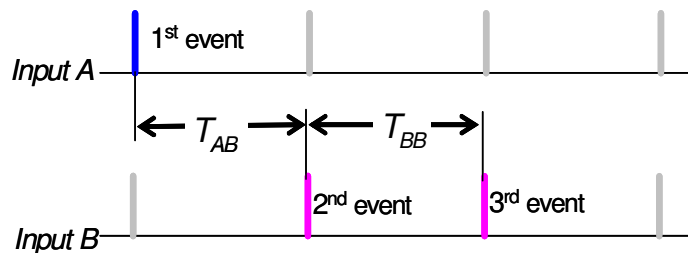


Fig.1.14. Event sequences at ET-device inputs

During tests the A033-ET measures test signals cyclically so that in the beginning of each cycle it captures a single event coming at the input A, and then - two events coming at the input B (Fig. 1.14). Under these test conditions the time interval  $T_{AB}$  is measured with some offset, but the time interval  $T_{BB}$  – without any offset by definition.

Correspondingly, the difference  $b_i = T_{AB} - T_{BB}$  is an estimate of offset value under current test conditions.

The test software opens and closes inputs A and B of the A033-ET to provide the measurement of corresponding events in each cycle and calculates the value  $b_i$ . The precision of the estimation  $b_i$  is considerably distorted by both the test signal jitter and random errors of event measurement. This distortion results in a certain evaluation error and such errors can dominate over offset drift. Taking into account that the offset drift is quite a slow process the test software averages 10000 sequential single estimates to minimize the evaluation error. This provides RMS of evaluation errors about 0.2 ps.

Together with the offset estimation the test program monitors the temperature in the incubator (the ambient temperature for the A033-ET), and displays the offset drift and temperature as functions of time.

Figure 1.15 demonstrates the result of the stability test for a particular A033-ET. As can be seen, the offset variation is related to slow ambient-temperature changes in the range from 20 to 25 °C and is less, than 0.2 ps/°C. Generally this parameter value is specific for every particular ET-device under test.

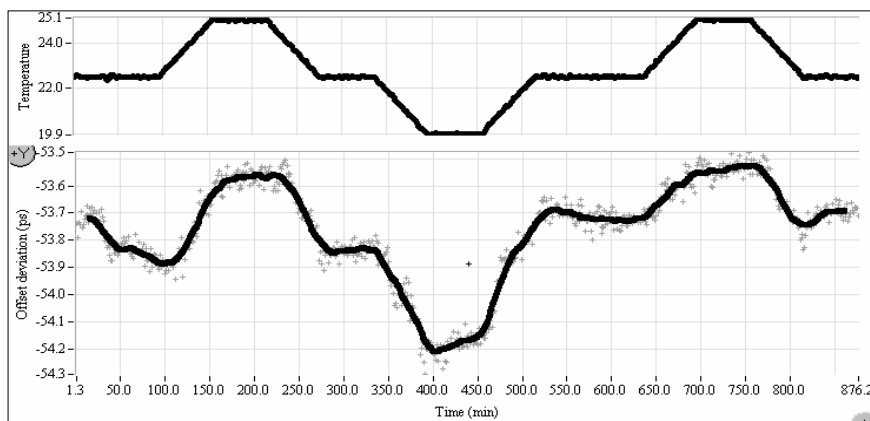
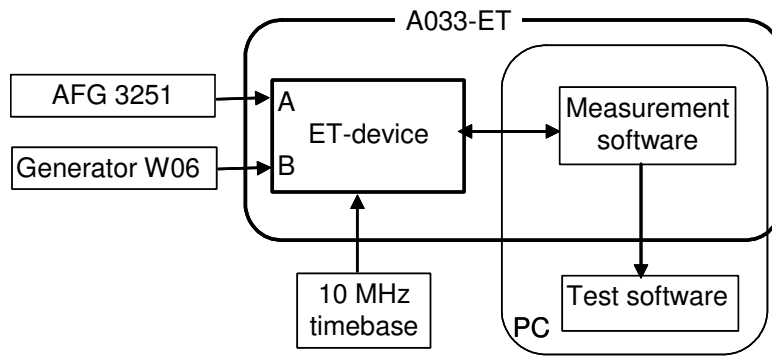


Fig.1.15. Offset variation at slowly changing temperature

### 1.2.2. Linearity Test - evaluation of non-linearity errors

The single-channel configuration of the A033-ET provides many benefits, but also brings about specific limitations in event measurement. The A033-ET needs from 40 up to 50 ns for single event measurement. During this “dead time” new events are not logged. But even after this time there is some damping transient, which affects a next measurement. The effect of that depends on the time interval from the previous measured event.

Typically the non-linearity of the A033-ET does not exceed a few picoseconds and is most noticeable for intervals close to “dead time” in the range up to 150 ns. But in the range exceeding 2000 ns the non-linearity is negligible. The linearity test is dedicated to define the dependence of non-linearity error from the measured time interval.



**Fig.1.16. Test setup for linearity measurement**

The test setup (Fig.1.16) contains two stand-alone mutually unsynchronized sources of test signals. One of them is the above mentioned Generator W06. Its period is surely greater than the length of transient process. Generator A is a NIM pulse generator without special requirements to its precision and stability (in our setup the generator AFG 3251 was used). It generates the pulse sequence with period greater than three periods of W06.

In such conditions for any event at the input A there are at least 3 events at the input B and the interval  $T_{AB}$  is changing in the range from the “dead time” value up to the W06 period (Fig.1.17). The events 3 and 4 are not affected by the transient process by definition, but the event 2 may be affected if the interval  $T_{AB}$  is less than the transient process. Taking into account the short term stability of the W06 the non-linearity error for  $T_{AB}$  will be defined by difference  $E(T_{AB}) = T_{B1} - T_{B2}$ .

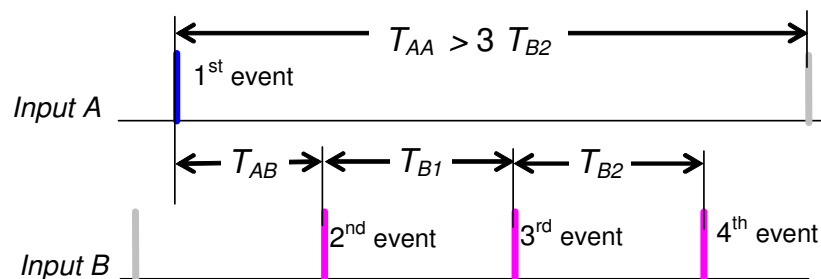


**Fig.1.17. Event sequences at ET-device inputs**

Other similar quads give non-linearity errors for some other, naturally randomized values of time interval  $T_{AB}$ . When a number of such quads are large enough, a set of values  $\{E_j\}$  corresponding to increasing time intervals  $T_{AB}$  characterizes a linearity function.

The test software separates the event coming at both inputs of A033-ET, calculates the corresponding intervals to get the non-linearity values, and displays results. Due to the big internal memory size of A033-ET (16K events) the accumulation of measured data and data processing can be carried out in parallel. While new data are accumulated the previous data are processed.

However these calculated values of linearity function include the evaluation errors caused by test signal jitter and random errors of event measurement. Typically the

evaluation errors considerably dominate over non-linearity errors. To find the values of linearity function the calculated values are averaged in uniformly spaced time increments. In our case this time step is 1 ns and is the compromise between volume of statistic and smoothness of linearity function.

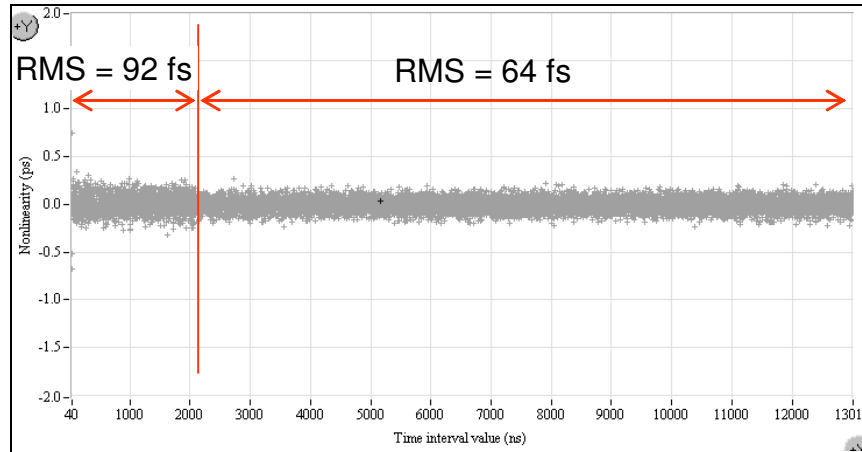


**Fig.1.18. Result of non-linearity evaluation**

Although the method is applicable for a wide range of time intervals (up to hundreds of ms) the A033-ET are normally tested in much smaller range, where the non-linearity is really expected. Figure 1.18 demonstrates a typical result of the linearity test. Total number of measurements was about 500 million (about 7900 initial estimates for each 1 ns increment).

It can be simply concluded from the test result that the non-linearity does not exceed 1 ps. However there is some appreciable difference between variances of measured values in the first sub-range up to 2048 ns and in the second sub-range exceeding 2048 ns (the calculated standard deviations: 92 fs and 64 fs, correspondingly). The reason is that the values in the second sub-range are practically only evaluation errors, but the values in the first sub-range are sums of non-linearity errors and evaluation errors. Assuming that these errors are statistically independent, it can be simply calculated that the RMS of non-linearity errors in this case is about 66 fs. In the very beginning of the range (up to 150 ns) the non-linearity is a little higher.

### **1.2.3. Resolution Test - evaluation of random errors**

The Event Timer A033-ET performs event measurement with some random error, resulting in random errors of calculated time intervals between the measured events. The standard deviation of the time intervals is of primary interest as it characterizes precision most adequately. It is a common practice to call this parameter “single-shot RMS resolution”, keeping in mind comparing readouts from the same instrument. The A033-ET provides the single-shot RMS resolution better than 5 ps under conditions, when input signals conform to the specified requirements and long-term instability of an external frequency standard is negligibly small during measurement.

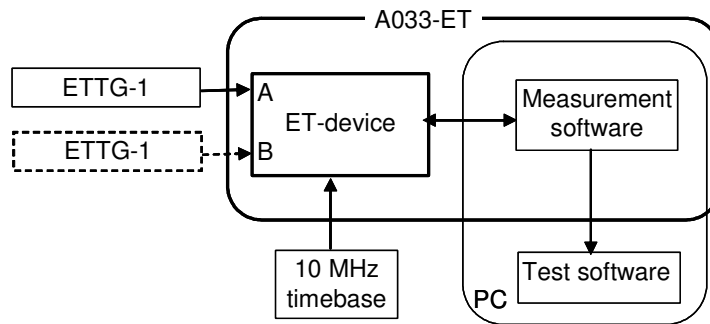


**Fig.1.19. Test setup for resolution monitoring**

The simplest and demonstrative way how to specify the RMS resolution is to perform the direct repetitive measurement of a test signal that has a jitter much smaller than expected random errors produced by the instrument. The test setup (Fig.1.19) contains the self-made Event Timer Test Generator ETTG-1. It can be switched at one of two inputs for each input test. The generator has low jitter (about 0.6 ps RMS [1.12]) and test signal period  $T = 20484.57\dots$  ns which is not a multiple of the A033-ET master clock period (10 ns). The last ensures uniformly distributed measured events within the interval of interpolation so that the evaluated resolution concerns all possible cases of event measurement.

Test software carries out the direct repetitive measurement of the test signal with predefined period. In each cycle 16K sequential single-shot measurements are accumulated in the internal memory of the ET-device. In parallel with data accumulation, the test program processes the previously measured data to calculate the standard deviation and displays it together with registered temperature versus time. It is assumed that the deviation of external reference frequency during such measurements (about 336 ms) does not have a noticeable impact on the test result.

Figure 1.20 demonstrates the test result, when the ET-device is placed into incubator that provides the slow temperature change in the range 20 to 25 °C. The calibration was done at temperature 22.5 °C. It can be seen that at the calibration temperature the RMS error is minimal. But the resolution degrades in line with the temperature drift (negative or positive). In the case of small drift this degradation is acceptable because the resolution does not exceed the one specified for the A033-ET (<5 ps). It must be noted that such estimates are slightly overstated due to an inevitable test signal jitter and the true RMS resolution of A033-ET is slightly better. Generally the best resolution and its temperature stability are slightly different for every ET-device under test.

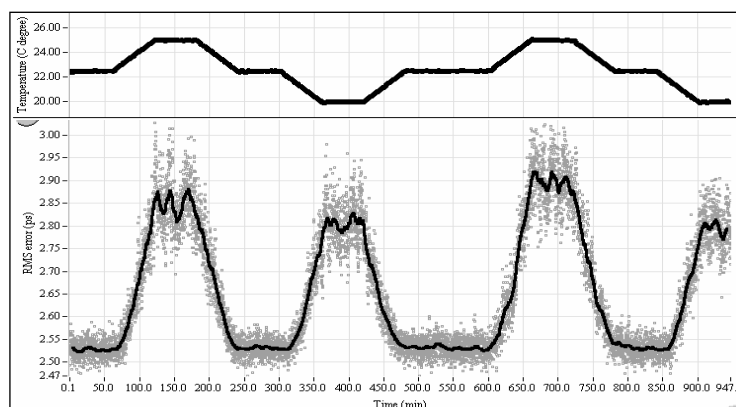


**Fig.1.20. Resolution versus time at changing temperature**

### **1.2.4. Conclusion**

The methods of reliable evaluation of these parameters are developed and successfully applied for each manufactured A033-ET. The distinctive features of the methods are as follows:

- differential test measurements to minimize the impact of test signal instability upon the test results;
- full automation of the tests and using of very large statistics to minimize the evaluation errors;
- there is no necessity of complex and expensive test instrumentation.

It is shown that the long-term instability of the A033-ET precision parameters is caused mainly by ambient temperature variation. This factor as a rule is taken into account by the end-users, who are placing the measurement instrumentation in closed cabinets with stabilized temperature.

Although currently the test methods are applied for testing the A033-ET, they also can be used for testing other event timers with similar architecture.

### **1.3. Event Timing System prototype for Sattelite Lazer Ranging**

The Riga Event Timing System (RTS) was designed and built in 2006 for Riga SLR station to upgrade its measurement equipment. The RTS maintained the basic functional possibilities of the previous Riga timing system, but was enhanced in many essential respects. Specifically, the RTS was based on employment of the previous model of the Riga Event Timer A032-ET [1.12].

A new system design is made to integrate the most of specialized hardware means with the latest model A033-ET, which provides much better single-shot resolution (3-4 ps RMS instead of the previous 10 ps) and smaller „dead time“ (50 ns instead of the previous 60 ns). There are new functional possibilities of digital signal processing and system control that will increase [increases] the SLR efficiency. Some optional functional capabilities are added for experimental investigations with the aim to improve the performance of Riga station as a whole.

All the special features of the previous RTS are left. They include the pre-processing of STOP pulses coming from either traditional single or special doubled receiver based on Photo Multiplier Tubes (PMT). The doubled receiver generates the pulses overlapping only when the true STOP pulse is being received. It makes possible to reduce the noise influence, when the satellite ranging is performed by day. Like the previous Riga timing system the new system performs PMT pulse amplitude measurement to correct the range bias.

#### **1.3.1. Principles of operation**

The RTS supports the following operational modes:

- SLR system calibration in the range from 9 to 375 m with parallel measurement of STOP-pulse amplitudes;

- Satellite ranging to 25,500 km at 10 Hz repetition rate with parallel measurement of STOP-pulse amplitudes;
- Integrated mode when the SLR system calibration and satellite ranging are performed simultaneously (for optional use);
- Measurement of pulse noises.

Structurally the RTS combines the RTS hardware and a PC with the RTS software (Fig.1.21).

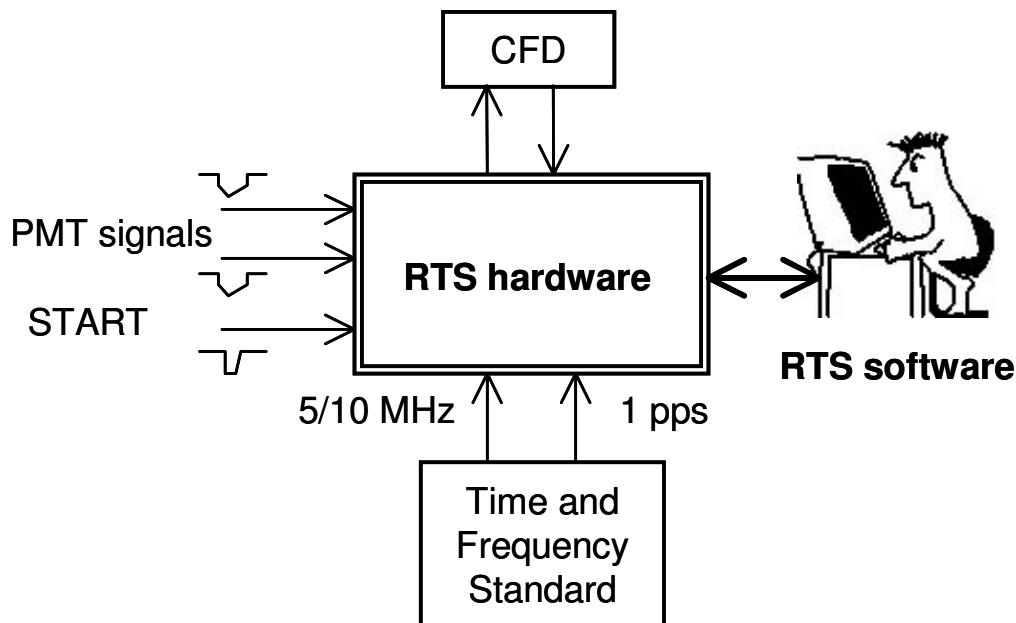


Fig. 1.21. RTS architecture

Additionally the RTS includes two commonly used external devices: Time and Frequency Standard and Constant Fraction Discriminator (CFD).

### 1.3.2. The RTS hardware

The RTS hardware contains three functional units: Signal Processing block (SPB), Event Timer Block (ETB) and Master Clock; each implemented as a separate board. These boards and their power supply are housed in 19'' 2U rack module.

The SPB receives the PMT pulses (3 to 7 ns width range; -0.1 to -3.0 V amplitude range) and, in interaction with the CFD, produces normalised NIM pulses for the ETB. The ETB measures time instants of these pulses and START pulses coming. Then the measurement results come to PC for further data processing, displaying and memorizing. The Master Clock represents a voltage-controlled crystal oscillator disciplined by an external high-stable 5 or 10 MHz reference frequency using PLL circuit. It generates a low-jittered 100 MHz clock signal required for precise event measurement and synchronization of SPB operation as a whole.

The SPB performs a few basic operations with PMT pulses before their measurement by the ETB (Fig.1.22).

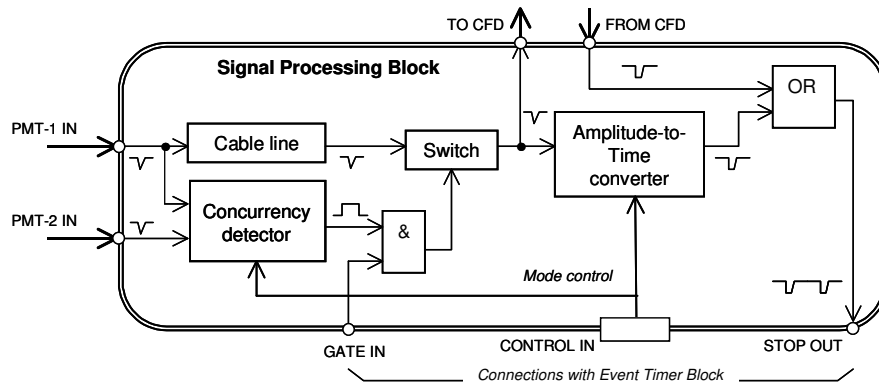


**Fig. 1.22. Functional diagram of the Signal Processing Block**

At first it selects PMT pulses, which probably conform only to the returned laser pulses. To do that either single (“PMT-1 IN”) input or two (“PMT-1 IN” and “PMT-2 IN”) inputs for PMT pulses can be used. In the last case it is supposed that the PMT pulses overlap only when the true return is being received. In the case of concurrency of these pulses one of them (“PMT-1”) is selected using the wideband switch. Such selection acts together with the online programmable gating provided by the ETB.

The selected pulses from the switch output come to the CFD. The CFD generates normalized NIM pulse in response to each input PMT pulse. This NIM pulse comes to the input “FROM CFD” of the SPB. However the CFD cannot fully avoid the time-uncertainty of PMT pulse coming. For this reason the amplitude of each PMT pulses is additionally measured as the amplitude values are related to the range bias. To do that, the Amplitude-to-Time converter generates the NIM pulse in response to the same PMT pulse with some delay proportional to the PMT pulse amplitude. In this way every selected PMT pulse is being converted into two NIM pulses, where the first one represents directly the returned signal and time interval from the first pulse to the second one reflects its amplitude (Fig.1.23). Resolution of such amplitude measurement is about 9 bits.

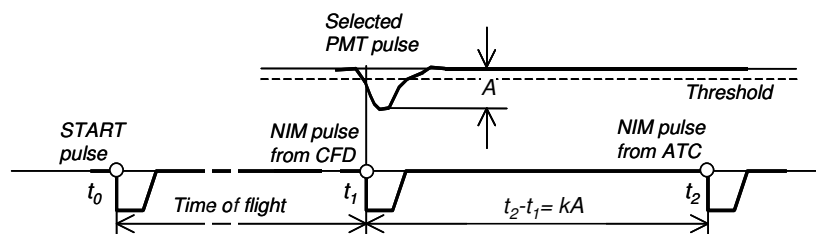


**Fig. 1.23. Time diagram illustrating PMT pulse amplitude conversion**

Then, the ETB measures time instants of these pulses and START pulse coming at each ranging cycle so as to give out complete data for further satellite ranging. As shown in [1.12], the mentioned technique of PMT signal amplitude measurement makes it possible to effectively correct the range bias caused by the PMT features.

The ETB precisely measures the instants at which input events occur. Every event is associated with certain fixed point on the leading edge of input NIM pulses. Used

method of event timing is untraditional in many respects. Specifically, it supports not only high precision, but high speed as well. Using 100 MHz internal clocks this method provides each single measurement with 7-8 ps RMS resolution during 60 ns only.

The event measurement is performed in two stages. At first, the ETB transforms every input event into single 64-bit timing data block (subsequently referred to as TD-block) and sequentially accumulates them in a FIFO memory. Each TD-block contains the counting data (39 bits; 10 ns resolution) and interpolating data (24 bits), as well as one-bit mark specifying the kind of measured event (either Start or Stop). The interpolating data are presented initially in an intermediate redundant form.

At the next stage the PC takes out TD-blocks from the FIFO memory and processes them to obtain the corresponding epoch time-tags in a unified form. Further these time-tags are additionally processed to display the ranging results in real time. To achieve the best precision, processing of TD-blocks takes into account the actual physical characteristics of time interpolation under actual operating conditions; these characteristics are defined through so called scaling (hardware calibration) before the measurement.

The ETB is flexibly controllable and allows writing TD-blocks in the FIFO memory and reading them by the PC in different order. Specifically, the RTS provides cyclical measurement of events. In the beginning of each cycle the RTS measures a single Start-event, and only then - a number of Stop-events. According to the modes of RTS operation, the ETB measures up to 3 events in the System calibration and Satellite ranging modes, up to 5 events in the “Integrated mode” and up to 16K events, when pulse noise is measured. In all cases the ETB at first accumulates TD-blocks in the FIFO memory during some defined waiting period, starting from Start-event registration. During this time the PC processes TD-blocks that have been read out from the ETB in the previous cycle. Then the PC stops the event registration, reads the currently accumulated TD-blocks and allows starting the next similar cycle. The waiting period is strictly adapted to the repetition rate (10 Hz) of RTS operation. Optionally the RTS can provide the repetition rate up to 30 Hz.

In addition to the event measurement the ETB generates NIM pulses, which come to the input “GATE IN” of the SPB to provide online programmable PMT pulse gating.

### **1.3.3. The RTS software**

The RTS software performs real-time procedures, which depend on the selected operating mode, current user control, etc. There are also various auxiliary procedures to prepare the system to operation (clock synchronization, calibration of measurement hardware, system checking, and so on). For example, in the conventional Satellite ranging mode the RTS software performs in real time the following procedures:

- periodically checks the ETB to detect the START pulse coming;
- when the START pulse is detected, triggers the internal time-out and begins processing of the previously taken data;
- after time-out stops the measurement, reads the data from the ETB, writes to it a new data concerning the STOP pulse gating and makes next cycle available.

Correspondingly the data processing performed during the time-out includes:

- conversion of TD-blocks to the unified form of epoch time-tags;
- calculation of the gate delay and residual, time interval reflected the STOP pulse amplitude and new data concerning the STOP pulse gating in the next cycle;
- displaying (Fig.1.24) and memorizing the measurement results.

The RTS software offers optionally an auto-tracking of satellite in range after its initial acquisition. When the auto-tracking is on, possible trend of the residuals is actually excluded due to the automatic gate delay correction. Algorithm of the auto-tracking is based on median selection of current residuals to exclude their possible abnormal values, and continuous generation of a special piecewise-linear function for gate delay correction. Every piece of this function is being determined using regression analysis of the current fraction of residuals. In this case the gate delay correction is performed at 1 Hz rate approximately, allowing considerable errors in initial predetermination of the function “RANGE vs. START TIME”.

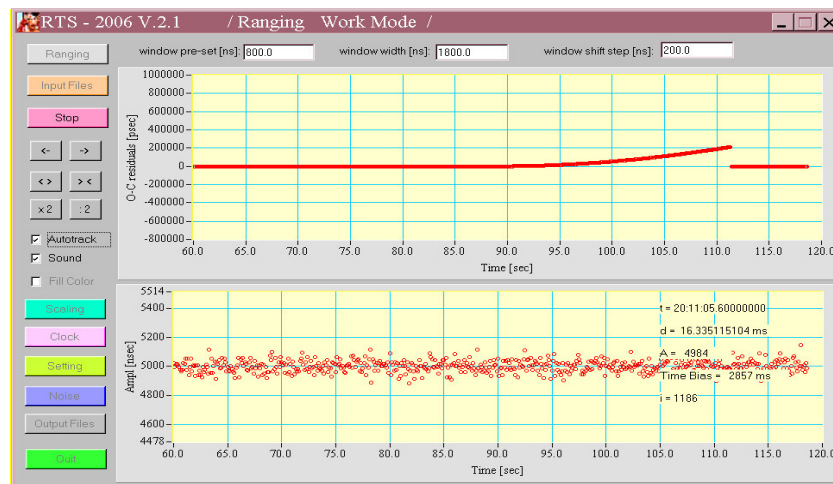


**Fig.1.24. Example of displaying the measurement results. Upper plot shows residuals; bottom plot indicates amplitudes of PMT pulses**

### **1.3.4. Conclusion**

As compared to the previous version of RTS, the new system offers better performance in terms of accuracy, functionality, and reliability in operation. This provides a good basis for further advancing the Riga SLR Station as a whole.

## **1.4. Network Timing System on the base of the A033-ET**

Network Timing System (NTS) has been developed to provide the time measurement not in situ, but from any place with a PC, which is connected to the Internet. NTS allows remotely controlling of the measurement process, get timing data and do any processing and visualization of collected information. In this case the developer of Event Timers can do any modifications in hardware and software, and

use any existing PC interfaces with the Event Timer hardware to provide the better performance only saving the existing NTS application protocol based on TCP/IP stack. In turn the user should not know about the hardware interface problems and deal only with the processing of timing data for its specific application.

### 1.4.1. Architecture

The A033-ET performs the measurement in interaction of the specialised hardware with a PC running the measurement software. The measurement software provides interfacing with user application program via TCP/IP network on the basis of well-known “Client/Server” scheme (Fig.1.25). The user program can control the A033-ET via this interface and receive measurement data for its application-specific processing.

The A033-ET is considered as a combination of a specialised timing device (subsequently referred to as ET-device), and a computer with a specialised Server program (subsequently referred to as ET-server) dedicated both to manage the ET-device and process timing data obtained from it (Fig.1.25). In this case the ET-client is a PC with a user program having the TCP/IP application protocol stack and running user-specific application. In some cases a single PC under MS-Windows can serve as both the ET-server and the ET-client although use of separate PC for the ET-server is preferable to achieve the highest operating speed.

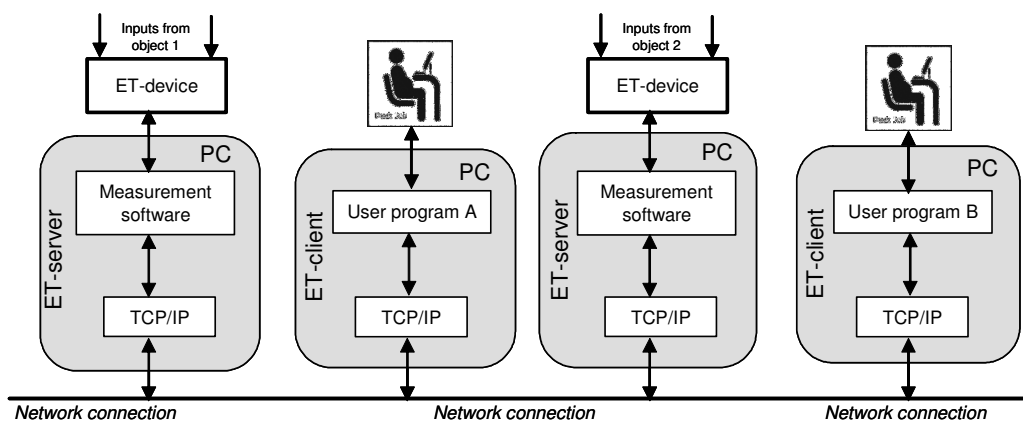


Fig.1.25. Network architecture of the A033-ET

### 1.4.2. Principles of operation

The A033-ET performs the timing of input events in two stages.

At first, the ET-device transforms every input event into a single 64-bit timing data block (subsequently referred to as TD-block) and sequentially accumulates such TD-blocks in a buffer memory. Each TD-block contains the rough data (39 bits) and interpolating data (24 bits) about the time of event incoming, as well as one-bit mark specifying the input (either Input A or Input B), where the measured event came from. The rough data defines the time-tag in 1.5 hours range approximately, meaning that the time intervals between adjacent events can be this long. Totally, such stage of

measurement continues from 40 up to 50 ns for each single event, defining the A033-ET dead time.

There are two successively connected FIFO-memories to accumulate the TD-blocks. First (highest-speed) FIFO-memory capacity is 1K events and it works with 4-byte words. The data from it are rewritten into second FIFO-memory with 8-bit input bus. In such combination the maximum burst rate is 20 MHz for 2,600 sequential events. Second FIFO-memory capacity is 16K events and it supports the maximum burst rate up to 12.5 MHz. However, the maximum average rate is considerably limited (down to tens of KSPS) by the carrying capacity of the ET-device interfacing with the ET-server.

TD-blocks represent the corresponding time-tags in the implicit form and should be additionally processed. Correspondingly, at the second stage of measurement the ET-server takes out TD-blocks from the ET-device and processes them to obtain the epoch time-tags. To achieve the best resolution, certain specific parameters of such processing are defined through ET-device calibration under current operating conditions.

The ET-device is flexibly controllable and has two different measurement modes:

- Continues mode, providing continuous (gapless) event measurement during practically unlimited time; and
- Cyclical mode, providing cyclical measurement of events that come at the separate inputs of the ET-device in a strict order.

For user convenience, these two modes are implemented by different Server programs. These program are working under MS Windows, but can be translated into other operating systems. In A033-ET current version it works with the device via PC Parallel Port. The special configuration file contains Parallel Port addresses and TCP port address, it can be edited in the Notepad in accordance with PC resources and hardware configuration. After the ET-server starts it writes own Network address into the same configuration file. This address should be used by any ET-client, which wants to work with this ET-server.

When the program is started, the ET-server control panel appears. For a technical staff convenience the panels of the ET-servers for Continuous and Cyclical modes differ by colour (see Fig.1.26 (a) and (b)).

The ET-server firstly recognizes the hardware, which is connected to the Parallel Port address from the configuration file. If the hardware is A033 and it is operable the panels indicate the port address and the device serial number. In operation session LEDs of these panels will indicate an actual state of the Event Timer in process of its further operation under network control from the ET-client. A click on the "HELP" button opens the message panel with short information about the A033-ET, control panel button functions and LED meaning. A click on the "QUIT" button stops all processes and closes the ET-server program.

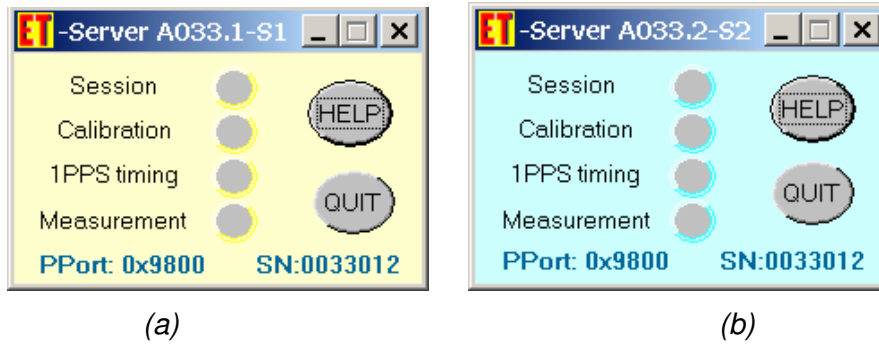


**Fig.1.26. Indicating panels of the ET-server for:**  
**(a) Continuous mode and (b) Cyclical mode.**

**In Continuous mode** the ET-device continuously accumulates TD-blocks in own memory in order of measured events incoming. Concurrently with this process, the ET-server continuously monitors the current state of this memory with some user-defined period  $T_M$  to detect the state, when the amount  $M$  of TD-blocks exceeds the user-selectable value  $(2^k - 1)$  TD-blocks,  $K = 4, 5, \dots, 11$ . The rest of the buffer memory capacity is used to absorb possible bursts of the input event rate.

When the specified memory state is detected, the ET-server takes out  $M$  TD-blocks from the ET-device, processes them and sends the corresponding time-tags to the ET-client (Fig.1.27). Such procedure is being cyclically repeated. In this way the continuous event recording goes together with cyclical timing data processing and sending the time-tags to the ET-client via TCP/IP interface.

The maximum average rate of such continuous measurement is limited mainly by the available reading and processing speed of the TD-block by the Server PC. The ET-server interacts with the ET-device via parallel port in EPP mode, supporting the average rate up to 30 KSPS if this PC port allows reading of 4-byte words. Otherwise the maximum average rate is reduced down to 12 KSPS.

In any specific application the monitoring period  $T_M$  and the amount  $M$  of TD-blocks can be adapted to the expected mean rate  $R$  of event measurement to avoid FIFO memory overflow. Generally the period  $T_M$  has to be defined so that it is a little less than the mean time  $M/R$  of accumulating  $M$  TD-blocks in the FIFO memory in view of the rate  $R$ .

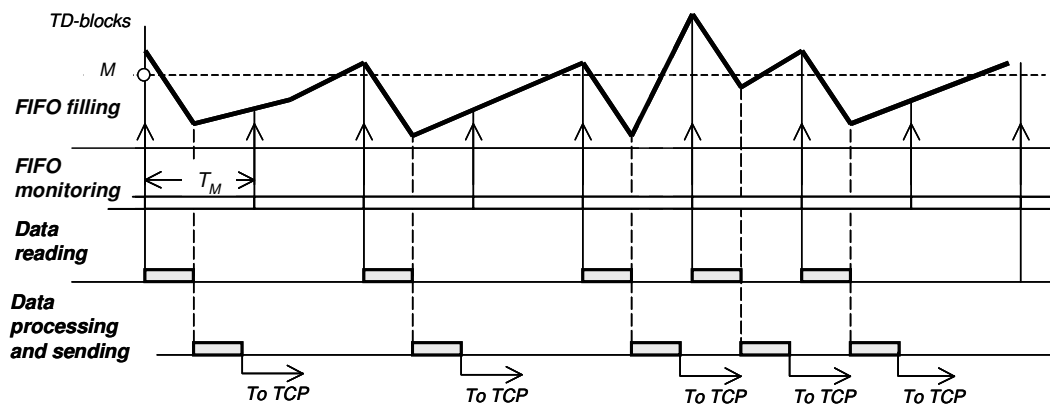


**Fig.1.26. Time diagram of the measurements in Continuous mode**

Note that the values  $M = 255$  and  $T_M = 15 - 25$  ms are applicable for any rate  $R < 10$  KSPS of continuous measurement. However, when the actual rate is much lower than 10 KHz, the accumulation time of TD-blocks before being read by the ET-server can be too large, resulting in too large delay of receiving the first time-tags by the ET-client. In some cases this may cause problems with real-time operation of the ET-client. In such cases it is recommended to decrease the  $M$  value as far as possible.

**In Cyclical mode** the special input control is used. In the beginning of each cycle the ET-device opens Input A only and waits a Start-event coming at this input of the ET-device. After that ET-device closes the Input A and after delay  $T_{Dj}$  opens the Input B for Stop-events (up to 16K) coming at this input (Fig.1.27). The gate delay  $T_{Dj}$  is online programmable by the ET-client in a wide range with 10 ns LSD resolution.

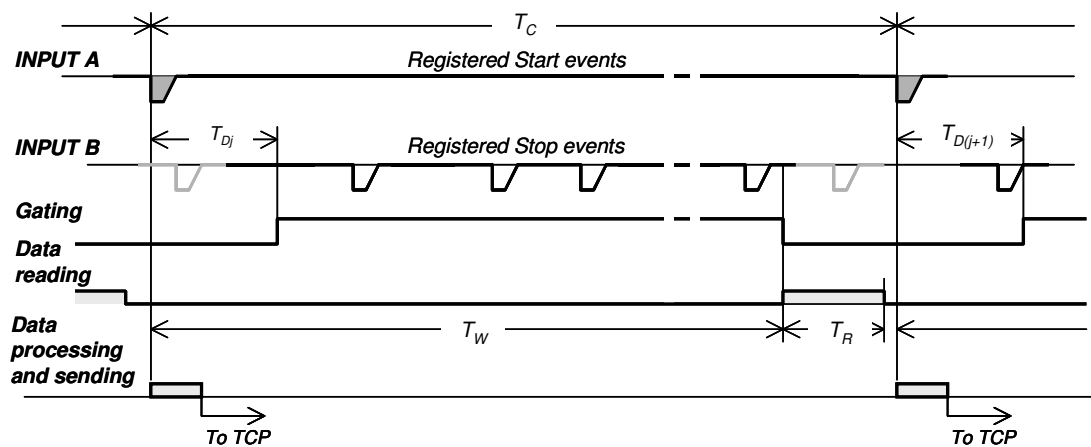


Fig.1.27. Time diagram of the measurements in Cyclical mode

Unlike the Continuous mode, in this case the ET-device at first accumulates TD-blocks in the FIFO memory during some user-defined waiting period  $T_W$ , starting from Start-event registration. During this period the ET-server processes TD-blocks, which are read out from the ET-device in previous cycle, and sends the corresponding time-tags to the ET-client. At the end of the waiting period the ET-server temporarily disables the event timing, reads the currently accumulated TD-blocks, and then allows starting the next similar cycle. In any case the amount of TD-blocks read by the ET-server does not exceed the user-defined value  $M$  (from 1 to 16K). The waiting period  $T_W$  can be defined in a wide range with 1 ms step.

During the waiting period  $T_W$  the ET-server can receive a command from the ET-client to restart the measurement with modified gate delay. In this case the next measurement cycle will be performed with a new gate delay. For example, the restart command containing a modified gating parameter can be cyclically sent by the ET-client in response to each received batch of timing data. In this way an online cycle-to-cycle controllable gating is possible (this is shown in the following part). However, it should be taken into account that the TCP/IP network may produce some unexpected delays of real-time data exchange, resulting in episodic loss of synchronism in such interactive operation at high (more than tens of Hz) repetition rate of measurement cycles.

The minimum available cycle duration  $T_C$  (i.e. maximum cycle repetition rate) depends on the amount of TD-blocks, that the ET-server reads, and actual network performance to provide necessary network interactions. That should be taken into account while choosing the parameters  $T_W$  and  $M$  so that they are well adapted to the specific measurement conditions.

Generally the Cyclical mode is oriented mainly to applications with cycle repetition rate up to tens of Hz (this is the case of routine Satellite Laser Ranging). But if the  $M$  value is not too large ( $<10$ ) the cycle repetition rate up to hundreds of Hz is quite practicable. In any case it is recommended to define the waiting period  $T_W$  as long as possible in view of the expected rate of Start-event repetition.

### 1.4.3. Controlling the Event Timer

The A033-ET operation is fully controlled by the ET-client via TCP/IP network. Initial ET-client actions for connection with one of the activated ET-Server and for ET-device arming to following measurements are executed via special server setting panels (Fig.1.28).

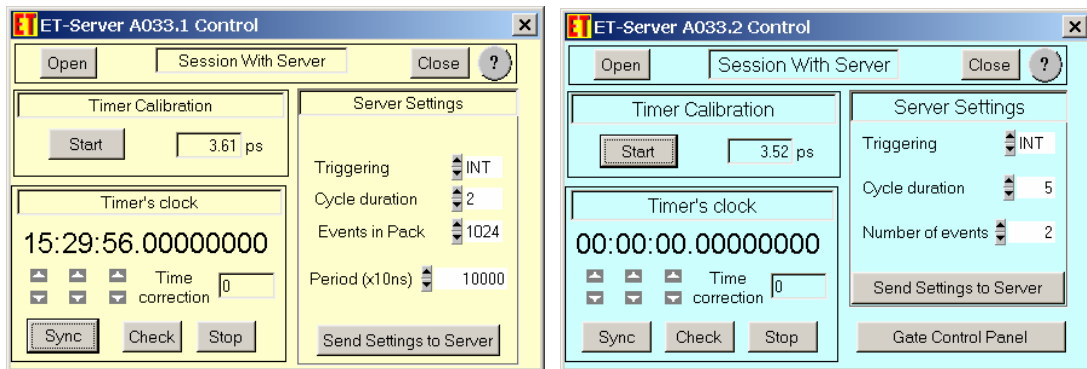


**Fig.1.28. Server setting panels of the ET-server for:**  
**(a) Continuous mode and (b) Cyclical mode.**

Generally the ET-server can be used in time-sharing mode by different ET-clients. So, every ET-client should establish a Session with the ET-server before any other interactions. In this way, the ET-client captures the ET-Server for exclusive use, up to the Session break.

The control procedures, available during the Session, include three preparatory procedures, which are identical for Continues and Cyclical modes:

- *Calibration*; the procedure renews the correction function of TDC;
- *Time synchronization*; the procedure synchronizes the internal time scale with GPS;
- *Time monitoring*; the procedure for monitoring of the internal time scale.

The forth preparatory procedure - setting - differs, because the arming parameters are different for Continues and Cyclical modes. For example, as it was explained above, the Waiting time in Cyclical mode defines how long the ET-Server will wait

Stop events after the Start event. But in Continues mode it is simply the periodicity for checking internal FIFO-memory state.

The basic procedures – measurements – have some distinctions, too. All these procedures will be explained in the next parts.

**Calibration** procedure (button “Start”, Fig.1.28) adapts the A033-ET to the actual operating conditions to achieve the best measurement precision. It includes the statistical identification of the ET-device physical characteristics under current operating conditions (mainly – under temperature conditions), modification of the processing parameters in a view of the identified characteristics, and self-estimation of an actual measurement precision offered after the calibration has been performed.

The A033-ET offers the best single-shot RMS resolution directly after calibration in steady-state operating conditions. Thereafter an ambient temperature variation can impair the RMS resolution.

As can be seen, the A033-ET supports the nearly best RMS resolution in the range of  $\pm 2^{\circ}\text{C}$  of ambient temperature variation (in relation to the temperature, when the ET-device has been calibrated). If the ambient temperature has changed markedly more after the latest calibration, the next calibration restores the best resolution.

Additionally, the calibration procedure includes checking of presence of the external 10 MHz reference signal. It is supposed that basically such signal is provided by a high-performance frequency standard. If the reference signal is not found, the ET-device still is able to operate, using automatically connected internal clock source (100 MHz/10 ppm VCXO).

After completing the calibration procedure the ET-server sends to the ET-client an estimate of actual precision (RMS resolution) that is offered for the following measurement. Typically this estimate should be less than 5 ps.

Normally the calibration procedure lasts about 20 seconds. It may be repeated by the ET-client at any instant, for example, with the aim to check once more the offered precision of measurement or refresh the previous calibration result.

**Time synchronization** procedure (button “Sync”, Fig.1.28), as well as the next procedure of time monitoring, can be performed only if 1 pps sync pulses and 10 MHz reference signal are strictly synchronized (i.e., they come from a common Time and Frequency standard). If this condition cannot be supported, both of the mentioned procedures can be omitted. In this case the Event Timer will be able for further operating, but output time-tags will not be synchronized to the Standard Time scale.

The procedure synchronizes the timer’s clock with 1 pps sync pulses, using the PC system clock to define the reference time. After this, if the PC system clock is not synchronized with the Standard Time scale, the time can be corrected by the arrows buttons in the „time correction” area (Fig.1.28).

In **Time monitoring** procedure (button “Check”, Fig.1.28), the ET-client can receive a sequence of Epoch time-tags corresponding to incoming the 1 pps sync pulses. In other words, the ET-client can see the current time obtained from the timer’s clock to use that for various purposes, for example, to check correctness of the time synchronization by comparing the timer’s clock with any other available clock. In the case of successful previous time synchronization all time-tags should be multiple to 1 sec approximately.

The ET-client can end this procedure at any instant by sending the command STOP to the ET-server (button “Stop”, Fig.1.28).

In the following two parts the measurement procedures for Continuous and Cyclical modes with the corresponding settings are considered.

#### 1.4.4. Measurements in Continuous mode

To start measurement the ET-server should get the necessary settings for corresponding measurement mode. There are 3 separate parameters to be set (Fig.1.28):

1. “Triggering” (either “INT” or “EXT”). If the “EXT” is chosen the start of a measurement will be additionally synchronized by an external pulse at the input “TRIG IN” of the ET-device; in the case of “INT” choice the measurement will be enabled directly by the ET-client, without additional synchronization;
2. „Cycle duration“ [ms] (the period  $T_M$  of the ET-device monitoring);
3. „Events in Pack“ (the number  $M$  of TD-blocks that will be got from the ET-device at one reading) .

The second and the third parameters should be set in a view of expected mean rate of event incoming. Generally the values Cycle duration = 15 ms and Number of Events = 255 are acceptable for any rate, but can be non-optimal for the specific case.

Clicking the button „Send Settings to Server“ leads to sending these three setting parameters and the previously defined time correction value (see above) to the ET-server.

As an example of the measured input signal the self-made Event Timer Test Generator ETTG-1 is taken. ETTG has two outputs for Start pulses and Stop pulses with controllable dividers and has very low jitter about 0.6 ps RMS [1.12]. Timing diagram of these pulses is shown in Figure 1.29. In this example ETTG generates two periodic sequences of test pulses that come at the Inputs A and B of the ET-device so that a group of 1023 periodic Stop pulses follows after each periodic Start pulse. The total rate of incoming the input pulses is about 16 KHz.

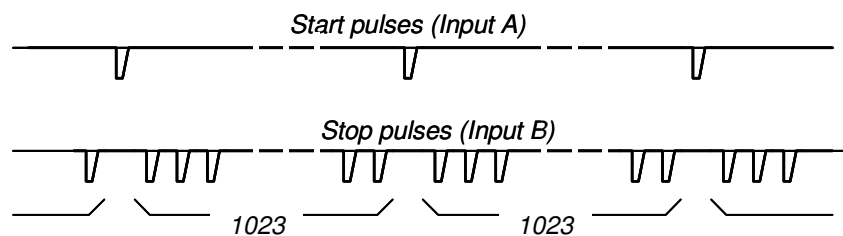


Fig. 1.29. Test pulse sequence for Continuous mode

Once the user pushes the button „RUN“ (Fig.1.30) the measurement starts. During the measurement the ET-server cyclically sends the batch of  $M$  time-tags to the ET-client. Each time-tag is presented by two integers: *data0* and *data1*, specifying the

time instant in the range 24 hours with 1 ps LSD resolution. Sign of the *data0* defines the input of the ET-device, where the measured event came from. To calculate the event time from {*data0*, *data1*} the following simple expression is used:

$$time[i] = (data0) \times 327680 + (data1) / 1000 \text{ [ns]},$$

where possible negative sign of the *data0* is set aside. Note that the size of batch received by the ET-client can differ from the size of batch sent by the ET-sever. Generally the TCP/IP protocol affords both splitting and merging the batch of data blocks to send it by the sequential packets depending on the actual network performance and load. This should be taken into account for the specific data processing by the ET-client.

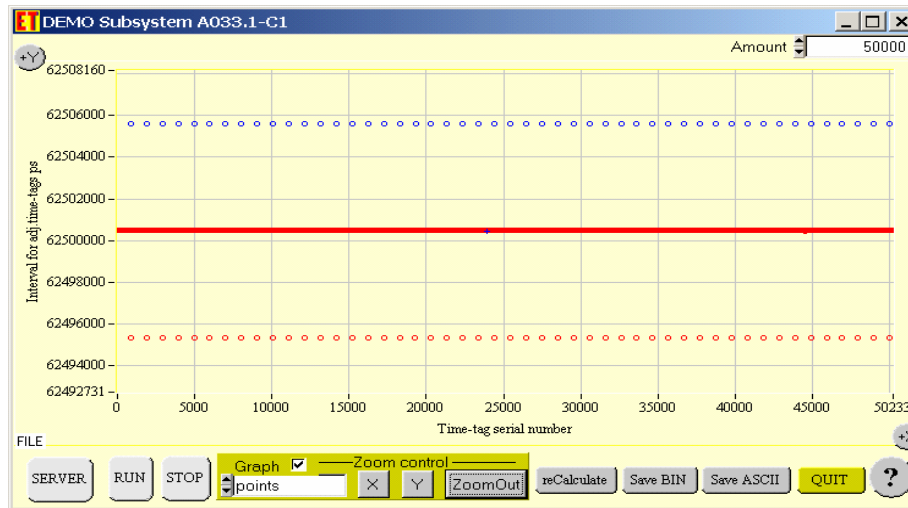


**Fig.1.30. Example of interval measurement in Continuous mode**

Measurement results (Fig.1.30) are presented as values of intervals between adjacent time-tags. The Start-Stop intervals are shown in blue and all others in red. Using zoom for Y-axis one can see each fraction of time intervals separately and calculate its basic statistics. For example, Figure 1.31. shows the central fraction of “Stop-Stop” time intervals. Mean and RMS deviation of these time intervals are 62500.510 ns and 3.3 ps respectively. This indicates that the jitter of test signal itself is negligibly small as compared to the predicted measurement resolution, and the actual timer resolution is even better than the predicted one.

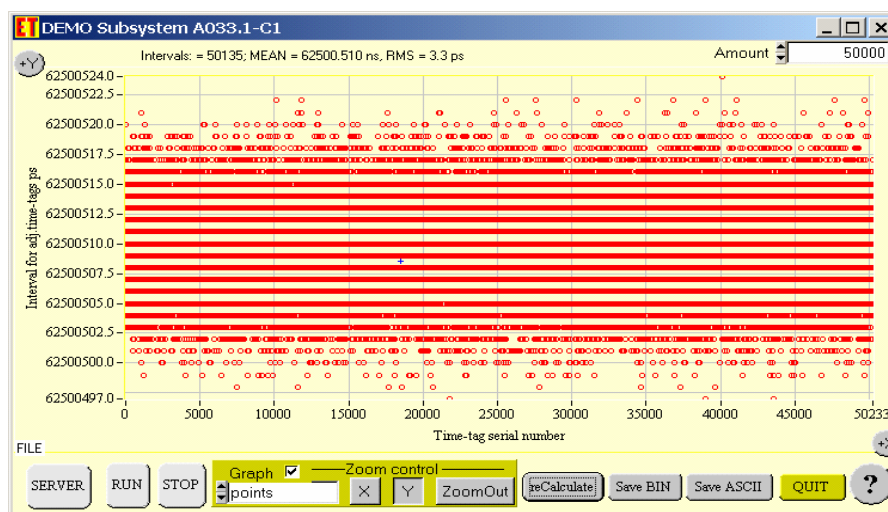


**Fig.1.31. Deviation of intervals between the measured time-tags**

As for “Start-Stop” time intervals (the upper fraction in Fig.1.30), mean and RMS deviation of them are 62500.51 ns and 3.3 ps respectively.

### 1.4.5. Measurements in Cyclical mode

As in previous mode to start measurement the ET-server should get necessary settings. The „Triggering“ parameter is the same, but the others are as follows (Fig.1.28):

- „Cycle duration“ [ms] (the period  $T_W$  defining the waiting time for Stops events);
- „Number of Events“ (the maximum number  $M$  of TD-blocks that can be accumulated in one cycle).

The Cycle duration and Number of Events should be set in view of expected rate of Start-event incoming.

Additionally in Cyclical mode there is a Gate control, which defines the time-out from the coming Start event at the Input A and till the Input B of the ET-device will be opened for the Stop events.

To demonstrate the system work in Cyclical mode the Gate control is used. These gates are generated as the time-out values in form of periodic triangle function within the range from 1 us up to 7000 us and increment/decrement step 10 us (Fig.1.32).

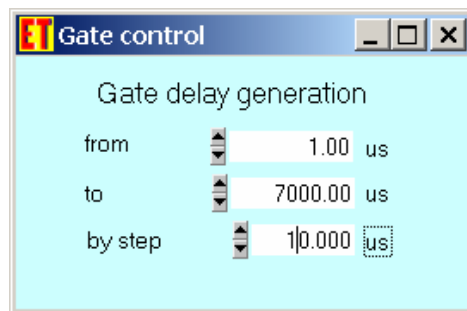


Fig.1.32. Gate control panel

A new value is generated at each Start event and represents a parameter in the start command, which ET-client sends to ET-server. This parameter acts for every measurement cycle as long as a new start command with other parameter will come. During the measurement the ET-client repeats the start command after acceptance of each data batch.

For demonstration of the system operation in Cyclical mode the signal from the ETTG is used as a Start event and generated gate delay as a Stop event. Timing diagram of these pulses generation is shown in Figure 1.33.

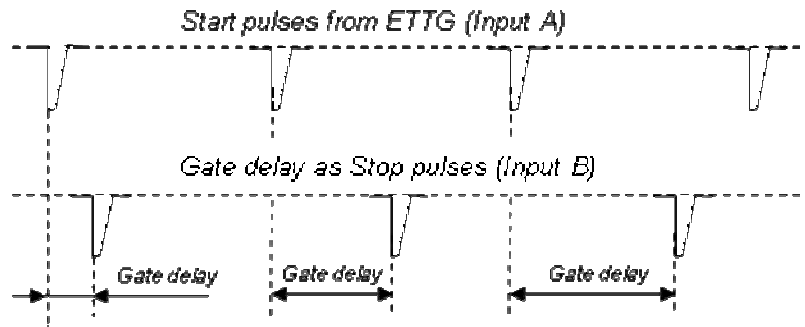


Fig.1.33. Test pulse sequence for Cyclical mode

A new value of the Gate delay is generated at each Start event and represents a parameter in the start command. This parameter acts for every measurement cycle as long as a new start command with other parameter will come. During the measurement the ET-client repeats the start command after acceptance of each data batch.

The ET-server cyclically sends to the ET-Client the time-tags obtained in every measurement cycle. Like in Continuous mode, each time-tag is presented by two integers: *data0* and *data1*. Sign of the *data0* defines the input of the ET-device, which provided the measured event (Start-event/Input A or Stop-event/Input B).

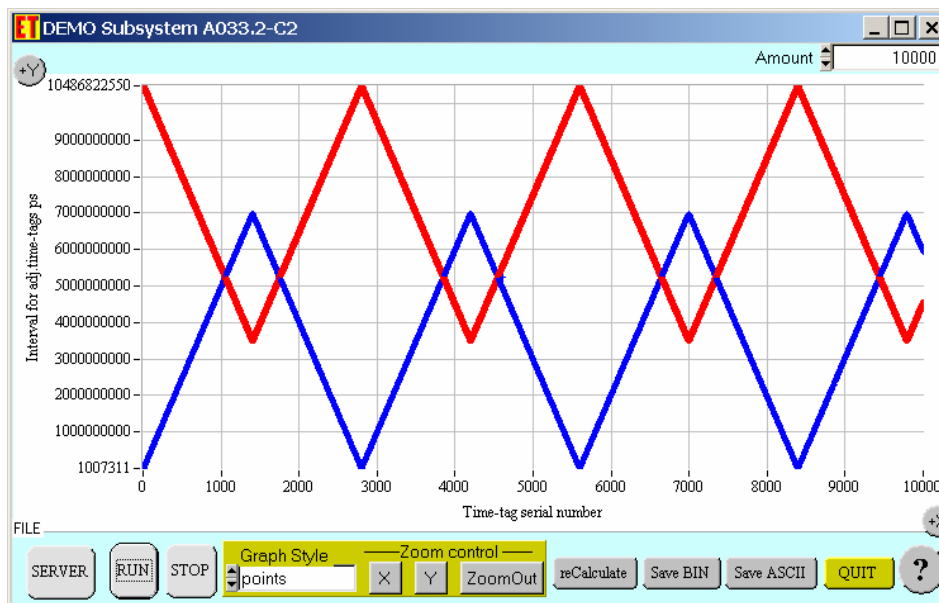


Fig.1.34. Gate delay variation during the measurement in Cyclical mode

In Figure 1.34 values of Start-Stop intervals, which are calculated from the time-tags, are shown in blue and present the Gate delay parameter. The red point shows the intervals from Stop to the next Start. When cycle repetition rate is not so high, gapless online control for gate delay is quite possible. Figure 1.34 illustrates such ability for 120 Hz cycle repetition rate. In this case there are no any gaps in delay control. However, the highest available rate of gapless Gate control may depend on the various objectives, e.g., the actual performance and charge of PC.

### **1.4.6. Conclusions**

Network Timing System on the basis of the A033-ET provides network interface using standard set of TCP/IP application protocol to interact with any remote application requiring precise event timing. Such interfacing is well suited for designing distributed multi-user event timer systems, where user's application software is separated from the specialised software supporting event measurement. In this case the user's software can fully remotely control the A033-ET operation. The configuration of distributed Network Timing system can include many ET-clients and ET-servers. For example, it can be one ET-client in a big town and it connects to the ET-servers, which are located at SLR stations along the path of the observing satellite, and gets the tracking data from these SLR station. Or in turn, if the ET-server is placed in the Scientific Research Centre many ET-clients can connect to this ET-server in time-sharing mode to execute own physical experiments.

### **1.5. Measurement signal digitizing based on timing operation providing for complexity-reduced digital filtering**

The method considered in this section is focused on the problem of reducing the complexity of analog input signal digital filtering and parameter estimation [1.13]. To reach this goal, specific digital representation of the analog signals is used. Crossing events of the input signal and a generated sinusoidal reference function are timed and sequences of these time instants are used for representing the analog input signals. As it is explained in [1.14], using this type of digitizing signals leads to obtaining constant envelope digital signals. Due to this unusual property of the used approach to digitizing, a wide variety of signals then can be converted into a specifically sampled sinusoidal function characterized by a given frequency, amplitude and phase angle. That makes it possible to perform digital filtering of this type of digital signals by using the required filter impulse response function for modulating this sinusoidal function, sampling of it at the time instants according to the digital representation of the respective input signal with subsequent calculations of the instantaneous values of the filter output signals. They are then defined as averaged values of the mentioned modulated sinusoid samples taken at the crossing time instants. This method for signal complexity-reduced digital filtering and parameter estimation leads to elimination of repetitious multiplications of a large quantity of multi-digit numbers required in the case of traditional digital filtering.

Thus a specific approach to signal digitizing [1.15-1.20] is considered and discussed in this paper. Time diagrams given in Figure 1.35 illustrate this approach and they are explained in the following subsections. A sequence of time instants when events of a signal and reference sine wave crossings occur is used in this case as the discrete representation of the respective continuous signal. That leads to specific conditions both for analog measurement signal digitizing and digital processing. Various aspects of performing signal digitizing in this way are described in [1.21]. A lot of attention is paid to using this approach to signal digitizing for multi-channel data acquisition from a large quantity of signal sources [1.15, 1.16, 1.22]. Here the emphasis is on the potential and advantages of this approach in the area of complexity-reduced digital processing of measurement signals converted in the

considered way. While some aspects of this capability have been considered before [1.22], the paper [1.13] is focused on the digital filtering application.

### 1.5.1. Timing of signal-reference crossing events

Analog input signals, before their digital filtering, apparently have to be converted into their digital counterparts. Using of timed signal and reference sine wave crossing events for digital representation of analog input signals is considered in this paper. This approach is illustrated in Figure 1.35.

While usually the digital signal is formed as a sequence of the original analog signal sample values  $x_1, x_2, x_3, \dots$ , to achieve the complexity reduction of the subsequent filtering process, it is proposed to perform the sampling operation as shown in Figures 1.35. Specifically, a sinusoidal reference function is generated and the analog input signal is digitally represented as a sequence of time instants when the events of the input signal and the reference function crossings occur. This specific digital signal fully represents the analog input signal. All types of input signals are converted in this way into a sampled sinusoidal reference waveform characterized by a given frequency  $f_r$ , amplitude  $A_r$  and phase angle  $\varphi_r$ . In other words, the information carried by the original analog input signal is transferred then to this specific digital signal. It is fully reflected by the points shown on the time axis as shown in Figure 1.35(b).

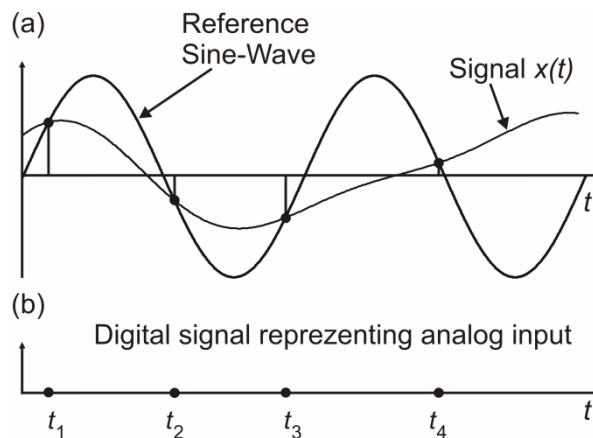


**Figure 1.35. Digital representation of an analog signal formed according to the considered method. (a) detection of signal and sinusoidal reference function crossing events; (b) sequence of timed crossing events fully representing the original analog signal, assuming that the parameters of the reference function are given.**

These points indicate the time instants  $\{t_k\}$  when the crossing events of the measurement signal and the reference function occur. Therefore the digital representations of the original analog input signals can be given in the form of this type of digital point processes shown in Figure 1(b). As the parameters  $f_r, A_r$  and  $\varphi_r$  of the reference sine-wave function are a priori given, the original signals could be reconstructed from such point processes  $\{t_k\}$ .

### 1.5.2. Basics of complexity-reduced filtering

The fact that input signals invariably are represented by the sampled reference sinusoid of given parameters makes it possible to transform the expressions typically used as the basis for digital filtering. To demonstrate this, the typically used approach to filtering might be compared with the considered method.

In the case where filtering is carried out according to the conventional method, the digital filter typically used for extracting the  $i$ -th frequency from the input signal  $x(t_k)$  is characterized by a response function given as

$$h(t) = \sin 2\pi f_i t$$

The estimate of a sample value  $y(t_n)$  of the output signal of such a selective digital filter is calculated as follows:

$$y(t_n) = \frac{2}{N} \sum_{k=0}^{N-1} x_k h(t_k) = \frac{2}{N} \sum_{k=0}^{N-1} x_k \sin 2\pi f_i t_k$$

Apparently  $N$  multiplications of the multi-digit numbers representing the sample values of the input signal  $x(t_k)$  and the response function  $h(t)$  have to be carried out to obtain this particular estimate of the respective single instantaneous value  $y(t_n)$  of the filter output signal. The considered here method makes it possible to obtain the same estimate without execution of these  $N$  multiplication operations.

The method for the complexity-reduced filtering exploits the fact that the digital representation of the input signal is a reference sinusoid of a fixed amplitude  $A_r$ , frequency  $f_r$  and phase angle  $\varphi_r$  sampled at the time instants when crossings of it with the input signal take place. This fact allows using of the respective sampling instant sequence as the digital signal representing the input signal. That in turn leads to the possibility of transforming the procedure of the considered selective filtering. If  $A_r = 1$  then the estimation of the sample value  $y(t_n)$  of the output signal of the selective digital filter extracting the  $i$ -th frequency according to the invented method is based on the following equation:

$$y(t_n) = \frac{2}{N} \sum_{k=0}^{N-1} \sin 2\pi f_r t_k \sin 2\pi f_i t_k$$

It reflects the fact that the required filter response is used for amplitude modulation of the reference function and that each instantaneous value of the output signal is calculated as the mean value of this amplitude modulated waveform. Evidently this equation can be converted and given as:

$$y(t_n) = \frac{1}{N} \sum_{k=0}^{N-1} \cos 2\pi(f_r - f_i)t_k - \cos 2\pi(f_r + f_i)t_k$$

$$y(t_n) = \frac{1}{N} \sum_{k=0}^{N-1} H(t_k)$$

Therefore filtering in this case is simply reduced to averaging the sample values  $H(t_k)$  taken from the following function at the discrete time instants  $\{t_k\}$  digitally representing the input signal:

$$H(t) = \cos 2\pi(f_r - f_i)t - \cos 2\pi(f_r + f_i)t$$

As this function is derived as a product of the multiplied generalized input signal waveform and the filter response function, it is denoted as  $H(t)$ , it is called and considered as a template for calculating the sample values of the filter output signal. The dimension of the instantaneous values  $H(t_k)$  of this template  $H(t)$  is equal to the dimension of the respective input signal.

### **1.5.3. Involved filtering procedures**

The following procedures have to be carried out to perform filtering:

- Generating a sinusoidal reference function of a given amplitude, phase angle and frequency with this frequency outside the frequency range of the analog input signal to be digitally filtered.
- Detecting the time instants of the input signal and the reference function crossings.
- Timing the crossing time instants and forming a sequence of the respective digital quantities.
- Generating the template for calculation of the filtered signal instantaneous values.
- Positioning this template so that its middle point coincides in time with the considered instantaneous value of the filter output signal.
- Sampling the properly positioned template at the crossing event timed instants.
- Calculating the respective instantaneous values of the filter output signal as the mean value of the sampled values of said template.
- Initiating the following cycles of filtering by shifting the template into the position for estimation the next output signal value.

This approach to filtering, in general, holds also for other types of filtering performed on the basis of more complicated filter response functions. That is how the digital representations of the input signals might be filtered and processed without performing a large quantity of repetitious multiplications of multi-digit numbers.

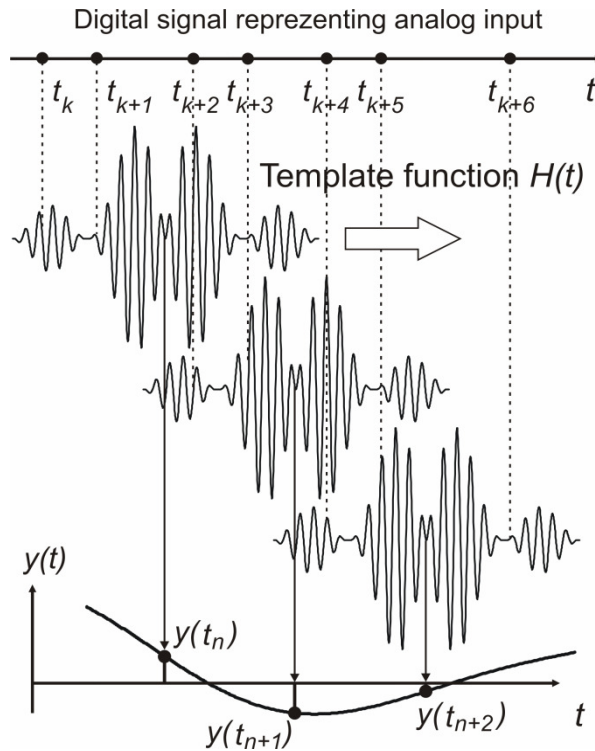


**Fig. 1.36. Diagram illustrating filtering performed according to the considered method.**

Figure 1.36. illustrates low-pass filtering performed according to this method. The template  $H(t)$  in this case is composed from a multiple cosine functions at frequencies covering the given filter pass-band  $M\Delta f$  with sufficiently small frequency steps  $\Delta f$  as follows:

$$H(t) = \frac{1}{M} \sum_{i=1}^M [\cos 2\pi(f_r - i\Delta f)t - \cos 2\pi(f_r + i\Delta f)t]$$

where  $i = 1, 2, \dots, M$ .

To perform the filtering operation, time-limited  $H(t)$  is positioned on the time axis so that the time coordinate of its peak coincides with time instant  $t_n$  for which the instantaneous value  $y_n$  of the filter output signal is to be calculated. Template  $H(t)$  then is sampled at the time instants belonging to row  $\{t_k\}$ . The output signal instantaneous value  $y_n$  directly below the peak of template  $H(t)$  is calculated as the average value of the particular set of the sample values  $H(t_k)$  of the template corresponding to the given position of  $H(t)$  on the time axis. To obtain the next output signal value  $y_{n+1}$ , template is shifted to the right for a time step  $\Delta t$  so that its peak is positioned at the time instant  $t_{n+1}$  and the above procedure is repeated. In general, the averaged values of the sampled templates represent the indicated instantaneous values of the output signal shown in Figure 1.36.

#### **1.5.4. Filter implementation specifics**

As it follows from the described filtering procedure, a multi-port memory storing the template  $H(t)$ , and attached array of adders performing averaging of read-out

template values are in the core of this type of filters. This part of the filter structure is shown in Figure 1.37. As can be easily seen, the basic advantage of the filter structure is provided by the design simplicity of this core.

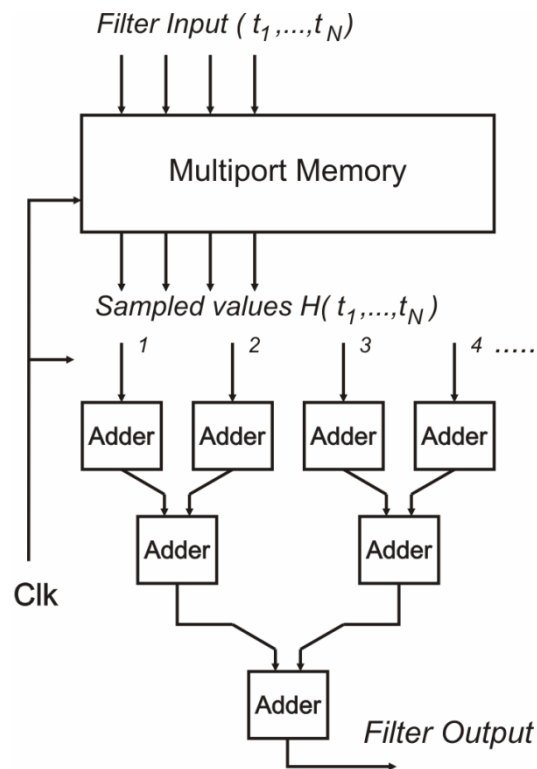


**Fig. 1.37. Considered structure of the filter.**

Specifics of the filter implementation on the basis of FPGA have been considered and the expected basic parameters evaluated. As performance of the filter basically depends on the design of this part of the whole filter, implementation of it as a FPGA structure has been considered and expected performance evaluated.

While shape of template  $H(t)$  obviously depends on the considered filter response function, it depends also on the conditions for input signal digitizing. Specifically, on the enabling function used at detection of the input signal and the reference function crossing time instants. If this crossing event detection is enabled during half periods of the enabling function as often is the case, then only half of the whole template digital values has to be kept in the memory.

Next filter parameter essentially affecting the filter design is the number of crossing points falling within the time span of the template. This parameter is similar to the count of filter coefficients used in the case of traditional digital filters. It depends on a several factors, such as the frequency of the enabling function used at digitizing the input signal and the required filtering precision. Equally important parameter is time resolution required at the crossing point detection. It basically depends on the first derivative of the template function and the required precision of the template sample values so that the needed time resolution can vary in a relative wide margin from a case to case.

While there are also various other factors defining the design of this type of filters and consideration of them is outside the scope of this paper, attention is drawn to the

fact that the mentioned multi-port memory actually consists of a number of basically the same type autonomous blocks. Therefore the complexity of the filter core first of all depends on the number of these memory sections and the capacity of them measured in numbers of words and bits per word. The number of words stored in a single memory section is reduced by using quantizing along the time axis.

Evaluation of the required filter resources were estimated using *Altera Quartus* software and taking into account parameters of *Cyclone II EP2C70F672C6N* FPGA chip. Simulation results show that if pipelining is included in the filter functions then the maximum frequency of the filter output data obtaining depends only on the respective FPGA chip clock frequency as the delay related to the involved filtering procedures are less than 10 nanoseconds. It means that in the case of the indicated chip this frequency is 100 MHz. At 8 bit time value  $(t_1, \dots, t_N)$  encoding for a memory segment, the needed memory capacity is reasonable even at 128 memory segments and then the memory does not slow down the systems clock frequency.

### **1.5.5. Conclusion**

As the considered method for multiplier-less filtering has been developed recently [1.13], there still are theoretical issues that have to be studied more to realize full potential of this method. Nevertheless it is already practically applicable and designing filters on the basis of it would lead to multiplier-less filter structures that are complexity-reduced, energy-efficient and fast. Timing of signal and reference function crossing events has to be carried out with good precision as performance of this type of filters to a large extent depends on that. While FPGA chips can be used for implementation of the described type of filtering, they do not contain microelectronic elements for the required input signal encoding. So it seems that for obtaining the best possible results in this area implementation of the considered filtering method should be based on ASIC.

### **References**

[1.1] Yu. Artyukh, "A method for continuous superprecise time-interval measurement". *Automatic Control and Computer Sciences*, Vol. 35, No.5, pp. 11-18, 2001.

[1.2] Yu. Artyukh, V. Bepal'ko, E. Boole, V. Vedin, "Advances of High-precision Riga Event Timers," *Proc. 16th International Workshop on Laser Ranging* (Poznan, Poland, October 2008), Vol.2, pp.398-403.

[1.3] Yu. Artyukh, E. Boole, J. Bule, "High-precise determination of correction function for reducing integral non-linearity of DSP-based event timer", In *Proc. 13th Biennial Baltic Electronics Conference (BEC2012)* , Tallinn, Estonia, October 3-5, 2012, pp.303-306.

[1.4] Yu. Artyukh, V. Bepal'ko, E. Boole, "Non-linearity Errors of High-precision Event Timing", *Automatic Control and Computer Sciences*, vol. 42, No. 4, pp. 191-196, 2008.

[1.5] Yu. Artyukh, E. Boole, "Jitter Measurement on the Basis of High-precision Event Timer", *Metrology and Measurement Systems*, Vol. XIII, No.3, pp.453-460, 2011.

[1.6] A.Mezerins and V.Vedin, "Reliability enhancement of event timer calibration by using a dual PLL for the calibrating signal generation", In Proc. 13th Biennial Baltic Electronics Conference (BEC2012) , Tallinn, Estonia, October 3-5, 2012, pp.113-114.

[1.7] Yu.Artyukh, V. Bepal'ko, E. Boole. Potential of the DSP-based Method for Fast Precise Event Timing. // *Electronics and Electrical Engineering - Kaunas: Technologija*, 2009, No. 4(92), p.19–22.

[1.8] Rybakov, A.S., Estimating of Time Position of the Pulse Signal Midpoint by a Small Number of Samples in High Precision Event Timing, *Autom. Cont. Comp. Sci.*, 2009, vol. 43, no. 1, pp. 9–16.

[1.9] Rybakov, A.S., Reconstruction of the Corrective Component of the Transfer Function of the Interpolator in the Process of Calibration of Precision Event Timer, *Autom. Cont. Comp. Sci.*, 2010, vol. 44, no. 1, pp. 11–21.

[1.10] A. S. Rybakov, „Improvement of the Accuracy of the Time Position Estimation of the Gravity Center of an Analog Signal on the Basis of Discrete samples“, *Automatic Control and Computer Sciences*, 2011, Vol. 45, No. 6, pp. 301–313.

[1.11] V. Bepal'ko, E. Boole, and J. Savarovskiy, „An Instability Estimation of Precision Time Intervals“, *Instruments and Experimental Techniques*, 2012, Vol. 55, No. 3, pp. 377–382.

[1.12] Yu. Artyukh, V. Bepal'ko, K. Lapushka, A. Rybakov. Event timing system for Riga SLR station. *Proceedings of the 15th International Workshop on Laser Ranging*, Canberra, Australia, October 16-20, 2006.

[1.13] Yu. Artyukh, I. Bilinskis, K. Sudars, "Method for complexity-reduced digital filtering and parameter estimation of analog signals", Assignee: Institute of Electronics and Computer Science of Latvia, *European patent Bulletin*, January 7, 2009.

[1.14] Yu. Artyukh, I. Bilinskis, K. Sudars, „Measured signal digitizing based on timing operation providing for complexity-reduced digital filtering“, *Metrology and Measurement Systems*, (in publication)

[1.15] I. Bilinskis, *Digital Alias-free Signal Processing*, John Wiley & Sons, UK, 2007.

[1.16] I. Bilinskis, K. Sudars, "Digital Representation of Analog Signals by Timed Sequences of Events", *Electronics and Electrical Engineering*, 3(83), 2008.

[1.17] V.R. Daria, C. Saloma, "High- accuracy Fourier Transform Interferometry, without Oversampling, with a 1-bit Analog-digital Converter", *Applied Optics*, 39(1), 2000.

[1.18] R. Kumaresan, Y. Wang, "On Representing Signals Using Only Timing Information", *J. Acoust. Soc. Am.*, 110(5), Pt. 1, 2001.

[1.19] M.A. Nazario, C. Saloma, "Signal Recovery in Sinusoid-Crossing Sampling by Use of the Minimum – negativity Constraint", *Applied Optics*, 37(14), 1998.

[1.20] Y.Y. Zeevi, A. Gravriely, S. Shamai-Shitz, "Image Representation by Zero and Sine-wave Crossings", *J. Opt.Soc. Am. A*, No. 4, 1987.

[1.21] K. Sudars, Z. Ziemelis, "Expected performance of the sine-wave crossing data acquisition systems", *Proceedings of DASP Workshop*, London, UK, 17 April 2007.

[1.22] I. Bilinskis, K. Sudars, "Processing of Signals Sampled at Sine-wave Crossing Instants", *Proceedings of DASP Workshop*, London, UK, 17 April 2007, p. 45-50.

## **2. Superplatjoslas tuvdarbības impulsu radara vairākantenu prototipa izstrāde un tā iegūto signālu efektīvas apstrādes optimizācija**

### **2.1. *Saskaņojošas iekārtas***

Veikti pētījumi saskaņojošas iekārtas (SI) izvēlei uztvērējam un raidītājam virsplatjoslas impulsa lokatoram:

1. saskaņojošas iekārtas izvēle raidītājā, lai saskaņotu ar simetrisku virsplatjoslas antenu, saskaņojošu rezistoru nominālu izvēle antenai Bow-tie;
2. saskaņojošas iekārtas izvēle uztvērējam antenai Bow-tie, pētījums ar mērķi iegūt maksimāli neizkropļotu signālu uztvērējā:
  - a. saskaņojoša iekārta – diferenciālais virsplatjoslas pastiprinātājs;
  - b. saskaņojoša iekārta – transformators - garā līnija;
  - c. saskaņojoša iekārta – platjoslas transformators;
  - d. saskaņojoša iekārta – garās līnijas pusviļņa posms;
  - e. saskaņojoša iekārta uz koncentrētiem elementiem;
  - f. saskaņojoša iekārta – koaksiālais transformators.

Tiek gatavota atskaite. Plašāks izklāsts Pielikumā #1 (krievu val.).

### **2.2. *Experiments with the 2D and 3D through wall imaging systems***

This work addresses object localization using UWB radio location in order to study the possibilities to locate an object behind a wall. The work was drawn up to solve topical problems in object positioning:

1. creation of a model for antennae systems for both 2D, 3D and extended 3D object localization;
2. establishing the algorithm of object localization and creation of a software application that localizes objects using the 2D and the 3D model;
3. discussion of the methods for signal processing to improve object localization: averaging and median approach, as well using the “window” and convolution filter;
4. discussion of the summing of offset signals in order to improve the signal/noise ratio.

The application of the methods referred to in this work resulted in a successful localization of the object with sufficiently high accuracy of localization.

### 2.2.1. Antenna system with 2D imaging possibility

In this model, using three receiving antennas and one transmitting antenna, the transmitting antenna is placed above the receiving antenna in the centre of the antenna system. Such location has been chosen to symmetrically divide the received signal between the antenna reflectors, see at Fig. 2.1.

Using three receiving antennas it's possible to make more accurate measurement.

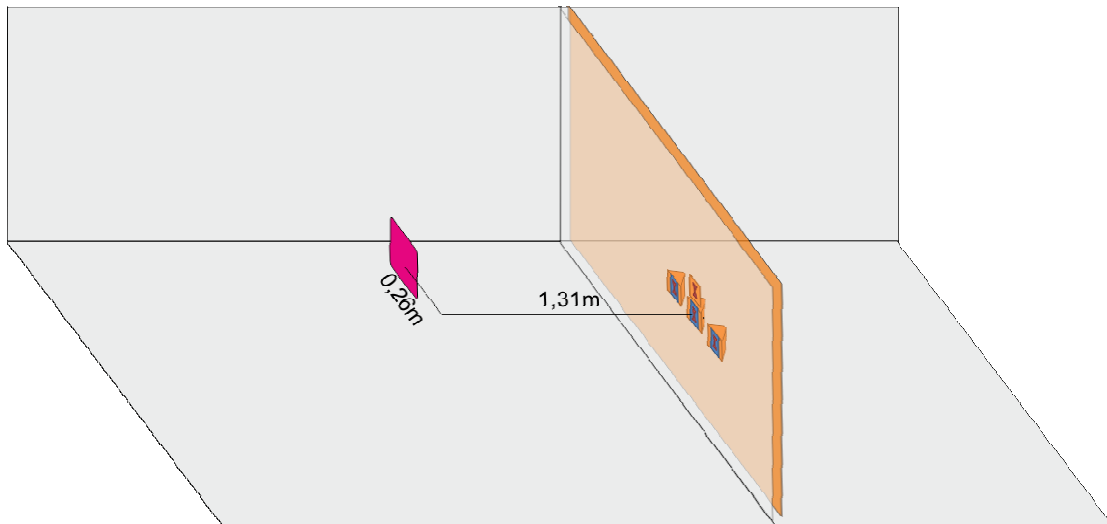


Figure 2.1 Receiving antenna placed in the same plane on the line

Using this type of antenna system, it's possible to get data for object positioning with 0,03m precision at 1,5 m distance. With 2D model it's possible to determine the distance between the object and antenna system and find out how far to the left or how far to the right from centre of antenna the object is positioned.

Model (Fig.2.2) has been used to detect the relative position of object.

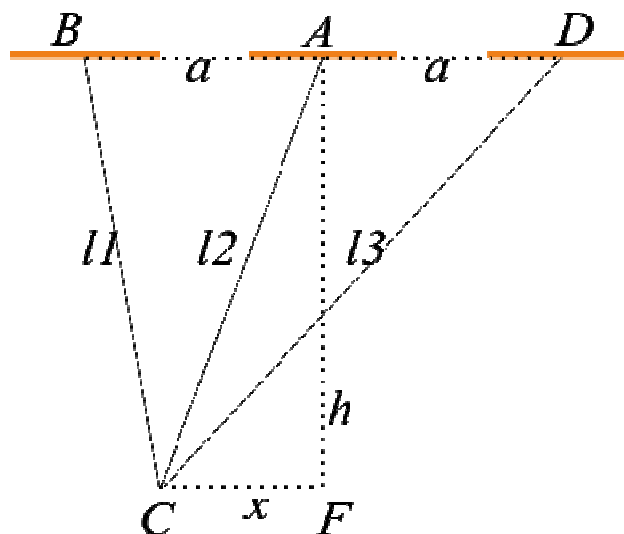


Figure 2.2 2D localization model

Let  $l_1$ ,  $l_2$  and  $l_3$  be the measured distances between receiving antennas and object. It is known that the distance between antennas is  $a$ . This allows the usage of formula which relates sides  $l_1$ ,  $l_3$  and  $2a$  of triangle with median  $l_2$ :

$$l_2^2 = \frac{1}{2}l_1^2 + \frac{1}{2}l_3^2 - a^2. \quad (1)$$

Due to inaccuracy of measurement, the formula (1) cannot be fulfilled. Let  $\Delta l_1$ ,  $\Delta l_2$  and  $\Delta l_3$  be the difference between real and measured distances. It allows speaking of exact equation:

$$(l_2 - \Delta l_2)^2 = \frac{1}{2}(l_1 - \Delta l_1)^2 + \frac{1}{2}(l_3 - \Delta l_3)^2 - a^2 \quad (2)$$

with yet to be determined  $\Delta l_1$ ,  $\Delta l_2$  and  $\Delta l_3$ . Assuming error of measurement to be normally distributed random variable,  $\Delta l_1$ ,  $\Delta l_2$  and  $\Delta l_3$  which fulfil (2) with the least

$$\Delta l_1^2 + \Delta l_2^2 + \Delta l_3^2, \quad (3)$$

can be viewed as the most probable values of error.

Solving (2) for  $\Delta l_3$  yields:

$$\Delta l_3 = l_3 + \sqrt{2l_2^2 - 4l_2\Delta l_2 + 2\Delta l_2^2 - l_1^2 + 2l_1\Delta l_1 - \Delta l_1^2 + 2a^2} \quad (4)$$

or

$$\Delta l_3 = l_3 - \sqrt{2l_2^2 - 4l_2\Delta l_2 + 2\Delta l_2^2 - l_1^2 + 2l_1\Delta l_1 - \Delta l_1^2 + 2a^2}. \quad (5)$$

Since  $l_3 > 0$  and square root of positive number is a positive number, (4) cannot be the solution.

Substituting (5) into (3) gives expression:

$$G = \Delta l_1^2 + \Delta l_2^2 + \left( l_3 - \sqrt{2l_2^2 - 4l_2\Delta l_2 + 2\Delta l_2^2 - l_1^2 + 2l_1\Delta l_1 - \Delta l_1^2 + 2a^2} \right)^2, \quad (6)$$

which has to be minimized with respect to  $\Delta l_1$  and  $\Delta l_2$ . In order to do it, let's find partial derivatives of (6):

$$G_{\Delta l_1} = - \frac{\left( l_3 - \sqrt{2l_2^2 - 4l_2\Delta l_2 + 2\Delta l_2^2 - l_1^2 + 2l_1\Delta l_1 - \Delta l_1^2 + 2a^2} \right) (2l_1 - 2\Delta l_1)}{l_3 - \sqrt{2l_2^2 - 4l_2\Delta l_2 + 2\Delta l_2^2 - l_1^2 + 2l_1\Delta l_1 - \Delta l_1^2 + 2a^2}} + 2\Delta l_1 \quad (7)$$

and

$$G_{\Delta l_2} = - \frac{\left( l_3 - \sqrt{2l_2^2 - 4l_2\Delta l_2 + 2\Delta l_2^2 - l_1^2 + 2l_1\Delta l_1 - \Delta l_1^2 + 2a^2} \right) (-4l_2 + 4\Delta l_2)}{l_3 - \sqrt{2l_2^2 - 4l_2\Delta l_2 + 2\Delta l_2^2 - l_1^2 + 2l_1\Delta l_1 - \Delta l_1^2 + 2a^2}} + 2\Delta l_2. \quad (8)$$

Equating (7) and (8) to zero, we obtain a system of equations. Solving it for  $\Delta l_1$  and  $\Delta l_2$ , as a solution we obtain:

$$\Delta l_1 = -l_1(-1 + H) \quad (9)$$

and

$$\Delta l_2 = 2 \frac{l_2(-1+H)}{-2+3H}, \quad (10)$$

where  $H$  is a root of

$$(9l_1^2 + 9l_3^2)Z^4 + (-12l_1^2 - 12l_3^2)Z^3 + (4l_1^2 - 2l_2^2 + 4l_3^2 - 18a^2)Z^2 + 24a^2Z - 8a^2 = 0. \quad (11)$$

(11) can be solved, for example, by dichotomy method. Substituting obtained  $Z$  in (9) and (10), we obtain correspondingly  $\Delta l_1$  and  $\Delta l_2$ . By substituting obtained  $\Delta l_1$  and  $\Delta l_2$  into (5), one can get the value of  $\Delta l_3$  but it's not required in determining the position of object. Indeed, sides of triangle  $l_1 - \Delta l_1$ ,  $l_2 - \Delta l_2$  and  $a$  uniquely determine the height of triangle ( $x$  position) and the size of side projection ( $y$  position).

We have made a computer program in C# to calculate object position using above-mentioned theoretical substantiation. An example of its application is seen in Fig. 2.3.

```

file:///c:/users/janis/documents/visual studio 2010/Projects/2d/2d/bin/Debug/2d.EXE
Pirmā faila vārds:
C:\Users\Janis\Desktop\tris antenu tests rindaa\l1.csv
Ātrasto pozīciju skaits2
-----Objekta pozīcija: 2042
-----Ātskaites punkts: 303

Otrā faila vārds:
C:\Users\Janis\Desktop\tris antenu tests rindaa\l2.csv
Ātrasto pozīciju skaits2
-----Objekta pozīcija: 2106
-----Ātskaites punkts: 306

Trešā faila vārds:
C:\Users\Janis\Desktop\tris antenu tests rindaa\l3.csv
Ātrasto pozīciju skaits2
-----Objekta pozīcija: 2142
-----Ātskaites punkts: 303

-----Sapientie attālumi pēc to apstrādes-----
1739 L1 garums
1800 L2 garums
1839 L3 garums

-----2D objekta konstatēšanas algoritms ar trīs antenām-----

Attālums metros no antenu bloka: 1,3091
Nohide metros pa X asi : 0,2587
Objekts atrodas pa labi no centra

```

Figure 2.3 Console 2D

### 2.2.2. Antenna system with 3D imaging possibility

This model uses three blocks, each of which consists of one transmitting and one receiving antenna, where the receiving antenna positioned adjacent to each of its transmitting antenna, as seen in Fig. 2.4. Such a model has been chosen to accurately determine the location of the object. Since the antenna blocks are separated by a relatively long distance the reflections from other blocks can be viewed as a noise.

Using this type of antenna system, it's possible to get data for object positioning with 0,07m precision at 1,5 m distance. With 3D model it's possible to determine the distance between the object and antenna system and find out how far to the left or how far to the right from centre of antenna and how high or low from centre of antenna system the object is positioned.

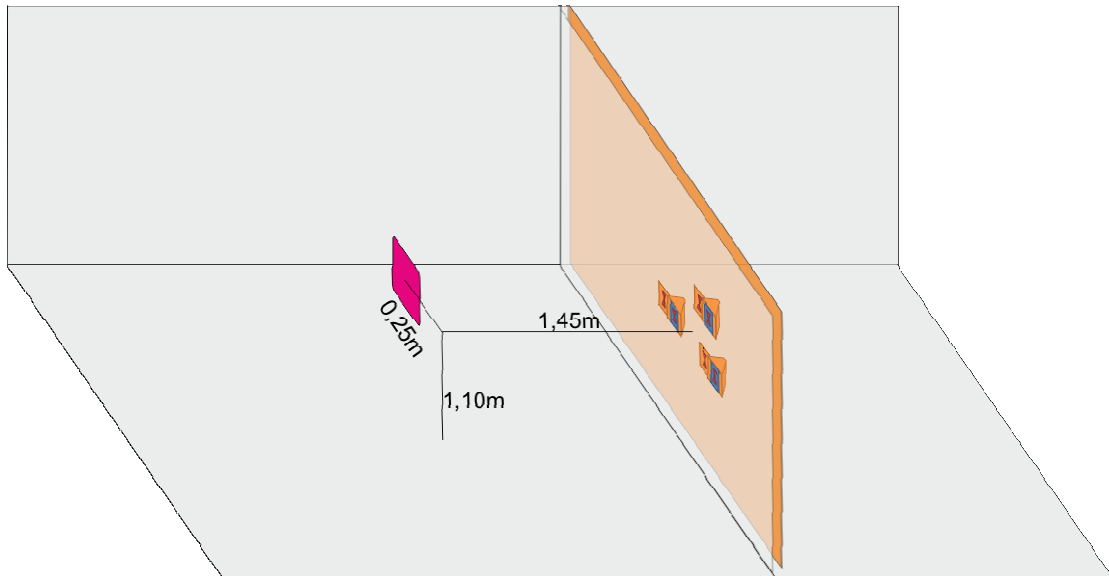


Figure 2.4 3D antenna system model

3D model (Fig.2.5.) has been used to detect the relative position of object.

3D localization algorithm is designed to detect the object position (coordinates) along the x, y and z axes. This localization pattern is using three antenna signals received by an antenna located in pyramidal form. Using the information received from the three antennas it's possible to locate objects in three dimensions. However, the 3D location with this model does not allow error correction due to lack of additional data, using which these steps could be performed.

In 3D localization, as well as in the previous model, geometric properties of triangles are used, see Fig. 2.5. Points B, A and D denote the position of radar receiver antenna, C is the position object.

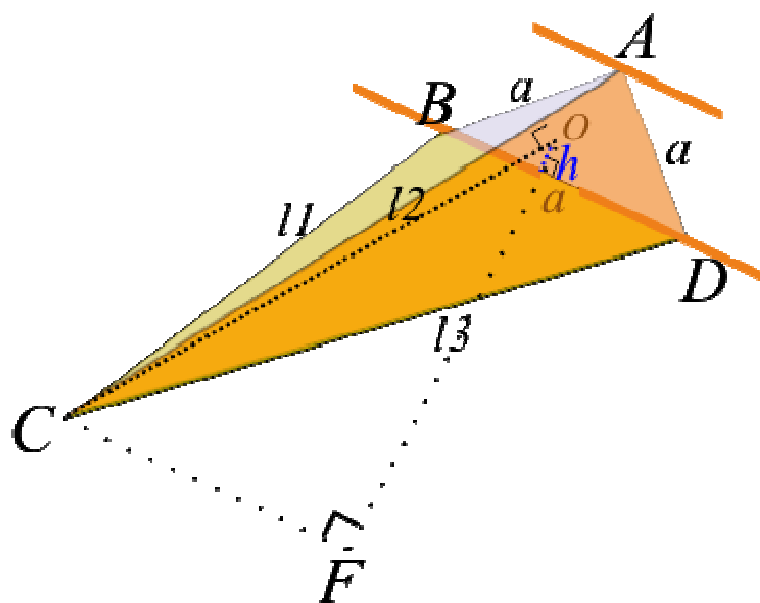


Figure 2.5 3D localisation model

It is known that it is possible to calculate the distance to object by using signal reflected from it. Due to it, reflection from object was recorded in each receiving antenna, see Fig. 2.6-2.8. In order to distinguish them they were labelled *signal1*, *signal2* and *signal3*.

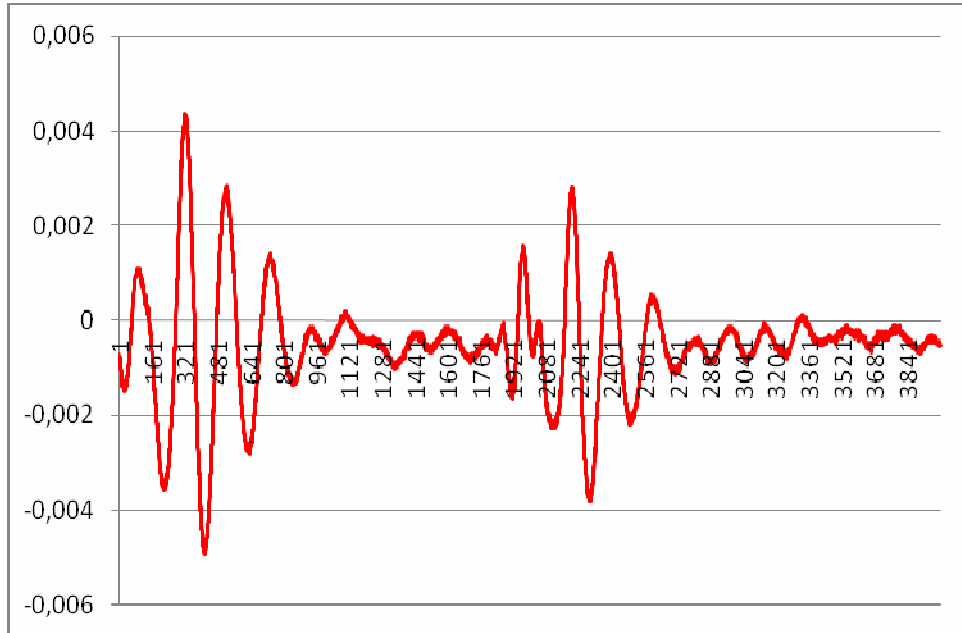


Figure 2.6 Reflection of object, as seen in antenna B - *signal1*

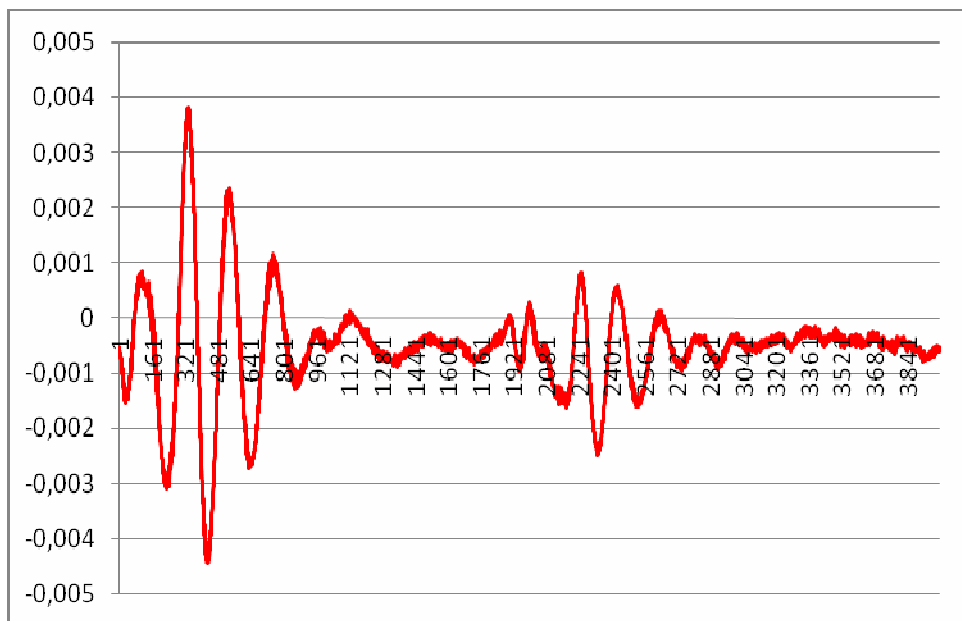


Figure 2.7 Reflection of object, as seen in antenna A - *signal2*

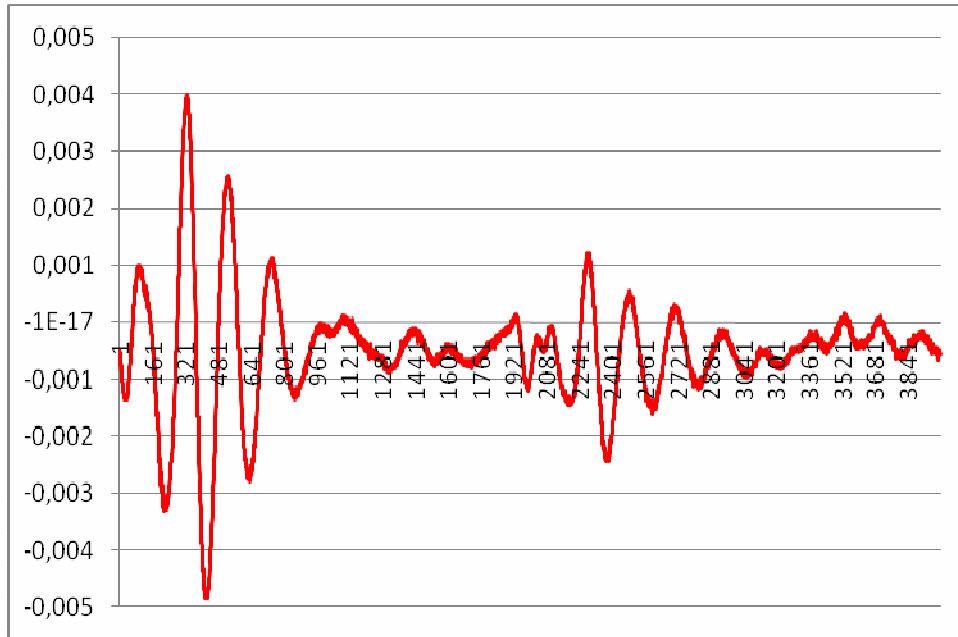


Figure 2.8 Reflection of object, as seen in antenna D – *signal3*

In records *signal1*, *signal2* and *signal3*, distances *l1*, *l2* and *l3* are hidden. Knowing these values and using the properties of triangles, it's possible to calculate the distance OF, corresponding to the object distance from the radar, the distance CF, which corresponds to the displacement of the object locator in the centre, as well as the vertical position *h* relative to the radar centre.

We have made a computer program in C# to calculate object position using above-mentioned theoretical considerations. An example of its application is seen in Fig. 2.9.

```

file:///C:/Users/Janis/Documents/Visual Studio 2010/Projects/3d/3d/bin/Debug/3d.EXE
Pirmā faila vārds:
C:\Users\Janis\Desktop\3d\l1.csv
Atrasto pozīciju skaits2
----Objekta pozīcija: 2291
----Atskaites punkts: 320

Otrā faila vārds:
C:\Users\Janis\Desktop\3d\l2.csv
Atrasto pozīciju skaits2
----Objekta pozīcija: 2313
----Atskaites punkts: 337

Trešā faila vārds:
C:\Users\Janis\Desktop\3d\l3.csv
Atrasto pozīciju skaits2
----Objekta pozīcija: 2280
----Atskaites punkts: 330

-----Šāpēntie attālumi pēc to apstrādes-----
1971 L1 garums
1976 L2 garums
1950 L3 garums

--3D objekta konstatēšanas algoritms ar trīs antenām piramidveida novietojums--

Objekta attālums no antenu bloka metros: 1,455
Nobīde metros horizontāli pa X asi : 0,0617
--Objekts atrodas pa labi no centra
Nobīde metros vertikāli pa y asi : -0,0527
--Objekts atrodas zem lokatora

Rezultāts reāls

```

Figure 2.9 Console 3D

### **2.2.3. Antenna system with 3D extended imaging possibility**

To improve 3D imaging, signal summing can be used. In this system is used six receiving antennas and three transmitting antenna, see Fig. 2.10.

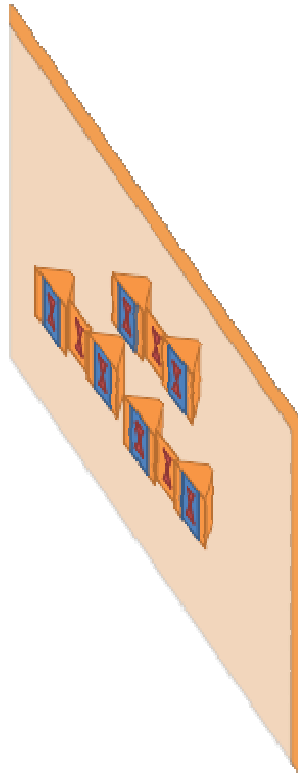


**Figure 2.10 3D extended antenna system**

The system consists of three blocks, consisting of three separate antennas – two receiving and one transmitting. In each block, signal of reflection of object is obtained and is passed to the program which calculates the position of object. The main reason to use such a block, is to get greater signal vs. noise ratio by combining the signals from both receiving antennas. Due to it, it's possible to achieve greater accuracy in object positioning.

The main key in tow receiving antennas is polarity. In this model one receiving antenna is opposite of second, see Fig. 2.11.

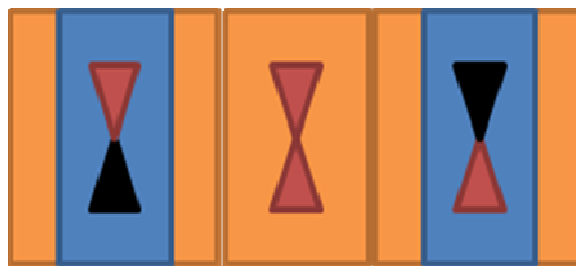


**Figure 2.11 Antenna block**

Received signals before summing are shown in Fig 2.12. Signals are summed in one channel using extra signal delay.

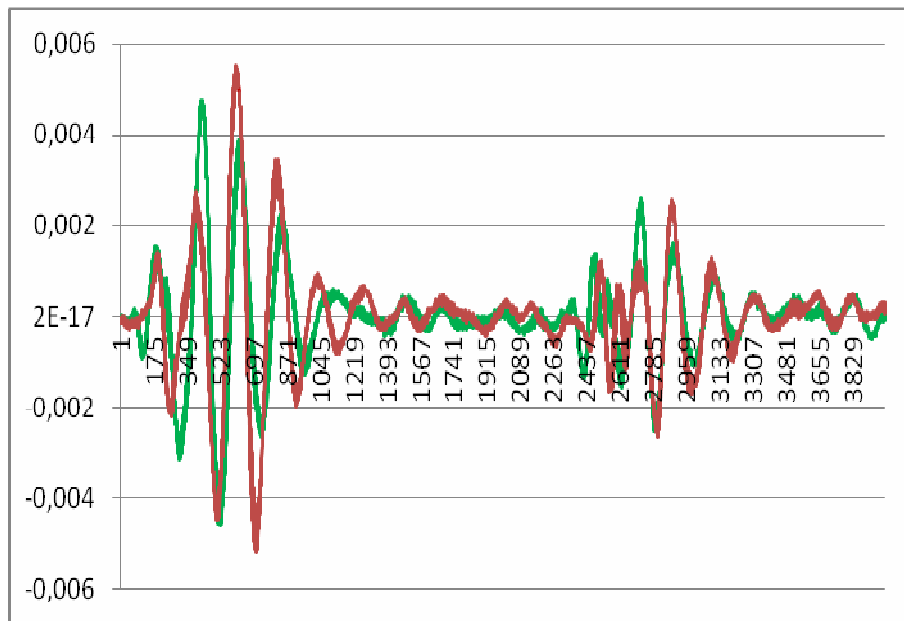


Figure 2.12 Signal from both receiving antennas

After summing we obtain a signal with much higher signal/noise ratio, see Fig. 2.13.

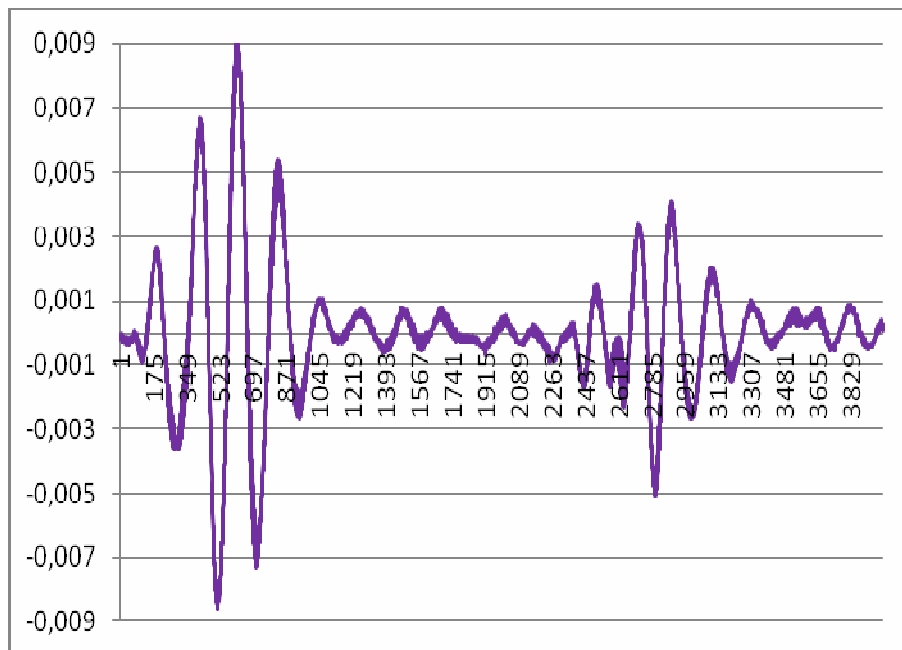


Figure 2.13 Result of signal summing

To sum signal from two antennas, signal summer from Fig. 2.14 is used.

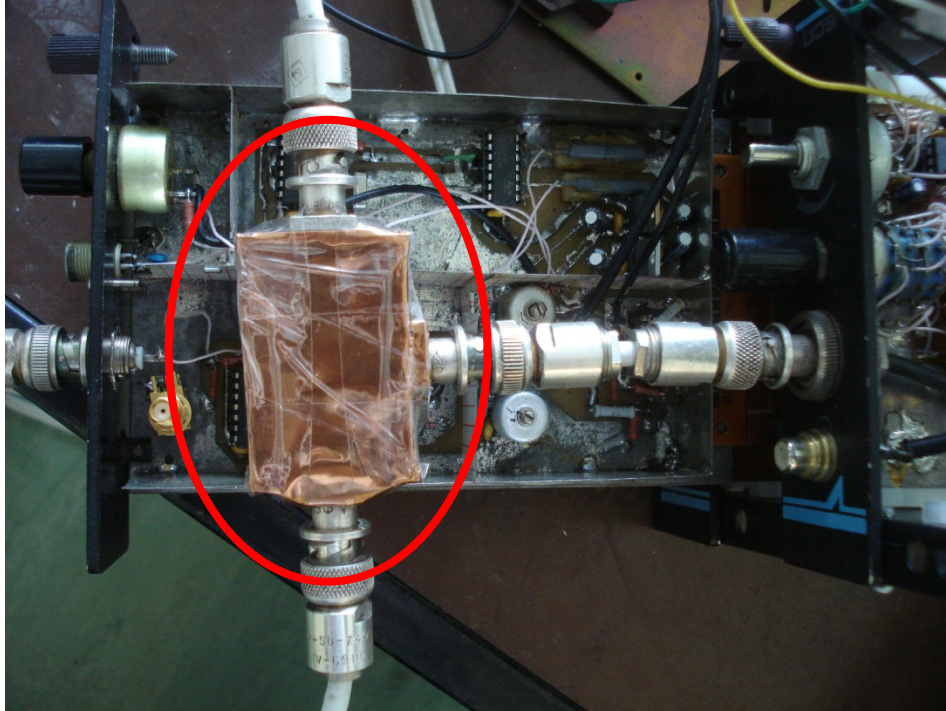


Figure 2.14 Signal summer

#### 2.2.4. The accuracy of establishing of target coordinates

The accuracy of establishing of target coordinates in 3D TWV radar depending on parameters of the receiving device (discrete stroboscopic converter), the method used in registration of the received signal and the algorithm of the coordinates calculation.

"Up-and-down" method was used for signal registration but the procedure of Matlab *fsolve* was used for calculation of coordinates.

Minimal configuration of 3D TWV antenna system consists of one transmitting and three receiving antennas. Let's consider the case where the transmitting antenna is placed in the centre of an equilateral triangle, but the receiving antennas are apexes of a triangle. Let's discuss this configuration in following rectangular coordinate system. Origin of it in the transmitting antenna and one of the receiving antennas is located on the "Y" axis. Assuming that the length of the side of the triangle is  $a$ , the coordinates  $x_i, y_i, z_i, i=1,2,3$  of receiving antennas will be following:  $(a/2, -a/\sqrt{3}), (-a/2, -a/\sqrt{3}), (0, 2a/\sqrt{3})$ . Let us denote the current coordinates of a moving target as  $x_k, y_k, z_k, k=1,2,\dots,N$ , which are determined in  $N$  positions.

The total delay between transmitted and reflected signal from the target at a given  $k$  value can be expressed as

$$\Delta \tau_{ik} = \frac{1}{c} (\sqrt{(x_k^2 + y_k^2 + z_k^2)} + \sqrt{((x_k - x_i)^2 + (y_k - y_i)^2 + (z_k - z_i)^2)}), i=1,2,3 \quad (12)$$

By measuring the delay  $\Delta \tau_{ik}$ , the system of equations (12) can be used to find the current target coordinates  $x_k, y_k, z_k$ .

Let's consider how accuracy of establishing of target coordinates is affected by distortions due to stroboscopic transform of reflected signal. These distortions, firstly, depends on the influence of additive noise which pools up with reflected signal, as well as a phase noise of clock signal. Besides, these distortions depend on parameters of "up-and-down" method: number  $n$  of comparisons of one instantaneous value and step  $s$ , according to which the value of signal in output of stroboscopic converter is changed after each operation of comparison.

For modeling experiments, exponentially decaying sinusoidal oscillation was used as a transmitted and reflected signal

$$u_s(t) = A_1 \exp(b_3 \cdot \frac{t}{T_z}) \sin(2\pi \frac{t}{T_z} + b_1 \cdot \pi \cdot \text{randn}), \quad (13)$$

where  $A_1$  determines the amplitude  $A'_1 \approx 0,765A_1$  of the signal;  $T_z$  is a period of sinusoidal signal, and coefficient  $b_1 \cdot \pi$  establishes standard deviation  $\sigma_f$  of phase noise. The coefficient of decay of exponent was chosen  $b_3 = -0.025$ , for approximate equality  $u_s(t) \approx 0$  to fulfil in point  $t = 3T_z$ .

The coordinates  $x_k, y_k, z_k$  were assigned in experiments,  $\Delta \tau_{ik}$  were calculated according to (12) and corresponding ideal signals  $u_{si}(t)$  were constructed. Additive noise  $u_{ni}(t)$  was added to these signals, the total signal  $u_{1i}(t) = u_{si}(t) + u_{ni}(t)$  (see Fig. 2.15a) was processed by "up-and-down" method and signals  $u_{2i}(t)$  (see Fig. 2.15b) were obtained.

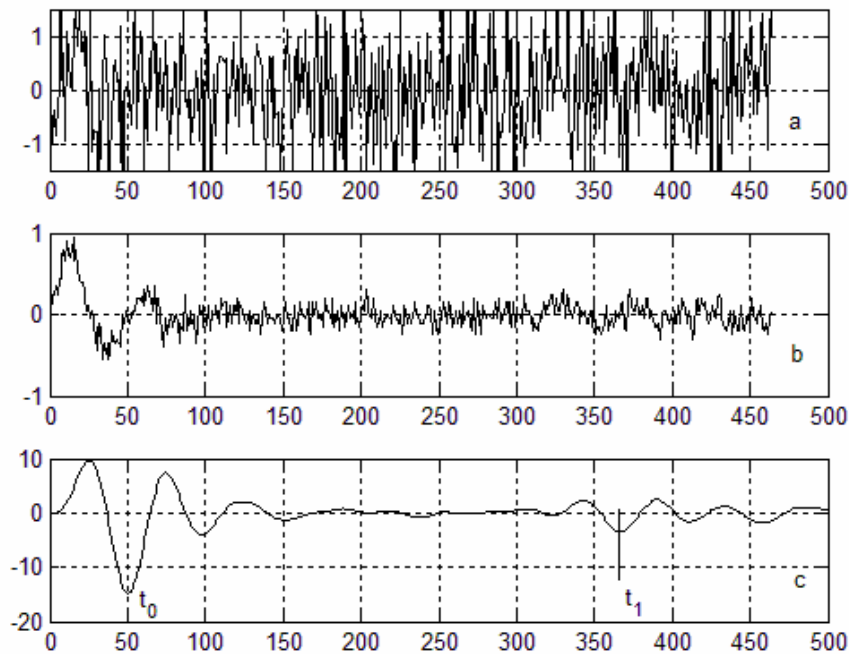


**Figure 2.15 Reflected signal (a), signal after stroboscopic transform (b) and transformed signal after convolution (c)**

Additional processing by convolution operation was carried for these signals:

$$u_{3i} = conv(u_{2i}, u_{et}), \quad (14)$$

where as an etalon signal  $u_{et}$  sinusoidal monooscillation with period  $T_z$  was used. Due to these actions signals  $u_{3i}(t)$  (see Fig. 2.15c) were obtained. Afterwards the delays  $\Delta\tau'_{ik} = t_1 - t_0$  between transmitted and reflected signals were detected by minimums of these signals. By fitting the obtained values of  $\Delta\tau'_{ik}$  in system of equations (1), one can calculate the coordinates of target  $x'_k, y'_k, z'_k$ .

Error of computation depends on accuracy of establishing  $\Delta\tau'_{ik}$  which depends on intensity of additive noise, as well as the phase noise of transmitted signal. It was assumed that the additive noise is normally distributed with standard deviation of  $b_2\sigma_1$ . Equality  $\sigma_1 = 1$  was assumed as well, amplitude of the signal will be measured in  $\sigma_1$  units.

Since the delay  $\Delta\tau'_{ij}$  is determined by minimums of  $u_{3i}$ , error in computation are either due to inexact detection of coordinates of minimums (time interval between measurable instantaneous values is too large; in region of signal minimum the noise influence is too large) or the case, when minimum of noise is more than the minimum of valid signal, is present. Since the position of such fraud minimum on time axe can be viewed as a uniformly random variable with mean value of half scan, then in case of such error the result of computation for current position almost always will be useless.

Let's investigate the means of averting such situation. It's known that the standard deviation of noise, transformed by "up-and-down" method, reduces to

$$\sigma_2 = \sqrt{0.625\sigma_1 s + 0.25s^2} \quad (15)$$

in output. In order to eliminate delays due to fraud minimums in computations, it's required that the amplitude  $A_{2i}$  of the signal  $u_{2i}$  would be bigger than the standard deviation of noise. Approximately one can assume that the condition

$$0.765 A_{2i} > 3\sigma_2 \quad (16)$$

must be fulfilled. In its order it means that the amplitude of transmitted signal has to be such, in order for amplitudes of reflected signals satisfy the condition (16) even at maximal delays.

The modeling has been carried on at following parameters of "up-and-down" method:  $s = 0.015\sigma_1; n = 50$ ; amount of instantaneous values to be measured (counted for period  $T_z$ )  $n_T = 50$ . The distance between receiving antennas was chosen to be equal to 1m, the position of object was determined in  $N = 50$  points. The length of scan was assumed to be 1024 points.

Calculation results for different trajectories of object differs relatively little. Below mentioned results are obtained for case when the coordinates of target changes in following way:

$$\begin{aligned}
 x(k) &= 3(1 - (k - 1) / N) m; \\
 y(k) &= 6(1 - 0.1x(k))^2 m; \\
 z(k) &= (4.5 + 1.1x(k)) m.
 \end{aligned}
 \tag{17}$$

Calculation results for  $A_1 = 0.4 \sigma_1$  (in case, when condition (16) is fulfilled) can be seen in Fig. 2.16 and 2.17. Spatial trajectory of object can be seen in Fig. 2.16, where the set trajectory is mapped with continuous line, but the computed through values of delays  $\Delta \tau'_{ik}$  - with points. In Fig. 2.17 corresponding dependencies  $y(k)$  and  $z(k)$  are shown ( $x(k)$  is not displayed, in order not to clutter up the graphic).

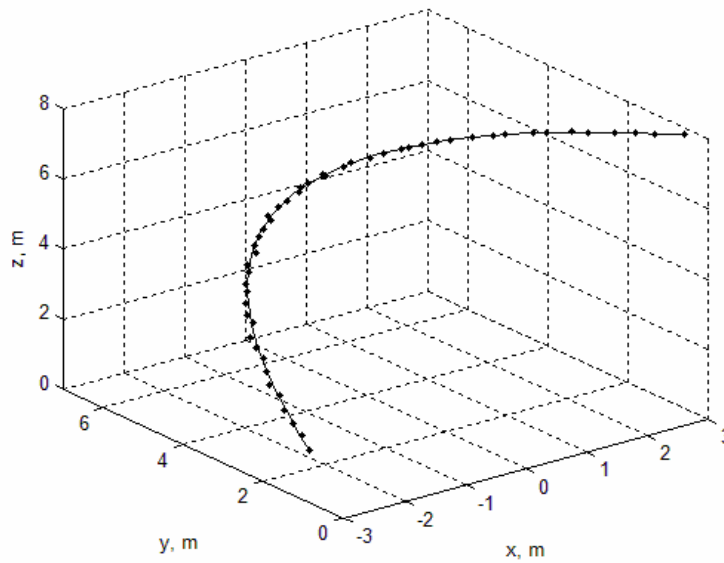


Figure 2.16 Spatial trajectory of object according to conditions (17) for  $A_1 = 0.4$

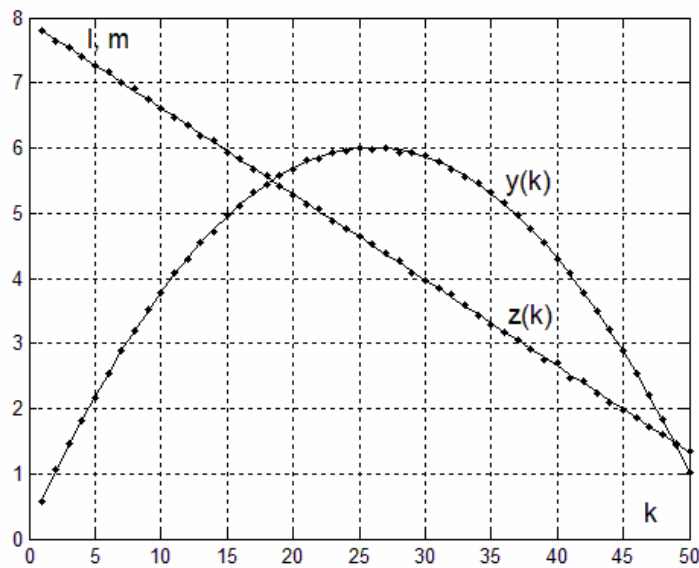
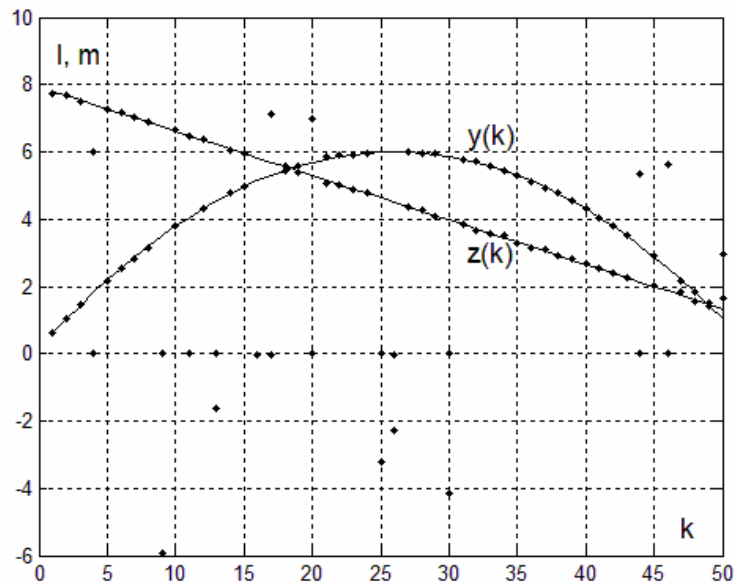


Figure 2.17 Set (continuous lines) and computed (points) dependencies  $y(k)$  and  $z(k)$

Since the condition (16) is fulfilled, then the error in calculation of coordinates depends only on accuracy of detection of minimums of reflected signals, which constitutes to approximately  $0.1 \div 0.15\%$  of the length of scan. The calculated coordinates of object differs from actual for not more than  $1.5 \div 2\%$  in whole diapason of values.

In Fig. 2.18 dependencies  $y(k)$  and  $z(k)$  at  $A_1 = 0.3$  are shown, when condition (16) is not met. It's visible, that with such value of  $A_1$  and with the used parameters of "up-and-down" method, considerable proportion of points of trajectory is determined with inadmissibly high error.



**Figure 2.18** Dependencies  $y(k)$  and  $z(k)$  at  $A_1 = 0.3 \sigma_1, n = 50, n_T = 50$

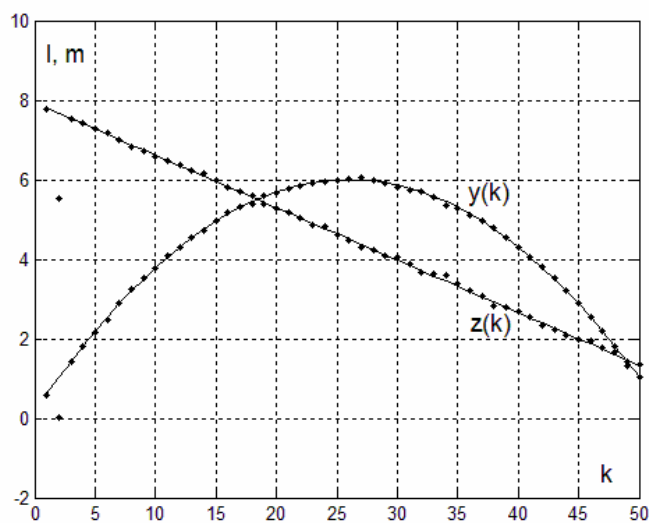


**Figure 2.19** Dependencies  $y(k)$  and  $z(k)$  at  $A_1 = 0.3 \sigma_1, n = 75, n_T = 50$

It's possible to improve these results by increasing  $n$  or  $n_T$  but keeping the same value of  $A_1$ . In Fig. 2.19 dependencies  $y(k)$  and  $z(k)$  are shown, which are computed at  $A_1 = 0.3\sigma_1, n = 75, n_T = 50$ . One can see that increasing  $n$  till 75 reduced the number of erroneously determined positions of object to just one. By repeating the calculations with chosen parameters, it was established that the amount of wrong calculations fluctuates from 0 till 4. Therefore, by even greater increase of  $n$ , large errors can be excluded. Similar results can be obtained through increase of  $n_T$  as well.

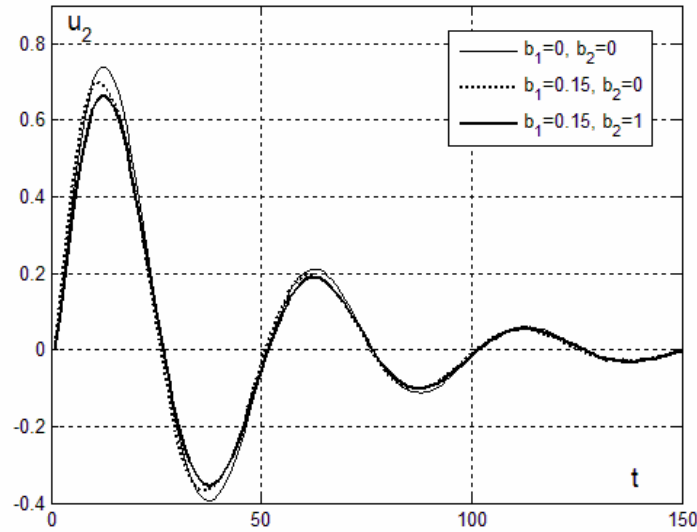


**Figure 2.20** Average values of transformed signal depending on values of coefficients  $b_1$  and  $b_2$

Finally, let's discuss the inaccuracy due to phase noise. Average values of transformed signal on three combinations of coefficients  $b_1$  and  $b_2$  are shown in Fig. 2.20. One can see that having  $b_1 > 0$  and  $b_2 > 0$  decreases the average value of amplitude of the signal. Due to it, the probability of determining value of  $\Delta\tau'_{ij}$  through fraud minimum increases.

Dependence of average value of standardized amplitude  $\eta$  of transformed signal from the coefficient  $b_1$  is shown in Fig. 2.21. Here  $\eta = A_{2b} / A_{20}$ , where  $A_{20}$  is the average value of transformed signal at  $b_1 = 0$  but  $A_{2b}$  - at  $b_1 > 0$ . It needs to be said that  $\eta$  practically doesn't depend on  $b_2$ .

Let's assess the value of  $b_1$  corresponding to transmitting device of locator, if  $T_z = 500 ps$  and phase noise is  $30 ps$ , which can be considered as quite large. Assuming that this value approximately corresponds to  $4\sigma_f$ , corresponding value of

$$b_1 = \frac{\pi}{30 \cdot 4} \approx 0.03. \text{ By using Fig. 2.21 with such value of } b_1, \text{ we obtain } \eta \approx 0.996.$$

Therefore we can draw the conclusion that the practically seen values of  $\sigma_f$  negligibly influence the errors in calculation of coordinates.

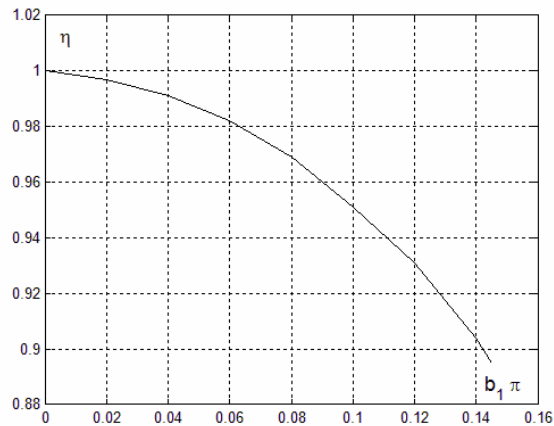


**Figure 2.21 Dependence of average value of standardized amplitude from the standard deviation of phase noise**

The amplitude  $A_1 = 0.3\sigma_1$  can be viewed as the lower bound for providing small registration errors with acceptable values of  $n$  and  $n_T$ . Modelling results at  $A_1 \leq 0.25\sigma_1$  testify that in order to obtain passable results, it's required to increase these values considerably. It implies the corresponding increase in registration time and decreases the chance of tracking of target.

### 2.2.5. Multiple signals in one channel

It's possible to transmit data from three different antennas in one channel, while preserving main features of each reflection, using just one stroboscopic transformer. The received signal is shown in Fig. 2.22. To obtain such a signal where there are three reflections in one channel, signal delays are used. In this way, the difficulty and cost is shifted from using three valuable stroboscopic transformers into one stroboscopic transformers and a bit more complex software.

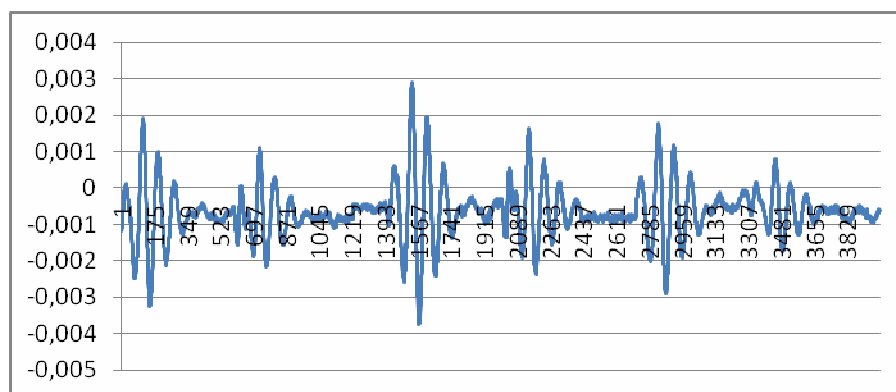


**Figure 2.22 Three distinguishable signals in one channel**

### 2.2.6. Computer user interface

The research has been done to view objects behind the wall and a computer user interface has been made to represent this position in 2D mode Fig. 2.23.

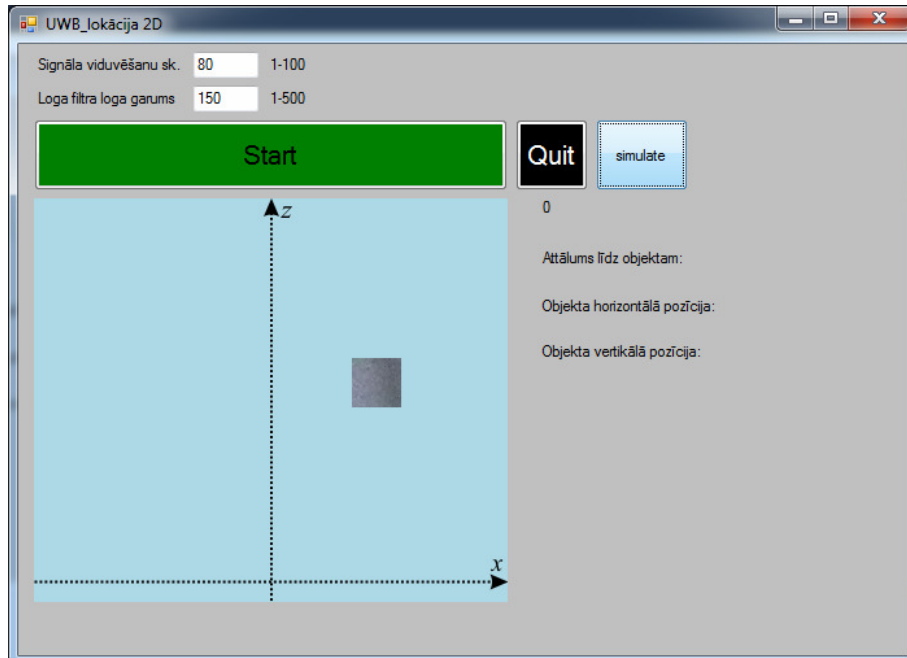


Figure 2.23 User interface

### 2.2.7. Data transfer between device and the computer

The mock-up has been made to manage the data transfer between stroboscopic transformer and computer, see Fig. 2.24.

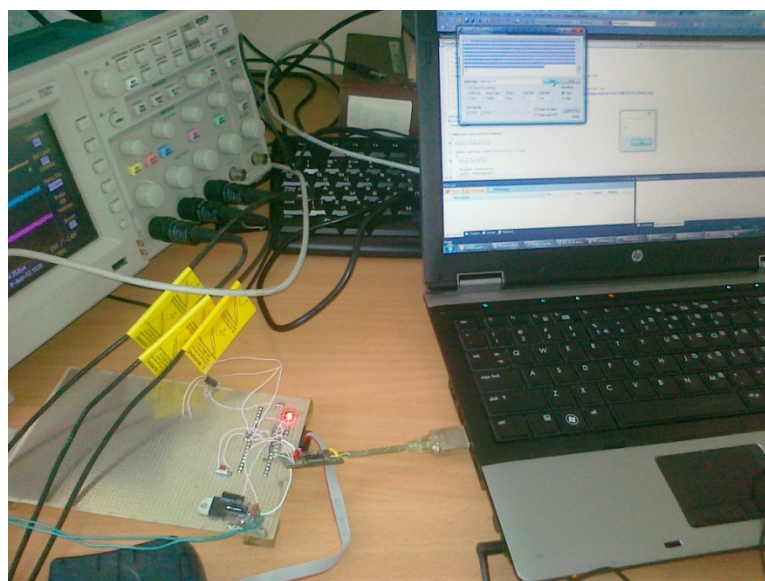


Figure 2.24 Application for data transfer between device and computer

Two programs: master program for computer and slave program for device CPU have been written.

### 2.2.8. Adjustable reflector setting

The research has been done to measure the influence of distance changes between antenna and its reflector, for that proposes we have made system that allows to adjust this distance Fig. 2.25.

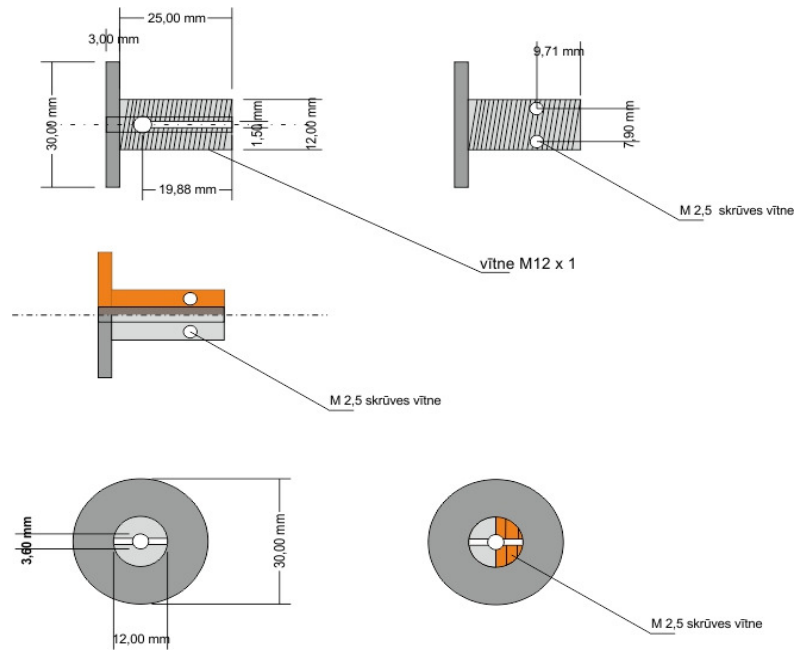


Figure 2.25 System for adjusting distance between antenna and reflector

Real life model in Fig. 2.26. and Fig. 2.27.



Figure 2.26 Antenna front side



Figure 2.27 Antenna back side

### **2.2.9. Further plans for 2D localisation model**

1. In reality, we'll see  $l_1 + l_2$ ,  $2l_2$  and  $l_3 + l_2$  instead of just  $l_1$ ,  $l_2$  and. It might increase the complexity of the first, and, consequently, other equations. Other fact, that without doubts will increase the complexity of analytical solution, is inability to put the middle receiving and sole transmitting antenna in the same place, therefore the distance between both will be some positive number  $d$ . As a workaround it's proposed to use  $a$  much larger than the abovementioned distance  $d$ .
2. Currently, a case of 2 objects, 3 receiving antennas and 1 transmitting antenna is investigated, therefore there are 6 distances. Even in the case of exact measurement, getting  $x$  and  $y$  coordinates of both objects seems complex enough due to obvious combinatorial explosion although with just 2 receiving antennas the distances provide unique solutions for positioning.

The results of object localization using UWB radio location related activities are described in 4 papers [2.1] [2.2] [2.3] [2.4] and used for 1 patent submission [2.5].

### **References**

[2.1] M. Greitans, V. Aristov, and T. Laimina "Application of the Karhunen–Loeve Transformation in Bio\_Radiolocation: Breath Simulation". ISSN 0146\_4116, Automatic Control and Computer Sciences, 2012, Vol. 46, No. 1, pp. 18–24. © Allerton Press, Inc., 2012.

[2.2] V. Karklinsh "The "Up\_and\_Down" Method with a Variable Step in Digital Sampling Conversion", ISSN 0146\_4116, Automatic Control and Computer Sciences, 2012, Vol. 46, No. 1, pp. 34–40. © Allerton Press, Inc., 2012.

[2.3] Грейтанс Модрис, Херманис Эвалдс, Аристов Владимир, "Обработка зашумленного сверхширокополосного импульсного сигнала методом главных компонент". Альманах современной науки и образования. Тамбов: Грамота, 2012. № 8. (63) , с. 30-35. ISSN 1993-5552.

[2.4] M. Greitans and V. Aristov, "Conservation of the Law of Phase Modulation for UWB Pulse Signals in the First Principal Component", "Automatic Control and Computer Sciences" Vol.46, Number 4, 2012 , Allerton Press, Inc. pp.179-184. М.Грейтанс и В. Аристов, „Сохранение закона фазовой модуляции UWB импульсного сигнала в первой главной компоненте”, "Автоматика и вычислительная техника" - АВТ, Выпуск No.4, 2012, с.47-54.

[2.5] 02.10.2012.g. Nr. P-12-152 . „ZIGZAG (BI QUAD) ANTENA, KONSTRUKTĪVI SAJŪGTA AR KOAKSIĀLO KABELI" Izgudrotāji: Modris GREITĀNS, Vladimirs ARISTOVS, Gatis ŠŪPOLS. Īpašnieks: Elektronikas un datorzinātņu institūts.

### 3. Viedo transporta sensoru tīklu, tai skaitā, auto mezglpunktu un satiksmē iesaistīto objektu ārpus auto, izstrāde, iekļaujot iegultu sistēmu pielietošanu un energo-efektīvas programmatūras izveidi

Turpinot iepriekšējus darbus, izstrādāts unificēts 802.11p *vehicle unit / road side unit* prototips, uz kura bāzes tiek veidots eksperimentāls 802.11p standarta datu pārraides tīkls. Balstoties uz iepriekš izstrādātajām metodikām ceļa seguma monitoringa veikšanai, izstrādāts eksperimentāls viedā transporta sensoru tīkla auto mezglpunkta prototips. Attīstot kooperatīvās krūzkontroles tematiku, uzsākta viedā auto stereoredzes prototipa izveide. Uzsāktas aktivitātes viedā transporta sensoru tīkla ārpus auto infrastruktūras objektu, t.sk. viedo ceļa stabiņu, tematikā.

#### 3.1. *Experimental IEEE 802.11p network*

A logical continuation of previous activities in the domain of IEEE 802.11p network communication was development of permanently usable vehicle unit and road side unit prototypes and subsequent development of experimental IEEE 802.11p data transmission network.

During previous activities and real world tests the need for certain temperature range inside the device housing was determined – if the environmental temperature was under zero degrees C, the device was tended to function unstable, most probably, due oscillator frequency shift. To solve this problem, an automatic temperature control system, consisting of two 12V 3W car bulbs and control unit based on LM393 comparator and NTC termistor was prepared for installing into device housings.

Development of experimental IEEE 802.11p data transmission network assumes creation of at least one mobile vehicle unit prototype and at least one stationary road side unit prototype. Due practical reasons as real world tests using several different vehicles the vehicle unit should be as possible suitable for universal installation and operation. Similar requirements are logical according road side unit as there is the need to test several data transmission network configurations and unit deployments. Therefore both above mentioned units was designed as unified construction, and mainly differs by mount accesories.



Figure 3.1 Unified 802.11p unit

The housings of the unified units (Fig. 3.1) are based on ETI IP65 wall mounted distribution boards ECH-8G [3.1.1]. These boards allow to ensure permanent usage of the devices outdoors. The antenna of the device is located on the top of the housing and therefore forms a single structure. Such approach reduces antenna cable length and protects it from mechanical damages. External connections of the unified units include 12V power supply from vehicle electrical network or external 220V/12V adapter and Ethernet computer network.



**Figure 3.2 First mobile vehicle unit prototype**

The first mobile vehicle unit prototype was installed on vehicle Dodge Caravan using factory roof bars (Fig. 3.2). The first stationary road side unit prototype was installed on facade of IECS towards Aizkraukles street (Fig. 3.3). The current location of stationary road side unit prototype allows to test the communication in the experimental IEEE 802.11p data transmission network in both modes – the vehicle is approaching road side unit and the vehicle is leaving road side unit. The configuration of the experimental IEEE 802.11p data transmission network allows to test communications distances in line of sight up to 350 meters as well as communication in real world urban environment.



**Figure 3.3 First stationary road side unit prototype**

The results of 802.11p domain related activities are described in paper „Accessible, Customizable, High-Performance IEEE 802.11p Vehicular Communication Solution” [3.1.2] as well as presented in the 1st International Workshop on Vehicular Communications and Applications (VCA 2012, June 19, 2012) in Ayia Napa, Cyprus.

## **3.2. Experimental vehicular wireless sensor node**

A sensor is a device used for the measurement of some physical quantity or physical state. Common result of this measurement is an analog signal that is converted to a digital signal using ADC and subsequently processed using some computing device. Typically there is a need to make measurements in several locations and therefore a number of sensors should be configured, deployed and serviced if necessary. This approach - usage of many static deployed sensors - has its drawbacks as sooner or later scalability and maintenance issues will arise. To overcome this problem a large number of static deployed sensors could be substituted by few mobile sensors. One type of objects that could be used as mobile sensor carriers are vehicles. Among the possibility to cover wide measurement area there are other advantages including energy utilization from sensor carrier as well as less strict limits on device dimensions, weight and power consumption.

There are several categories of data that could be acquired using vehicles as sensor carriers. First of them is data about vehicle itself, for example, driving speed and position. Next data source is vehicle driver characterized by pulse and reaction time. Environment measurements could be collected, for example, data about acoustic noise and air pollution. Last but not least - vehicle usage depends on dedicated infrastructure including road surface, and regular monitoring of this infrastructure could help optimize required maintenance works.

The main purpose of the CarMote embedded device described in this paper is monitoring of road surface using microphone and accelerometer sensors as well as collection of meteorological data for creation of detailed road meteorology maps. This research was inspired by successful verification of previously developed methods for road surface monitoring using general purpose computing devices and Android smartphones as well as by a challenging task - implementation of these methods using customized embedded device.

### **3.2.1. Related work**

By our knowledge the term "vehicular sensor networks" was introduced in 2006 when researchers from University of California and University of Bologna declared a new network paradigm - the use of vehicles as sensors [3.2.1]. This paradigm was characterized by high computation power and high storage space therefore potential costs for network deployment and maintenance could be relative high. As primary application of vehicular sensor network was declared urban monitoring, for example, imaging of streets, recognizing of license plates and distributing of relevant notifications to drivers or police agents [3.2.2]. Other applications developed by other researchers include monitoring of infrastructure items like road surface [3.2.3], collection of real time vehicular parking information [3.2.4], measuring air quality in city areas [3.2.5] and mobile surveillance [3.2.6].

Additionally to communication between vehicles (V2V or vehicle-to-vehicle) vehicular sensor networks could include communication between vehicles and Road Side Units (V2I or vehicle-to-infrastructure) [3.2.7] [3.2.8]. In this case, as the number of network nodes could be very large, an effective identity verification should be ensured [3.2.9]. In contrast to traditional wireless sensor networks where network nodes are placed in static locations vehicular sensor networks are characterized by

dynamic changes in network topology. Therefore the best possible connectivity could be achieved using appropriate combinations of transmission time and transmission range [3.2.10]. Nevertheless data gathering using these dynamic networks and data muling and multi-hop forwarding strategies is supposed to have specific delays [3.2.11].

Our proposed CarMote embedded device assumes usage of relatively low computation power and low storage space that is characteristic for common wireless sensor network nodes. Combination of these aspects with vehicles as sensor carriers allows performing tasks where a large number of low cost deployed and maintained network nodes have advantages over a small number of high cost deployed and maintained network nodes.

### **3.2.2. Approach**

The development of the first prototype of the CarMote embedded device was performed on the basis of the first version of the LynxNet collar device developed during past research activities related to wild animal monitoring using sensor networks. This approach already fulfilled a part of the predefined requirements. In addition, common hardware basis for both device types facilitates reusability of the software.

#### **3.2.2.1. Hardware**

The heart of the first prototype of the CarMote embedded device (Fig. 3.4) is TMote Mini wireless sensor network module. This module contains TI MCU MSP430F1611, TI/Chipcon transceiver CC2420 and ST EEPROM M25P80. The same MCU is used in other wireless sensor network modules, for example, EPIC, 3MATE! and others. Selection of this popular MCU device allows to use the experience from previous developments as well as compatibility with available open source software.



**Figure 3.4 First prototype of the CarMote embedded device**

To ensure the possibility of implementation of the RoadMic approach [3.2.12] the main board was equipped with attachable board consisting of electret microphone

BCM9765P-44 and corresponding amplifier stage built using operational amplifier TS952ID. The output of the amplifier stage is connected to the ADC input #7 of the MCU.

To ensure the possibility of implementation of the Potroid approach [3.2.13] the main board was equipped with IMU Analog Combo Board from SparkFun. This board contains triple axis accelerometer ADXL335 and dual-axis gyroscope IDG500. Outputs of accelerometer X, Y and Z axis are connected to the ADC inputs #0, #1 and #2, but outputs of gyroscope axis X and Y - to the ADC inputs #3 and #4 of the MCU.

To ensure the possibility of experiments in creation of detailed road meteorology maps the main board was equipped with humidity and temperature sensor SHT15 as well as light sensor TEMA6000. First of them was connected to MCU using I2C interface, but second - using ADC input #5.

To ensure the possibility to add position metadata using GPS the main board was equipped with attachable board consisting of GPS module Fastrax IT300. This board is connected to MCU using USART #0 interface and NMEA protocol.

To ensure the possibility to use electrical system of the vehicle as main power source two sequential voltage regulators were used. First of them is dedicated to acquire 5V but second one - 3.3V. Four AA size battery pack is used as internal power source. Automatic switching between external power source and internal power source is ensured using low-loss Schottky diodes.

To ensure the possibility to store acquired sensor data and corresponding position metadata on media SD flash memory card was used. This removable media is connected to the MCU using SPI mode and accordingly configured USART #1 interface.

To ensure the possibility to transmit acquired sensor data and corresponding position metadata two options were selected. First of them is Wi-Fi that could be used for medium range communication and the second one - Bluetooth that could be used for short range communication. Hardware for Wi-Fi communication was implemented as attachable board consisting of Roving Networks module RN-131C but hardware for Bluetooth communication - as attachable board consisting of Rayson module BT-220A2. Both attachable boards have serial interface for communication with MCU. During device prototyping stage just one module with serial interface (GPS, Wi-Fi, Bluetooth) is connected to MCU interface USART #0 at the same time. Software driven multiplexer for commutation of several modules is left for future work.

### **3.2.2.2. Software**

In order to program CarMote, we have adapted MansOS operating system [3.2.14], a small and energy constrained device OS developed at the University of Latvia and Institute of Electronics and Computer Science (EDI). The OS aims to be user-friendly and easy to learn for individuals with C and UNIX programming experience.

The MCU of CarMote has a built-in 12-bit ADC. We sampled accelerometer's Z channel to evaluate the sampling speed. Sample rate 1820 samples per second (sps) was achieved without logging the data and 1400 sps when logging the data to SD card. The rates are sufficient for the kind of applications CarMote was designed for, such as pothole detection.

An essential component of a highly mobile device is positioning system. MansOS supports data interface with GPS devices including NMEA protocol parsing and online processing.

Last but not least, SD card support is included. It can be used either in *raw* mode or by writing data to a filesystem. We have developed a custom filesystem to efficiently use local storage devices; although it is primary targeted for flash chips with no automatic rewrite options, it can be used for SD card as well. The filesystem provides buffering and automatic error detection features.

MansOS configuration system can enable these components when needed or disable them to optimize compilation length. In either case, the system automatically detects when a component is not used and optimizes binary code by pruning unused components from the final executable.

A declarative scripting language SEAL is available on top of MansOS. SEAL is targeted towards domain experts and novice programmers. SEAL features extremely concise syntax for describing common tasks: sensor sampling, data processing and data communication. A few complete application examples are given in Listing 1 and Listing 2.

---

### Listing 1 SEAL code for accelerometer sampling and measurement storing

---

```
// define sensors
define AccelX AnalogIn, channel 0;
define AccelY AnalogIn, channel 1;
define AccelZ AnalogIn, channel 2;
// sample the sensors
read AccelX; read AccelY; read AccelZ;
// store sampled data to SD card
output LocalStorage;
```

---

---

### Listing 2 SEAL code for pothole detection with STDEV algorithm

---

```
// define sensors
const ACCEL_Z 2;
define AccelZ AnalogIn, channel ACCEL_Z;
define Deviation stdev(take(AccelZ, 10));
// when STDEV value exceeds threshold:
when Deviation > 100:
    // read the detection time
    read Uptime;
    // indicate a pothole presence via beep
    use Beeper, on, duration 200ms, frequency 1000;
end
// log the detection time to SD card
output LocalStorage (Uptime);
```

---

### 3.2.3. Evaluation

To evaluate the described CarMote embedded device the following set of the activities were performed:

- test drive with Android smartphone HTC Desire and CarMote embedded device;
- acquisition of the accelerometer data for pothole detection using Potroid
- comparative analysis of acquired accelerometer data.

Accelerometer data acquisition was performed 37 times per second using CarMote embedded device and 53 times per second using Android smartphone (Fig.3.5). Analysis of the acquired data revealed that, taking into account slightly different positioning of both data collection devices, acquired data are practically identical and therefore data from CarMote embedded device are suitable for usage for pothole detection using Potroid approach. Relatively better sensitivity of the CarMote embedded device in the context of accelerometer Z axis value could be considered an advantage because this axis value is the most affected by potholes passed by vehicle.

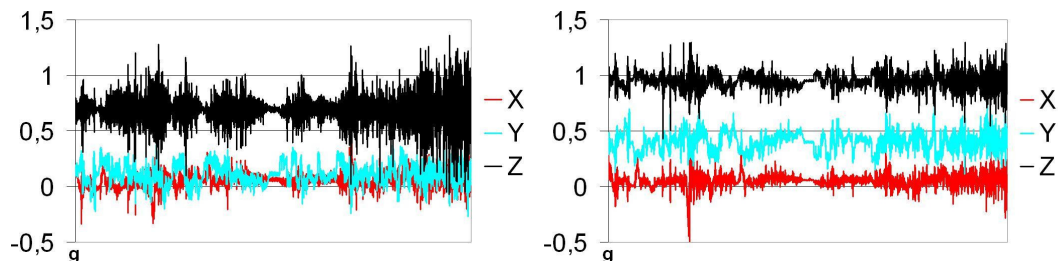


Figure 3.5 Accelerometer data acquired using CarMote embedded device and Android smartphone HTC Desire

Serious advantage of CarMote embedded device over Android smartphone equipped according Potroid approach and laptop computer equipped according RoadMic approach is the native possibility to use electrical system of the vehicle as main power source. In this case long term data acquisition and processing sessions are possible almost eliminating the risk of empty internal power source.

The results of vehicular wireless sensor node related activities are described in paper „Embedded Solution for Road Condition Monitoring Using Vehicular Sensor Networks” [3.2.15] as well as presented in the 6th International Conference on Application of Information and Communication (AICT 2012, October 17-19, 2012) in Tbilisi, Georgia.

## 3.3. Stereo vision for smart vehicle with cooperative cruise control

### 3.3.1. Passive stereo machine vision

Passive stereo machine vision is a technique that allows acquiring depth or disparity information using two general purpose cameras. The idea is based on natural human vision. Passive means that the scene is only observed and no active element like IR light or laser is used.

The depth information is gathered from rectified camera images using stereo triangulation. Stereo triangulation allows calculating distance to a point knowing the position of this point in both left and right images. The horizontal offset then is calculated which is proportional to the distance to the point. This can be seen in Fig. 3.6.

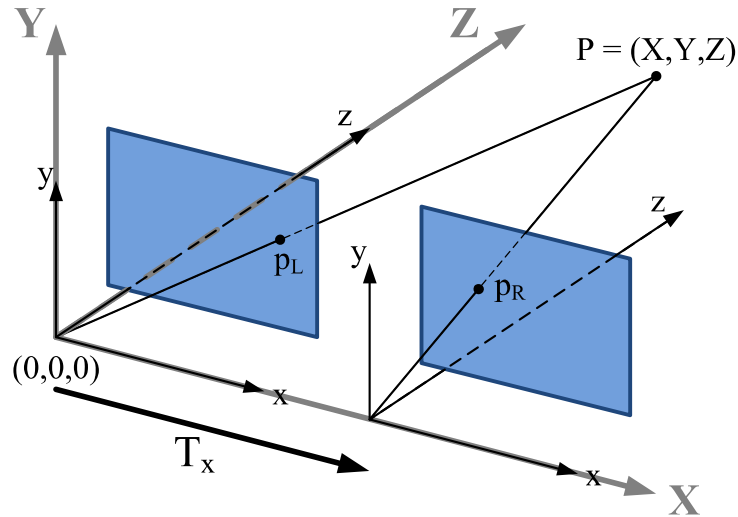


Figure 3.6 Stereo triangulation

### 3.3.2. Passive stereo machine vision applications

**Biometrics.** Passive stereo machine vision can be used in biometrics to identify a person by using the 3D model of the persons face. This can be much more robust than using plain image. Example can be seen in Fig. 3.7 [3.3.1]



Figure 3.7 3D reconstruction for biometric purposes

**3D reconstruction.** Passive stereo machine vision can be used to digitize and reconstruct 3D model of the surroundings like a city or specific objects. This can be used in robotic and automatic navigation applications, as well as content generation for special effects and computer games [3.3.2] [3.3.3]

**Adaptive cruise control system.** Passive stereo machine vision can also be used in an adaptive cruise control system where distance to the front car is calculated via

the stereo vision and then used to control cars speed depending on the distance to the frontal car. The current output of the written software can be seen in Fig. 3.8 and Fig. 3.12.



**Figure 3.8** The graph showing distance to the car (top) and the change of speed (bottom)

### **3.3.3. Previous work in intelligent car systems using 3D vision**

Karlsruhe Institute of Technology project AnnyWay uses two color and two monochrome cameras for image acquisition, a LIDAR for laser range sensing and GPS/IMU for additional sensor information. Then they use this information to calculate the motion, disparity and other parameters. The project doesn't use this for adaptive cruise control or adaptive driving however [3.3.4].

The *DARPA Urban challenge 2007* had many autonomous vehicle entries and most of the teams used either active sensors like LIDAR or passive cameras in a non-stereo setup. The goal was to create an autonomous vehicle that could move over large distances in high speed without a driver [3.3.5] [3.3.6].

### **3.3.4. Hardware**

The prototype is using two Flea2G 1.3 MP Mono FireWire 1394b cameras which were chosen because of their low noise, reasonable price, large customization options and the possibility to synchronize two cameras via the FireWire bus. Synchronization is essential as temporal changes between images make depth calculations unpractical.

Optics for the camera has been chosen to be Edmund Optics *NT58-365* Varifocal Video Lens 4mm - 12mm Focal Length lenses. They have been chosen for the large field of view and price. The field of view is 60 degrees for the 1/3 inch sensor of Flea2G. Large field of view allows monitoring more road lanes and larger area in front of the car in general.

The car is a Dodge Caravan and has the cameras positioned on the roof-racks using a custom built rig. The cameras during setup and indoor testing while being attached to the rig can be seen in Fig. 3.9.



**Figure 3.9** Cameras and the rig

Even though the optics were marketed as low-distortion, distortions were still very noticeable. Especially radial distortions which manifests as fish-eye effect where vertical and horizontal lines are bent near the edges of the image. This made calibration quite difficult. This can be observed in Fig. 3.10. For disparity calculations these distortions need to be corrected. This is done during camera calibration.

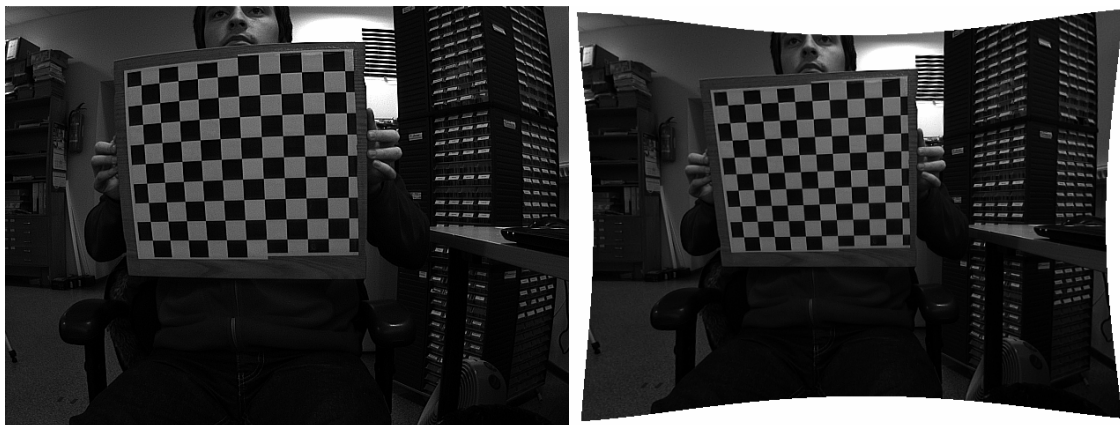


**Figure 3.10** Left: Unrectified image. Right: Rectified image

### **3.3.5. Software**

Current software uses OpenCV for general purpose IO and drawing. LIBELAS library for fast disparity calculations, PointGray FlyCapture SDK for synchronized camera input and custom code for camera tracking and distance calculations. It is written in C++. The software is coded in modular fashion to keep as much of the systems separate. Synchronization should happen through FireWire bus automatically because of the common clock signal, so the main reason for FlyCapture SDK was that the cameras don't work correctly with OpenCV camera interface. The FlyCapture SDK also has problems with C++ interface for non MS Visual C++ environments, so C interface was used instead. FlyCapture SDK did allow synchronization of camera parameters like gain and exposure between the cameras while one of the cameras has these settings set automatically. Current modules and the pipeline is shown in Fig 3.11..

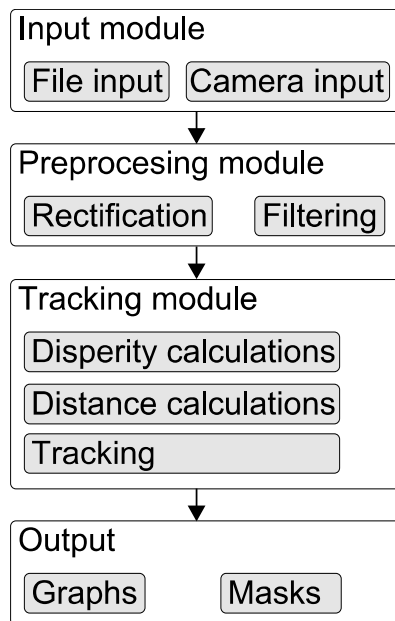


**Figure 3.11 Current software modules and their relations**

Currently to initiate tracking an object has to be selected. After that the tracking is automatic and works in the combined field of vision of the cameras.

Tracking involves calculating the disparity in a region of interest around the tracked object and then use segmentation on this depth map. Ground plane is removed so its gradient doesn't influence the segmentation.

Then the object is segmented in disparity map using depth with thresholding values. The segmentation is flood fill bases and requires at least one point on the surface. This is why the object has to be selected at start. Segmentation gives the surface of the object, like the back of a car. Then the distance is calculated for all the points on this surface and the distance to surface is obtained by averaging all the distances. This allows mitigating noise and disparity calculation errors.

After that the centroid is calculated for surface. The previous frame's calculated centroid, bounding box for the surface and other parameters are then interpolated with the new ones. This removes erratic behavior because of erroneous disparity value or fast moving objects. These are basically temporal constrains that take into account the fact that nothing can change these values infinitely quickly. Like if the car is detected 5m away and in the next calculation the car is 30m away, then there probably has been an error, as that would indicate a speed of 540km/h (at 30fps) which is improbable. The interpolated centroid is then the tracking point at the next frame and all is started from the beginning. The distance changes then can be used to get speed and acceleration/deceleration. This information then can be used to control the car.

This method allows very fast and efficient tracking of objects. However, for this to work reliably there has to be automatic detection and partial tracking in image space as well, not just disparity space. This is needed because the current method alone is very unforgiving to losing the object. That usually leads to erratic jumps which require reselecting the target. This loss of object can be detected however and that allows using image space detection and tracking to retarget the object.

The current method also doesn't take into account occlusions like one car driving in front of the other, but that is intentional as in adaptive cruise control the tracked

object should be the one closest in front of the cars path. This can be taken into account however by tracking the distance and looking for jumps in value, which is similar to the temporal constraint already mentioned.

The workings of the algorithm with region of interest, disparity calculation, ground plane removal, segmentation, surface bounding box and centroid can be seen in Fig. 3.12.



Figure 3.12 Software output of a car being tracked

### **3.4. Smart road studs for dangerous road situation warnings**

Transportation is an important aspect of our lives. Yet it produces significant amount of injuries. In the USA 5080 pedestrians, cyclists and other traffic participants outside motorized vehicles were killed in 2010, 130000 injured [3.4.1]. Rear-end collisions constituted 29% of all injury crashes in the USA, in 2006 [3.4.2]. More than 70% of rear-end crashes happen during the dark time of the day [3.4.3]. Research shows, that additional visual hazard warnings may reduce accidents by up to 50% in some cases [3.4.4].

Intelligence for accident reduction and additional awareness can be introduced in transportation in multiple conceptually different ways: (1) by creation of smart cars; (2) upgrading infrastructure, (3) changing environment and laws; and (4) augmenting pedestrians and cyclists. While smart-car direction is popular in recent years, its applicability is limited in low-income regions and countries, such as Thailand, where bicycles and motorbikes are more popular than cars [3.4.4]. Creation of environment and juridical laws, where traffic participants are maximally separated, is effective, yet it requires huge investment to build advanced highways with many line car roads and dedicated cyclist tracks. Augmenting of pedestrians and cyclists has the drawback of “forgetfulness” – people often do not assess the importance of safety and forget to instrument themselves.

#### **3.4.1. Related work**

One of the main tasks for the intelligent vehicles as well as intelligent road infrastructure is detection of nearby located vehicles. This task could be solved in several non-intrusive ways, including vision-based approach and active or passive optical sensors [3.4.5], or emitted RF noise from the vehicles [3.4.6]. To ensure reliable vehicle detection and low power consumption several detection techniques

with different credibility and energy consumption characteristics can be used subsequently – optical sensors for initial detection and magnetic sensors for confirmation [3.4.7]. Specific case of this task is vehicle detection during night time or low visibility conditions. In this case vehicle detection is based on light sources analysis as potential other vehicles head or tail lights and acquired information is usable for automatic switching of vehicle headlights between high and low beams [3.4.8].

Monitoring of light is one of the most typical environment sensing tasks. Besides stand-alone monitoring, light sensing can also function as data source for closed-loop control system, such as adaptive lighting in operational road tunnels [3.4.9]. Specific case of this task is detection of the fog as additional reason for low visibility during night time. It can be performed using image analysis and detection of backscattered veil induced by the vehicle ego lights as well as halos around light sources in the vehicle environment [3.4.10].

The main method for detection of creatures, including wild animals and humans, in total darkness is thermography. This method is based on measurement of their own and the reflected heat radiation within the infrared spectrum, and allows investigations of phenomenon as bird-turbine collisions at offshore wind farms [3.4.11], [3.4.12]. Relatively simple thermography solutions based on passive infrared (PIR) sensors are widespread used in intrusion detection and automatic lighting systems. Other animal detection methods assume usage of microwave radar sensors, infrared or laser beams [3.4.13] as well as equipment of the animals with GPS collar devices [3.4.14].

There are recent research activities related to advanced road infrastructure: intelligent road studs magnetically coupled from power wires buried in the surface [3.4.15], road studs with protection against predetermined wavelengths of solar radiation [3.4.16], road studs with incoming and outgoing optical communication [3.4.17], and solar powered microcontroller based road studs [3.4.18]. Compared to existing solutions, instead of installation of completely new road infrastructure items, our approach assumes augmentation of existing road infrastructure.

Most similar to our proposed solution are Road Nail system [3.4.19], [3.4.20] developed in University of Novi Sad, and wireless sensor package to instrument roadways for Intelligent Transportation Systems [3.4.21] developed in Massachusetts Institute of Technology (MIT). Road Nail system consists of a number of solar powered wireless sensor network nodes mounted near the road edge. Main activities of the system are detection of approaching vehicles and emitting signalization light. Our proposed solution uses similar hardware concept, yet different activities are performed, including detection of several relatively typical dangerous road situations and visual warnings to drivers. Wireless sensor package developed at MIT counts passing vehicles, measures the average roadway speed, and detects ice and water on the road. Clusters of sensors can transmit this information in near real-time to base stations. Our proposed solution has different packaging approach that is based on existing road infrastructure items and does not require intrusive installation work.

### **3.4.2. Approach**

The detection of predefined dangerous road situations is performed using the following algorithms:

- 1) if ChargingFromSolar panel is false  
and LightFromPassedVehicle is true  
set DangerPassingVehicle to true for 2 min.
- 2) if AirTemperature is below +2C  
and AirTemperature is above -5C  
set DangerousRoadSituationTwo to true  
else set DangerousRoadSituationTwo to false
- 3) if ChargingFromSolar panel is false  
and LightFromPassedVehicle is false  
and InfraredFromObject is true  
set DangerAnimal to true for 1 min.

Priority of dangerous road situation II exceeds situation I as air temperature could not be estimated without appropriate measurement device. DangerAnimal situation has the highest priority as there exists real danger from detected object not only possible danger due to potentially slippery road.

### 3.4.2.1. Hardware

The heart of the IMilePost embedded device shown in Fig. 3.13 is Texas Instruments 16-bit microcontroller MSP430G2553. This microcontroller was selected due its ultra low-power consumption significant for autonomously operated device.

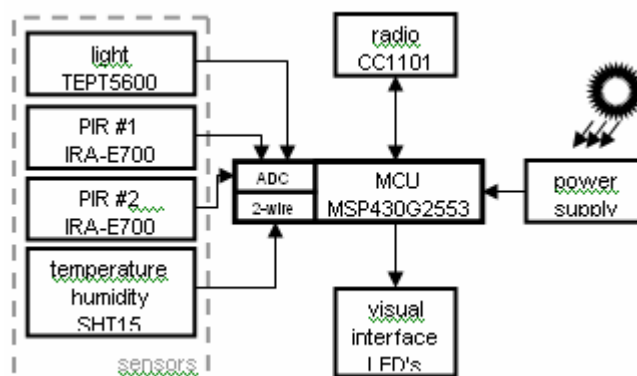


Figure 3.13 Structure of IMilePost embedded device

Sensing part of the device consists of ambient light sensor TEPT5600 used for detection of approaching vehicles head lights, temperature and humidity sensor SHT15 used for detection of temperature range characteristic for road ice formation and two dual type pyroelectric infrared (PIR) sensors IRA-E700 used for detection of wild animals and pedestrians. The light sensor and both PIR sensors are attached to the microcontroller using its ADC inputs but temperature and humidity uses digital 2-wire serial interface.

Visual interface part of the device is designed as a set of ultra bright LED's with different colors therefore the possibility to report different dangerous road situations to drivers is provided.

Apart from function as independent sense-and-report item, in the future the IMilePost device could function as separate node in homogeneous or heterogeneous wireless sensor networks. This functionality is provided by addition of Texas Instruments low-power sub-1 GHz RF transceiver CC1101 that can be configured for operating in the 315/433/868/915 MHz ISM/SRD bands.

### 3.4.2.2. Solar power supply

+3V power supply voltage has been chosen for the whole system and maximal / average estimated current consumption is 7mA / 1mA. The solar power supply unit has been chosen and calculated for minimal day time in winter 6h with maximal solar energy about 600W/m<sup>2</sup>, so solar energy must be accumulated in an ultra capacitor in quantity enough for feeding of the connected electronic device in the night time for at least 18h.

Solar power supply unit must contain a solar cell with open circuit voltage +3.3V and short circuit current 0.4A, separating diode D, ultra capacitor with capacitance at least 200F and maximal voltage +2.7V for energy accumulation, connected to input of the DC/DC converter with stabilized output voltage +3.0V. TLV61224 has been chosen as the most appropriate DC/DC converter, made by Texas Instruments. It has input voltage range +(0.8-3.0)V, very small internal current consumption, output voltage +3.0V and maximal possible output load current 40mA. Inductance L (4.7uH) is an outside part for DC/DC converter. Full schematic diagram of the solar power supply unit (excluding auxiliary noise reduction capacitors) is given on Fig. 3.14.

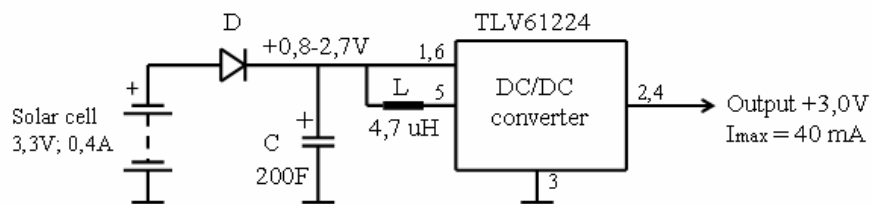


Figure 3.14 Schematic diagram of the solar power supply unit

The solar cell 2V, 200mA and ultra capacitor 100F have been used in the first experimental model of the solar power supply unit. Parameters of some parts may be slightly adjusted after field testing of full experimental device in real conditions.

### 3.4.2.3. Packaging

Experimental device has a form of a vertical steel tube with diameter 60 mm, upper end of which is located about 1 m over ground, but underneath end is fixed at least 0,5 m in the ground (Fig. 3.15). Main electronic parts - all sensors, microcontroller and flashing alarm light LED's are mounted in the electronic compartment - separate steel tube piece of the same diameter on the upper end of the main tube. A solar panel with compartment for ultra capacitors is mounted on two steel disks with diameter 144 mm, hereto underneath disk is tightly mounted on the upper end of the electronic compartment tube, but upper disk together with solar panel compartment can be rotated round up in steps 30 o and fixed by 4 screws on the underneath disk. So light sensor and flashing alarm light can be oriented to cars on the

road by right fixing of main tube in the ground, but solar panel in every case can be oriented directly to the sun.

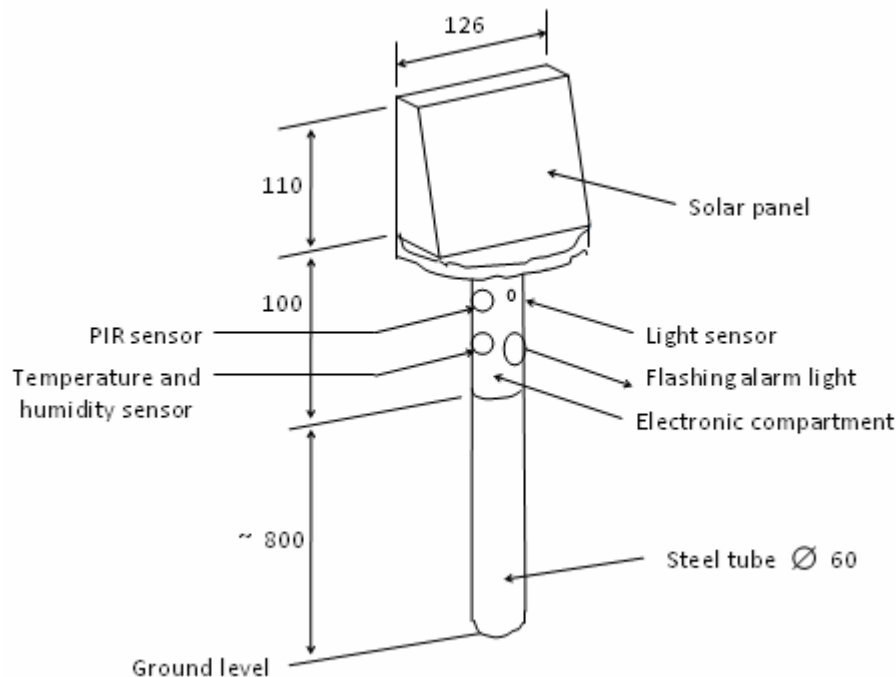


**Figure 3.15 Design of an experimental device (measures in mm)**

The results of smart road studs related activities are used for forthcoming paper „IMilePost: Embedded Solution for Dangerous Road Situation Warnings”.

## References

[3.1.1] IP65 Wall mounted distribution boards ECH. [Online]. Available: [http://www.eti.si/files/userfiles/ETI\\_SLO/novi\\_izdelki/ECHEN.pdf](http://www.eti.si/files/userfiles/ETI_SLO/novi_izdelki/ECHEN.pdf)

[3.1.2] N. Agafonovs, G. Strazdins, and M. Greitans. Accessible, Customizable, High-Performance IEEE 802.11p Vehicular Communication Solution. Proceedings of International Workshop on Vehicular Communications and Applications (VCA 2012), p. 127-132, 2012. IEEE Xplore Digital Library, 2012.

[3.2.1] U. Lee, E. Magistretti, B. Zhou, M. Gerla, P. Bellavista, and A. Corradi, “Efficient data harvesting in mobile sensor platforms,” in Proceedings of the 4th annual IEEE international conference on Pervasive Computing and Communications Workshops, ser. PERCOMW '06. Washington, DC, USA: IEEE Computer Society, 2006, pp. 352–.

[3.2.2] U. Lee, B. Zhou, M. Gerla, E. Magistretti, P. Bellavista, and A. Corradi, “Mobeyes: smart mobs for urban monitoring with a vehicular sensor network,” *Wireless Commun.*, vol. 13, no. 5, pp. 52–57, Oct. 2006.

[3.2.3] J. Eriksson, L. Girod, B. Hull, R. Newton, S. Madden, and H. Balakrishnan, “The pothole patrol: using a mobile sensor network for road surface monitoring,” in Proceedings of the 6th international conference on Mobile systems, applications, and services, ser. MobiSys '08. New York, NY, USA: ACM, 2008, pp. 29–39.

[3.2.4] S. Mathur, S. Kaul, M. Gruteser, and W. Trappe, "Parknet: a mobile sensor network for harvesting real time vehicular parking information," in Proceedings of the 2009 MobiHoc S3 workshop on MobiHoc S3, ser. MobiHoc S3 '09. New York, NY, USA: ACM, 2009, pp. 25–28.

[3.2.5] S.-C. Hu, Y.-C. Wang, C.-Y. Huang, and Y.-C. Tseng, "Measuring air quality in city areas by vehicular wireless sensor networks," *J. Syst. Softw.*, vol. 84, no. 11, pp. 2005–2012, Nov. 2011.

[3.2.6] C.-M. C. Kun-chan Lan and H.-Y. Wang, "Using vehicular sensor networks for mobile surveillance," September 2012.

[3.2.7] M. J. Piran, G. R. Murthy, and G. P. Babu, "Vehicular ad hoc and sensor networks; principles and challenges," *CoRR*, vol. abs/1108.2776, 2011.

[3.2.8] P. R. K. Reddy, P. Joshna, and G. Sireesha, "Data collection through vehicular sensor networks," *CoRR*, vol. abs/1206.6281, 2012.

[3.2.9] C. Zhang, R. Lu, X. Lin, P.-H. Ho, and X. Shen, "An efficient identity-based batch verification scheme for vehicular sensor networks." in INFOCOM. IEEE, 2008, pp. 246–250.

[3.2.10] H. Conceicao, M. Ferreira, and J. a. Barros, "On the urban connectivity of vehicular sensor networks," in Proceedings of the 4th IEEE international conference on Distributed Computing in Sensor Systems, ser. DCOSS '08. Berlin, Heidelberg: Springer-Verlag, 2008, pp. 112–125.

[3.2.11] C. E. Palazzi, F. Pezzoni, and P. M. Ruiz, "Delay-bounded data gathering in urban vehicular sensor networks," *Pervasive Mob. Comput.*, vol. 8, no. 2, pp. 180–193, Apr. 2012.

[3.2.12] A. Mednis, G. Strazdins, M. Liepins, A. Gordjusins, and L. Selavo, "Roadmic: Road surface monitoring using vehicular sensor networks with microphones," in NDT (2), ser. Communications in Computer and Information Science, F. Zavoral, J. Yaghob, P. Pichappan, and E. El-Qawasmeh, Eds., vol. 88. Springer, 2010, pp. 417–429.

[3.2.13] A. Mednis, G. Strazdins, R. Zviedris, G. Kanonirs, and L. Selavo, "Real time pothole detection using android smartphones with accelerometers," in DCOSS. IEEE, 2011, pp. 1–6.

[3.2.14] G. Strazdins, A. Elsts, and L. Selavo, "Mansos: easy to use, portable and resource efficient operating system for networked embedded devices," in Proceedings of the 8th ACM Conference on Embedded Networked Sensor Systems, ser. SenSys '10. New York, NY, USA: ACM, 2010, pp. 427–428.

[3.2.15] A. Mednis, A. Elsts, and L. Selavo. Embedded Solution for Road Condition Monitoring Using Vehicular Sensor Networks. Proceedings of the 6th International Conference on Application of Information and Communication Technologies (AICT 2012), p. 248-252, 2012. IEEE eXpress Conference Publishing, 2012.

[3.3.1] Akarun, L., B. Gökberk, A.A. Salah, "3D Face Recognition for Biometric Applications", in Proc. European Signal Processing Conference, Antalya, 2005

[3.3.2] Nader S. and Mariette Y., „Surface Reconstruction from Multi-View Stereo of Large-Scale Outdoor Scenes”, in *The International Journal of Virtual Reality*, 2010

[3.3.3] Motilal Agrawal, Kurt Konolige and Robert C. Bolles "Localization and Mapping for Autonomous Navigation in Outdoor Terrains : A Stereo Vision Approach" in *IEEE Workshop on Application of Computer Vision (WACV)*, Austin Texas, 2007

[3.3.4] Andreas G. and Philip L. and Raquel U., „Are we ready for Autonomous Driving?”, in *Computer Vision and Pattern Recognition*, 2012

[3.3.5] Prof. Mark Campbell et.al. , „Team Cornell: Technical Review of the DARPA Urban Challenge Vehicle”, 2007

[3.3.6] Mark Rosenblum, „DARPA Urban Challenge 2007 Team Urbanator Technical Description”, 2007

[3.4.1] U.S Department of Transportation, “Traffic Safety Facts 2010”, 2010. [Online]. Available: <http://www-nrd.nhtsa.dot.gov/Pubs/811659.pdf>

[3.4.2] Science Daily, “Avoiding Rear-end collisions”, 01.05.2008. [Online]. Available: [http://www.sciencedaily.com/videos/2008/0501-avoiding\\_rearend\\_collisions.htm](http://www.sciencedaily.com/videos/2008/0501-avoiding_rearend_collisions.htm)

[3.4.3] J.Luoma, M.Sivak, M.J. Flannagan, "Effects of dedicated stop-lamps on nighttime rear-end collisions," Technical report No. UMTRI-2005-15, May 2006.

[3.4.4] M.Peden, R.Scurfield, D.Sleet, D.Mohan, A.A.Hyder, E.Jarawan, C.D.Mathers, et.al., “World report on road traffic injury prevention”, 2004. [Online]. Available: [http://www.who.int/violence\\_injury\\_prevention/publications/road\\_traffic/world\\_report/summary\\_en\\_rev.pdf](http://www.who.int/violence_injury_prevention/publications/road_traffic/world_report/summary_en_rev.pdf)

[3.4.5] Z. Sun, G. Bebis, and R. Miller, “On-road vehicle detection: A review,” *IEEE Transactions on Pattern Analysis and Machine Intelligence*, vol. 28, no. 5, pp. 694–711, 2006.

[3.4.6] Y. Ding, B. Banitalebi, T. Miyaki, and M. Beigl, “Rftraffic: a study of passive traffic awareness using emitted rf noise from the vehicles,” *EURASIP Journal on Wireless Communications and Networking*, vol. 2012, pp. 1–14, 2012.

[3.4.7] E. Sifuentes, O. Casas, and R. Pallas-Areny, “Wireless magnetic sensor node for vehicle detection with optical wake-Up,” *IEEE Sensors Journal*, vol. 11, no. 8, pp. 1669–1676, 2011.

[3.4.8] P. F. Alcantarilla, L. M. Bergasa, P. Jimenez, M. A. Sotelo, I. Parra, D. F. Llorca, and S. Mayoral, “Night time vehicle detection for driving assistance lightbeam controller,” in *Intelligent Vehicles Symposium. IEEE*, 2008, pp. 291 –296.

[3.4.9] M. Ceriotti, M. Corrà, L. D’Orazio, R. Doriguzzi, D. Facchin, S. Guna, G. P. Jesi, R. L. Cigno, L. Mottola, A. L. Murphy, M. Pescalli, G. P. Picco, D. Pregnotato, and C. Torghelle, “Is there light at the ends of the tunnel? Wireless sensor networks for adaptive lighting in road tunnels,” in *IPSN, X. D. Koutsoukos, K. Langendoen, G. J. Pottie, and V. Raghunathan, Eds. IEEE*, 2011, pp. 187–198.

[3.4.10] R. Gallen, A. Cord, N. Hauti`ere, and D. Aubert, "Towards night fog detection through use of in-vehicle multipurpose cameras," in Intelligent Vehicles Symposium. IEEE, 2011, pp. 399–404.

[3.4.11] M. Desholm, "Thermal Animal Detection System (TADS). Development of a method for estimating collision frequency of migrating birds at offshore wind turbines," National Environmental Research Institute, Copenhagen, DK, NERI Technical Report No 440, Mar. 2003.

[3.4.12] M. Desholm, "Preliminary investigations of bird-turbine collisions at Nysted offshore wind farm and final quality control of Thermal Animal Detection System (TADS). Autumn 2003 and spring 2004," National Environmental Research Institute, Copenhagen, DK, Report commissioned by Energi E2, Apr. 2005.

[3.4.13] M.P. Huijser, and P.T. McGowen, "Overview of animal detection and animal warning systems in North America and Europe," UC Davis: Road Ecology Center, 2003. [Online]. Available: <http://escholarship.org/uc/item/2cc2s81w>

[3.4.14] M.S. Zahrani, K. Ragab, and A.U. Haque, "Design of GPS-based system to avoid camel-vehicle collisions: A review," Asian Journal of Applied Sciences, vol. 4, no. 4, pp. 362-377, 2011.

[3.4.15] A.W. Green, and J.T. Boys, "Intelligent road-studs - lighting the paths of the future", Transactions of the Institution of Professional Engineers New Zealand: General Section, vol. 24, no. 1, pp. 33-40, 1997.

[3.4.16] M. Dicks, "Road stud," International patent WO 2011/158004 A1, December 22, 2011.

[3.4.17] M. Dicks, "Improved road studs," International patent WO 2011/110800 A1, September 15, 2011.

[3.4.18] S.C. Tam, K.W.E. Cheng, Y. Bao, D. Wang, and W.P. Yau, "Battery operated devices," International patent WO 2011/083424 A1, July 14, 2011.

[3.4.19] D. Samardzija, E. Kovac, D. Isailovic, B. Miladinovic, N. Teslic, and M. Katona, "Road nail: Intelligent road marking system testbed," in VNC. IEEE, 2010, pp. 134–138.

[3.4.20] D. Samardzija, N. Teslic, B. Todorovic, E. Kovac, D. Isailovic, and B. Miladinovic, "Road nail: Experimental solar powered intelligent road marking system," JOURNAL OF ELECTRICAL ENGINEERING-ELEKTROTECHNICKY CASOPIS, vol. 63, no. 2, pp. 65–74, 2012.

[3.4.21] A. Knaian, A Wireless Sensor Network for Smart Roadbeds and Intelligent Transportation Systems, Massachusetts Institute of Technology, 2000. [Online]. Available: <http://books.google.lv/books?id=EXtYNwAACAAJ>

## **4. Biomedicīnas signālu reģistrācijas iekārtu prototipu izstrāde, iesaistot sensoru tīkla tehnoloģijas un attīstīto signālapstrādes algoritmu adaptāciju konkrētiem pielietojumiem**

This year we are continuing to work on acquisition and interpretation of biological signals. The goal of this research is to provide better insight and tools for reading and understanding biological signals, and also to use this knowledge as a tool for behavioral improvement by providing feedback to the acquired actions.

As in the previous year, this section consists of three separate sub-sections: “Electroencephalographic helmet for analysis, interpretation and processing of cortical EEG signal” (Section 4.1), “Smart solutions in diagnostics and hindering the development of scoliosis based on biofeedback generated by sensor networks” (Section 4.2) and “ Biometric person recognition system based on palm vein patterns” (Section 4.3).

### ***4.1. Electroencephalographic helmet for analysis, interpretation and processing of cortical EEG signal***

During this reporting period design of electroencephalographic helmet and brain signal studies - previously expressed plans, were continued.

As mentioned, systems based on EEG signal interpretation can be useful both for medical (diagnostics and treatment) and non medical (computer games, neuro controllers, management systems, education) applications.

In 2011 the designing of EEG (electroencephalographic) helmet was started. We aim to develop a system, which the subject will be able to set up and use himself at home, so the basic requirement is its' convenience. To achieve high results for EEG system it is important to provide sufficient spatial resolution (have enough EEG channels). As it is planned to make a wireless system, it has to be energy efficient - view section 4.1.3.

For better understanding of electroencephalographic information EMOTIV EPOC research kit was bought and, using EPOC, brain signals in different subject's conditions were gathered. Results of the research on EEG contained events, which are achieved to date, are described in sections 4.1.1. and 4.1.2.

The results obtained in this period:

1. Experimental EEG data gathering and processing.(Section 4.1.1).
2. Studies of evoked potentials related to visual stimuli and brain rhythms (Section 4.1.2).

Future work:

1. EEG helmet prototype
2. Brain signal studies

### 4.1.1. Experimental EEG data gathering and processing

Using the Emotiv EPOC wireless EEG recording device, several fragments of the EEG signal were gathered.

Subject was put in different mental conditions from calmed to stressed. Visual stimuli were applied. We used letter/symbol matrix from EPOC software and direct light for stimulation.

First real time EEG was visualized in EMOTIV EPOC software, but for better understanding signal processing algorithm was elaborated and implemented in Matlab environment (Fig. 4.2). General principle of experiment is shown in Fig. 4.1.

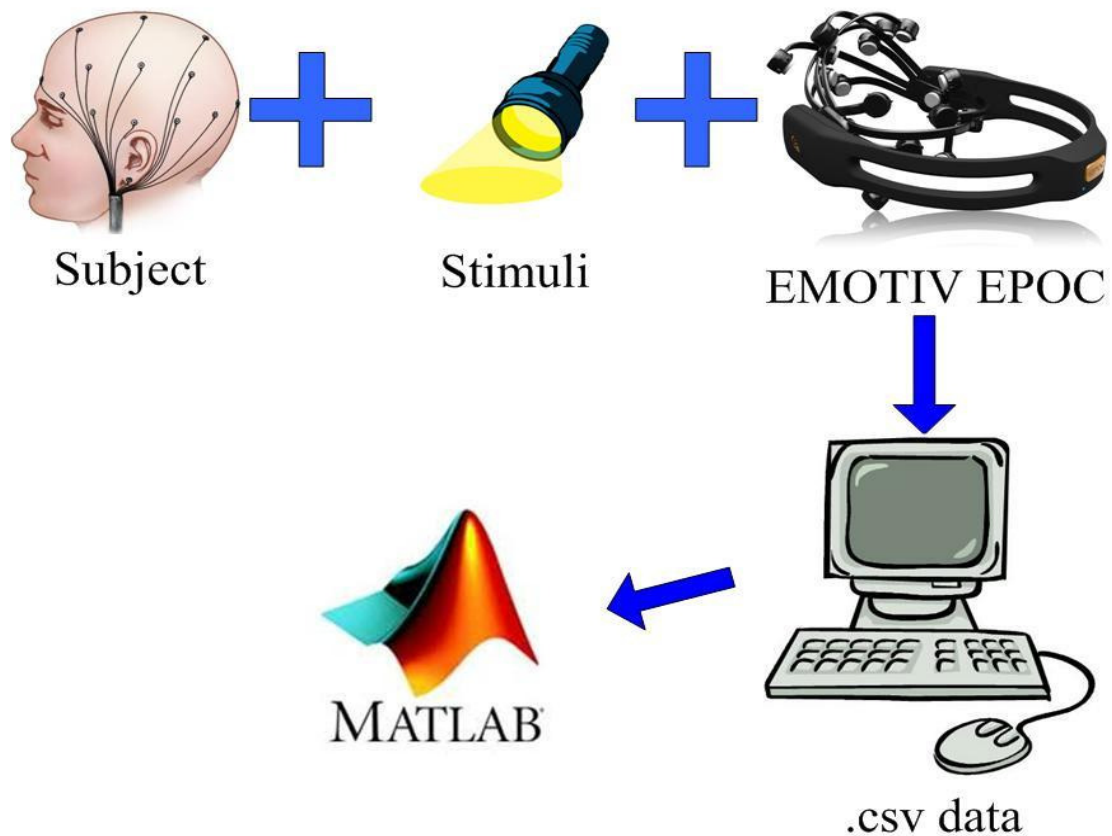
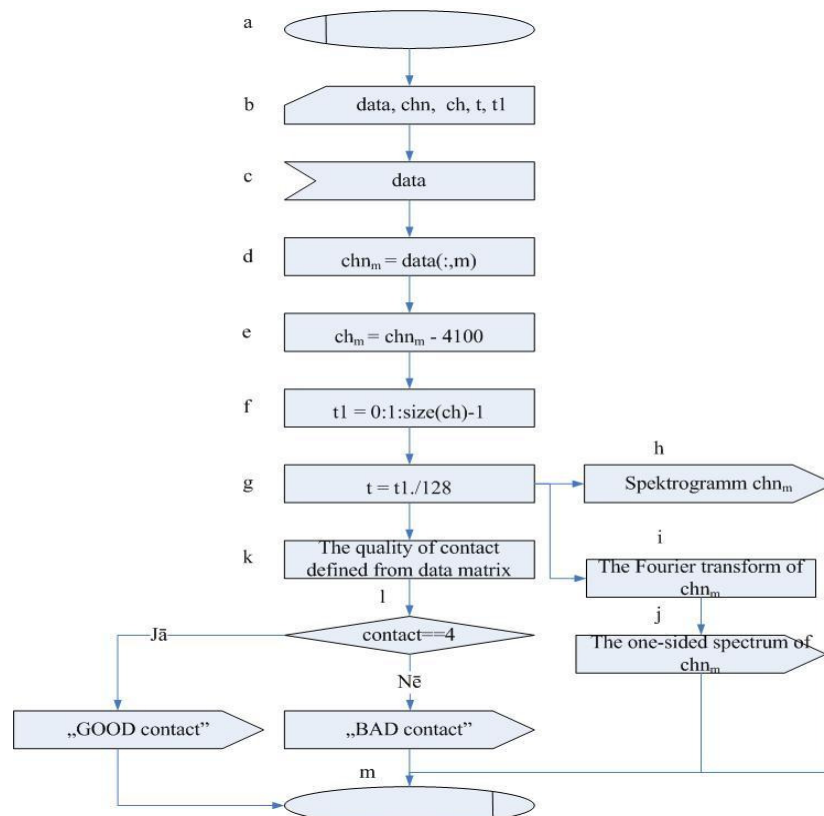


Figure 4.1 The principle of the experiment

Using elaborated algorithm, registered EEG data were imported to MatLab, a signal spectra and spectrograms of the different channels were obtained.

The signal parameters on which it is possible to classify brain rhythms and event related potentials (ERP) were defined [4.1.2]. Based on defined parameters, we dealt with frequency, time and amplitude-based analysis methods. Voltage projecting and time-frequency analysis (amplitude frequency characteristics and spectrograms) methods were chosen for studying the signal in three dimensions - amplitude, time, frequency [4.1.3].



**Figure 4.2 Flowchart of MatLab algorithm**

Fig. 4.2 shows flowchart of MatLab algorithm. Below an explanation is given:

- a) The beginning of the algorithm.
- b) The definitions of variables that are used in calculations (for processing). Variable *data* is the data matrix, which contains all of the EEG signal for each channel and the contact details of the electrode quality of the subject's head. Variable *chn* is a signal for one channel without deprivation of artifacts. Variable *ch* - the real value of the EEG, but *t1* and *t* is the times value's vector's definition.
- c) the data are entered into MATLAB by importing them from \*. csv file.
- d) The next step is the channel value's vector - *chn*, each channel has its own vector.
- e) Then, the artifacts are subtracted from the value of each vector, resulting in the EEG signal for each channel - *ch*.
- f) Time vector *t1* is defined.
- g) *t1* is divided by the sample rate - 128Hz. Real-time values are inversely proportional to sampling frequency.
- h) Spectrum estimation for each channel using the built-in MATLAB function spectrogram.
- i) The Fourier transform of each channel using the built-in MATLAB *FFT* function.
- j) After the Fourier transform the one-sided signal spectrum is drawn. You can use the one-sided spectrum of the final length of the signal. The spectrum is plot as a separate figure.

- k) In this step, the EEG channel true name, such as AF4, F8, is expressed as a channel electrode contact quality value.
- l) The resulting contact quality value is compared with a "4" and defined as *good* or *bad*
- m) The end of the algorithm.

### 4.1.2. Studies of evoked potentials related to visual stimuli and brain rhythms

All experimentally obtained data were subjected to MatLab algorithm described in chapter 4.1.1. and fast Fourier transform. According to each mental stimulation and activity type [4.1.4], the channels were selected from the data sets and later subjected to short time Fourier transform. Below an example of analysis of two channels from one data set is. But the reader must understand, that spetrograms, one-sided spectrum and a short time Fourier transform were used for all data sets in order to determine the type of brain rhythms, thus determining the type of stimulation.

To determine the rate and type of stimulation at each EEG data set, specific channels were selected from EEG voltage projections, which we were able to evaluate, using EPOC software. For example, during the registration of data sets *r1* the subject was static and the aim was to record the  $\alpha$ -rhythms, so channels *O1* and *O2* were chosen for the signal analysis, as in these regions  $\alpha$ -rhythms are projecting. Similar it was with other conditions of the subject. Experimental channels were chosen for each condition (mental activity or stimulation) depending on theoretical knowledge about cortical regions. *O1*-one-sided channel spectrum is shown in Fig. 4.3.a, but *O2* one-sided spectrum - Fig. 4.3.b.

As can be seen in Fig. 4.3, in these channels low frequency dominates, which is normal characteristic of EEG signal. Larger amplitudes in both channels appear around 10-13Hz frequency range.

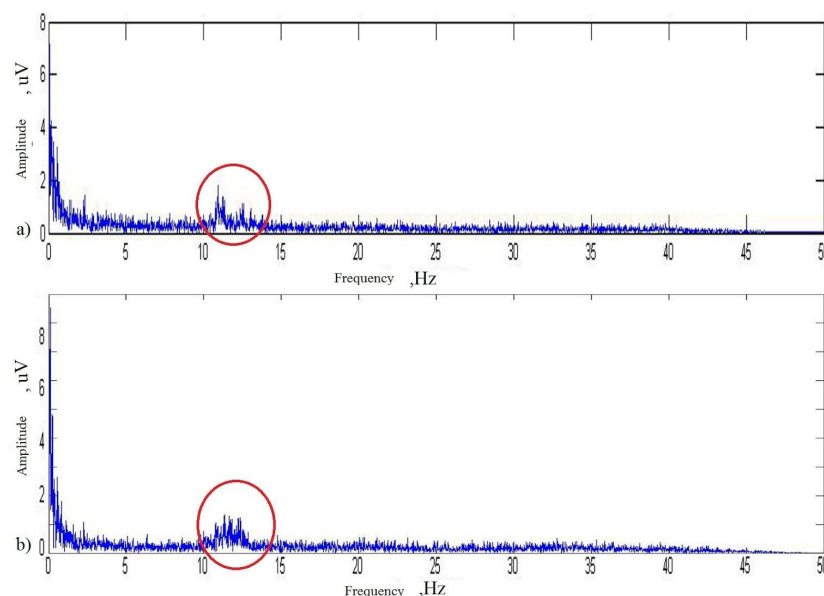


Figure 4.3 *O1* and *O2* one-sided spectrum

From Fig. 4.3 it can be seen that, dominating frequency range corresponds to  $\alpha$ -rhythms' frequency range [4.1.5] . It means, that the subject was relaxed with his eyes closed.

The attached figure is just an example, how data analysis methods implemented in MatLab environment allows to recognise events in brain signals.

## **4.2. Smart solutions in diagnostics and hindering the development of scoliosis based on biofeedback generated by sensor networks**

In the first year of the research study for scoliosis detection and prevention we developed a scoliosis detection device prototype with 12 sensors and accompanying software capable of drawing basic model of the shape taken by this prototype system. This year we have continued work on this system and made several improvements, both in precision and usability. Also our results have been published and presented as described in sections below.

The results obtained in this period:

1. Device prototype improvements (Section 4.2.1).
2. Data processing improvements (Section 4.2.2).
3. Smartphone (Android) application (Section 4.2.3).
4. Published results (Section 4.2.4).

Future work:

1. Gather and analyze real life dynamic data from both healthy people and diagnosed scoliosis patients.
2. Create more precise algorithms for detection of unwanted postures
3. Work on increasing the precision of the system as a whole

### **4.2.1. Device prototype improvements**

Continuing the work started in previous year, device prototype has gone through several improvements. These improvements are listed below

- **Increase in the number of sensors:**

For more equal horizontal and vertical resolution 4 more sensor nodes were added to the sensor network. This resulted in 16 sensor network arranged in a grid formation of four rows and four columns. The new sensor network provides more data than the previous 12 sensor network and covers the surface more evenly.

- **Development of elastic harness:**

For the device to be wearable a special elastic harness was developed for the latest version of prototype. The harness was specifically developed for testing purposes - it consists of elastic bands and variable length Velcro closures, allowing test subjects of different ages and body shapes. Additionally sensors

are connected to the harness with removable Velcro straps allowing easy removal for upgrades or repairs and also easy relocation for testing of different sensor network configurations.

- **Battery powered:**

For the device to be wearable outside of laboratory it was equipped with rechargeable batteries replacing power cord. Although in early experiments 2 rechargeable AA batteries were sufficient (2.4 V), later when device was equipped with wireless communications at least 3.3 V were required. Because of this reason the battery pack was upgraded to 3 rechargeable AAA batteries (3.6 V) of similar weight and size. Because the latest prototype model with wireless communication only spends approximately 50mA, this battery pack containing 3 average rechargeable AAA batteries of 900mAh capacity can sustain the device for approximately 48 hours.

- **Wireless communication:**

For full mobility while wearing the device it was equipped with wireless transmission capabilities. This allows transmitting data to external computing device such as personal computer or mobile phone for further calculations. Wireless communication was realized in two stages.

The first stage used antenna and wireless module of the eZ430-RF2500 module which was already used for the MCU located on it. This approach used very energy efficient data transfer algorithm SimpliciTI™ developed by Texas Instruments for use with their sensor modules. Although this approach had some benefits, there were several drawbacks, such as high processing load on MCU or the requirement for specific external receiving module which must be plugged into personal computer before data can be received.

Second wireless communication version was devised based on Bluetooth communication. This standard was chosen because it is widely available on mobile phones and personal computers, so no additional setup is needed on the receiving side. On the device side a standard BTM-112 Bluetooth module was used. This module takes care of all the actions necessary for wireless communication and in doing so leaves the MCU free for other calculations.

- **Enclosure:**

The central processing module together with Bluetooth wireless module and battery pack were enclosed in protective enclosure. This allows the prototype unit to be worn for prolonged periods of time without damaging it. On switch and informative diodes were added to the enclosure for easier operation (Fig. 4.4)



**Figure 4.4** Enclosure protecting the central processing module and Bluetooth module

As a result of these improvements the latest prototype version (Fig. 4.5) is fully mobile, wearable by a wide variety of people and capable of sending gathered data over Bluetooth to their mobile phone for future processing and storage.

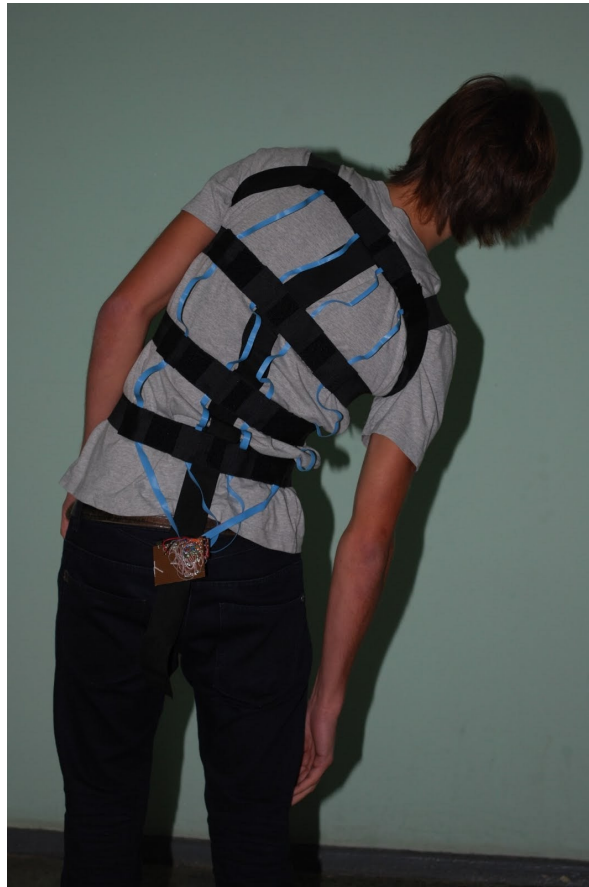


**Figure 4.5 Prototype device harness**

### ***4.2.2. Data processing improvements***

Specially designed software in MatLab environment was used for development of more advanced data processing algorithm and more precise approximated surface model construction. Algorithms were designed to be simple and effective to allow them to be implemented on portable devices such as smartphone.

In the new approach surface model consists of four strips of mutually connected vectors. Every strip is constructed from four fixed length vectors, each starting from the end of the previous one. The structure of approximated model corresponds to sensor networks 4 by 4 grid architecture. These four strips are then connected to a base line to mutually connect each of them. This base line is rotated along with one of the vectors in first row, to obtain more realistic surface model. In initial conditions every vector is defined as parallel to earth gravity (vertical), thus resulting initial shape is flat vertical surface. Then each vector is rotated from its vertical position to orientation of its corresponding shape (Fig. 4.6). This provides that the approximated model shape correspond to shape of physical device. This approach has some limitations arising from segment rotations around vertical axis, however, method is sufficient for basic shape approximation and analysis.

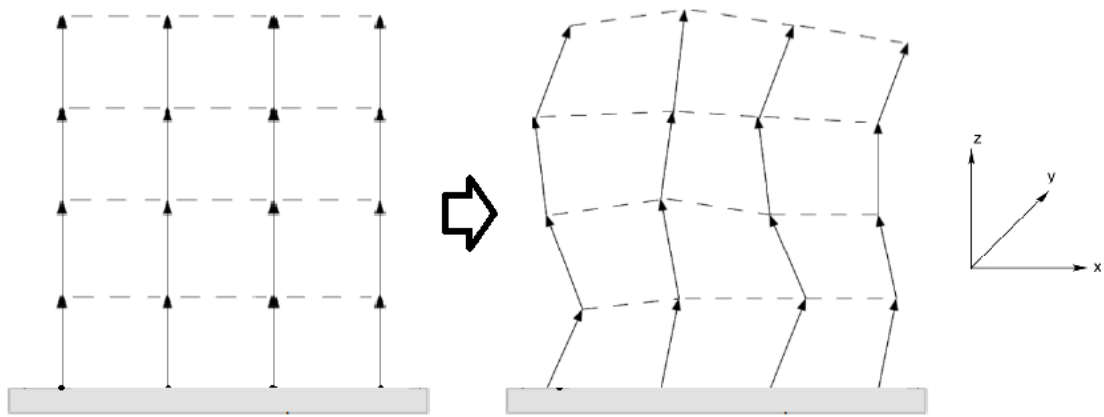


Figure 4.6 Structure of approximated surface model [4.2.1]

For description of sensor orientations a quaternion representation was used. This method allows to overcome problems such as non-unique representation and gimbal lock which are present when using Euler angles. Quaternions are numbers with three imaginary parts, and can be used to represent any rotation around any given axis. The orientation of sensor is defined as a vertical normal vector, which is rotated for an angle  $\theta$  around axis  $\underline{n}$  (Fig. 4.7).

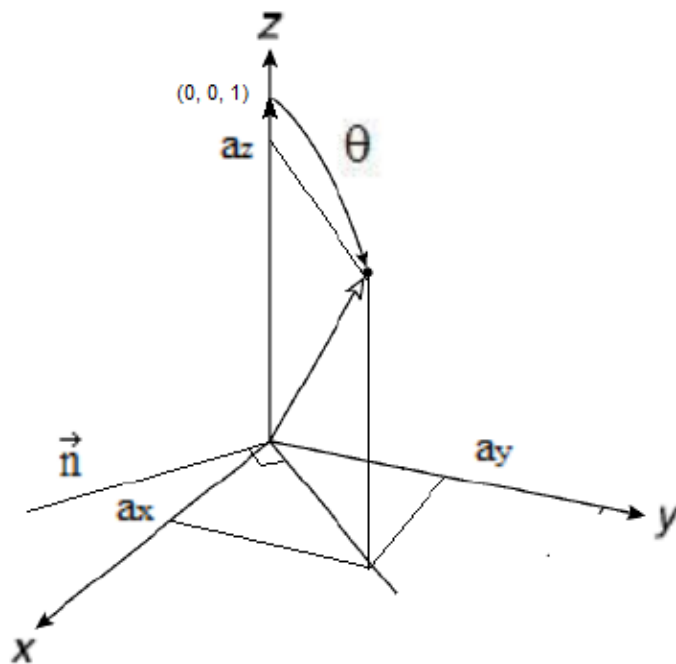


Figure 4.7 Quaternion representation of sensor orientation [4.2.1]

If we have normalized accelerometer data  $a_x$ ,  $a_y$ ,  $a_z$ , angle  $\theta$  can be obtained as:

$$\theta = \arccos[(a_x, a_y, a_z) \cdot (0, 0, 1)]. \quad (4.2.2.1)$$

The direction of  $n$  can be calculated from:

$$\underline{n} = (a_x, a_y, a_z) \times (0, 0, 1). \quad (4.2.2.2.)$$

Using these parameters we can construct the rotation quaternion:

$$\begin{aligned}q_0 &= \cos\left(\frac{\theta}{2}\right) \\q_1 &= n_1 \cos\left(\frac{\theta}{2}\right) \\q_2 &= n_2 \cos\left(\frac{\theta}{2}\right) \\q_3 &= n_3 \cos\left(\frac{\theta}{2}\right)\end{aligned}\tag{4.2.2.3}$$

This quaternion can be used to rotate any given vector. This can be done either by constructing quaternion rotation matrix, or using quaternion multiplication [4.2.2].

### **4.2.3. Smartphone (Android) application**

For mobile data gathering and feedback testing a smartphone application was developed.

Because of its open source nature and abundant availability of online support the open source smartphone platform Android was chosen for the development of first mobile software prototype.

The software is capable of:

- Connecting to the sensor system via Bluetooth connection
- Storing correct back position selected by a doctor for the best self correction of deformations
- Selecting the sensitivity - how much the subject has to move away from the correct posture before a feedback signal is sent
- Selecting the type of notification - whether feedback is sound based, vibration based or both
- Running the monitoring software, which keeps track of how much time proportionally is spent within the correct posture parameters versus the time spent in the incorrect posture, while providing feedback at the same time
- Real time animation - the software is capable of displaying the current calculated shape of the back, together with a grid representing the correct shape which needs to be maintained. This allows the user to train the correct posture more precisely.

### **4.2.4. Published results**

Within the last year our system has been described in one masters paper by Atis Hermanis [4.2.3], presented in one poster session in International Symposium on Biomedical Engineering and Medical Physics (ISBEMP) [4.2.4] and also published in one scientific conference - Baltic Electronics Conference (BEC2012) [4.2.1]. In BEC2012 the presented article also received reward “for the composition and presentation of the best paper”.

### 4.3. **Biometric person recognition system based on palm vein patterns**

Palm vein pattern is unique to each person, making it possible to identify person. During this project, a computer based device is developed, that acts like biometric door lock, by allowing person to enter the room only if information about his or hers palm vein signature is equal or similar enough to record in database.

During recognition process, image of palm is captured in IR spectrum, making palm veins more visible. Using location of gaps between fingers, ROI location is calculated, and ROI is extracted from rest of the picture.

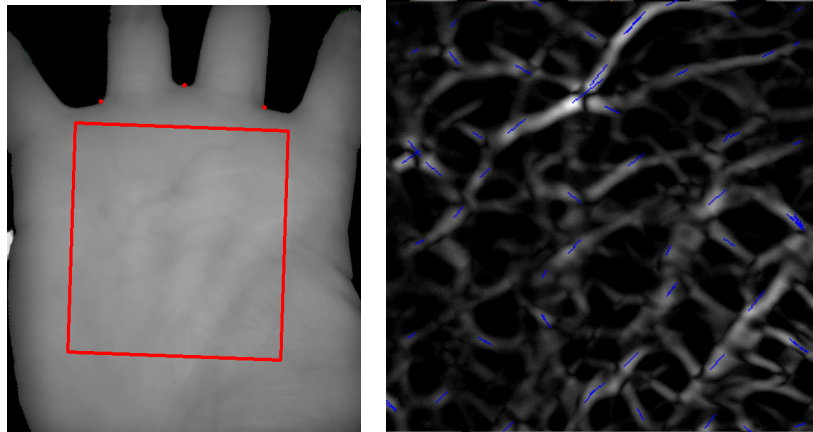


Figure 4.8 Palm and palm vein pattern

Using Fast NH-CMF filter, vectors describing palm vein pattern are acquired from original image. Image gets divided into 8x8 cells storing only most intensive vector in each cell, in form  $(X_0; Y_0; dX; dY)$ ; where  $X_0$  and  $Y_0$  are starting coordinates for vector relative to ROI dimensions (thus in range  $[0;1]$ ),  $dX$  and  $dY$  are projection of vector on X and Y axis respectively. From stored vectors, data vector is created in form of:

$$(X_1, Y_1, dX_1, dY_1, X_2, Y_2, dX_2, dY_2, \dots \\ \dots, X_{64}, Y_{64}, dX_{64}, dY_{64}, +1, +1, +1, +1, +1, \dots, +1)$$

where +1 is +1 if respective vector is in 50% of most intensive vectors, and -1 otherwise.

For data vector elements with indexes (1-based)  $i = [257; 320]$  respective vectors are described in elements  $(i-257)*4+1$  to  $(i-257)*4+4$ .

Person unique biocode is derived from data vector by hashing it using Biohash, for safe storage in database, meaning, palm vein pattern could not be restored even if biocode is stolen.

For better performance, system is trained for each person recognition, that is, 5 sample images are taken from each person, and average biocode is calculated, as well as information about bit stability is stored, making it possible for more stable bits to contribute more on similarity, than less stable bits.

### **References**

[4.1.1] Webster J.G. Medical Instrumentation: application and design. Fourth Edition. – New Jersey: John Wiley & Sons, Inc., 2009. – 675 p.

[4.1.2] J.Chambers S.Sanai. EEG Signal Processing. Cardiff, UK: John Wiley & Sons Ltd, 2009.

[4.1.3] A.Rosso S.Blanco, A.Figliola. Time-frequency analysis of electroencephalogram series. Third Edition. – New Jersey:Wiley Publishing, 2008.–9p.

[4.1.4] V.Terzis M.A. Klados. The impact of visual stimulation on alpha brain oscillations: An EEG study. Inf. Syst. Dept., Univ. of Macedonia, Thessaloniki, Greece, 2010.-4p.

[4.1.5] M.Vavrecka. Classification of the EEG feature components. Czech Tech. Univ. Prague, Czech Republic, 2010 - 4 p.

[4.2.1] A. Hermanis and K. Nesenbergs, „Grid shaped accelerometer network for surface shape recognition,” in Proc. 13th Biennial Baltic Electronics Conference, Tallinn, Estonia, October 3-5, IEEE 2012, pp. 203-206.

[4.2.2] A. Hanson. Visualizing Quaternions. The Morgan Kaufmann Series In Interactive 3D Technology. Morgan Kaufmann, 2005.

[4.2.3] A. Hermanis, “Inertial sensor network for surface shape detection”, master’s thesis, RTU, 2012.

[4.2.4] A. Hermanis and K. Nesenbergs, “Accelerometer Network for Human Posture Monitoring”, Riga Technical University 53rd International Scientific Conference, Riga, 2012, p. 684.

## 5. Uz rotācijas leņķiem balstītas vispārinātas signālu analīzes metožu attīstība un algoritmu modelēšana

### 5.1. Vispārinātās Jakobi matricas (EGURM) faktorizācija

2012. g. tika veikti pētījumi, lai faktorizētu vispārināto Jakobi matricu (EGURM – Elementary Generalized Unitary Rotation Matrix), kas ļauj izpildīt elementāro vispārināto rotāciju, izmantojot 5 reālu vērtību rotācijas [5.1].

#### 5.1.1. EGURM kā triju kompleksu matricu reizinājums

Algoritma pamatā ir Jakobi matricas izteikšana ar trīs retinātu kompleksu matricu reizinājumu (agrāk zināma lieta):

$$\mathbf{T}_{412} = \begin{bmatrix} c_\phi \cdot e^{-j\psi} & s_\phi \cdot e^{-j\gamma} \\ -s_\phi \cdot e^{j\gamma} & c_\phi \cdot e^{j\psi} \end{bmatrix} = \begin{bmatrix} 1 & 0 \\ 0 & e^{j(\gamma+\psi)} \end{bmatrix} \cdot \mathbf{T}_G(-\phi) \cdot \begin{bmatrix} e^{-j\psi} & 0 \\ 0 & e^{-j\gamma} \end{bmatrix}. \quad (5.1)$$

Pētījuma piensums ir EGURM faktorizācija:

$$\mathbf{T} = \mathbf{T}(a, b_R, b_C, u) = \mathbf{T}_3(u) \cdot \mathbf{T}_2(a, b_R, b_C) \cdot \mathbf{T}_1(u), \quad (5.2)$$

kur divas no matricām ir kompleksas

$$\mathbf{T}_3(u) = \begin{bmatrix} 1 & 0 \\ 0 & e^{j(S(2,u)\gamma - S(1,u)\psi)} \end{bmatrix}, \mathbf{T}_1(u) = \begin{bmatrix} e^{S(1,u)j\psi} & 0 \\ 0 & e^{-S(2,u)j\gamma} \end{bmatrix}, \quad (5.3)$$

vidējā matrica ir Givena matrica ar permutētām rindām ( $\mathbf{R}$ ) un kolonnām ( $\mathbf{C}$ ):

$$\mathbf{T}_2 = \mathbf{T}_R(\phi) = \mathbf{T}_R(\phi, a, b_R, b_C) = \mathbf{R}(a, b_R) \cdot \begin{bmatrix} c_\phi & -s_\phi \\ s_\phi & c_\phi \end{bmatrix} \cdot \mathbf{C}(b_C), \quad (5.4)$$

bet zīmju matrica

$$\mathbf{S} = \begin{bmatrix} +1 & -1 & +1 & -1 \\ +1 & +1 & -1 & -1 \end{bmatrix} \quad (5.5)$$

nosaka atbilstošo matricu elementu zīmes.  $s_\phi = \sin(\phi)$ ,  $c_\phi = \cos(\phi)$ . Mainīgie  $a$ ,  $b_R$ ,  $b_C$  un  $u$  nosaka konkrētu EGURM izskatu (*shape*).

### 5.1.2. Reālu vērtību EGURM ekvivalenta faktORIZĀCIJA

Ja kompleksā ieejas signāla vektora (2 kompleksi elementi), kuru ir jātransformē, pārraksta kā reālu vērtību 4-u elementu vektoru, mēs varam izteikt EGURM "reālo" ekvivalentu kā triju 4x4 reālu retinātu matricu reizinājumu:

$$\mathbf{y}_r = [y_{\text{Re1}} \ y_{\text{Im1}} \ y_{\text{Re2}} \ y_{\text{Im2}}]^T = \mathbf{T}_r \cdot \mathbf{x}_r = \mathbf{T}_{3r} \cdot (\mathbf{T}_{2r} \cdot (\mathbf{T}_{1r} \cdot [x_{\text{Re1}} \ x_{\text{Im1}} \ x_{\text{Re2}} \ x_{\text{Im2}}]^T)), \quad (5.6)$$

kur

$$\mathbf{T}_{1r} = \begin{bmatrix} \mathbf{T}_\psi & 0 & 0 \\ 0 & 0 & \mathbf{T}_{-\gamma} \\ 0 & 0 & 0 \end{bmatrix}, \mathbf{T}_{3r} = \begin{bmatrix} 1 & 0 & 0 & 0 \\ 0 & 1 & 0 & 0 \\ 0 & 0 & \mathbf{T}_{\gamma-\psi} \\ 0 & 0 & 0 & 0 \end{bmatrix}, \mathbf{T}_{2r} = \mathbf{P} \cdot \begin{bmatrix} \mathbf{T}_R(\phi) & 0 & 0 \\ 0 & 0 & 0 \\ 0 & 0 & \mathbf{T}_R(\phi) \\ 0 & 0 & 0 & 0 \end{bmatrix} \cdot \mathbf{P}, \text{ kur } \mathbf{P} = \begin{bmatrix} 1 & 0 & 0 & 0 \\ 0 & 0 & 1 & 0 \\ 0 & 1 & 0 & 0 \\ 0 & 0 & 0 & 1 \end{bmatrix} \quad (5.7)$$

un faktorizētās matricas satur reālas rotācijas struktūras:

$$\mathbf{T}_\psi = \mathbf{T}_G(S(1,u) \cdot \psi), \quad \mathbf{T}_{-\gamma} = \mathbf{T}_G(-S(2,u) \cdot \gamma), \quad \mathbf{T}_{\gamma-\psi} = \mathbf{T}_G(S(2,u) \cdot \gamma - S(1,u) \cdot \psi). \quad (5.8)$$

No iepriekšējām izteiksmēm izriet, ka, lai īstenotu komplekso EGU-rotāciju, ir nepieciešamas 2+2+1 = 5 reālas rotācijas, virkne leņķu pārrēķinu (ņemot vērā izvēlētās EGURM konkrēto izskatu) un permutāciju.

### 5.1.3. EGURM daudzveidība un precizitāte

Atkarībā no  $\mathbf{T}_G$  rotācijas leņķa diapazona, EGURM ir iespējami no 4 līdz 64 dažādi izskati (*shapes*). Leņķu diapazoni, adresu intervāli un izskatu skaits ir apkopots nākamajā tabulā

$\phi, \gamma, \psi$ (deg)	$a, u$	$b_R$	$b_C$	$N_r, N_s$
[0, 45°]	[1, 4], [1, 4]	[0, 1]	[0, 1]	16, 64
[-45°, 45°]	[1, 4], [1, 4]	[0, 1]	0	8, 32
[0, 90°]	[1, 2], [1, 2]	[0, 1]	[0, 1]	8, 16
[-90°, 90°]	[1, 2], [1, 2]	[0, 1]	0	4, 8
[0, 180°]	1, [1, 2]	[0, 1]	[0, 1]	4, 8
[-180°, 180°]	1, [1, 2]	[0, 1]	0	2, 4

Samazinot pamatrotatora  $\mathbf{T}_G$  leņķa diapazonu līdz [0, 45°] ir iespējams paaugstināt rotācijas precizitāti (līdz pat 8 reizēm), ja rotācijas leņķi mainās plašākās robežās ([-180°, 180°]). Tas notiek uz EGU-rotatora struktūras sarežģītības palielināšanas rēķina.

## 5.2. Doplera radara (DR) signālu ciparapstrāde

2012. g. tika veikti pētījumi, kas saistīti ar DR signālu ciparapstrādes algoritmu izstrādi. Algoritmi ir balstīti uz minimālo kvadrātu metodes un atstaroto signālu modeļiem. Izstrādājami algoritmi ir paredzēti tādu transporta līdzekļu (TL) kustības parametru iegūšanai kā: ātrums, izmēri, kategorija un kustības josla [5.2] [5.3].

### 5.2.1. DR signāla ciparapstrādes algoritmi

#### 5.2.1.1. Viena atstarojošā punkta modelis

Algoritmu pamatā ir DR signāla modeļa izvēle. Pats vienkāršākais ir viena atstarojošā punkta/zonas (*scattering point*) modelis:

$$x(t) = A(t) \cdot \sin(2 \cdot \pi \cdot f_D(t)), \quad (5.9)$$

kur

$$f_D(t) = k \cdot V_{xy}(t) = k \cdot V_0(t) \cdot \cos(\phi(t)). \quad (5.10)$$

Apstrādes algoritmā pēc būtības tiek ignorēta apliecēja  $A(t)$  un tika izmantota informācija tikai par frekvences  $f_D(t)$  izmaiņām. Apliecēja tika izmantota tikai TL atstarotā signāla sākuma un beigu detektēšanai. Galvenā algoritma funkcija ir novērtēt TL ātrumu  $V_0(t)$ .

#### 5.2.1.2. Minimālo kvadrātu metode

Algoritms operē ar starpību starp modelī ietvertu un eksperimentāli noteikto frekvences izmaiņu laikā:

$$\Delta(t_k) = f_{\text{exp}}(t_k) - f_D(t_k), \quad (5.11)$$

pieprasot, lai atšķirību kvadrātu summa būtu minimāla, kas noved pie vienādojumu sistēmas

$$\sum_{k=1}^K \Delta(t_k) \frac{\partial(f_D(x, t_k))}{\partial x} = 0, \quad (5.12)$$

kur  $x$  ir izvēlētais parametrs (ātrums, attālums līdz joslas centram utt.)

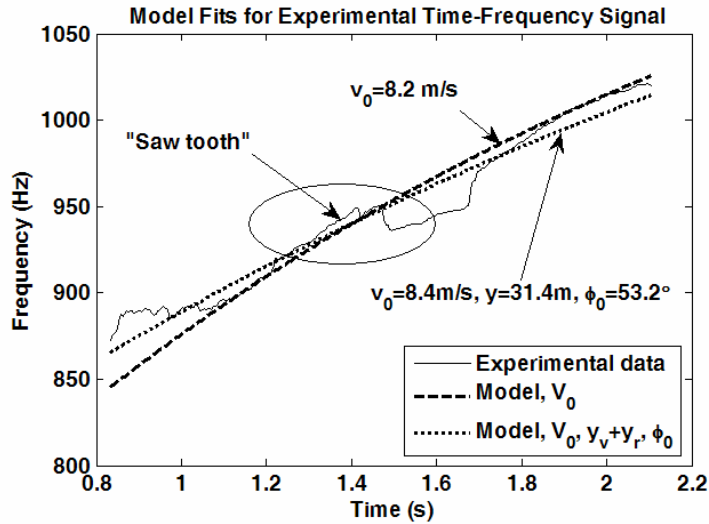


Figure 5.1 Divu modeļu pielaikošana eksperimentālajam laika signāla (no viena TL), raustīta līnija – lokalizācija ir dota, punktēta līnija – lokalizācija ir atrasta

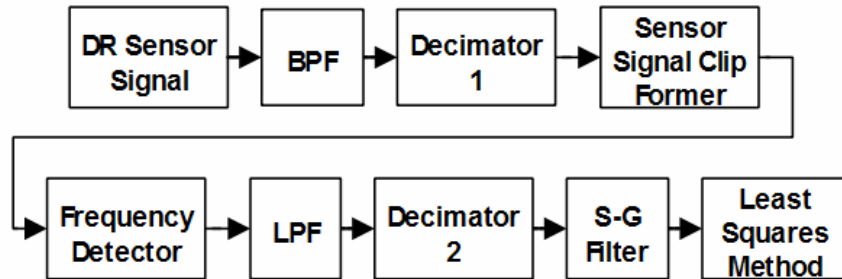


Figure 5.2 TL kustības parametru novērtēšana, izmantojot frekvenču detektēšanu un minimālo kvadrātu metodi

### 5.2.1.3. Vairāku atstarojošo punktu modelis

Ja ir vajadzība paaugstināt TL kustības parametru novērtēšanas precizitāti, tad ir jāizmanto vairāku atstarojošo punktu modelis:

$$s_{\Sigma}(t) = \sum_i^N I_i(t) \cdot \cos(2\pi f_i(t)t). \quad (5.13)$$

Šāds modelis ļauj atpazīt arī aptuvenu (viļņa garums 1.25 cm) TL formu. Pētījumā ir izmantots 5 ( $N$ ) punktu modelis.

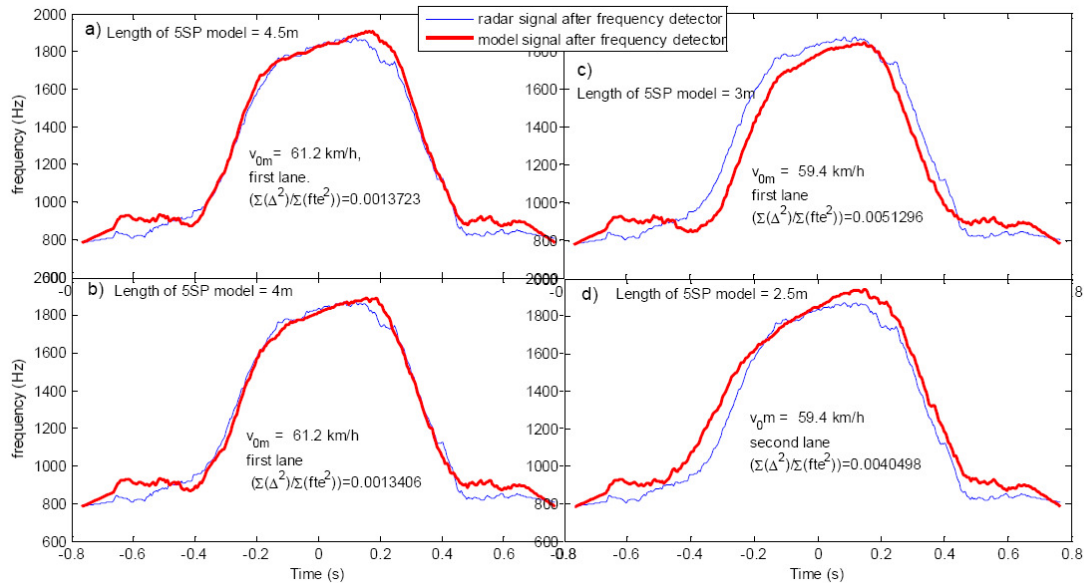


**Figure 5.3 TL kustības parametru novērtēšana, izmantojot frekvenču detektēšanu un minimālo kvadrātu metodi 5 punktu modelim. Sarkanā līkne – pēc modeļa restaurētais laika-frekvences signāls, zilā līkne oriģinālais laika-frekvences signāls**

#### **5.2.1.4. Perspektīva - uz rotācijas leņķiem balstītu funkciju modelis**

Atrodas izstrādes stadijā. Izskatās, ka ļaus būtiski ietaupīt skaitļošanas apjomu un FPGA resursus. Te ir pilnīgi jaunas patentējamas lietas.

### **5.3. Uz rotācijas leņķiem balstītu signālu ciparapstrādes ierīču moduļu izstrāde un mikrominiaturizācija (ASIC/FPGA)**

Moduļu izstrāde un mikrominiaturizācija 2012.g. ir noritējusi vairākos virzienos. Šeit aplūkosim tikai galveno pienesumu VPP.

#### **5.3.1. EGU-rotatora arhitektūra balstīta uz reālu vērtību rotatoriem**

Kā jau minēts iepriekš, fakts, ka EGURM var interpretēt kā 5 reālas rotācijas, ļauj EGU-rotatoru realizēt kā trīs pakāpju ierīci.

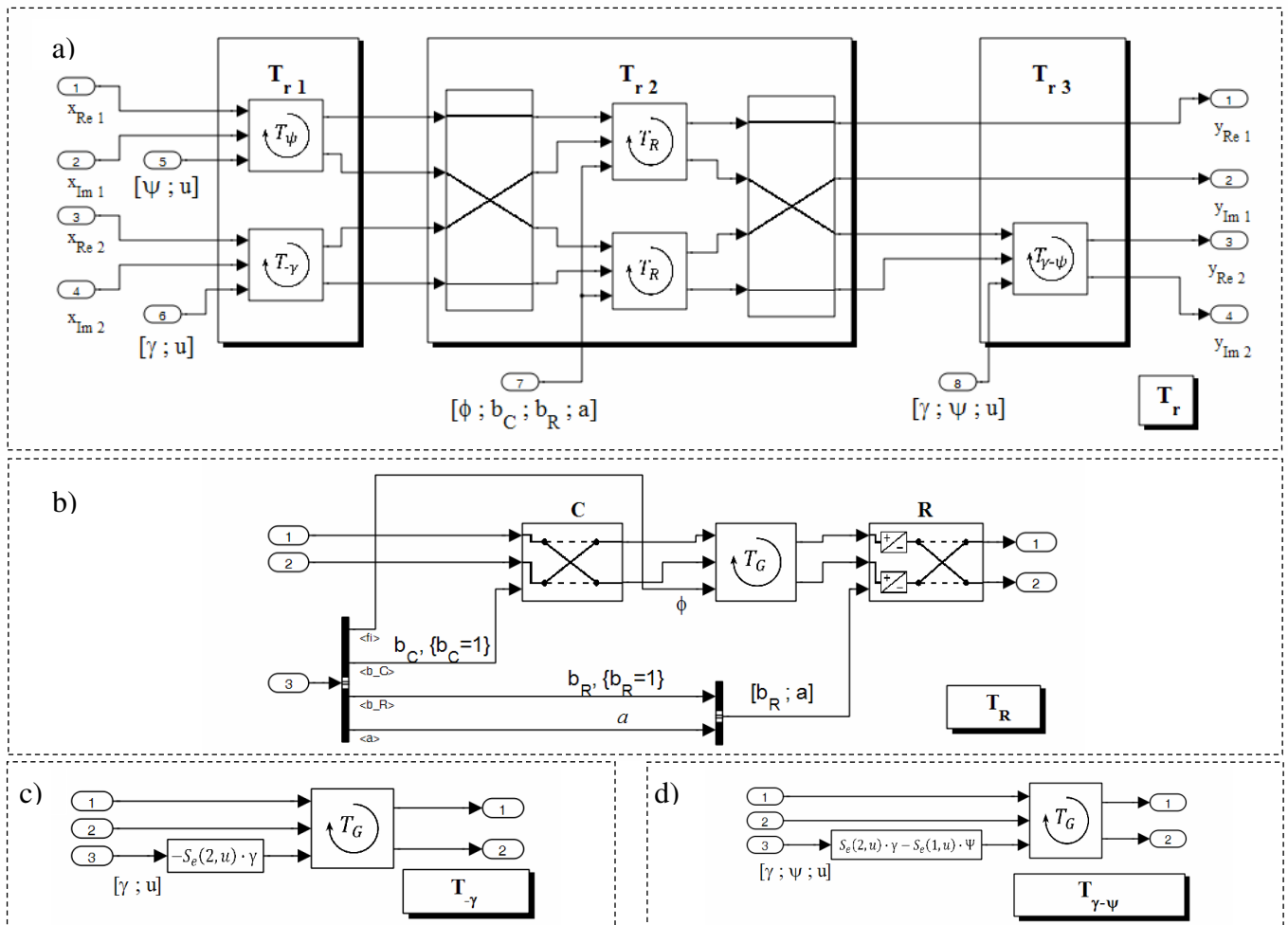


Figure 5.4 EGU-rotatora arhitektūra, kas balstīta TG (Givena) rotatoriem, a) kopējā blokshēma, b) bloks TR, c) bloks T- $\gamma$ , d) bloks T- $\gamma$ - $\psi$

Rotatora simulācijai, vienkāršai testēšanai un sintēzei tika izmantota attēlotā Simulink blokshēma.

### 5.3.1.1. EGU-rotatora VHDL koda sintēze

Koda sintēzes automatizācija tik veikta izmantojot *Matlab/Simulink*, *Altera Quartus II* un *Mentor Graphics ModelSim (Xilins ISE)* programmas. Minētās programmas tiek lietotas sekojošu uzdevumu veikšanai:

- *MatLab* – Automatizācijas vadība, rotācijas matricu faktorizācija un unitaritātes pārbaude, izmantojot Symbolic Math Toolbox(SMT). Rezultātu iegūšana izmantojot peldošā punkta aritmētiku (double precision) un iegūto izteiksmju pārveidošana fiksētā punkta aritmētikā ar **fi()** objektu.
- *Simulink* – Rotatora simulēšana fiksētā punkta aritmētikā, VHDL koda ģenerēšana izmantojot *HDL coder*,
- *ModelSim* – VHDL koda simulēšana (*Altera*),
- *Quartus II* – VHDL koda kompilācija izvēlētajai *Altera* FPGA mikroshēmai,

FPGA programmēšana.

- *ISE* - VHDL koda kompilācija izvēlētajai *Xilinx* FPGA mikroshēmai, FPGA programmēšana.

### 5.3.1.2. Sintezētā rotatora resursu patēriņa salīdzinājums

Resursu salīdzināšana tika veikta gadījumam, kad Given rotators tiek realizēts ar CORDIC-a algoritmu *Altera* un *Xilinx* platformām.

Usage of Device Resources in Dependence on the Wordlength for Single CORDIC Cell, Iterations - 10-16

Device, (Speed Grade)	Resource	Wordlength (WL)		
		16	24	14-32
EP4CE40 (8)	<i>REG</i>	64	136	~6.7×WL-33
	<i>LUT</i>	880-930	~1025	~44×WL-78
	<i>MUL(18×18)</i>	2	10	-
XC6SLX75 (2)	<i>REG</i>	102-114	153-177	~5×WL+40
	<i>LUT</i>	230-315	395-525	~24×WL-60
	<i>MUL(18×18)</i>	6	12	-

Redzams, ka *Altera* FPGA mazāk patērē reģistrus un reizinātājus, bet *Xilinx* kombināciju shēmas (*Look Up Table*). Resursu patēriņš praktiski nav atkarīgs no izvēlētajās saimes un ierīces un ātrdarbības (*Speed Grade*). Kopējais visa EGU-rotatora resursu patēriņš ir aptuveni **4.9** reizes lielāks nekā vienai rotatora šūnai.

### 5.3.1.3. Perspektīva

Pašreiz rotators tiek iekļauts iepriekš izstrādātajā EGURIT (Elementary Generalized Unitary Rotation Instrumentation Tool) un izstrādājamajā UNITIT (UNITary Transform Implementation Tool – Unitāru Pārveidojumu Īstenošanas Rīks). Tiek strādāts pie rotatora hibrīdajiem algoritmiem – CORDIC kopā ar iepriekš izmantotajiem reizinātāju-summatoru (M-A) algoritmiem [5.1]. Algoritms tiek izmantots veidojot vispārinātā OFDM blokus.

### 5.3.2. DR signālu ciparapstrādes modulis

Ir izveidoti eksperimentāli FPGA moduļi [5.3], kas ir sintezēti, izmantojot Simulink HDL Coder. Nākamajā tabulā ir dots loģisko elementu (LE) patēriņš 5 punktu modeļa FPGA moduļim.

TABLE I. PRELIMINARY ESTIMATION OF LE FOR IMPORTANT SIGNAL PROCESSING STAGES IN DSP MODULE OF RADAR

Signal processing stage	Number of LE for Cyclone IV GX
Signal preprocessing	1648
Sensor signal clip former	2898
Frequency detector	36768
First 3 stages	41263
Doppler shift signal simulation for 5SP model	20349
Doppler shift signal simulation for vehicle model (10 scattering points)	40660
Doppler shift signal simulation for 5SP model with following frequency detector	57628
Doppler shift signal simulation for 10SP model with following frequency detector	77997

#### **5.4. Uz Vispārinātās Ortogonālās Nesinusoidālās Frekvenču balstītas datu pārraides sistēmas pilnveidošana**

2012. gada gaitā turpinājās darbs pie vispārinātās datu pārraides sistēmas. Tika izstrādāta vispārinātās sakaru sistēmas laika un frekvences sinhronizācija. Pētījumu rezultāti tika prezentēti 2 starptautiskajās IEEE konferencēs “BEC2012” un “TELFOR2012”. Turklāt, gada vidū konferencē “Electronics 2012” tika prezentēts sakaru kanāla novērtēšanas un izlīdzināšanas algoritms, kas tika izstrādāts 2011-2012. gadā [5.4] [5.5] [5.6].

##### **5.4.1. Kanāla izlīdzināšana**

Lai veiktu izlīdzināšanu Vispārināto Unitāru Pārveidojumu (VUP) apgabalā, ir nepieciešams veikt nediagonālas un ne Teplica kanāla matricas inversiju. Viens no veidiem kā invertēt matricu ir sākumā to diagonalizēt. Kanāla matricas diagonalizēšanai tiek piedāvāta singulāro vērtību dekompozīcija (SVD). Simulācijas, kas tika veiktas izlīdzinātāja testēšanai parādīja izcilus rezultātus un apstiprināja piedāvātās metodes pielietojamību uzstādītā uzdevuma atrisināšanai. Tiek salīdzināti 3 kanāla novērtēšanas algoritmi savienojumā ar izlīdzinātāju, kas balstās uz SVD. Simulācijas parādīja, ka SVD ir ļoti jūtīgs pret kanāla novērtējuma kļūdām. Pie pietiekoši precīza novērtējuma, kas tika iegūts lietojot LMS, iegūtais izlīdzinātājs nodrošināja augstāku datu pārraides sistēmas veiktspēju nekā OFDM ar tādu pašu nesēju skaitu.

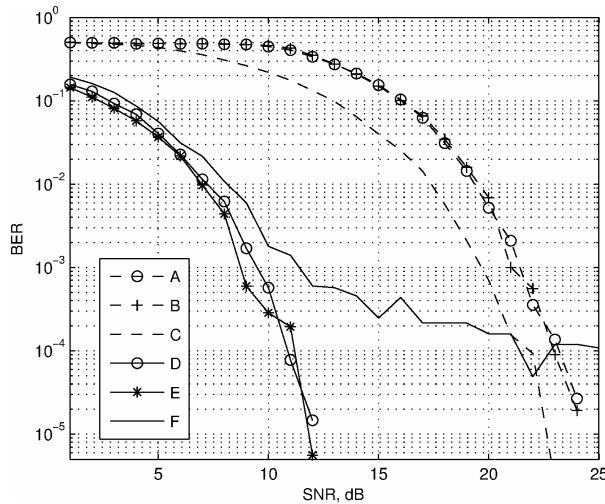


Figure 5.5 Datu pārraides sistēmas veiktspējas salīdzinājums pie dažādām novērtēšanas metodēm atkarībā no attiecības signāls/troksnis

### 5.4.2. Bloku sinhronizācija

Nemot vērā, ka vispārinātā sakaru sistēma veic pārraidi pa blokiem, bija nepieciešams izstrādāt algoritmu, kas nodrošinātu precīzu bloku sākumu atrašanu neatkarīgi no pielietojamās transformācijas. Klasiskie laika nobīdes novērtēšanas algoritmi, kas tiek lietoti OFDM izrādījās nepietiekoši precīzi lai nodrošinātu sinhronizāciju 1 čipa robežās. Tiek piedāvāts oriģināls, uz šķērskorelāciju balstīts algoritms, kas nodrošina augstu precizitāti, bet relatīvi vāju traucējumnoturību. Lai uzlabotu traucējumnoturību, tiek piedāvāts lietot kombinēto novērtētāju, kas izmanto gan autokorelāciju gan šķērskorelāciju. Rakstā aprakstītā automātiskās vadības cilpa, kas balstās uz PID un nodrošina automātisku laika sinhronizāciju pie neliela iterāciju skaita. Izstrādātais sinhronizācijas risinājums parāda augstu traucējumnoturību un precizitāti.

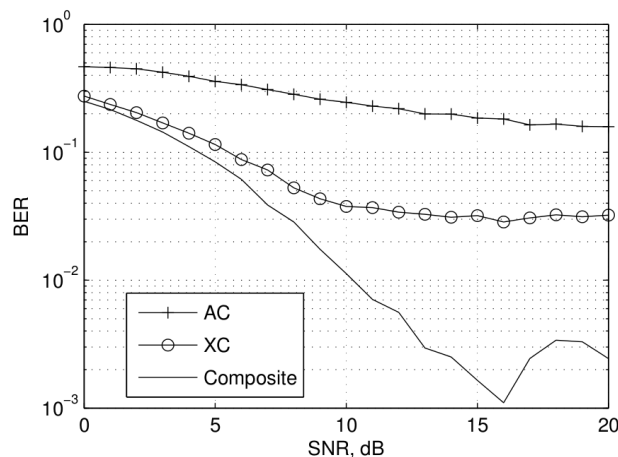


Figure 5.6 Datu pārraides sistēmas veiktspējas salīdzinājums atkarībā no bloku sinhronizācijas risinājuma

### 5.4.3. Frekvences sinhronizācija

Bez laika sinhronizācijas, jebkurā sakaru sistēmā ir jānodrošina frekvences sinhronizāciju. Tiek piedāvāti 3 oriģināli nesējfrekvences (carrier frequency) nobīdes novērtēšanas algoritmi, kas balstās uz šķērskorelāciju. Minēto algoritmu galvenā priekšrocība salīdzinājumā ar klasiskajiem, uz autokorelāciju balstītiem algoritmiem, ir tā, ka tie:

- spēj nodrošināt daudz plašāku frekvences nobīdes diapazonu;
- kanālos bez dispersijas (AWGN) tie nodrošina augstāku precizitāti;

Izstrādāto algoritmu galvenie trūkumi ir:

- garu treniņsecību lietošanas nepieciešamība;
- vāja noturība pret dispersiju sakaru kanālā;

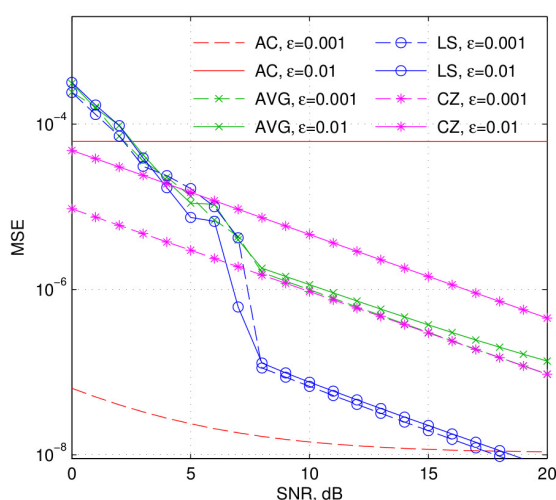


Figure 5.7 Datu pārraides sistēmas veiktspējas salīdzinājums dažādiem frekvenču sinhronizācijas algoritmiem

## 5.5. Izstrādātie funkciju/programmu moduļi MATLAB/Simulink bibliotekām "Phi-FunctionsToolbox/Blockset"

2012.g. saistībā ar "izgudrotajiem" pārveidojumiem tika/tiek izstrādāti un pilnveidotās vairākas interaktīvas Matlab/Simulink programmas [5.7] [5.8]. Vislielākais piensums ir Doplera radara DSP moduļa prototipēšanas vide, kuras funkcionalitāti nodrošina, galvenokārt, Matlab/Simulink (ML/SL)

### 5.5.1. DR DSP moduļa izstrādes-prototipēšanas vide

Ir izveidota vide, kura sevī ietver sekojošu aparatūru un programmatūru:

- DR sensoru (*DR Front End*), kas ļauj
  - apstarot kustīgu objektu ar CW (*Continues Wave*) augstas frekvences elektromagnētisko vilni un uztver atstaroto vilni,

- saformēt Doplera efekta radīto ZF signālu;
- DR signāla analizatoru-prototipēšanas līdzekli (ML/SL), kas tiek izmantots, lai prototipētu DR DSP moduļa izstrādi, kas ļauj
  - novērtēt TL ātrumu,
  - saskaitīt TL,
  - identificēt kustības joslu,
  - novērtēt TL izmēru/kategoriju,
  - aptuveni atpazīt TL formu;
- ar videokameru aprīkotu automatizētu analīzes palīg līdzekli (ML/SL), kas, veicot attēlu apstrādi, ļauj
  - detektēt kustīgu TL,
  - sekot kustīgajam TL,
  - atrast TL ātrumu,
  - detektēt kustības joslu,
  - novērtēt TL kategoriju un saskaitīt TL;
- virtuālo simulatoru (ML/SL), kas ietver sevī
  - TL trafika imitatoru (izmantojot zināmus kustības trafika modeļus),
  - 3D vizualizatoru;
- virkni tādu programmatūras līdzekļu kā
  - ML/SL ar rindu izstrādes līdzekļu kopu (*Toolboxes*),
  - *Altera Quartus II* un *Mentor Graphics ModelSim*;
- *Altera* un *Terrasic* FPGA izstrādes līdzekļus (DE2 un DE3).

Vides struktūra ir redzama nākošajā attēlā 5.8.

### **5.5.2. Perspektīva**

Aptuvena formas atpazīšana ir iespējama izmantojot uz rotācijas leņķiem balstītus divdimensionālos pārveidojumus, kuru izstrāde turpinās. Pašreiz, iepriekš izstrādātais virtuālais attēlu analizators-sintezators (**VIMANSY**) tiek adaptēts prototipēšanas videi.

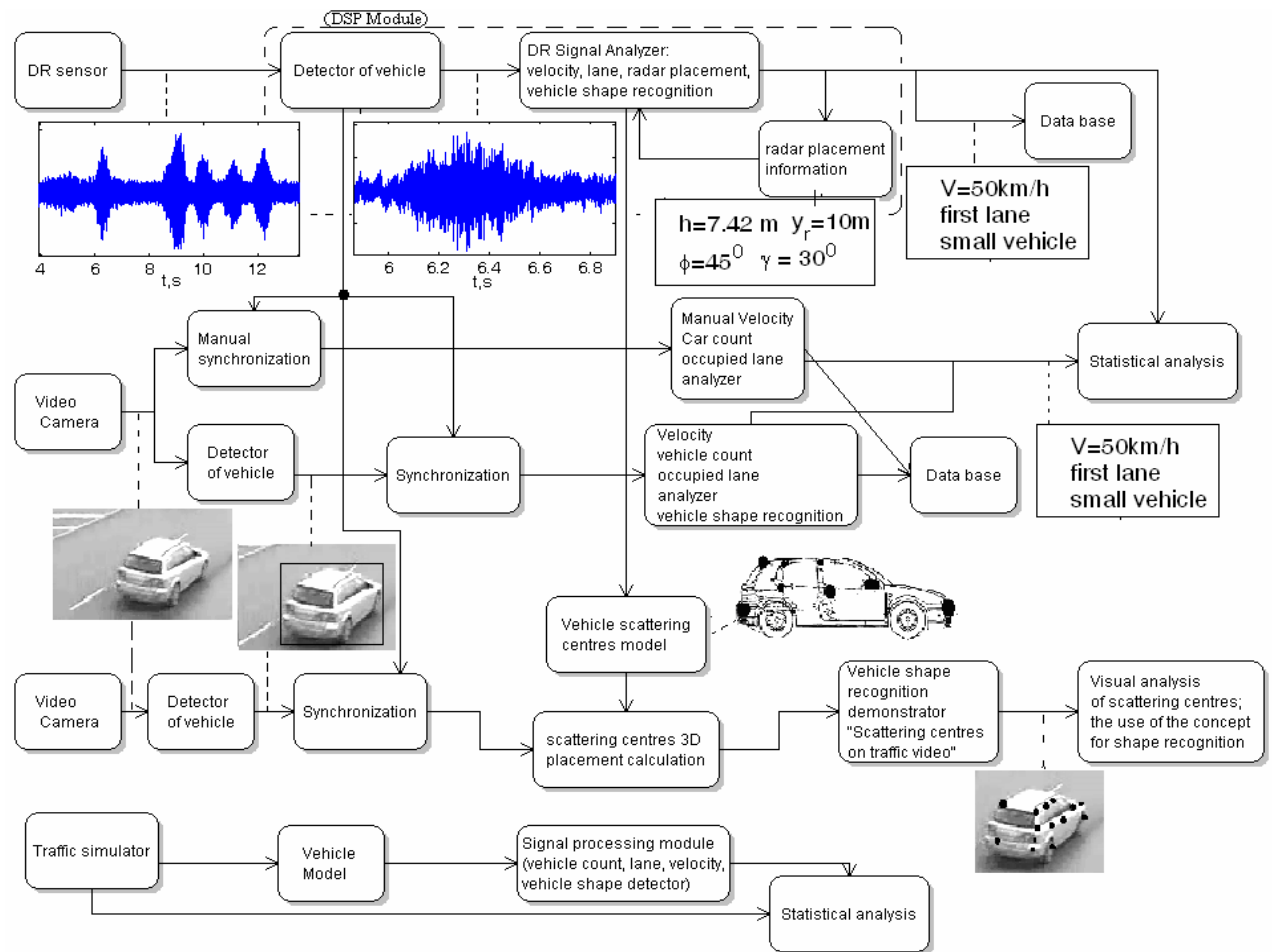


Figure 5.8 Prototipēšanas vides struktūra

## References

[5.1] P. Misans, U. Derums, V. Kandars, "FPGA Implementation of Elementary Generalized Unitary Rotation with CORDIC Based Architecture: Preliminary results", in Proc. of 30th IEEE Norchip 2012 Conference, Copenhagen, Denmark, Nov.12-13, 2012, 6 pages, IEEE Catalog No. CFP 12828-USB, ISBN 978-1-4673-2223-2/12/.

[5.2] P. Misans, M. Terauds, "CW Doppler Radar Based Land Vehicle Speed Measurement Algorithm Using Zero Crossing and Least Squares Method", in Proc. 13th Biennial Baltic Electronics Conference (BEC2012), October 3-5, 2012, Tallin, Estonia, pp. 161-164. IEEE Catalog No. CFP 12BEC-CDR, ISBN 978-1-4673-2773-2/12/.

[5.3] M. Terauds, "Implementation of FPGA Based DSP Module for CW Doppler radar: Preliminary results", in Proc. of 30th IEEE Norchip 2012 Conference, Copenhagen, Denmark, Nov.12-13, 2012, 6 pages, IEEE Catalog No. CFP 12828-USB, ISBN 978-1-4673-2223-2/12/.

[5.4] A. Aboltins, P. Misans, "Singular Value Decomposition Based Phi Domain Equalization For Multi-Carrier Communication System," in the Journal "Electronics and Electrical Engineering", KTU, Kaunas, vol. 18, No. 9, 2012, 71-74 pp., <http://www.ejournal.ktu.lt/index.php/elt/article/download/2811/1993>.

[5.5] A. Aboltins "Block Synchronization Using a Unique Word for a Generalized Unitary Rotation Based Communication System", Proc. 13th Biennial Baltic Electronics Conference BEC2012 (on CD), October 3-5, 2012, Tallin, Estonia, pp. 149-152, IEEE Catalog No. CFP 12BEC-CDR, ISBN 978-1-4673-2773-2/12/.

[5.6] A. Aboltins, "Carrier Frequency Offset Estimator Based on Unique Word Cross correlation", in Proc. of 20th IEEE TELFOR'2012 Conference (on CD), Nov. 20-22, 2012, Belgrad, Serbia, pp. 486-489, IEEE Catalog No. CFP 1298P-CDR, ISBN 978-1-4673-2984-2/12/.

[5.7] P. Misans, M. Terauds, D. Liepkalns, "Development of CW Doppler Radar Prototyping Environment Used for Vehicle Recognition and Parameter Estimation", Proc. 13th Biennial Baltic Electronics Conference (BEC2012), October 3-5, 2012, Tallin, Estonia,, pp. 165-168. IEEE Catalog No. CFP 12BEC-CDR, ISBN 978-1-4673-2773-2/12/.

[5.8] U. Derums, P. Misans, "Virtual Image Analyzer-Synthesizer Based on the Novel Discrete Orthogonal Transforms", in Proc. of the IEEE European Modeling Symposium EMS'2012 (on CD), Malta, Luqa, Nov. 14-16, 2012, pp. 213-218, IEEE Catalog No. CFP1228I-CDR, ISBN 978-0-7695-4926-2/12/.

## 6. Radioviļņu daudzceļu izplatīšanās modeļu uzlabošana izplatīšanās apstākļos ar gariem koridoriem un dzelzsbetona griestu pārsegumiem

The results obtained in this period:

- Ranged models and parameters of radio wave propagation models in the fast fading environment (Section 6.1).
- Performed analysis of Doppler frequency shift parameters of radio wave propagation models in the fast fading environment (Section 6.2).

Future work:

- Results obtained have shown the power delay profile for dynamic conditions in the multipath environment. i.e. including the motion.
- Further analysis will perform the multipath attenuation estimation for communication channel with the moving antenna.

### 6.1. Ranged models for fast fading environment

A number of models have been introduced along the lines of a general Hata-like power law with standard deviation of an error around 10 dB for these models.

To improve these models an empirical wide-band model is evaluated for delay spread and average power delay profile (PDP). These factors together with Doppler characteristics as field direction-delay spread and space dependent channel impulse response and time-dependent channel response are required as the key elements for the system simulation.

Typical results from [6.1] is shown in Table 1.

Table 1

Delay spread and power delay profile shape in different environment

<i>Environment</i>	<i>Average rms delay spread [ns]</i>	<i>Variability of rms delay spread [ns]</i>	<i>Profile shape</i>
<i>Dense</i>	<i>19.3</i>	<i>3.4</i>	<i>exponential</i>
<i>Open</i>	<i>27.7</i>	<i>3.6</i>	<i>power</i>
<i>Large</i>	<i>67.4</i>	<i>4.3</i>	<i>exponential</i>

As seen in the Table 1 the PDP in dense environment follows the exponential dependence. In open environment the PDP follows the power function and large environment again follows the exponential one.

$$\frac{1}{\tau_0} e^{-\frac{\tau}{\tau_0}}$$

Description for exponential delay profile  $\frac{1}{\tau_0} e^{-\frac{\tau}{\tau_0}}$  and power delay profile

$$\frac{1}{\sqrt{2\pi}} e^{-\frac{1}{2}\left(\frac{\tau}{\tau_0}\right)^2}$$

is dependent on average delay  $\tau_0$ . Time variations of the indoor radio channel mainly result from the 3 sources: a receiving antenna position change have produced spatial fluctuations of the electric field translated into time delay variations; time variance is observed due to changes in the antenna orientation from non-uniform antenna field pattern; and movement of the scattering objects (as person with a transmitter) results in the time-variant system function.

Under the general assumptions of the radio wave propagation on uniform distribution of the phases of the incident signal the time-variant channel is wide sense stationary uniform scattered over the time interval  $[T, \infty]$  with the scattering function [6.2]:

$$P(\tau, \nu) = P(\tau)P(\nu)$$

where  $P(\tau)$  un  $P(\nu)$  are the power delay profile and normalised power Doppler profile of the channel, respectively.

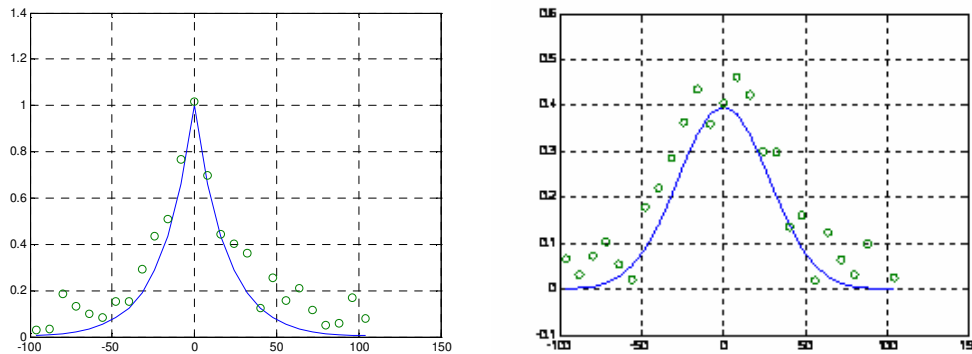


Figure 6.1 Delay spread for dense ( $\sigma_\tau=3.4$  ns) and open ( $\sigma_\tau=3.6$  ns) environment (simulated)

Wide band model delay spread has been tested for RTU ETF building on the second floor.

**Conclusion.** We need detail adjustment for better estimation for dominant path [6.3] of the delay spread for moving objects in the further evaluation.

## 6.2. Doppler frequency shift estimation

Traditional empirical propagation models estimate the mean path loss at a given location. In practice for models it is important to know the statistics of received signal. Long term and short term fading could be estimated. For indoor long term fading can reflect measured mean value over the distance of some wavelengths. According to [6.4] the indoor long term fading reflects lognormal distribution with  $\sigma=2.7-5.3$  dB. Short term fading as fast fluctuations of the signal level caused by movement reflects

Rice distribution from negative values for non-line of site up to 14.8 dB in clear line-of-site conditions.

Rayleigh, Weibull and Nakagami distributions [6.5] have been used for successful description of the fading environment.

## **References**

[6.1] Digital Mobile Radio Towards Future Generation Systems. COST 231 Final Report. 1995. 474 p.

[6.2] Balodis G. Mobilie sakari Rīga, RTU 2012, 183 lpp.(elektroniskā versija)

[6.3] Dominant Path Prediction Model for Indoor Scenarios Wölfle G. Wahl R. Wertz P. Wildbolz P. Landstorfer F. GeMiC 2005 pp. 176-179

[6.4] Karlsson P. Indoor Radio Propagation For Personal Communications Services Ph. D. Thesis, Uni. Of Lund, 1995

[6.5] Hasemi H. A Study Of Temporal And Spatial Variations Of The Indoor Radio Propagation Channel Proc. PIMRC'94, 1994, pp. 127-134.

## 7. Starpautomobiļu komunikācijas sistēmas modeļa izstrāde un mobilo objektu vietas noteikšanas pētījumi, izmantojot satelītu reāllaika kinemātikas datu apstrādi, un transporta līdzekļa pārvietošanās modeļa izstrāde, lai noteiktu zudumus, kas rodas bāzes stacijām pārslēdzoties

### 7.1. Starpautomobiļu datu pārraides sistēmas izpēte, kustības drošības paaugstināšanai.

#### 7.1.1. Vadības sistēmas uz V2V bāzes.

As is well known, any intersection is a high-risk source for cars, especially intersection without traffic lights. Road intersection safe crossing task sufficiently difficult to solve using traditional methods. Therefore there are a lot of interest in a safe intersection crossing facility that is based of mutual knowledge of the current road situation in the location of the participants and their motion parameters (Fig. 7.1 and Fig. 7.2).

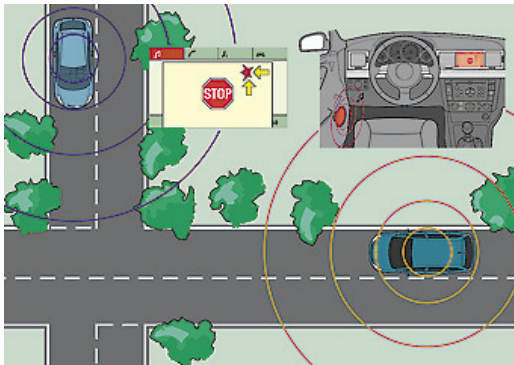


Figure 7.1 Intersection without traffic light crossroad along

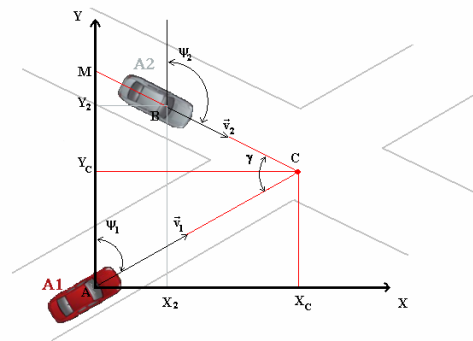


Figure 7.2 Cars approaching a intersecting courses

Results of the simulation are show in Fig.7.3 and Fig. 7.4.

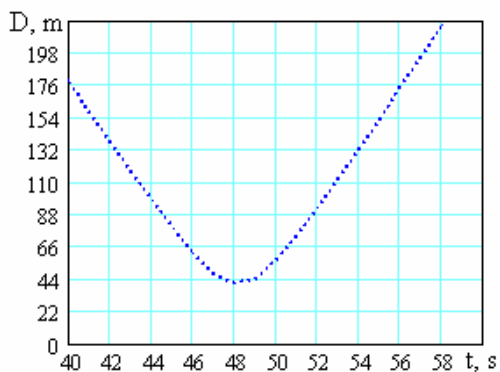


Figure 7.3 Intercar distance/time relationship at relationship at  $v_1 = 50 \text{ km/h}$ ,  $v_2 = 50 \text{ km/h}$

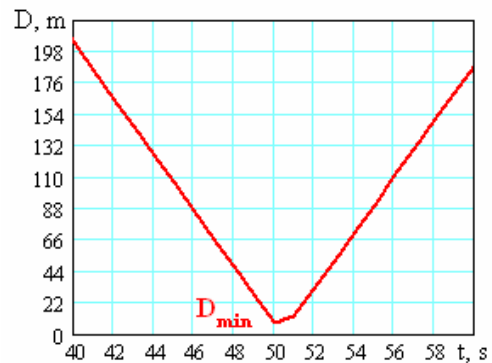


Figure 7.4 Intercar distance/time  $v_1 = 50 \text{ km/h}$ ,  $v_2 = 50 \text{ km/h}$ ,  $a_2 = -0.05 \text{ m/s}^2$

**Algorithm for assessment (estimator) of the possibility of safe intersection passing.**  
 Here is an algorithm for the safe crossing of intersection, based on the processing of information about location, speed and heading obtained by GPS. (Fig. 7.5). The data exchange is carried out with the help of DSRC. The result of the calculations is the predicted minimal distance between the cars. Using these data the system produces a warning message for the car driver [7.1.1].

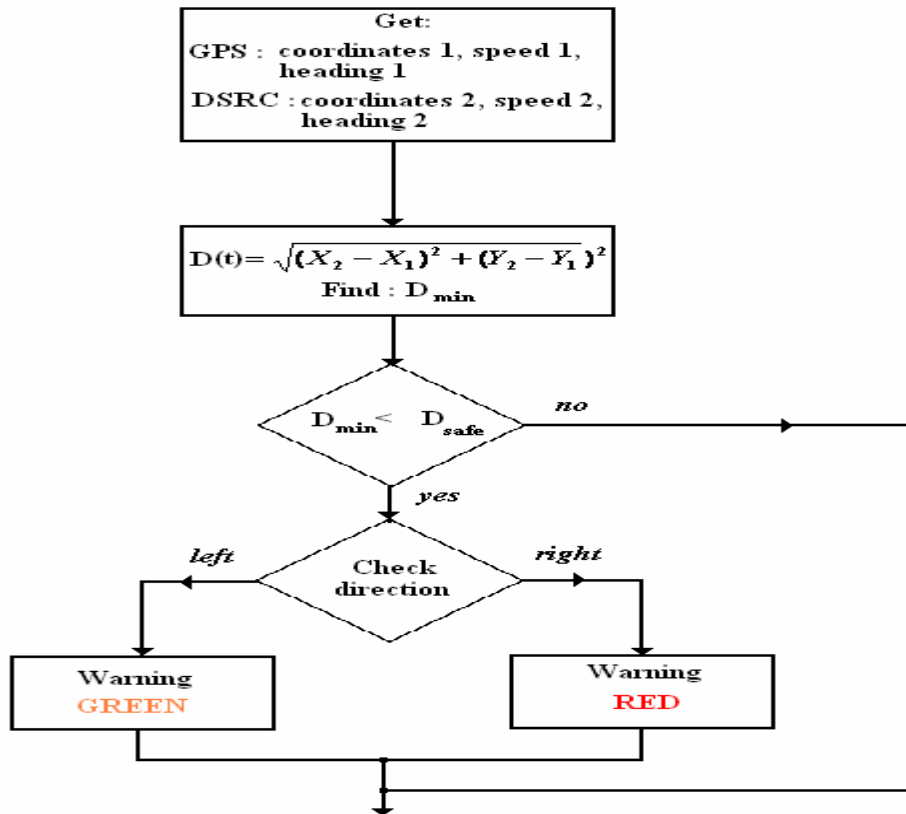


Figure 7.5 Algorithm for the safe crossing of intersection

Wheel to wheel prototype. There is used firms RF Microdevice transceiver ML 5805.(Fig. 7.7) for wheel to wheel networking communication which is providing information exchange about vehicle location.

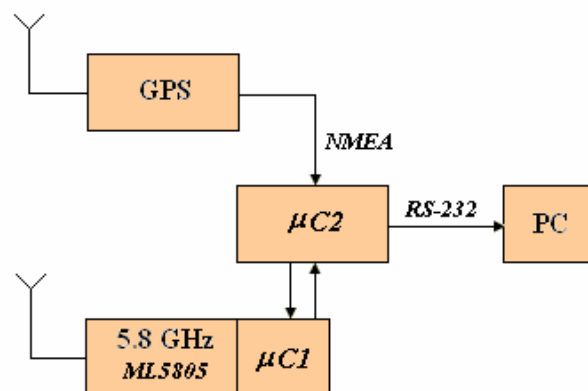


Figure 7.6 Structural flowchart of vehicle onboard equipment

It was assumed that the cars are not equal - own car is Master, but other is Slave. In this way, the whole process of exchange of information to initialize and is run from the Master car. Equipment mode of operation is half duplex, it's mean that the transmission and reception take place at different time points.



**Figure 7.7 RF Microdevice transceiver ML 5805**

**Features:**

- Highly Integrated 5.8 Ghz FSK Transceiver with Selectable Data Rates; 576kbps, 1.125 Mbps, 1.536 Mbps;
- Low-IF Receiver Eliminates External IF Filters;
- Fractional-N Synthesizer with 30Hz Resolution;
- +21dBm Typical Output Power From Integrated PA;
- -97 DbM Sensitivity (0,1% BER) WITH Integrated LNA.



**Figure 7.8 The control circuit microcontroller based on PIC18F2550 (Microchip)**

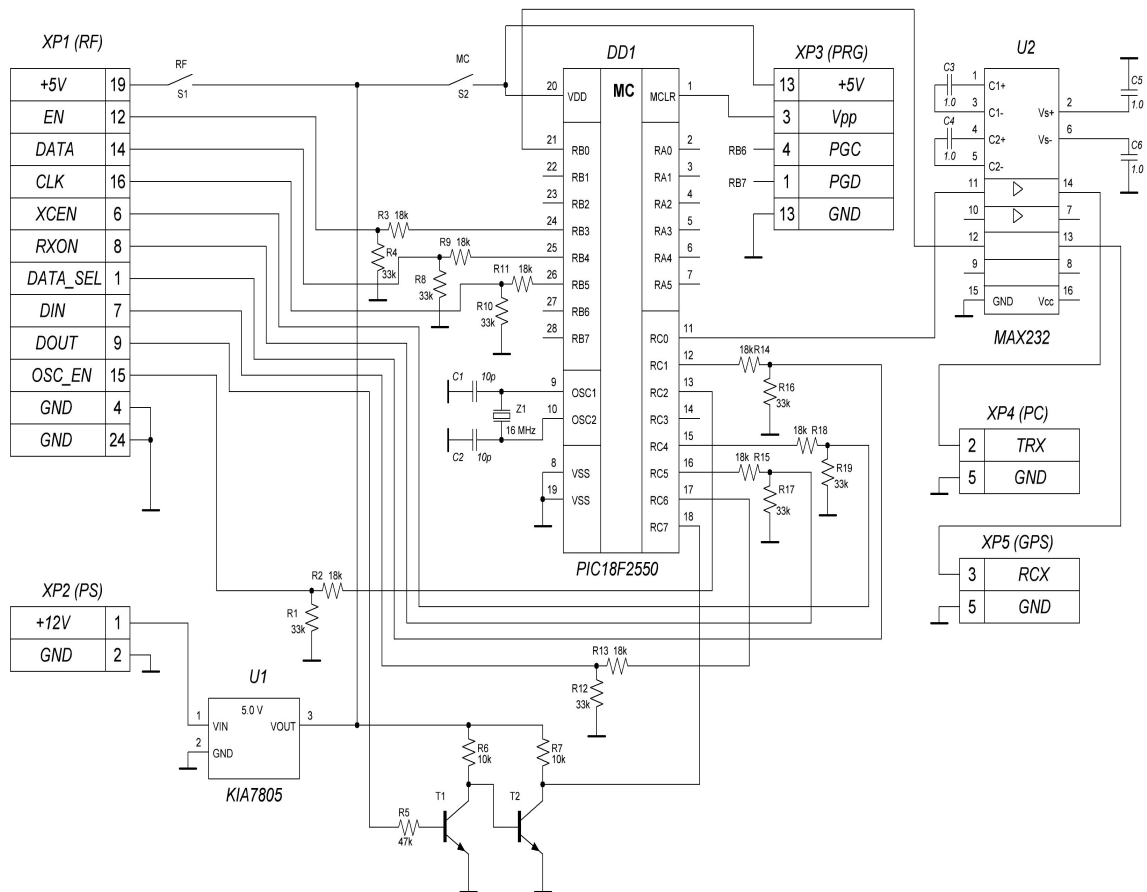


Figure 7.9 Principal scheme of control circuit

### 7.1.2. Mobilo objektu vietas noteikšanas pētījumi ar augstas precizitātes GPS aparatūru dažādos mērījumu režīmos.

For these measurements was chosen point T8 from geodetic network RG2 A class. RG2 is a Riga city network. The aim of this network is to provide a city and its surrounding area with the high accuracy geodetic points. The network was established in year 2000 through year 2004. The network RG2 is formed in such way to make possible to use this network as a reference for forming other geodetic points or to control the other geodetic points, including GPS reference network [7.1.2].

The conditions during forming the network were to achieve accuracy of the geodetic points within 1-2cm.

Total there are 65 points in RG2 network. Depending on type of point fastening and conditions of GPS measurements points are divided in two groups:

- RG2 A – benchmarks and other points which are fastened deeper than 0.7 m with good GPS sky view conditions – without influence of buildings, relief, trees and other influences;
- RG2 B – benchmarks with possible influence of buildings, trees or other obstructions and less than 0.7 m deep fastened points.

Point T8 was chosen because it is located in good conditions for GPS observations and influence of environment and buildings is minimal. And this point is located in the centre of the EUPOS-RIGA GPS reference network. These conditions reduce possible errors. It is important because the aim was to establish the accuracy of the GRS-1 receiver using different measurement modes.

The chosen point is shown in Fig. 7.10.



**Figure 7.10 Geodetic point T8**

As a possible imperfection is that during measurements antenna was placed on 128mm tall holder. As the surface of the point is 300x300mm it can originate the influence of.

Official T8 coordinates in LKS-92:

- $X = 309177,035\text{m}$
- $Y = 508228,007\text{m}$
- $h = 4,746\text{m}$

Should be mentioned that height is shown above the Riga geoid. Difference between geoid and ellipsoid on point T8 is 21,047m.

Accuracy of T8 coordinates (root mean square), during formation RG2 network are:

- $\sigma_x = 2\text{mm}$
- $\sigma_y = 1\text{mm}$
- $\sigma_z = 2\text{mm}$

Measurements were held in six different modes:

- RTK with GPS and GLONASS correction;
- RTK with GPS correction;
- DGPS with GPS and GLONASS correction;
- DGPS with GPS correction;
- Autonomous mode with GPS and GLONASS;
- Autonomous mode with GPS.

In each mode 4 measurement sessions were held:

- 50 measurements with recording 1x/1sec;
- 50 measurements with recording 1x/5sec;
- 30 measurements with recording 1x/10sec;
- 30 measurements with recording 1x/20sec.

Recording 1x/1sec means that coordinates are recorded into receiver memory once a second, 1x/5sec – coordinates are recorded once in 5 seconds as an average from 5 epochs, 1x/10sec – average from 10 epochs and 1x/20sec – average from 20 epochs.

In total about 950 measurements were made. The antenna during measurement session was stationary. The session of measurement was 3 hours long within 15:30 and 18:30. At first the RTK measurements were made, next were DGPS and at the end were made the autonomous measurements. As the measurement session was rather long, than changes in satellite constellation could affect results of the measurements through number of visible satellites and geometry of constellation.

Due to the large amount of the results let's further focus only on measurements which were held once a second.

At the beginning let's take a look at the total results of all measurement modes (Fig.7.11). On this figure is shown the deviations of measurements in all modes from true value. As it can be seen on figures than best results are in RTK GPS and RTK GPS+GLONASS modes just as expected.

X Coordinates in AUTONOMOUS GPS mode fluctuates from 309176.0152m up to 309177.4980m and it makes range of 1.4828m. Y coordinates fit in a range of 1.1594m, but range of height coordinates is 2.2901m.

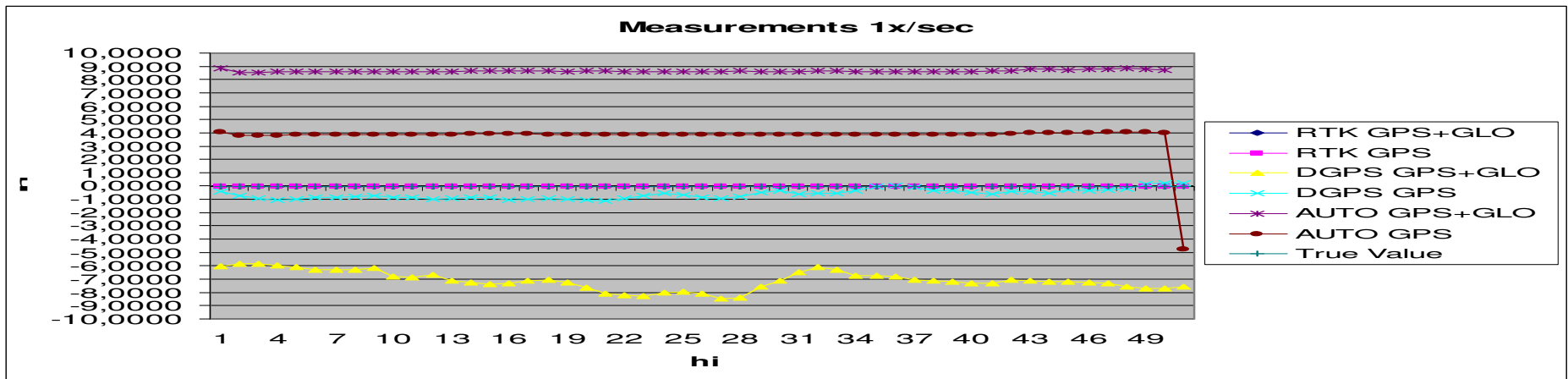
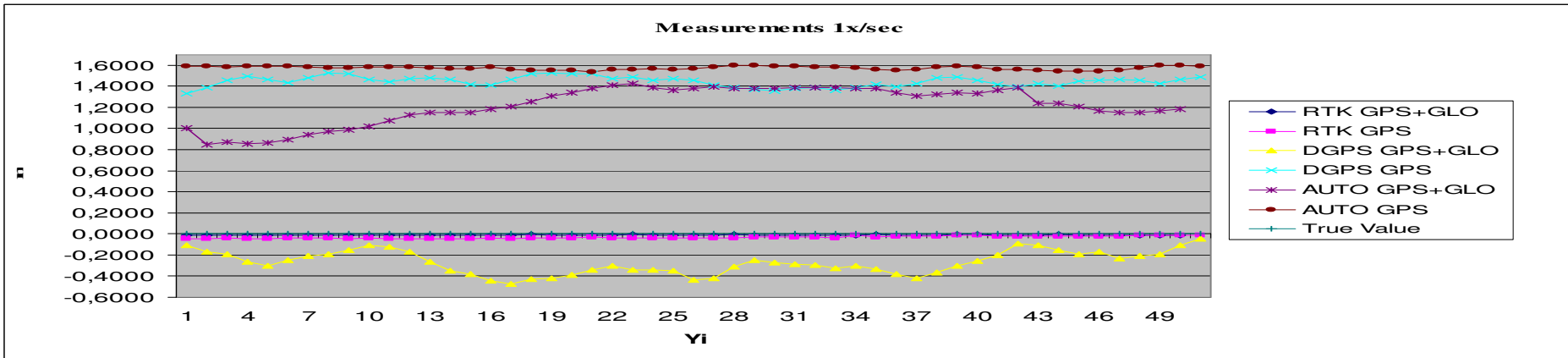
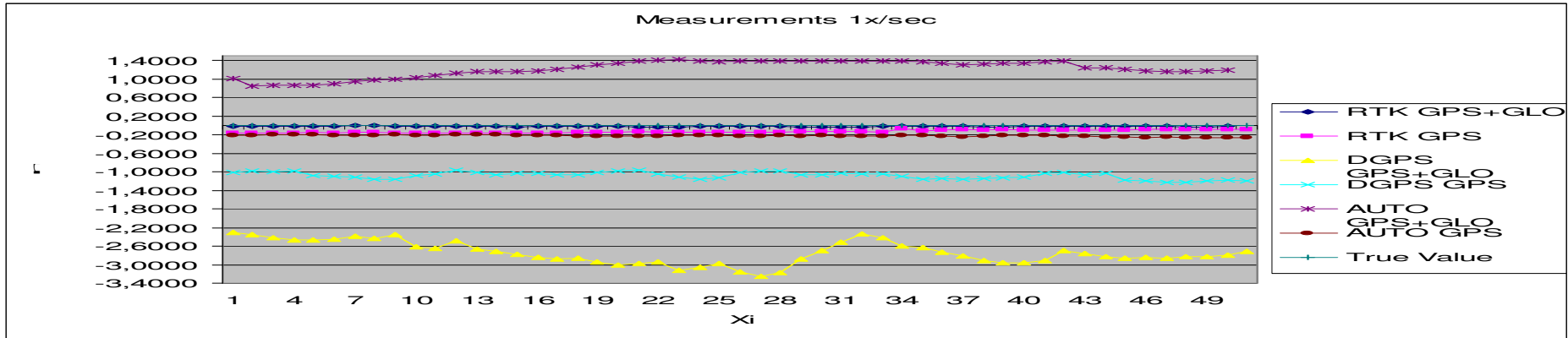


Figure 7.11 Measurements of coordinates in different modes on point T8

Further let's take a look to the results of AUTONOMOUS mode with using GPS and GLONASS satellites. Considering that larger amount of visible satellites provides higher accuracy then accuracy of measurements in this mode should be better than in previous one. In this case the range of X coordinates measurements is 1.7782m, Y – 1.0869m, h – 9.6014m. If we compare these results with previous ones we see that in previous case results for X coordinate and height measurements are better than in this one but worse for the Y coordinate. As the accuracy with using larger amount of visible satellites is worse then the results are unexpected.

If we examine results which are captured using DGPS GPS correction we see that: X coordinate measurement range is 0.9856m, Y – 0.571m, h – 2.7919m. Comparing these results with previous ones we see that only height measurements are worse, but this difference is small enough to pronounce that total results in DGPS GPS mode are better than previously seen.

If we examine the results of DGPS GPS+GLONASS mode we see that results fluctuate more than in DGPS GPS mode just as in the case of AUTONOMOUS mode with GPS and with GPS+GLONASS modes. In this case the range of X coordinate measurements is 2.9374m and this is the worst one so far. Y coordinates makes range of 2.1582m, and this is also the worst result so far, and h – 11.8152m. Taking into account that in this case a DGPS correction is used we can admit that the results are very poor.

Now let's take a look to the measurement mode with potentially highest achievable accuracy. If we examine the results acquired in RTK mode with GPS corrections we see that X coordinate have range of 0.1736m, Y – 0.0525m, h – 0.0859m.

And in the end let's take a look to the results which should have highest accuracy, respectively RTK mode with GPS and GLONASS corrections. From the results we see that X coordinate have the range of results 0.0385m, Y coordinate – 0.0342m and h – 0.0839m. Making comparison of the results we see that the latest measurement mode has the best accuracy just as expected. Should be mentioned that during measurements 1x/1sec in RTK mode with GPS correction some unknown influence took place and affected results badly. The results have errors up to 0.17m; of course this affects total result of RTK GPS mode. Probably it is some rude error and may be eliminated.

If examine charts shown in Fig.7.11. we clearly can see that the best results is acquired in RTK GPS and RTK GPS+GLONASS modes. It corresponds with the expectations at the very beginning. Charts show some interesting tendency. In AUTONOMOUS and DGPS measurement sessions with using both GPS and GLONASS satellite systems the accuracy is worse than in those sessions with using only GPS satellites. It leads to think that GLONASS decreases accuracy of GPS. Unfortunately it is not possible to switch off GPS system and make measurements only with GLONASS satellites in GRS-1 receiver to figure out the reason of such tendency. But accuracy do not decrease using RTK mode with GPS and GLONASS in comparison with RTK GPS mode.

To better understand the difference between accuracies of different measurement modes let's take a look to some following charts. Those charts represent the errors of the measurements. Let's examine results acquired in modes with use of the GPS and GLONASS satellites. Fig.7.12 shows the distribution of the errors for X coordinate measurements in three different modes. As first is shown distribution of the errors in AUTONOMOUS mode, next follows DGPS and the RTK in the end. Fig.7.13 shows distribution of errors of Y coordinate, Fig.7.14 – errors of the height.

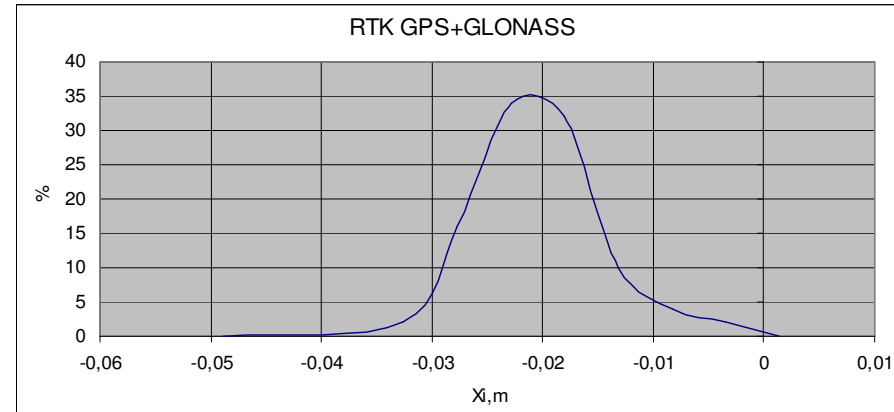
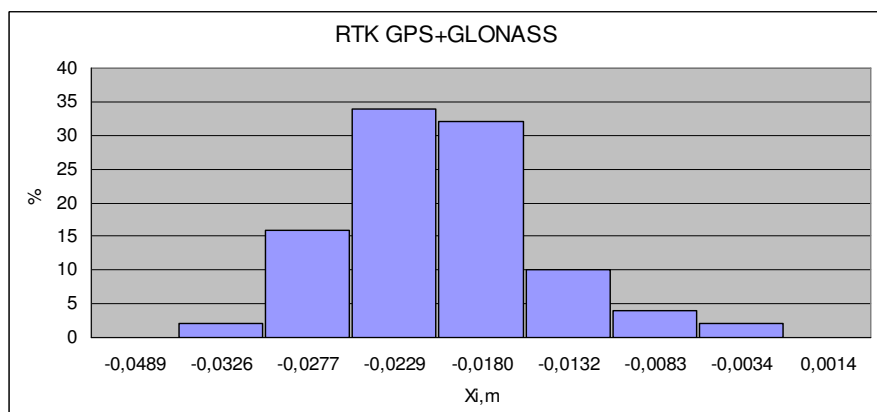
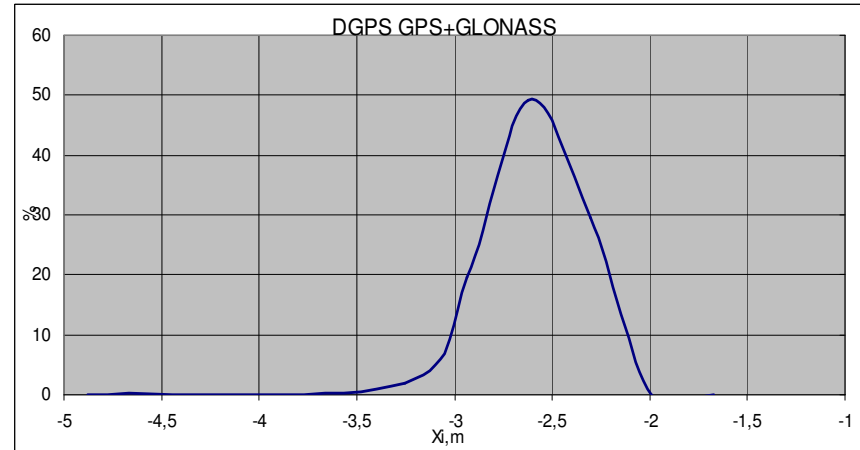
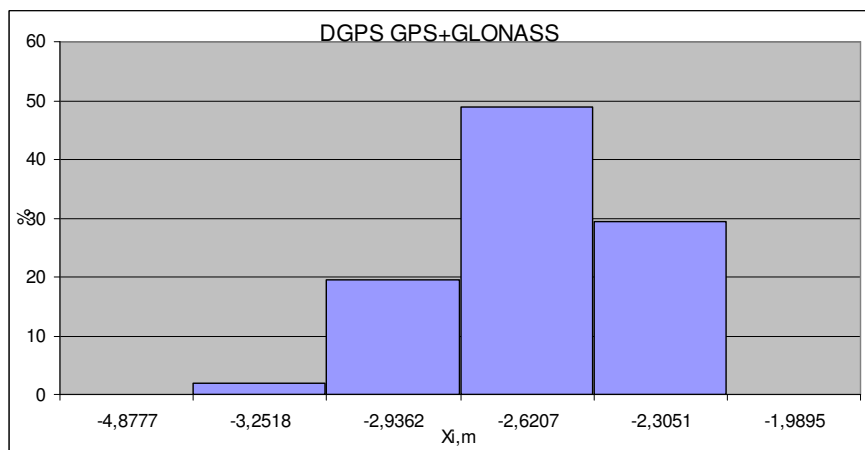
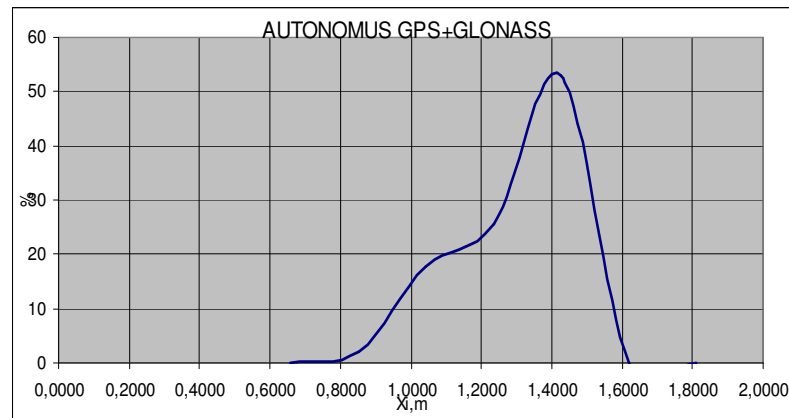
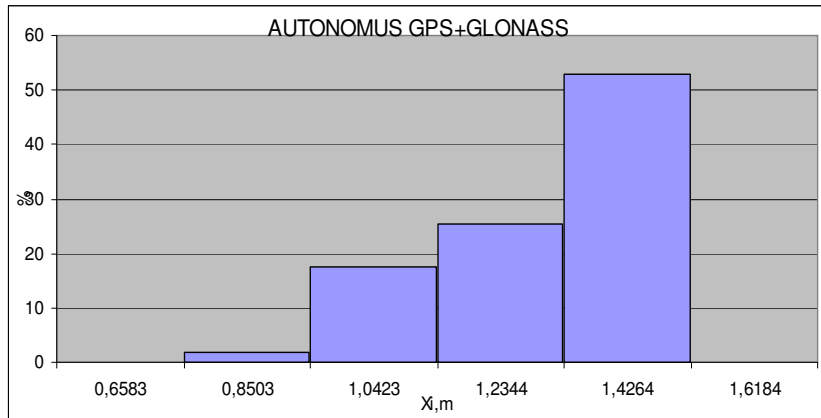


Figure 7.12 Distribution of the X coordinate errors for measurement modes using GPS and GLONASS

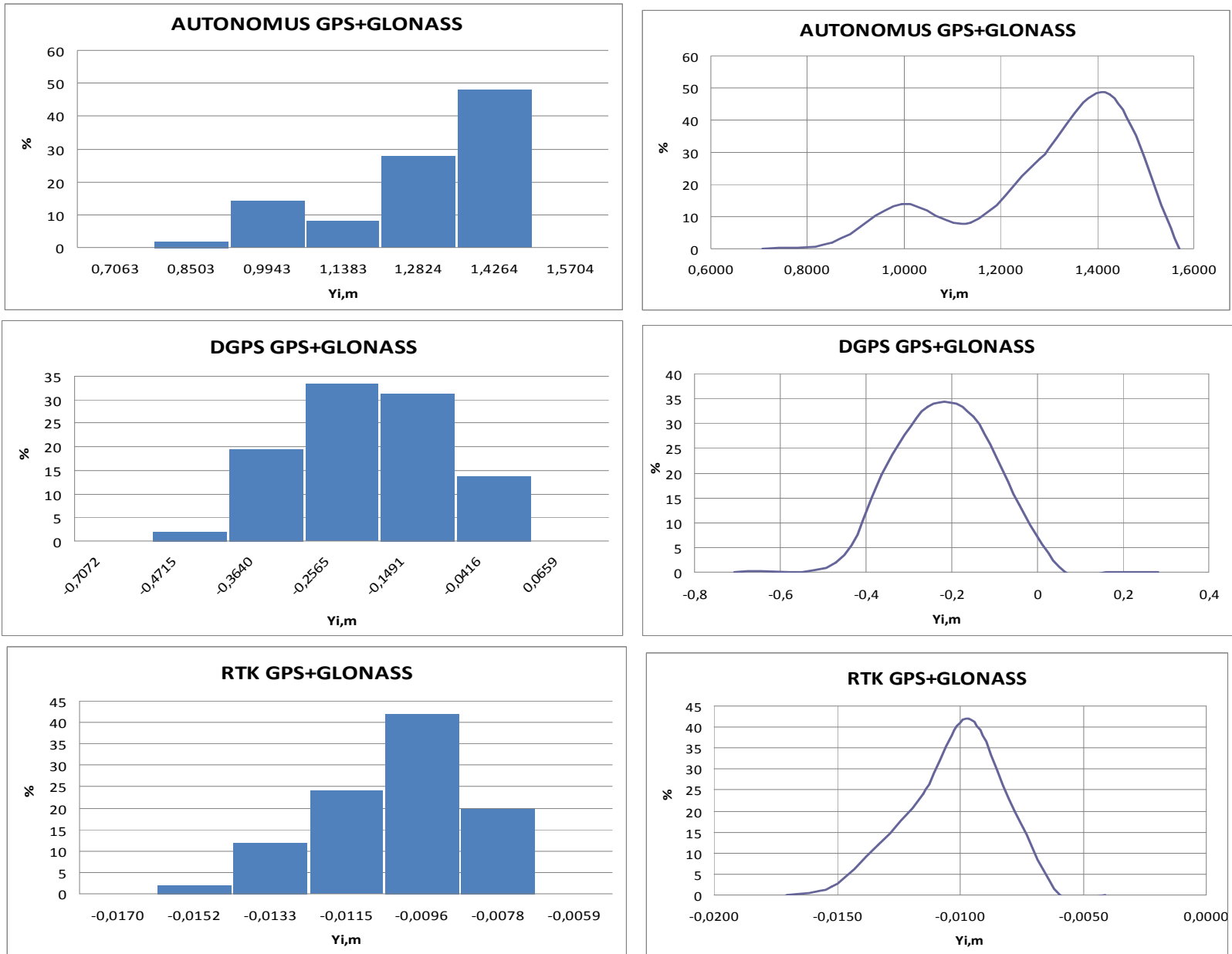
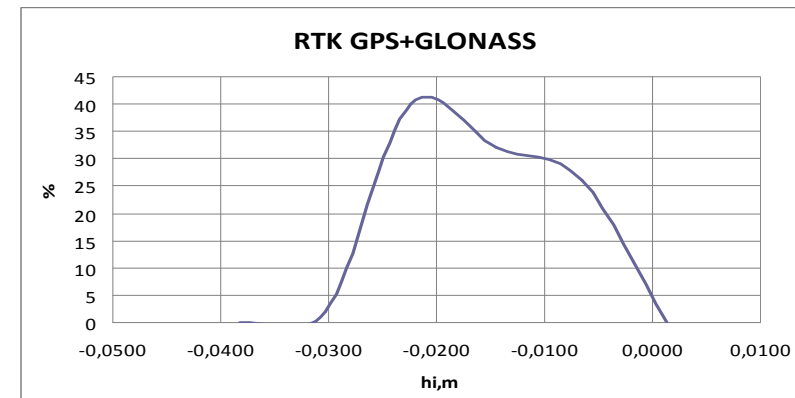
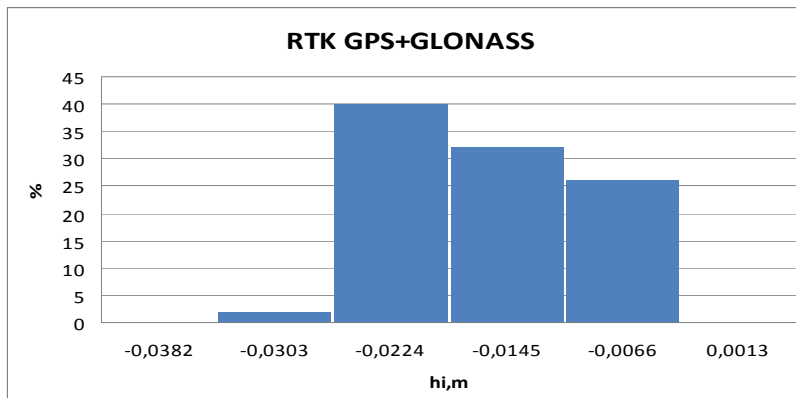
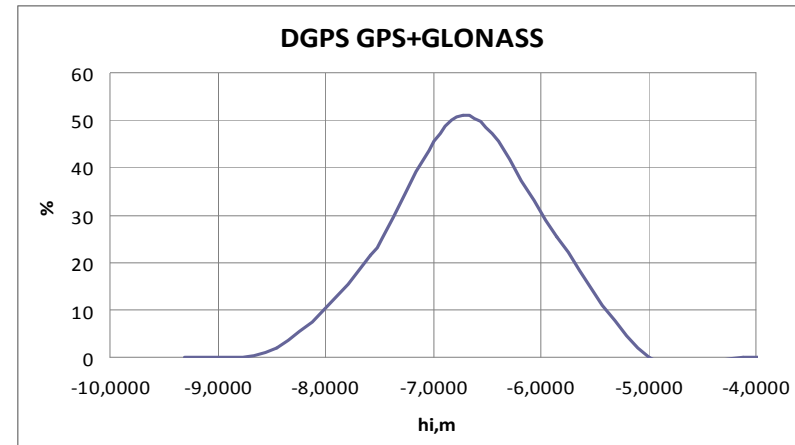
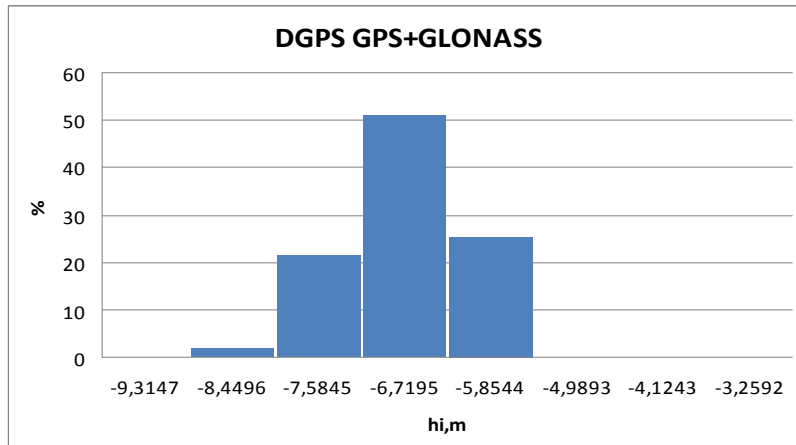
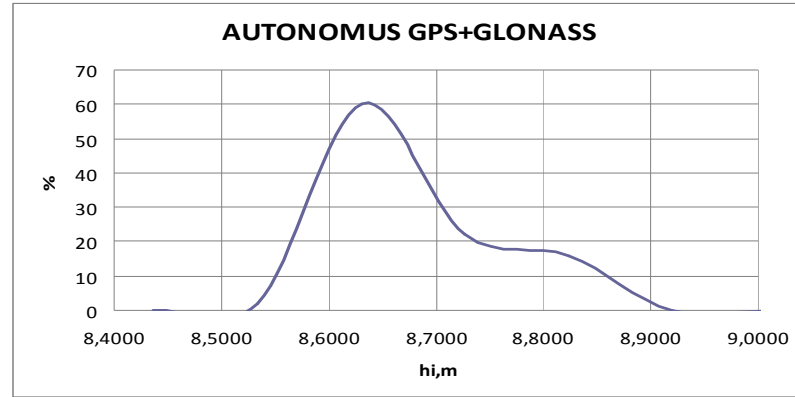
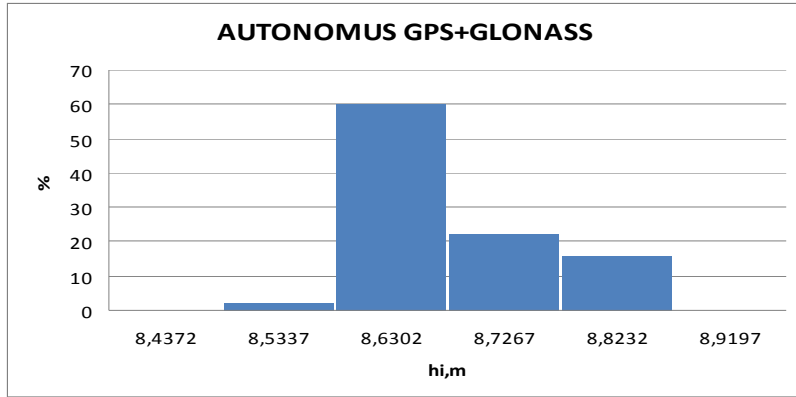


Figure 7.13 Distribution of the Y coordinate errors for measurement modes using GPS and GLONASS



**Figure 7.14 Distribution of the height component errors for measurement modes using GPS and GLONASS**

Let's shortly analyze the acquired results. In the beginning let's analyze results for X coordinate (Fig. 7.12). As can be seen on charts in AUTONOMOUS mode approximately 52% of errors are 1.4m and only 2% of the results have error of 0.85m. Next DGPS mode in this case approximately 50% of the measurements has error 2.6m and in 29% of the measurements error is less than 2.3m. As expected in the beginning of the measurements most precise are measurements of RTK mode. In this case 82% of the results have error less than 0.023m.

Now let's analyze measurements of the Y coordinate. In this case also we see that errors using AUTONOMOUS mode in comparison with modes with corrections are much larger. 48% of measurements have error between 1.29m and 1.43m. If we look at the DGPS mode we see that amount of errors is much smaller than in AUTONOMOUS mode – only 22% of measurements have error larger than 0.364m. And now RTK mode – in this mode 86% of measurements have error less than 0.012m.

And finally let's take a look to the distributions of the errors measuring height component. Usually these measurements have the largest errors. In AUTONOMOUS mode error of the height component measurements are much bigger than measuring X and Y coordinates. In this case 60% of the measurements have errors between 8.54 and 8.72m, it is considerable as the low accuracy measurements. If looking to the results of the DGPS mode only small decreasing of the amount of errors is noticeable. In DGPS mode 50% of the results have errors between 5.86 and 7.58m. And one more thing errors in DGPS mode are negative but in AUTONOMOUS mode – positive. And finally results of the RTK mode. In this case 98% of the results have error less than 0.0224m and 26% of measurements errors are not larger than 0.0066m. According to these results we strongly can say that RTK mode is much more precise than other measurement modes. If the RTK mode is used errors are considerably smaller than using DGPS or AUTONOMOUS mode [7.1.3.].

## ***7.2. Transporta līdzekļa pārvietošanās modeļa izveide, sasaistot to ar datu pārraides ātrumu starp kustīgā objekta iekārtām un bāzes stacijām.***

### ***7.2.1. Cikliskais bezvadu tīkls***

For the sake of a simpler mathematical model, let's make the following assumptions. First, the processed tasks are homogeneous. A homogeneous task flow is a common characteristic for network systems controlling technological processes in real time. Second, the processing moment for every task is accidental and is exponentially distributed with a mean value corresponding by element. Third, elements and tasks being processed are mutually independent.

The terminal count in each vehicular wireless network is usually high. It is possible to replace conveyor transfer of files with a consistent transfer on evaluation of bandwidth. Following the obtained practical results we will calculate the base station performance at variable client count. In our case the 200 meters long base station operational zone of is divided to 5 zones, 40 meters each, the third zone being the most adjacent to the base station, as shows Fig. 7.15. We assume that N vehicles

enter the operational zone of the base station, starting at the speed of zero. Then velocity increases exponentially [7.2.1].

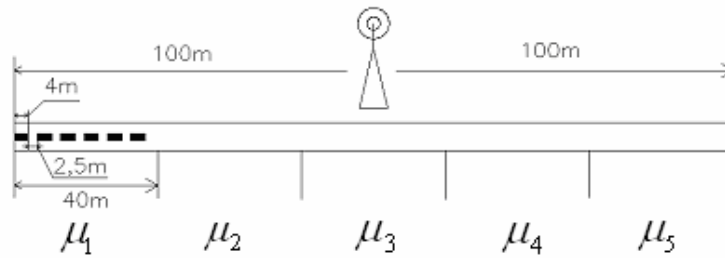


Figure 7.15 200 meter segment consisting of 5 zones, 40 meters each

Let's investigate a closed network consisting of  $M$  independent nodes with  $N$  incoming queries. Distribution is exponential with the parameter  $\mu_i$ . According to this research the speed of vehicle movement on highway is characterized by density. If the interval length equals  $S_i$ , and vehicle movement speed equals  $g_i$ , then the intensity of vehicle service by road interval equals:

$$\mu_i = \frac{g_i}{S_i} \quad (7.1)$$

Vehicles pass all  $M$  intervals successively, and the total number of vehicles in the base station's range of operation is  $N$ .

Such a system can be described in a form of a closed cyclic mass service system network with  $M$  service devices,  $N$  queries and exponentially distributed service time. Query service intensity in the  $i$ -th interval equals  $\mu_i$ , as show in Fig. 7.16. We will assume that  $N$  vehicles enter the operational zone of the base station, starting at the speed of zero.

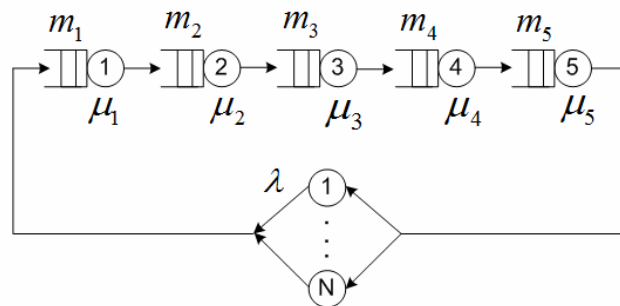
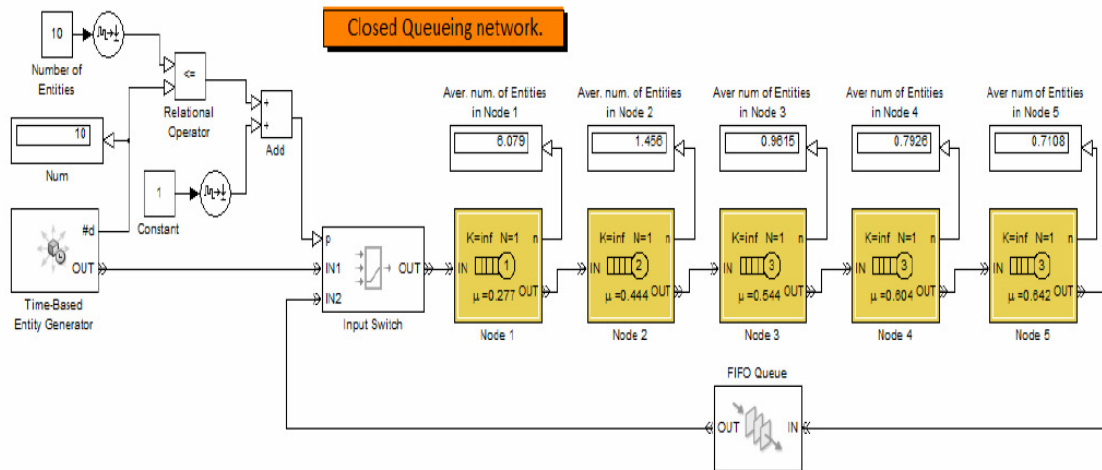


Figure 7.16 Closed cyclic system

The model (Fig. 7.17) has been created in the graphical Simulink environment of MATLAB package. The blokset SimEvents has been used as a source of source blocks.



**Figure 7.17 Closed model in Matlab**

The scheme consists of 5 nodes (Node  $k$ , where  $k = 1 \dots 5$ ), offered in which contain more convenient interface for the introduction of parameters as well as more pictorial.

$N$  vehicles are entering the base stations operating zone, with initial velocity of zero after that velocity grows exponentially, as show Fig.7.18:

$$\mathcal{G} = \mathcal{G}_0(1 - e^{-ar}) \quad (7.2)$$

where  $r$  – distance to base station.

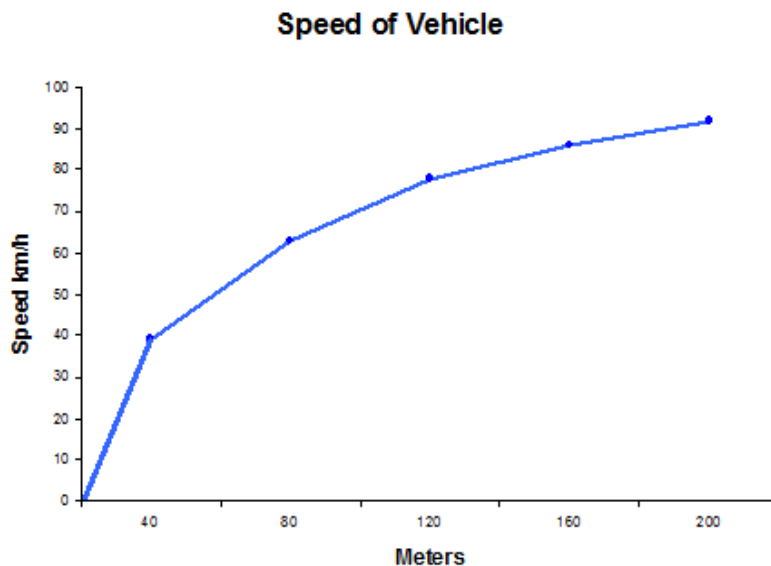


**Figure 7.18 Speed of vehicle**

The Table 7.1 shows the technical data of the car that was used in the experiment. The speed grow can be dependent on the vehicle data.

Table 7.1

**Vehicle data**

<i>Parameter</i>	<i>Value</i>
<i>Car brand</i>	<i>VW PASSAT</i>
<i>Capacity</i>	<i>1.8 litre</i>
<i>Max power</i>	<i>90PS (66kW)</i>
<i>Gearbox</i>	<i>5 speed manual</i>
<i>Weight</i>	<i>1600kg</i>

Vehicle speeds in various zones are presented in Table 7.2:

Table 7.2

**Vehicle speed**

<i>Zone number i</i>	<i>1</i>	<i>2</i>	<i>3</i>	<i>4</i>	<i>5</i>
<i>Distance (m)</i>	<i>40</i>	<i>80</i>	<i>120</i>	<i>160</i>	<i>200</i>
<i>Velocity <math>g_i</math> (km/h)</i>	<i>38</i>	<i>49</i>	<i>59</i>	<i>67</i>	<i>74</i>
<i>Intensity <math>\mu_i</math></i>	<i>0,264</i>	<i>0,34</i>	<i>0,41</i>	<i>0,465</i>	<i>0,514</i>

Here  $x_i$  is estimated by the system of equations:

$$\mu_i x_i = \sum_{i=1}^M \mu_i x_i p_{ij} \quad (7.3)$$

Buzen's algorithm is among the most effective methods for closed network analysis. Buzen's matrix, at the row  $i$  and column  $j$  can be calculated using the formula:

$$g(i, j) = g(i, j-1) + g(i-1, j)x_j$$

where  $G(N)$  – normalizing constant, resulted either from adding up and equating to one all probabilities either by Buzen's method. Naturally, there are no limitations for the number of vehicles (queries) in the  $i$ -th interval, as shown in Fig. 7.19.

Average number of queries (vehicles) in  $i$ -th interval:

$$E[n_i] = \sum_{K=1}^M (x_i)^K \cdot \frac{G(N-k)}{G(N)} \quad (7.4)$$

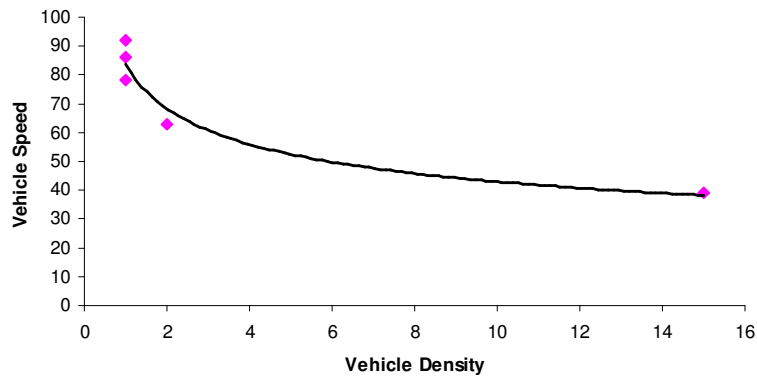


Figure 7.19 Average number of vehicles

Each vehicle in sub-zone  $i$  can exchange packets with base station with intensity  $\lambda/\beta < 1$ .

Then we know the general form of the equilibrium distribution for  $N \leq \min_i m_i$ .

Goodput of a station providing service for the region  $i$  can be obtained from this formula and can be seen in the Fig. 7.20:

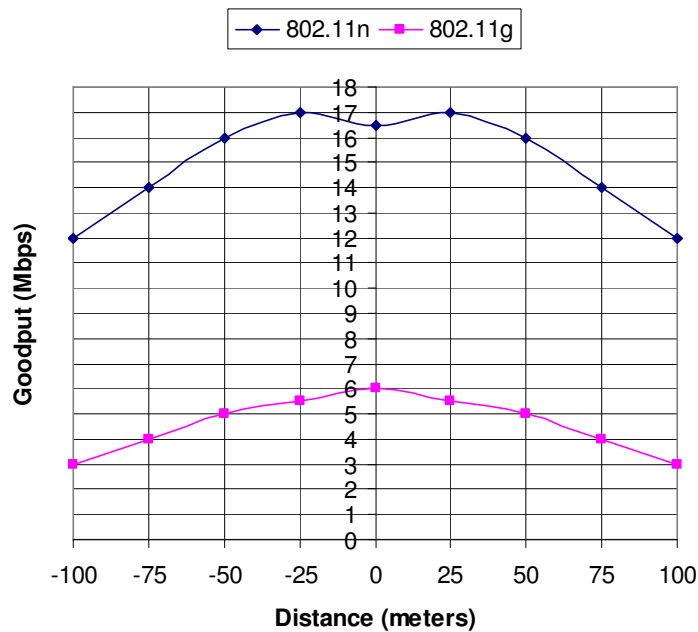


Figure 7.20 Goodput in wireless network with one router depending on distance for 802.11n and 802.11g

Goodput of a station providing service for the region  $i$  can be obtained from this formula and can be seen in Fig. 7.21:

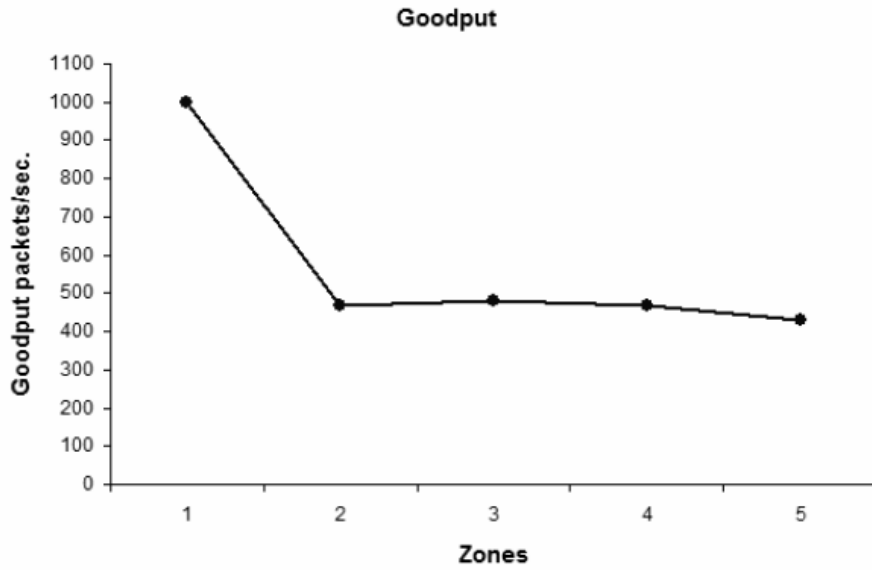


Figure 7.21 Goodput for moving with 10 vehicles

Using the  $M/M/1/N^i$ , model for every sub-zone  $i$ , we find the probability of base stations idleness:

$$P_0(i) = \left[ \sum_{k=0}^{E(n_i)} \left( \frac{\lambda_i}{\beta_i} \right)^k \frac{E(n_i)!}{(E(n_i)-k)!} \right]^{-1} \quad (7.5)$$

Goodput for moving, as show Fig.7.22:

$$\eta_i = (1 - P_0(i))\beta_i \quad (7.6)$$

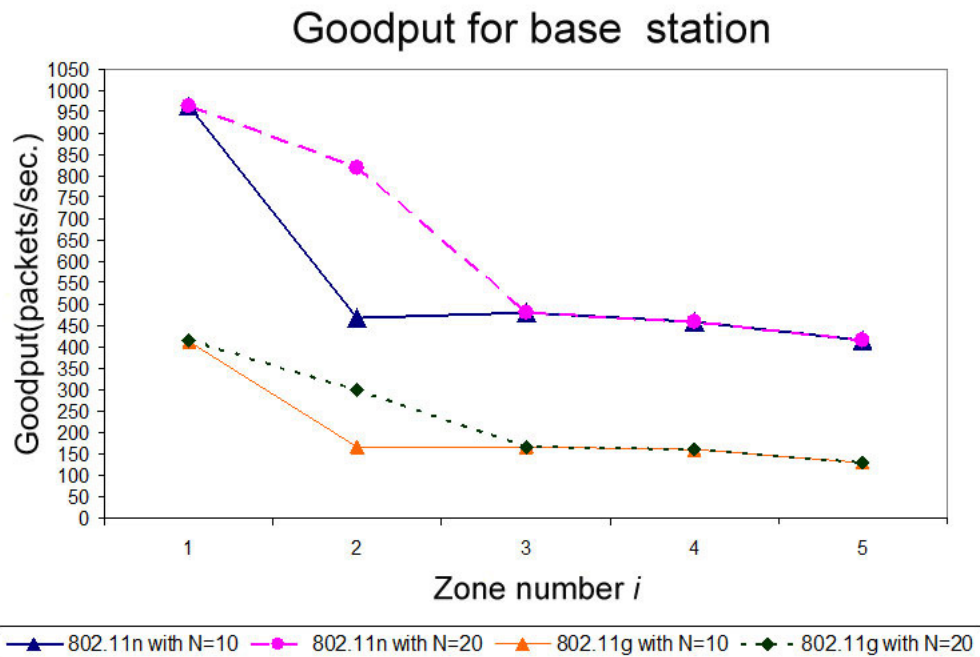


Figure 7.22 Goodput for moving with 10 and 20 vehicles

The wireless network for mobile users has been created and installed in this experimental work.

The wireless network with one access point has been installed. Wireless network throughput has been detected in different modes. In this research the experimental data about data transfer rate in wireless networks of 802.11.g/n standard connecting moving objects are presented. Basing on the experimental data the mathematical patterns have been developed binding characteristics of vehicular flow with characteristics of data transfer system. This paper has presented a performance evaluation of the two layer and cyclic network model.

A calculation of goodput for each node of two layer network has been explained. Two layer and closed cyclic model for real data transfer rate estimation depending on number N of moving objects located in the wireless network base stations operational zone has been developed. Basing on this research, the real data transfer rate depends on the number and distances from the base station of objects interacting with base station. This work gives a good tool for modeling Vehicular network system [7.2.1].

## ***7.2.2. Wlan veikspēja autotransporta vidē***

Now, wireless communication network research of road environment is up to date, and is regarded as a new challenge for science and industry. Objectives and benefits of such a communication system is already clearly defined in the various countries or union road development guidelines and long-term plans for future. The main goal is to develop intellectual transport systems [7.2.2]. At a time when the vehicle flow increases with every passing day, the latest communication technology solutions for the needs of intellectual transport systems can provide an important road traffic and safety requirements. The main objective is to study the performance of short-distance communication system, which is based on wireless LAN technologies, highly mobile vehicle environment, and examine the hypothesis that at a certain road speed of movement can achieve optimal wireless LAN throughput. Therefore is used mathematical model to approximate practical results [7.2.3].

### ***7.2.2.1. Results of practical measurement***

Using WDS technology it is possible to extend the WLAN area without datacommunication gap, but the switching phase medium data throughput is reduced by 90% [7.2.4]. Application-level data throughput is dependent on road traffic parameters. At higher speeds the movement of the average throughput decreases and the practical measurement curve shows the IEEE802.11 g and n standards (Fig. 7.23) [7.2.5].

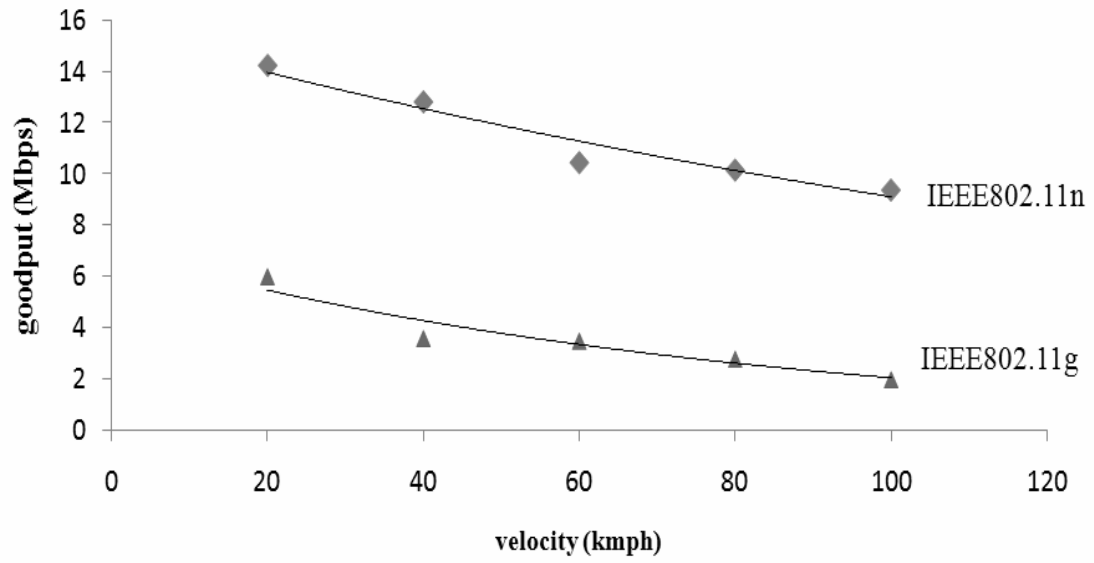


Figure 7.23 WLAN access point performance

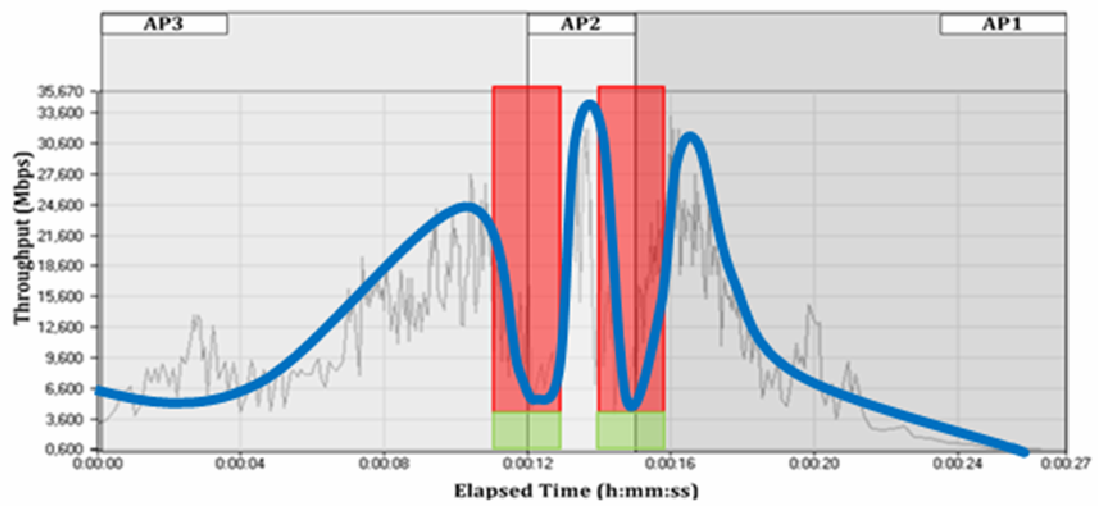
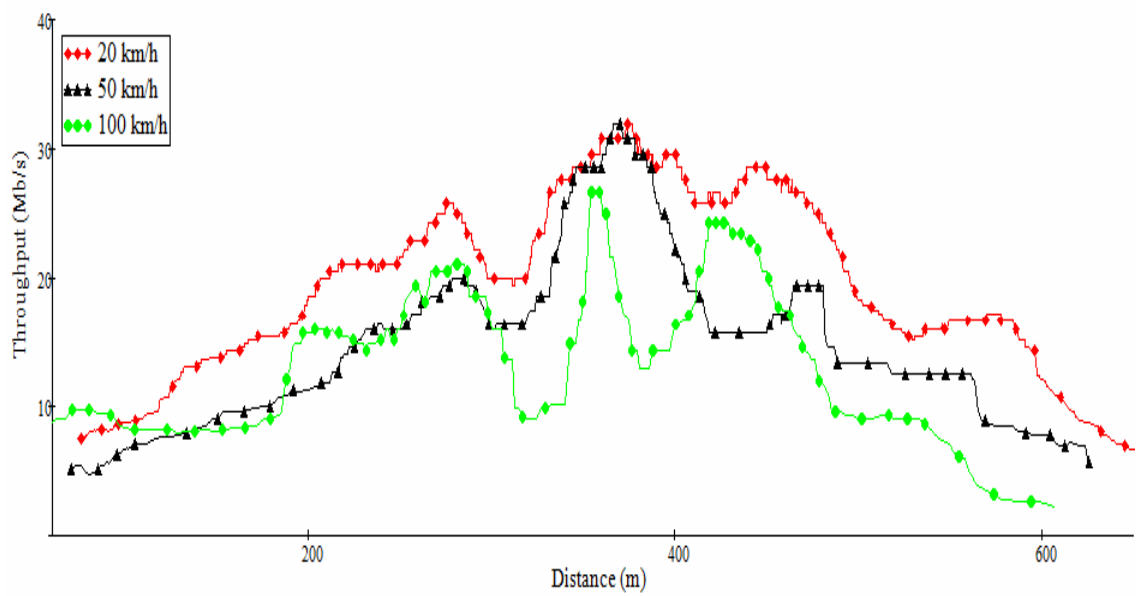
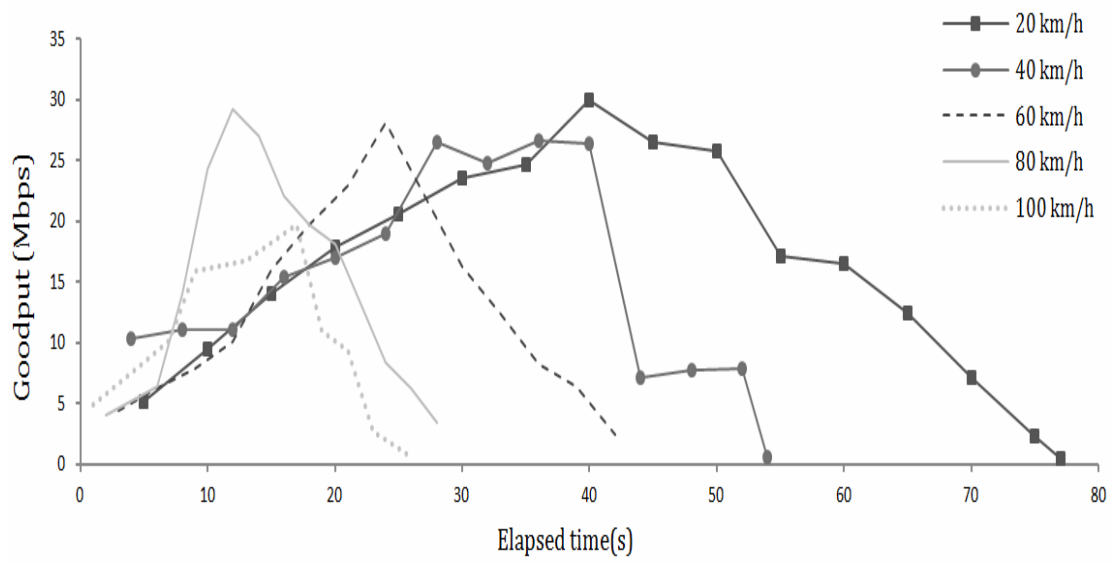


Figure 7.24 WDS connection with three WLAN equipments



**Figure 7.25 WLAN real-time performance depending on the speed**

### 7.2.2.2. Results of the mathematical models

With IDM model can determine the number of motor vehicles in WLAN area.

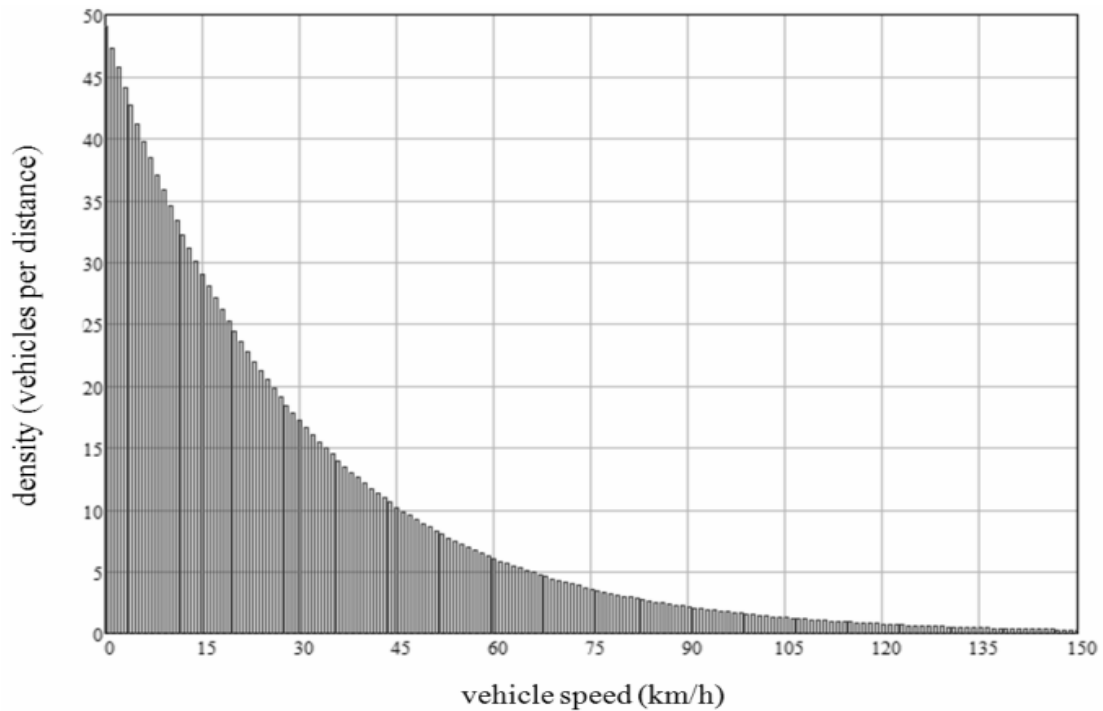


Figure 7.26 Evaluation of number of users depending on the road speed of the WLAN area

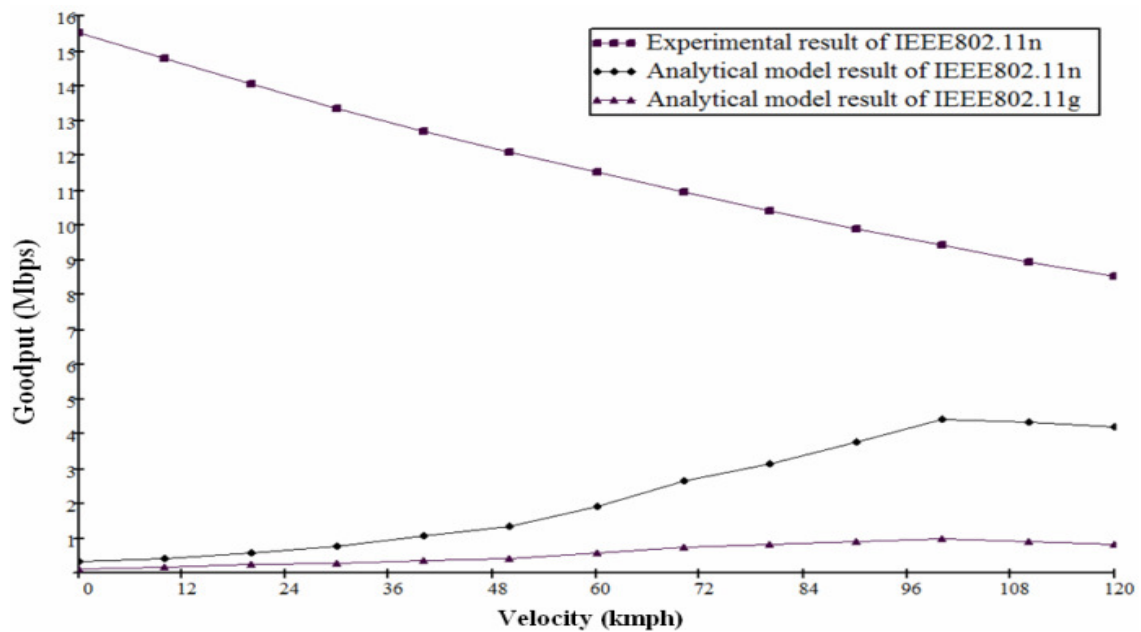


Figure 7.27 Evaluation of performance of client number, which varies depending on the speed

Chart compares small road scenario of experimental results with near real-road analytical model results, showing that at low speeds the movement of vehicles is increasing, according to active clients. This means that each individual client will

receive less WLAN network resources, as evidenced by the results of the mathematical model. But with increasing vehicle speed, there are decreasing the number of users and network resources are provided over each user. According to the experimental results when increasing the speed, WLAN performance decreases. As a result, at 100 km / h is optimal WLAN performance.[7.2.4]

### 7.2.2.3. Results of Simulation software NCTUns7.0

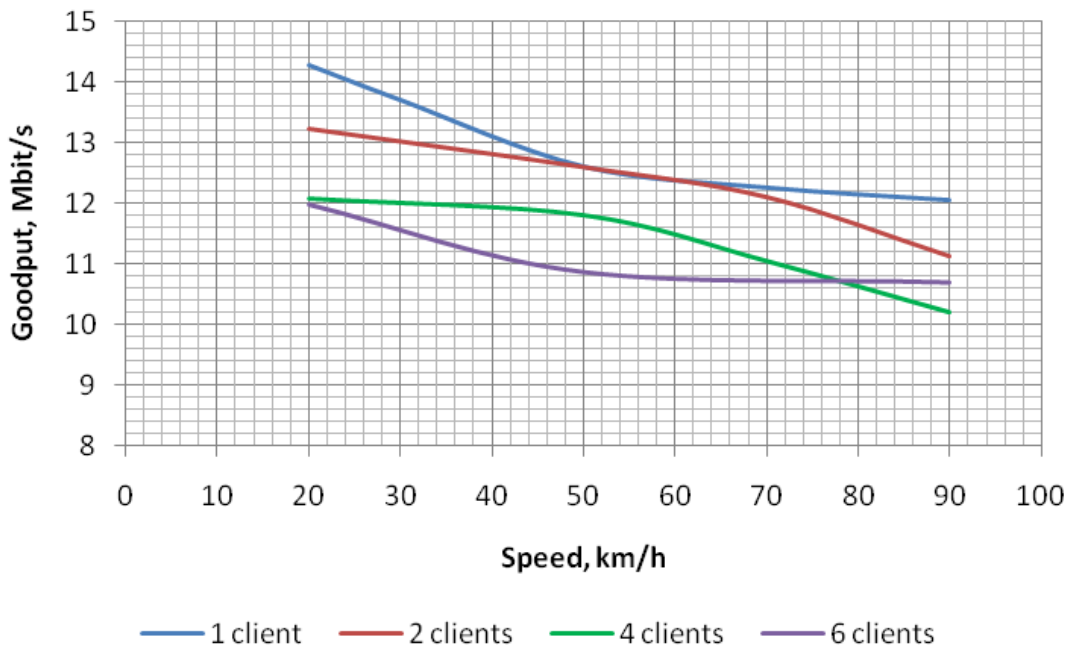
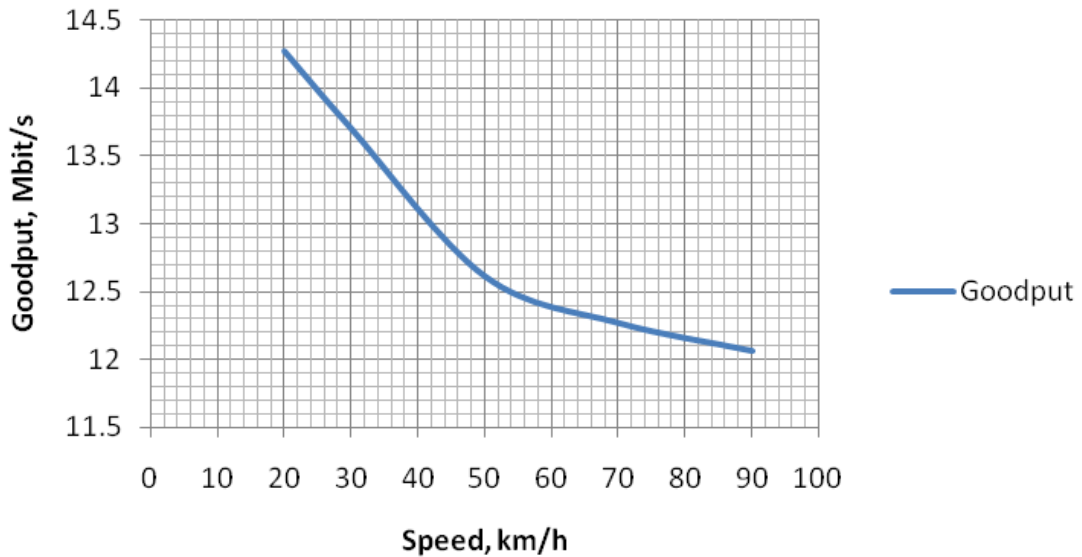


Figure 7.28 Measuring the performance of WLAN

**Conclusion:** Road traffic is the the transport flow in certain place and in the time interval, which depends on the velocity and density of the vehicles. As the speed of

the traffic increases, the WLAN data effective throughput decreases. The speed of vehicle traffic is dependent on the density of traffic.

## **References**

[7.1.1] Ahrems J., "Algorithms for Determination of Safety Intersections", in Proc. of 13th Biennial Baltic Electronics Conference (BEC 2012), Tallinn, Estonia, pp.175-178, October 3-5, 2012

[7.1.2] Klūga A., Klūga J., Mitrofanovs I. GPS Receiver with Phase Measuring Precision Estimation // Proceedings of 13th Biennial Baltic Electronics Conference (BEC2012), Igaunija, Tallina, 3.-5. oktobris, 2012. - 169.-172. lpp.

[7.1.3] Beļinska V., Klūga A., Klūga J. Application of Rauch-Tung-Striebel Smoother Algorithm for Accuracy Improvement // Proceedings of 13th Biennial Baltic Electronics Conference (BEC2012), Igaunija, Tallina, 3.-5. oktobris, 2012. - 157.-160. lpp.

[7.2.1] Bogdanovs N., Pētersons E., Šarkovskis S. Modelling of Vehicular Network for Short Range // Proceedings of the 12th International Conference „Reliability and Statistics in Transportation and Communication” (RelStat-12), Latvia, Riga, 17.-20. October, 2012. - pp 195-203.

[7.2.2] Jansons J., Bogdanovs N., Ipatovs A. Vehicle-to-Infrastructure Communication Based on IEEE 802.11g // International Journal of Digital Information and Wireless Communications. - Vol.2, No.1. (2012) 858.-862. lpp.

[7.2.3] Jansons J., Doriņš T. Analyzing IEEE 802.11n Standard: Outdoor Performance // The Second International Conference on Digital Information Processing and Communications (ICDIPC2012): Proceedings, Lietuva, Klaipeda, 10.-12. jūlijs, 2012. - 26.-30. lpp.

[7.2.4] Jansons J., Pētersons E., Bogdanovs N. Vehicle-To-Infrastructure Communication Based on 802.11n Wireless Local Area Network Technology // 2nd Baltic Congress on Future Internet Communications (BCFIC 2012): IEEE Conference Proceedings: IEEE Xplore Digital Library, Lietuva, Vilnius, 25.-27. aprīlis, 2012. - 26.-31. lpp.

[7.2.5] Jansons J., Pētersons E., Bogdanovs N. A Measurement Study of WLAN Link Recovery Using WDS in a Vehicular Environment // Proceedings of the 13th Biennial Baltic Electronics Conference (BEC2012), Estonia, Tallinn, 3.-5. October, 2012. - pp 173-174.

## **8. Efektivitātes paaugstināšana daudzu ceļu datplūsmu sadarbības scenārijiem mobilos bezvadu ad-hoc tīklos (MANET) izmantojot OSI starp-līmeņu saites un viedo (cognitive) radio tīklu tehnoloģijas**

### **8.1. Introduction**

Video separation into multiple streams and simultaneous transmission over multiple paths has proven to be beneficial for MANETs [8.1-8.4]. It is possible to achieve higher aggregated data transmission rate while choosing several spatially distributed paths, thus benefitting from the spatial reuse of a wireless channel. Multiple paths have uncorrelated loss patterns that decrease the chance of video interruption.

However, there are cases when network is not capable to handle video streams with the given data rate and network congestion occurs. To avoid it, we propose coding intrusive approach. Video coding parameters are adjusted to the network quality receiving feedback from the network, thus ensuring “network friendly” transmission. Additionally, techniques to improve path quality can be applied e.g. equip nodes with smart antennas what helps to mitigate inter-path interference.

The 8.2 chapter comprises survey on state-of-the-art practices on multiple path video transmission over MANET. It has been attempted answering questions: what is appropriate multi-stream coding method, optimal number of streams, bitrates and other parameters. To fully exploit multi-path advantages one should evaluate network performance. Therefore network transmission quality metrics and their influencing factors have been described in 8.4 chapter. Since inter-path interference is one of main factors influencing path bandwidth [5] technique on mitigating node mutual impact with smart antennas has been described in 8.5 chapter.

### **8.2. Survey of multiple path video transmission**

There are different multi-stream coding methods and parameters that can be influenced to ensure “network friendly” transmission. In this section the survey on state-of-the-art practices in multiple path video transmission over MANETs is performed.

#### **8.2.1. Coding methods**

For transmission of video over multiple paths over MANETs, the primary task is to choose the most appropriate multi-stream coding method. In combination with multi-path routing it ensures video transmission over the network. Depending on a number of paths and their reliability, one or another coding method can be used. Most popular choices are: layered coding (LC) and multiple description coding (MDC).

In LC method video frames are coded in base layer (e.g. I frames) and in several enhancement layers (e.g. P and B frames). Reception of base layer alone provides acceptable video quality, whereas reception of additional enhancement layers further

improves the quality. Without the base layer the enchantment layers alone can't be decoded. Therefore, the base layer should be sent over the most reliable path to avoid packet losses. To inform a sender about the lost base layer, packet retransmission requests can be used. In [8.4] it is suggested to send retransmission request over a different path, rather than over the one, where base layer packets were lost, in order to avoid additional losses. Layer coding has been used in scalable video coding (SVC) extension of the H.264/AVC standard. It seems promising for MANETs as it allows once-encoded content to be adapted not only to varying network conditions, but also to heterogeneous client devices. In addition to scalable quality it provides opportunity to reduce picture size (spatial resolution) and frame rate (temporal resolution) by removing some parts of the bit stream at the client side. However, cost for the scalability is increased decoding complexity and up to 10% higher bitrate if compared to nonsalable H.264/AVC [8.6]. The higher number of data packets in the SVC stream leads to a more frequent channel access and, thus, to eventual contention at Media Access Control (MAC) layer [8.7].

The MDC method allows using several streams of equal importance. Every separate stream provides the basic quality, but each additional stream improves it. As packet losses in any stream don't affect other streams, there is no need for packet retransmissions.

Several authors [8.8, 8.4, 8.9] link effectiveness of MDC and LC with the network characteristics, such as delay and path reliability. In [8.9] both methods were compared using two paths and considering different levels of the packet loss. Peak signal-to-noise ratio (PSNR) was measured at a receiver. The results revealed that without retransmission LC gives the worst results both for low and high packet losses. MDC and LC (with retransmissions) showed similar effectiveness at low packet loss level, but at the high number of packets loosed, LC outperformed MDC. In addition LC showed better results, when one path was more reliable than another. However it was also noted that delay was not critical for the experiments that may not be the case for real time video applications. The survey done in [8.8] concludes that if delay constrains limit retransmissions, MDC is better at the high packet loss levels. Therefore, MDC is more appropriate for delay-sensitive streaming over a less reliable network.

### **8.2.2. Optimal number of streams**

An optimal number of video streams and thus, the number of routing paths is another issue that should be considered. Theoretically, as pointed in [8.10], total aggregated bandwidth increases additively with the number of streams and probability of packet losses decreasing exponentially with the number of disjoint paths. In its turn jitter decreases as  $1/\sqrt{N}$ , where  $N$  – number of disjoint paths. However, as it has been proven by the real-life experiments performed in [8.5], in order to achieve a higher aggregated bandwidth, not only the node-disjoint but also non-interfering paths must be selected.

On the one hand optimal number of streams depends on a coding method used, but on the other hand - on a network topology and on the effectiveness of multiple paths routing protocol. For MDC an error recovery arises with two paths, while further increasing in the number of paths doesn't give significant improvement in the quality of performance [8.10]. The cross-layer routing scheme was proposed in [8.1] for LC

video, that takes path mobility and reliability into account. Simulations showed that for a network consisting of 100 mobile nodes it is optimal to use three paths by separating I/P/B video frames. If the number of paths is increased to 4 or 5, the packet lose rate and jitter increase considerably, because these paths introduce higher delays. Additionally it was suggested to manage queue priorities by setting a higher priority to I frames.

### **8.2.3. Video data rate**

Optimal video data rate for each stream is another coding parameter, which requires information about network performance to provide optimisation. In [8.2] it was shown that, when video rate in a stream exceeds certain threshold, the video quality quickly degrades because of the congestion in a network. There exists an optimal video data rate, when the highest PSNR could be achieved at the same time avoiding the overloading of a network. Additionally, as noted in [8.11], if data rate is too high, the performance of equipment CPU can be insufficient to forward traffic.

### **8.2.4. Multi-path routing**

Selection of a path set is done by a multi-path routing protocol. In this paper we consider only those protocols, which select several paths for simultaneous transmission of the multiple streams, not for backup purposes of a single stream.

A number of good paths found strongly depends on an “intelligence” of the protocol. The more video critical network metrics are taken into account, the more suitable for video streaming the selected paths are. Although, as noted in [8.12] including all effective routing metrics in one protocol may cause high overhead because of the control messages. Multiple path selection metrics, which separately or in combinations are included in multiple path routing protocols are: bandwidth, delay, mobility, reliability with respect to packet loss and reliability with respect to disjointness etc. However, as it has been proven by the analyses made in [8.13] and the experiments performed in [8.5], it is also crucial to consider eventual interference between the nodes. Effectiveness to a great extent is also influenced by the protocol type: proactive, reactive or hybrid. There is also no consensus on the issue of, which type is the most appropriate. In [8.11] is stated that best multi-path routing protocols for MANETs are reactive, but at the same time, in the works on the analysis of video streaming in MANETs [8.3, 8.14, 8.15] the proactive protocols are also applied, e.g. Optimized Link State Routing (OLSR) protocol extensions. According to [8.4], the proactive protocols provide faster decision and path recovery after a link failure, what is critically important for video applications. Another advantage noted is that the proactive protocols have more complete picture about network topology and metrics, thus resulting in the better sets of paths. The use of the reactive protocols is justified by a lower traffic overhead due to control messages that is also important in MANETs.

Multipath routing protocol must be integrated with the video coding method. Two examples showing good results are considered:

- a-MMDSR (adaptive-Multipath Multimedia Dynamic Source Routing) protocol for LC methods [8.15]. Prior to transmission it sends out probe packets from source to

destination over each of the paths discovered to measure its quality. This process is repeated over a certain period to adaptively cope with dynamic nature of MANETs.

- MP-OLSR (Multipath OLSR) protocol for MDC is proposed in [8.16]. It includes Multipath Dijkstra Algorithm to discover multiple disjoint routes and source routing approach to forward the packets. It can be regarded as a hybrid multipath routing. Control messages are sent out periodically to be aware of the network topology (like OLSR), however, it only computes the routes, when there are data packets needed to be sent out.

### 8.3. An Algorithm to select optimal parameters

The analyses made in the previous section show that there is no single approach to select optimal coding parameters. There are many suggestions on the selection of the best coding method for the given network conditions, but other parameters (e.g. optimal number of paths) are case-sensitive and depend on every particular situation. Therefore, network quality metrics should be estimated every time as video is being prepared for transmission. In addition, coding and paths selection algorithm should take into account the network quality during transmission to adapt to unexpected circumstances or wrong initial estimates. In this section we offer general algorithm of how coding should be adjusted and which factors should be taken into account to ensure the optimal video transmission in MANETs.

Video transmission over a network usually is characterized by a set of parameters (also called metrics): bandwidth, delay, jitter and packet loss. Estimation of these quality metrics is a complicated task since they are determined by several mutually interdependent network parameters. The more detailed analysis of the parameters and their interdependences is provided in next section. In Fig. 8.1 the idea is presented graphically.

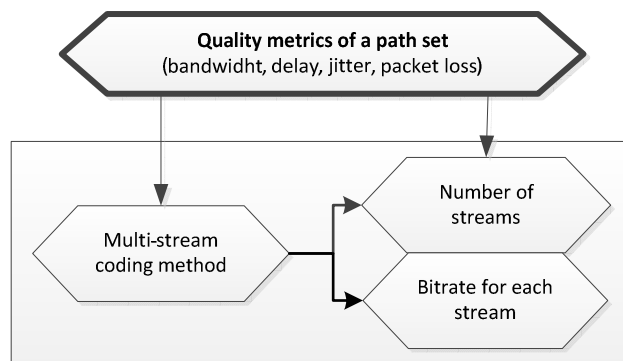


Fig.8.1. Schema of the algorithm

If paths and their eventual quality metrics are known it is possible to choose optimal coding parameters. Suggestions presented below are based on the analyses done in the second chapter of the present paper:

- coding algorithm (LC or MDC) choice depends on the packet loss [8.8, 8.9] and spread of delay among the paths, since if some limit has been exceeded it may cause

additional losses [8.13]. We assume that a routing protocol is able to work with any of the coding methods;

- number of streams depends on coding algorithm [8.1, 8.10] and number of paths offered by the routing protocol;
- bitrate for stream must be chosen according to maximum allowable bandwidth for a path to avoid the network congestion [8.2];
- stream allocation to paths depends on the packet loss and delay metrics in a path (important for LC) [8.1].

#### **8.4. Video transmission quality metrics**

Video transmission over a network can be characterized by a set of parameters (also called metrics) describing the capability of the network to ensure video transmission. These metrics usually are bandwidth, packet-loss, delay and jitter.

**Bandwidth** defines maximum possible data rate for a video stream at a given network conditions. In the case of multipath streaming it is important to estimate the path bandwidth to determine maximum achievable video rate for each stream. This parameter is important, since if the video data rate exceeds the network capacity, it results in a sharp increase of packet delays, jitter and throughput degradation due to congestion.

**Packet loss** may cause video quality degradation or even disruption. If a packet is lost and not retransmitted in time it will get discarded. Packet loss characterises path reliability. Single path reliability metric helps to select the best path for a more important stream (e.g. I-frames in LC algorithms) and discard non-reliable paths. Overall reliability characteristics of the set of available paths can help to select the most suitable coding algorithm.

**Delay** characterizes a time interval from packet generation until its reception. Delay metric can be analysed from different aspects. In case of one direction video streaming (Video on Demand) using single path delay parameter does not affect the quality if only its variation (jitter) is kept low. It is different in the case of several paths. If video frames (sequence of packets) are sent through multiple paths each with different delay, frame order can be lost. To be able to recover initial frame order a spread of delay among the paths must not exceed capacity of buffer. If the buffer cannot compensate delay, some frames will be lost causing video quality degradation. In the case of two-way streams (videoconferencing) there are much higher requirements for delay.

**Jitter** reflects delay variation of consequent packets in multi-hop transmission. If jitter exceeds certain buffered limit some packets may be lost. Jitter frequently appears when network is overloaded with a video stream having higher data rate than it can normally handle. Packets accumulate in queues in forwarding nodes where they wait for different time intervals until being forwarded. Changes in network conditions may also influence jitter, e.g. a route failure may delay some packets till a new route is found. If video streaming parameters are optimised for network performance then jitter will be negligible.

For efficient video transmission over the network one must choose some paths possessing an optimised set of described parameters/metrics. It is a complicated task

to determine these metrics directly from some measurements before real video traffic is transmitted over the network. Therefore we should look for other techniques how to indirectly estimate and forecast these metrics through other parameters.

The main factors influencing video transmission quality metrics are basic network characteristics and path selection (Fig. 8.2).

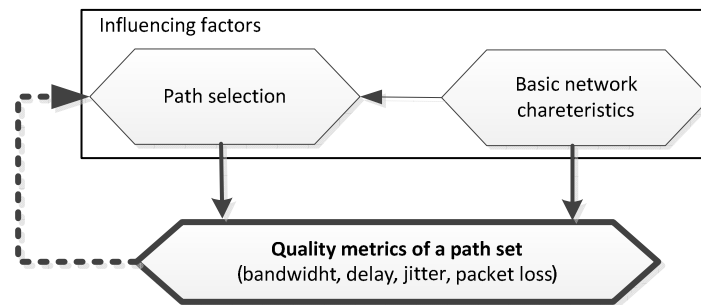


**Fig. 8.2. Schema of influencing factors**

Basic characteristics are performance of the devices, protocols deployed (e.g. wireless standard, routing protocol, multiple-access technique), network structure (e.g. number of nodes, density), state of radio channel (e.g. fading, weather, mutually interfering devices), network dynamics (e.g. mobility of nodes) and network load created by other applications. All these basic characteristics together determine the potential of the network, which has to be used in the most efficient way. The path selection is another factor which has an impact on the network quality metrics mainly due to the mutual interference of nodes. Therefore, it can be assumed that the basic network characteristics together with the path selection algorithm determine video transmission quality metrics.

Quality of paths strongly depends on the intelligence of path selection algorithm. An intelligent algorithm should base its decisions not only on basic network characteristics (mobility, path length), but also on the potential impact of selected paths on the quality metrics at the time, when a video transmission starts. Since such information could be obtained from analysing network parameters (interference, packet loss etc.), the feedback is introduced in the scheme (Fig. 8.2).

### **8.4.1. Basic network characteristics**

#### **8.4.1.1. Performance of the network devices**

MANETs usually consists of portable devices with a limited energy and processing resources. It should be considered whether performance of devices is sufficient to forward video traffic. As it was observed in the experiment described in [8.11] transit traffic consumes a significant amount of CPU resources. Experiments were conducted with different wireless network interfaces, CPU architectures, drivers and operating systems. Different video formats created different network load, since packet number was different.

The simplest way to determine CPU performance metric is to use information about CPU clock speed and average load, which can be gathered from nodes within paths.

### **8.4.1.2. Protocols deployed**

The effective routing protocol is crucial, as it was already discussed before. Routing protocol determines whether the chosen set of paths is the best of all possible options. The effectiveness is influenced also by protocol type: proactive, reactive or hybrid. According to [8.4] proactive protocols provide faster decision and path recovery after link failure and have a more complete representation of network topology resulting in better sets of paths. The use of reactive protocols is justified by less traffic overhead due to control messages [8.12].

A wireless standard deployed determines the link capacity, the delay, as well as the network connectivity. Today the most popular are IEEE802.11g and IEEE802.11n standard based technologies. When knowing the standard, one can make estimation of maximum achievable data rates, as well as transmission distances and other technology related parameters. IEEE802.11 standard defines Carrier Sense Multiple Access with Collision Avoidance (CSMA/CA) as a multiple access technique which coordinates channel access by concurrent users. As will be explained in subsection B, it has a significant impact on mutual interference between nodes.

### **8.4.1.3. Network structure**

Network connectivity is also determined by such network characteristics as number of nodes, distances between nodes, density. These parameters affect a chance to find a good set of paths, because the possible number of combinations increases with the number of nodes and the density. Node distance and transmission range along with environmental factors will also influence link quality and achievable data rates, as it will be explained in the next section.

### **8.4.1.4. Radio channel**

Every link in a path influences the whole path capacity and reliability. A link quality between two nodes depends on radio channel characteristics, such as attenuation, multipath propagation effects, interference from other electronic devices and networks. All these conditions influence achievable data rate, as well as possible packet losses in a link between any two devices.

*Link capacity.* In real radio channel, the transmitted signal is attenuated between the transmitter and the receiver. The signal attenuation in the channel increases with the distance between the both nodes. That in turn influences the data rate in a link between the nodes, since it depends on received Signal to Noise plus Interference Ratio (SNIR). SNIR at receiver  $j$  is calculated:

$$\text{SNIR}_j = \frac{G_{ij} \cdot P_i}{P_N + P_I} \quad (1)$$

where  $G_{ij}$  is channel gain between transmitter  $i$  and receiver  $j$ ,  $P_i$  - power of transmitter  $i$ ,  $P_N$  - thermal noise and background interference at receiver  $j$ ,  $P_I$  - interference from other transmitting nodes in same channel. SNIR determines the maximum bitrate that can be used between the transmitter and the receiver to satisfy given BER requirement.

Analytically received signal strength is calculated by using radio propagation models. The accuracy of the result depends on how well the model describes the environment and the physical processes in the channel. However, in a real network this parameter can be obtained from Received Signal Strength Indicator (RSSI) measurement in physical layer.

*Packet loss.* This parameter quantitatively characterises the reliability of a link in respect to eventual packet loss. In [8.14] it was attempted to experimentally find relation between packet loss and both SNIR and RSSI. As it was concluded, loss rate increases when both parameters drop below a certain threshold (SNIR=10dB and RSSI=-82dB). However, as authors noticed, it was hard to find a direct relationship between the measured parameters and the packet loss rate. It was possible to discover the difference between a good and a bad link but not easy to calculate an exact packet loss rate (Fig. 8.3).

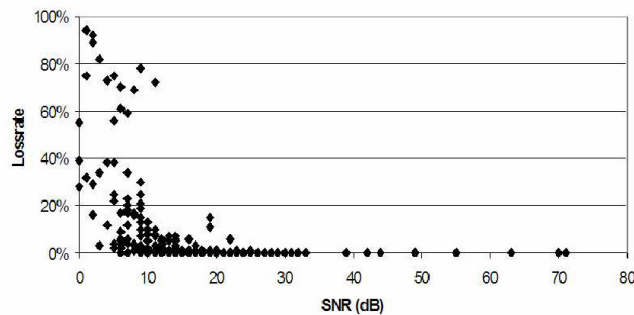


**Fig. 8.3. Dependence of packet loss rate on SNR [14]**

Packet loss may also influence bandwidth of the channel because of retransmissions of the lost packets.

#### **8.4.1.5. Network dynamics**

In mobile network, links between nodes are likely to change over time resulting in instability of throughput or even break of the link causing bursty packet losses. That in turn may result in video quality degradation and streaming interruption respectively.

The time in which video stream is resumed after link failure depends on the ability of the routing protocol to discover a problem and find a new route. Proactive routing protocols discover the failure of link from absence of regular control messages, but reactive - from error messages sent by node attempting to forward traffic through broken link.

Paths with higher mobility experience more frequent link failures, therefore such paths have lower reliability metric. Path mobility dynamics can be characterized by

nodes mobility within the path. As offered in [8.17], each node's mobility metric is calculated as a relative change of signal strength with respect to other neighbour nodes. If two successive packets are received from neighbouring node, it is possible to determine mobility at node<sub>1</sub> with respect to neighbour (node<sub>2</sub>) using equation

$$M_{node_1}^{rel}(node_2) = 10 \log_{10} \frac{P_{Rx(node_2 \rightarrow node_1)}^{new}}{P_{Rx(node_2 \rightarrow node_1)}^{old}} \quad (2)$$

Negative  $M_{node_1}^{rel}$  value means that nodes move away and positive value - move closer with respect to each other. Aggregate mobility at node 1 ( $M_{node_1}$ ) is expected value (E) of the squares of relative mobility from all its neighbours

$$M_{node_1} = E \left[ \left( M_{node_1}^{rel} \right)^2 \right] \quad (3)$$

Mobility of path is calculated by adding all  $M$  values determined for each node within a path and getting mean value by dividing it with total hops number in the path [8.1].

#### **8.4.1.6. Network load**

Depending on a network usage, there may exist other traffic generated by commonly used applications (e.g. HTTP, FTP) and even concurrent video streams. Background traffic creates not only a load on nodes carrying it but also increases interference level in the network. Therefore, it must be taken into consideration to correctly estimate available path capacity.

For this reason, background traffic load (BTL) metric is introduced. As offered in [18] BTL can be obtained at each node in a network by measuring packets that traverse a node. This includes packets transmitted by node or destined to the node itself and packets received from the others but not destined to the node itself. Since traffic has a dynamic nature, BTL readings over some period should be collected and weighted average computed by assigning the higher weight to the latest readings.  $BTL_{ir}$  is a load of a  $i^{th}$  node in the  $r^{th}$  path. BTL of a  $r^{th}$  path is considered as

$$BTL_r = \max(BTL_{1r}, BTL_{2r}, \dots, BTL_{ir}). \quad (4)$$

In [8.18] such assumption is justified by simulations proving that degradation of throughput depends on the most congested node in the path. The BTL collection mechanism can be implemented at MAC (Media Access Control) layer where packet information is available.

#### **8.4.2. Path selection**

Network parameters which are directly influenced by selected set of paths are: disjointness of paths, hop count and interference level.

### 8.4.2.1. Path disjointness

Depending on path selection algorithm there may exist several paths sharing common nodes or even links. Such sets of paths are less reliable because transmission failure in any of shared nodes causes disruption of data streams in all related paths. The more disjoint paths are the less probability to have packet losses in all of them simultaneously (losses are uncorrelated).

Another drawback is that shared nodes may reduce path capacity, since they aggregate traffic from several paths. That may cause path capacity degradation and even unexpected delays if traffic is too intense. Such situation can be accounted as self-interference.

Path disjointness characteristic can be obtained from routing table available from network layer of server node. In [8.19] a method is offered to calculate shared nodes ratio, which indicates level of disjointness of two routes which have the same destination. It can be calculated in the following way:

$$\text{shared\_nodes\_ratio} = \frac{\text{number\_of\_shared\_nodes}}{\text{Length\_of\_the\_shorter\_route}} \quad (5)$$

Such ratio has to be calculated for every pair of paths.

### 8.4.2.2. Hop count

Hop count has impact on two quality metrics – end-to end delay and path reliability. Majority of routing protocols select paths following hop count metric and prefer paths with fewer hops. That is reasonable because the number of hops increases end-to-end delay in almost linear relation. An approach described in [20] proposes to calculate the approximate value of average delay per packet taking into account only delays introduced by intermediate nodes and transmission delay. Processing time and CSMA/CA delay in intermediate nodes is approximately 6ms. Average delay  $D$  can be calculated from equation

$$D = \frac{L \cdot N_{\text{ret}}}{v} \cdot n_h + D_I \cdot (n_h - 1), \quad (6)$$

where  $L$  packet size in bits,  $v$  – data rate (bps),  $N_{\text{ret}}$  – number of retransmission of packet,  $n_h$  – number of hops,  $D_I$  - delay in intermediate nodes.

Hop count influences also path reliability because packet loss probability of each link adds to the overall packet loss probability of a path. Due to more hops in the path there is higher probability of packet loss in one of the links. The probability of a successful packet delivery in the path can be calculated:

$$P = (1 - P_{\text{loss\_link}})^{n_h - 1}, \quad (7)$$

where  $P_{\text{loss\_link}}$  is stable packet loss probability in each link.

### 8.4.2.3. Interference

Only few routing protocols take into account mutual interference between network nodes when paths are selected. Interference may considerably limit the capacity of a path. There are two kinds of interference: interference caused by contention at MAC layer and physical interference of signals.

Channel access in MANET is controlled by CSMA/CA protocol. Before transmission node senses the channel and transmits only if the signal level from other nodes is below a certain threshold. MAC contention caused interference arises when nodes being one in another sensing range have to transmit simultaneously. Only one node is allowed to transmit at a time while others are blocked.

Physical interference (also called co-channel interference) may arise from other transmitting nodes which are outside a carrier sensing range. Signals from distant nodes interfere with the signal from the actual transmitter and worsen the reception conditions at the receiver site. The conditions are characterized by SNIR (1).  $P_I$  reflects power level received at node (receiver) from all interfering nodes (transmitters) and is calculated:

$$P_I = \sum_{k:k \neq i} G_{kj} P_k, \quad (8)$$

where  $G_{kj}$  channel gain between node  $k$  and receiver  $j$ ,  $P_k$  transmit power of node  $k$ . Higher interference level results in lower SNIR value and accordingly lower link capacity to keep BER level low.

Lower data rate means also that the channel will be occupied for longer time by a single pair of transmitting-receiving nodes. Time to send  $N$  bits with data rate  $v$  is:  $\tau = N/v$ . That in turn results in longer waiting for free channel by neighbouring nodes because of MAC contention.

Both types of interference influence nodes not only in the same path (intra-path interference), but also nodes from different paths (inter-path interference). As shown in [8.5], if data streams were transmitted via paths which are close one to another, then throughput of each path decreased considerably. In the next subsection these results are presented in more detail.

### 8.4.3. Interdependence graph of the network characteristics

As it follows from analysis in the previous chapter, there is a great variety of network characteristics and many of them are interlinked. This makes overall evaluation of network conditions for video data transmission very complex.

To visualize relation between interdependent network parameters, they are grouped in several levels and presented as a graph with internal links between separate elements (Fig. 8.4). The graph can be useful for several purposes. Firstly, it shows different characteristics and factors that have effect on network and determines its parameters. Secondly, the interdependencies between parameters are shown, that allows to predict how changes in one parameter will affect the other. Thirdly, following the graph from top to bottom, one can step by step determine the video

transmission quality metrics (bandwidth, delay, jitter and packet loss). To quantitatively estimate network characteristics and thus the performance for video transmission, also possible measurements of parameters have been included.

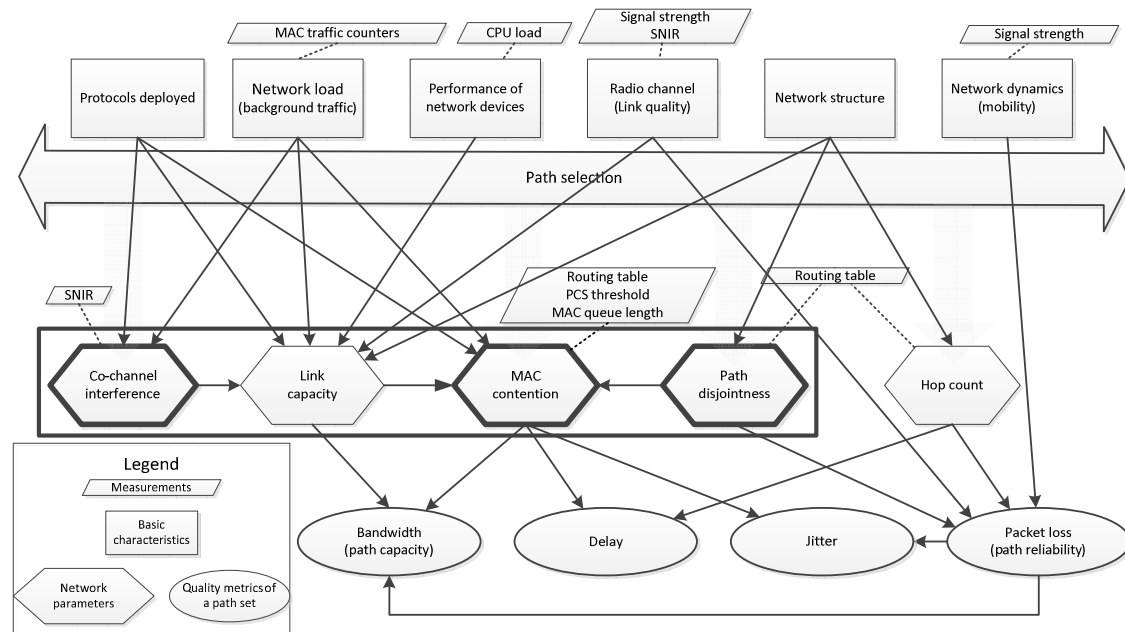


Fig. 8.4. Dependency graph of different network parameters characterizing path quality

#### 8.4.4. Techniques to improve transmission quality metrics

As one can conclude from graph, interference (contention at MAC layer, co-channel and path coupling) impacts all the transmission quality metrics (emphasised blocks in Fig.8.4). Therefore it should be assumed as one of the main parameter's describing path quality. Knowing the interconnections between network parameters and characteristics allow us to suggest techniques and solutions on how to decrease inter-path interference:

- select paths that have less mutual impact;
- use equipment and protocols that provide higher data rate to occupy channel for shorter periods;
- enhance CSMA/CA protocol with adaptive carrier sense mechanism which tunes sensing range for every particular situation;
- use smart antennas which can decrease the influence from interfering transmitter from neighbour path by adapting its antenna beam pattern.

#### 8.5. Smart antennas for interference mitigation

Traditionally omni-directional antennas are used for 802.11 devices. Since they radiate in all directions it causes high inter-node and inter-path interference. Equipping MANET nodes with smart antennas may help to mitigate interference. In

this chapter we describe implementation of directional antenna in MATLAB Simulink 802.11 model.

Smart antenna is multiple antenna element system allowing to automatically manipulating antenna pattern. It is accomplished both at software and hardware level. There are two basic types of smart antennas: switched beam and adaptive antenna (Fig. 8.5) [8.21].

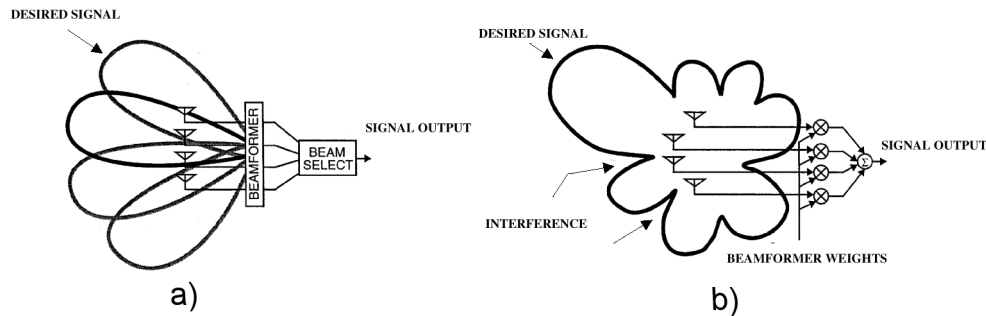


**Fig 8.5. Basic types of smart antenna a) Switched beam antenna, b) adaptive antenna[8.21]**

Switched beam antenna forms narrow beam towards desired direction. Beams are switched by predefined angle (sectors). Performance of output signal may suffer from side lobes and inability to point main lobe maxima dowered desired direction.

Adaptive array forms beam so that performance of antenna output signal is maximised. It is achieved by maximizing beam towards desired direction and minimizing towards interferers. Output of each antenna element is multiplied by weight which is calculated by control mechanism.

Although, switched beam antennas doesn't allow full adaptively, they are relatively easier to implement in currently used wireless devices.

### **8.5.1. Directivity control mechanism**

In scope of the work directivity model based on IEEE802.11b has been elaborated. To achieve automatic directivity control, existing 802.11b MATLAB Simulink model has been modified using method described in US7609648 [8.22] patent.

First, coordinates of potential receivers are delivered. Next they are summarized in table of directions (Fig.8.6) specifying identifier of receiver and antenna direction. Using MAC layer frame information, a recipient is identified. The information later is used to change antenna-subsystem parameters and steer pattern towards desired receiver.

Requirements for Simulink model:

- Transmission range: 100m
- Number of antenna sectors (beams): 8
- Receivers are Omni-directional
- Table of directions has been already prepared

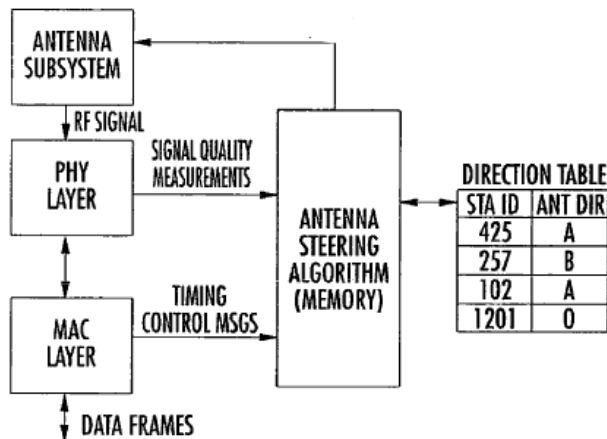


Fig.8.6. US7609648 directivity model scheme [8.22]

### 8.5.2. Elaborated model

Matlab Simulink block scheme of the elaborated model is given in Fig. 8.7.

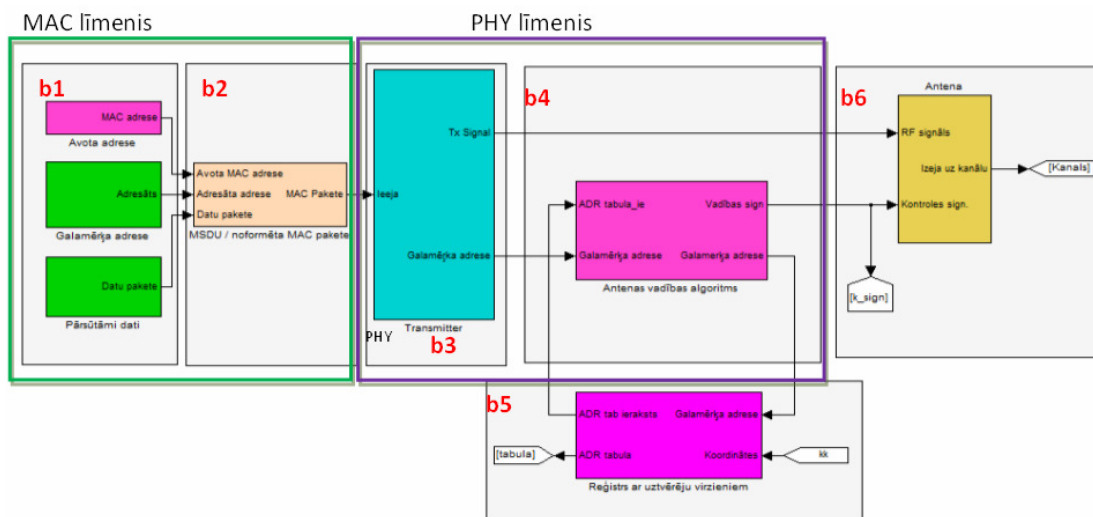


Fig. 8.7. Block scheme of the elaborated system

Descriptions of separate blocks:

- b1+b2 MSDU generation block** Contains generators of source and destination MAC address as well as data to be transmitted.
- b3 Transmitter** Forming of physical signal
- b4 Antenna control mechanism** From b5 information about destination is obtained and antenna control signal is formed.
- b5 Registry of receivers' directions**
- b6 Antenna block** Depending on the control signal from b4, beam is switched towards destination and transmission power is adjusted

Simulation output of the described system shown in 2-dimensional spatial diagram (left side of Fig. 8.8). Receiver Rx3 (yellow dot) is out of coverage, Rx2, Rx0 (red and blue dots) is in the same antenna sector, Rx1 is in the other, currently inactive sector. On the right side spectral density of the received signal for each receiver is shown. Additionally it is possible dynamically adapting transmission power level considering distance to a receiver. In this case (Fig.8.8) Rx2 doesn't "hear" a signal which is transmitted in Rx0 direction.

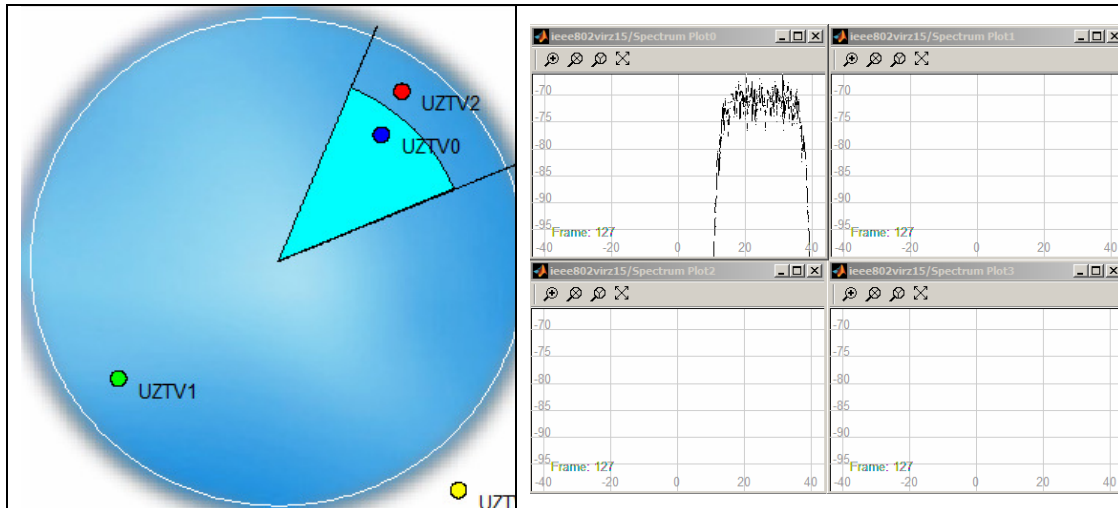


Fig. 8.8. Simulation output.

Results above are for ideal channel conditions where noise and interference are not taken into account.

## 8.6. Conclusions

Network characteristics should be foreknown for efficient multi-path video streaming in MANETs. There are some quality metrics (bandwidth, delay, jitter and packet-loss) which characterize network potential for video transmission. Estimation of these quality metrics is a complicated task since they are determined by several mutually interdependent network characteristics: performance of the devices, protocols deployed, network structure and dynamics, state of radio channel, as well as network load created by other applications. Video transmission quality metrics are determined by the network characteristics and the path selection algorithm.

A coding intrusive algorithm has been proposed, where coder has a feedback about network characteristics required to ensure "network-friendly" video streaming. Such an approach is an alternative to other methods, where coding is done without reference.

Smart antenna has been suggested as technique to mitigate interference. Antenna model has been elaborated which allows to form narrow beam towards receiver and adapt transmission power.

This work will serve as a basis for future development of cognitive systems to improve multiple path video transmission in MANET's. Implementation of the coding scheme requires cross-layer information exchange in each network device as well as between devices. For evaluation and appropriate coding parameter selection at the sender side some kind of

artificial intelligence (AI) techniques might be used. Since the task involves both the parameter optimisation and decision making several AI techniques can be applied simultaneously, e.g. fuzzy logic and evolutionary algorithms.

## **References**

[8.1] V. C. Frias, G. D. Delgado, and M. A. Igartua, "Multipath routing with layered coded video to provide QoS for video-streaming over MANETs," in 14th IEEE International Conference on Networks, vol. 1, pp. 1-6, Sept. 2006.

[8.2] E. Setton, X. Zhu, and B. Girod, "Minimizing distortion for multi-path video streaming over ad hoc networks," in International Conference on Image Processing, vol. 3, pp. 1751-1754, Oct. 2004.

[8.3] S. Mao, Y. Hou, H. Sherali, and S. F. Midki\_, "Multimedia-centric routing for multiple description video in wireless mesh networks," IEEE Network, vol. 22, no. 1, pp. 19-24, Jan.-Feb.2008.

[8.4] S. Mao, S. Lin, Y. Wang, S. Panwar, and Y. Li, "Multipath video transport over ad hoc networks," IEEE Wireless Communications, vol. 12, no. 4, pp. 42-49, Aug. 2005.

[8.5] L. Cikovskis and I. Slaidins, "Impact of physical carrier sense range on network throughput in wireless ad-hoc networks," Scientific Journal of RTU. 7. series. Telecommunications and Electronics, vol. 11, pp. 16-21, 2011.

[8.6] H. Schwartz and M. Wien, "Standards in a nutshell: The scalable video coding extension of the h.264/avc standard," IEEE Signal Processing Magazine, vol. 25, no. 2, pp. 135-141, 2008.

[8.7] A. Fiandrotti, D. Gallucci, E. Masala, and J. D. Martin, "High-performance h.264/svc video communications in 802.11e ad hoc networks," Lecture Notes in Computer Science, vol. 5464 LNCS, pp. 200-210, 2009

[8.8] M. Lindeberg, S. Kristiansen, T. Plagemann, and V. Goebel, "Challenges and techniques for video streaming over mobile ad hoc networks," Multimedia Systems, vol. 17, no. 1, pp. 51-82, 2011.

[8.9] Y. Wang, S. Panwar, S. Lin, and S. Mao, "Wireless video transport using path diversity: Multiple description vs. layered coding," in International Conference on Image Processing (ICIP'02), vol. 1, pp. I/21-I/24, 2002.

[8.10] J. G. Apostolopoulos and M. D. Trott, "Path diversity for enhanced media streaming," IEEE Communications Magazine, vol. 42, no. 8, pp. 80-87, 2004.

[8.11] P. Xue and S. Chandra, "Revisiting multimedia streaming in mobile ad hoc networks," in Proceedings of the 2006 international workshop on Network and operating systems support for digital audio and video, 2006.

[8.12] M. Tarique, K. E. Tepe, S. Adibi, and S. Erfani, "Survey of multipath routing protocols for mobile ad hoc networks," Journal of Network and Computer Applications, vol. 32, no. 6, pp. 1125 - 1143, 2009.

[8.13] L. Cikovskis, and I. Slaidins, "Analysis of wireless ad-hoc network parameters for efficient multipath video transmission," Digital Information Processing

and Communications (ICDIPC), 2012 Second International Conference on , vol., no., pp.16-21, 10-12 July 2012.

[8.14] J. Karlsson, H. Li, and J. Eriksson, "Real-time video over wireless ad-hoc networks," in International Conference on Computer Communications and Networks, ICCCN, vol. 2005, p. 596, 2005.

[8.15] M. A. Igartua and V. C. Frías, "Self-configured multipath routing using path lifetime for video-streaming services over Ad Hoc networks," Computer Communications, vol.33, no.15, pp.1879-1891, 2010.

[8.16] J. Yi, E. Cizeron, S. Hamma, and B. Parrein, "Simulation and Performance Analysis of MP-OLSR for Mobile Ad hoc Networks," in Wireless Communications and Networking Conference, pp. 2235-2240, 2008.

[8.17] P. Basu, N. Khan, and T. Little, "A mobility based metric for clustering in mobile ad hoc networks," in 2001 International Conference on Distributed Computing Systems, pp. 413 -418, Apr 2001.

[8.18] K. Kuladinithi, "Wireless Multi-hop Ad hoc Networks: Evaluation of Radio Disjoint Multipath Routing". PhD dissertation, Univ. Bremen, Bremen, Germany, 2009.

[8.19] C.-O. Chow and H. Ishii, "Enhancing real-time video streaming over mobile ad hoc networks using multipoint-to-point communication," Computer Communications, vol. 30, no. 8, pp. 1754-1764, Jun. 2007.

[8.20] H. Asif, T. R. Sheltami, and E. Shakshuki, "Power consumption optimization and delay minimization in MANET," in The 6th International Conference on Advances in Mobile Computing and Multimedia, pp. 67-73, 2008.

[8.21] Winters J. Smart antenna techniques and their application to wireless ad hoc networks. - IEEE Wireless Communications, IEEE, 2006. – 7 p.

[8.22] Hoffmann J. E., Nelson Jr. G. R., Regnier J. A., Johnson K. P. Antenna Steering For An Access Point Based Upon Control Frames US7609648, US Patent, 2009. – 25 p.

## Pielikums #1

### Необходимость согласующих устройств

Как правило, антенны импульсного радиолокатора находятся на некотором удалении от активной (передающей или приёмной) его части. Для частот  $\leq 5$  GHz ( $\lambda \geq 0.06\text{m}$ ) удаление  $L > 0,5\text{m}$  ( $\lambda_{\min} = L$ ) уже требует применения длинной линии для передачи сигнала. В качестве таковой на таких частотах применяется коаксиальный кабель. Особенности работы линии передачи требуют её согласования, т.е. чтобы выходное сопротивление источника сигнала и сопротивление нагрузки были равны волновому сопротивлению линии  $R_0$  (принимая, что в рабочей полосе частот оно является чисто активным). Удовлетворение этих условий позволяет добиться от линии трёх важных её возможностей:

- 1- максимальную передачу мощности сигнала;
- 2- избежать искажения сигнала посредством минимизации отражений сигнала от концов линии;
- 3- в случае симметричной антенны – перехода от симметричной антенны на несимметричный кабель.

### Согласующие устройства передающего тракта.

Согласующее устройство (СУ) в передатчике импульсного локатора позволяет достичь передачи максимальной мощности импульса возбуждения антенны и избежать повторных возбуждений через интервалы времени, отличные от периода повторения импульсов задающего генератора.

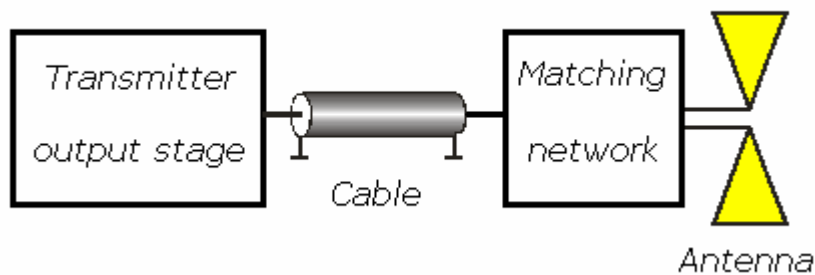


Figure1. Схема включения согласующего устройства в тракт передатчик – антенна

На Figure 1 представлена схема включения СУ в тракт оконечный каскад передатчика – антенна. Предполагается, что выходное сопротивление оконечного каскада передатчика равно  $R_0$ . Поэтому на этом участке согласование уже выполнено. СУ, включенное в конце линии согласует  $R_0$  с входным сопротивлением антенны  $Z_a$ , которое, как правило, является комплексным  $Z_a = R_a + jX_a$ . Поэтому в функцию СУ входит помимо приведения  $R_a$  к значению  $R_0$ , также и компенсация реактивной составляющей  $X_a$ . Если возбуждение антенны производится импульсами со

сверхширокополосным спектром, то соответственно антенна выбирается также сверхширокополосной. В исследовании в качестве таковой была выбрана антенна типа «bow-tie».

Эта антенна является симметричной, её основные характеристики остаются практически неизменными в полосе перекрытия  $f_{\max} / f_{\min} \geq 3$ . Входное сопротивление равно  $R_a = 188 \text{ Ом}$  (теоретически). Исходя из этих характеристик, задачей СУ является :

—согласование волнового сопротивления подводящего кабеля  $R_0$  (как правило  $R_0 = 50 \text{ Ом}$ )

с входным сопротивлением антенны  $R_a = 188 \text{ Ом}$ .

—осуществить переход с несимметричного кабеля на симметричную антенну.

Применение сверхширокополосного возбуждающего импульса накладывает требования аналогичной сверхширокополосности к СУ, а это в районе 2 – 3 GHz. Практическая реализация такого сверхширокополосного СУ затруднена. Компромиссом является возбуждение антенны парафазными импульсами, подаваемыми по двум отдельным кабелям, согласованными на конце. С учётом того, что окончательное обострение импульсов возбуждения производится в непосредственной близости от входных клемм антенны с помощью диода с накоплением заряда (SRD), схема СУ + обостритель приобретает вид, представленный на Figure 2.a, где :

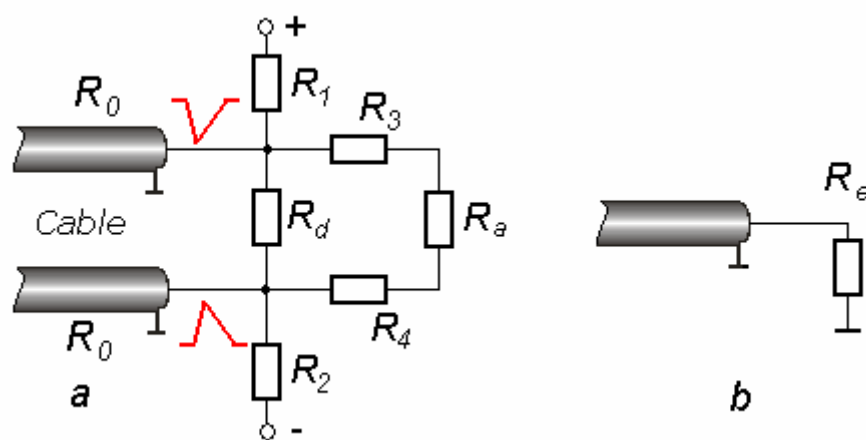


Figure 2. Схема сопротивлений обострителя, согласующего устройства и антенны ( a ) и их эквивалент ( b )

$R_1, R_2$  - через эти сопротивления производится накачка SRD,  $R_1 = R_2 = 3 \text{ КОм}$ ;

$R_d$  - дифференциальное сопротивление SRD;

$R_3, R_4$  - согласующие сопротивления,  $R_3 = R_4 = 68 \text{ Ом}$ ;

$R_a$  - входное сопротивление антенны,  $R_a = 188 \text{ Ом}$ ;

Перерасчёт схемы упрощает её вид (Figure 2.b), и даёт эквивалентное сопротивление  $R_e$ , являющееся нагрузкой для каждой линии. Значение  $R_e$  равно

$$R_e = \frac{R_1 \left( \frac{(R_3 + R_a + R_4)R_d}{R_3 + R_a + R_4 + R_d} + \frac{R_2 R_0}{R_2 + R_0} \right)}{R_1 + \frac{(R_3 + R_a + R_4)R_d}{R_3 + R_a + R_4 + R_d} + \frac{R_2 R_0}{R_2 + R_0}}$$

(1)

Для используемых в экспериментальной схеме значений сопротивлений выражение (1) упрощается и принимает вид:

$$R_e = \frac{3000 \left( \frac{324R_d}{324 + R_d} + 49,2 \right)}{3049 + \frac{324R_d}{324 + R_d}}$$

(2)

Работа обострителя импульсов на SRD характеризуется резким изменением дифференциального сопротивления диода  $R_d$  от низкого значения (единицы Ом) до высокого ( $\geq 20$  КОм). Отобразим выражение (2) в виде графика функции  $R_e = f(R_d)$ .

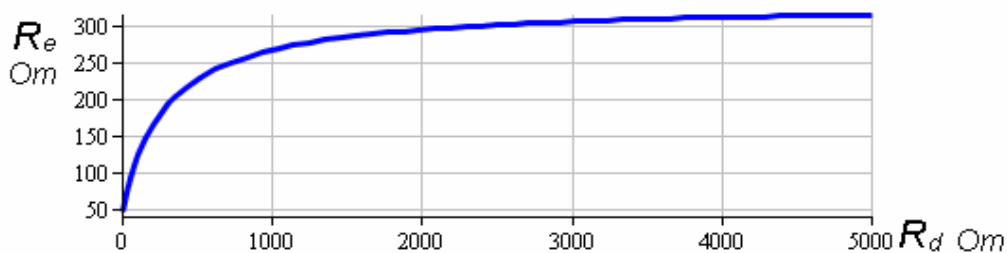


Figure 3. Зависимость эквивалентного сопротивления  $R_e$  от величины

дифференциального сопротивления  $R_d$  SRD

При низких значениях  $R_d$ , т.е. при стремлении его к нулю, величина

$$R_e = \frac{R_1 R_2 R_0}{(R_2 + R_0) \left( R_1 + \frac{R_2 R_0}{R_2 + R_0} \right)}, \text{ и если } R_1 \gg R_0, R_2 \gg R_0, \text{ то } R_e \approx R_0 = 50$$

Ом. Это означает, что в интервале времени когда происходит накачка SRD и в начале запускающего импульса, когда диод ещё не переключился, линии согласованы и переотражения не происходит.

При высоких значениях  $R_d$ , т.е. при стремлении его к 20 КОм и более,

$$\text{величина } R_e \rightarrow \frac{R_1 (R_3 + R_a + R_4 + R_0)}{R_1 + R_3 + R_a + R_4 + R_0}, \text{ или при подстановке значений}$$

сопротивлений,  $R_e \rightarrow 328$  Ом

Это означает, что при переключении диода происходит рассогласование линий

с вытекающими из этого последствиями: коэффициент стоячей волны  $SWR = 6,6$ ; коэффициент отражения  $\Gamma = 0,74$ ; Return Loss = 2,7 dB. Эти величины сохраняются для сформированного крутого фронта запускающего импульса и оставшейся его части. Происходит потеря части мощности запускающего импульса и переотражение. И, если выход генератора не согласован с кабелем, то отражённый импульс через интервал, эквивалентный длине этого кабеля обратно возвращается на SRD и при достаточной его амплитуде повторно его запускает. Все эти переотражения приводят к шуму, не дающему возможности правильно оценить полезный сигнал.

Как было сказано выше, согласование антенны осуществляется

сопротивлениями  $R_3$  и  $R_4$ . Вследствие того, что на антенну подаются как фронт возбуждающего импульса так и импульс, сформированный с помощью SRD и оба вносят вклад в излучение, то выбор значений этих сопротивления является компромиссом. Для согласования в случае  $R_d \rightarrow 0$  необходимо брать  $R_3 = R_4 = 94 \text{ Ом}$ ; Для согласования в случае  $R_d \rightarrow 20 \text{ Ком}$  необходимо брать  $R_3 = R_4 = 45 \text{ Ом}$

Компромиссным значением выбрано значение равное 68 Ом и подстраивается при экспериментировании для достижения наилучших результатов.

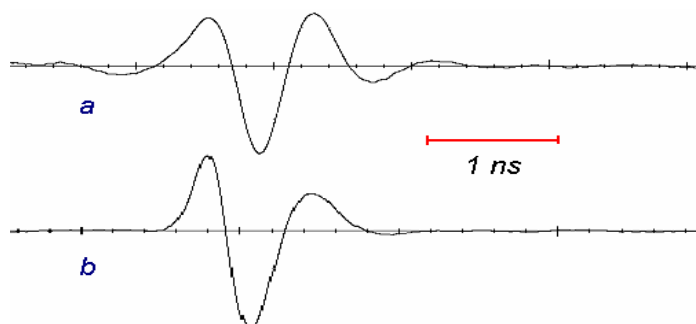


Figure 4. Форма сигнала, соответствующая прямому прохождению из антенны в антенну : а) передающая антенна не согласована; б) передающая антенна согласована.  
Согласующие устройства приёмного тракта.

На передающей стороне влияние рассогласования можно минимизировать путём временного разделения. На приёмной стороне данный приём не подходит. Все паразитные переотражения, попадающие во временное окно полезного сигнала, маскируют его, затрудняя дальнейшую обработку. Поэтому для СУ на приёмной стороне предъявляются повышенные требования. По существу они должны выполнять те же функции, что и для передающей стороны, а именно : 1) максимизировать передачу мощности сигнала с приёмной антенны на вход первичного преобразователя; 2) устранять паразитные переотражения, маскирующие полезный сигнал; 3) в случае несовпадения симметрии приёмной антенны и первичного преобразователя, производить их симметрирование. Аналогичные требования и по широкополосности СУ.

Исследования проводились как для симметричных, так и для несимметричных антенн. При допущении, что мы используем

сверхширокополосную передающую антенну, отражённый от цели сигнал также является сверхширокополосным и представляет собой радиоимпульс с большим дикрементом затухания  $\delta = 1..2$ , соответствующим низкой добротности системы ( $Q \leq 1$ ). В лучшем случае это радиоимпульс с  $1,5 \div 3$  периодами колебания на центральной частоте. Коэффициент широкополосности такого сигнала, определяемый, например по выражению

$$\eta = \frac{f_{\max} - f_{\min}}{f_{\max} + f_{\min}}, \text{ больше } 0,25. \text{ Принять такой сигнал возможно лишь с}$$

помощью специальных сверхширокополосных антенн. Последние могут быть как симметричными так и нет с выходным сопротивлением в общем отличным от стандартного значения 50 (75) Ом. Поэтому для передачи сигнала от антенны к входу первичного преобразователя применение СУ обязательно.

#### Выбор СУ для приёмной антенны типа «bow-tie»

Исследования проводились с приёмной антенной аналогичной передающей и её описание приведено выше. Качество СУ и его пригодность для работы оценивались по косвенным признакам : а) широкополосность – по анализу спектра сигнала; б) согласование сопротивлений – по наличию переотражений в окне полезного сигнала.

1. СУ – дифференциальный сип усилитель. Наиболее идеальным вариантом согласования является использование сип дифференциального усилителя с большим входным сопротивлением, подключенным непосредственно к клеммам приёмной антенны. Он работает как идеальный вольтметр, без искажения измеряющий напряжение на клеммах антенны. С 50-омного выхода усилителя напряжение подаётся по кабелю на вход осциллографа. Схема такого подключения приведена на Figure 5. В качестве усилителя использовался активный пробник P7360 с полосой 6 GHz от осциллографа реального времени Tetronix DPO 70604.

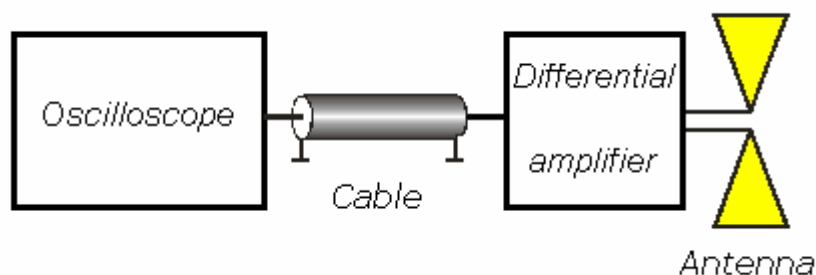


Figure 5. Схема подключения дифференциального усилителя в качестве СУ

Сигнал и соответствующий ему спектр при таком согласовании представлены на Figure 6.

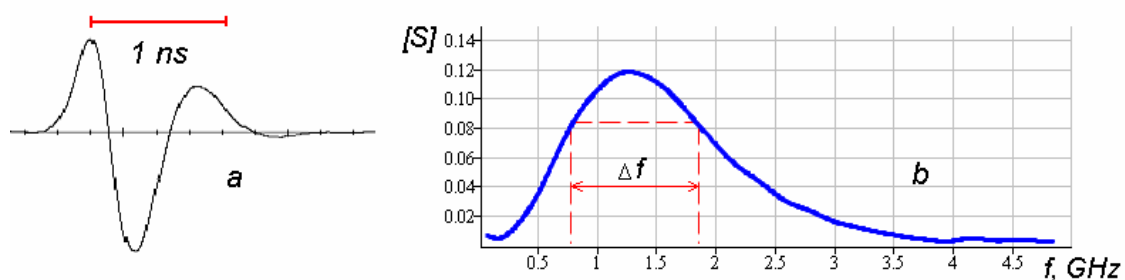


Figure 6. Согласующее устройство – дифференциальный усилитель. а – форма принимаемого сигнала; б – модуль спектральной плотности принимаемого сигнала.

Как следует из анализа сигнала и его спектра :

- центральная частота равна 1,25 GHz;
- количество периодов в сигнале – 1,5;
- наличие переотражений в рабочем окне (20ns) – отсутствуют
- ширина полосы спектра сигнала на уровне 0,7 – 1,1 GHz
- коэффициент широкополосности сигнала – 0,4

Как следует из приведённых данных, СУ полностью удовлетворяет вышеописанным критериям, поэтому примем это СУ за эталон.

2. СУ – трансформатор – длинная линия. Широкополосным СУ является так называемый трансформатор-длинная линия (ТДЛ). Он представляет собой несколько длинных линий, для компактности расположенных на ферритовом кольце. Количество линий, их волновое сопротивление и схема взаимного включения выбираются исходя их желаемого коэффициента трансформации входного и выходного сопротивлений и вида симметрии входа/выхода. Применительно к симметричной антенне типа «bow-tie», входное сопротивление которой равно 188 Ом, требуется такое СУ, которое позволяет перейти от симметричного сопротивления 188 Ом к несимметричному 50 Ом. Волновое сопротивление линий трансформатора для такого СУ находится по формуле  $R_0 = \sqrt{50R_a} \approx 100 \text{ Ом}$ . Реализованная и исследуемая схема подключения такого ТДЛ представлена на Figure 7.

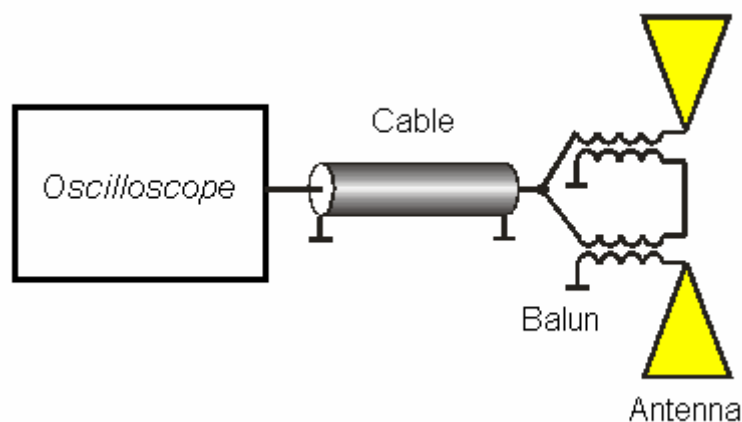


Figure 7. Схема подключения трансформатора длинная линия в качестве СУ

Сигнал и соответствующий ему спектр при согласовании ТДЛ представлены на Figure 8.

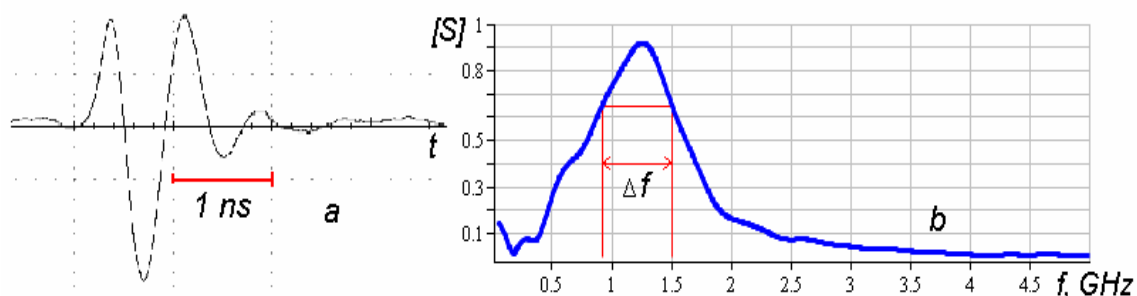


Figure 8. Согласующее устройство – трансформатор длинная линия. a – форма принимаемого сигнала; b – модуль спектральной плотности принимаемого сигнала.

Как следует из анализа сигнала и его спектра :

- центральная частота равна 1,25 GHz;
- количество периодов в сигнале – 2,5;
- наличие переотражений в рабочем окне (20ns) – 10% от максимума
- ширина полосы спектра сигнала на уровне 0,7 – 0,58 GHz
- коэффициент широкополосности сигнала – 0,24

Как следует из приведённых данных СУ на ТДЛ уступает по своим характеристикам дифференциальному усилителю, а именно :

- в рабочем окне сигнала появились незначительные переотражения;
- полоса сигнала сузилась в 1,9 раз;
- по критерию сверхширокополосности сигнал близок к его границе (0,25)

3. СУ – широкополосный трансформатор. Наиболее простым вариантом согласования входного  $R_{in}$  и выходного  $R_{out}$  сопротивлений является использование трансформатора на ферритовом сердечнике, сохраняющем свои магнитные свойства до гигагерца и выше. Подбирая количество витков первичной  $n_1$  и вторичной  $n_2$  обмоток по формуле  $R_{in} / R_{out} = n_1^2 / n_2^2$  можно добиться удовлетворительного согласования. Наличие паразитных ёмкостей превращает трансформатор в два связанных контура, обладающих резонансными свойствами. Однако конструкция специальных трансформаторов выполняется так, чтобы понизить добротность этих контуров. Одним из таковых является трансформатор ADT1-1WT. Схема подключения трансформатора представлена на Figure 9.

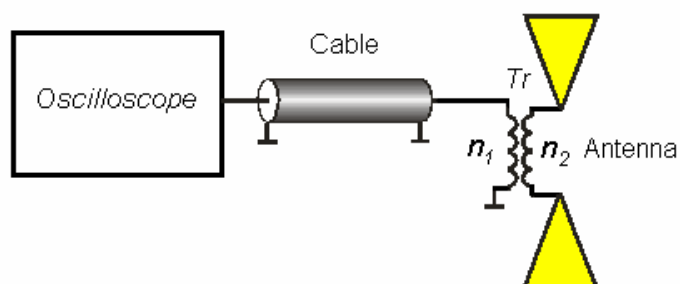


Figure 9. Схема подключения широкополосного трансформатора в качестве СУ

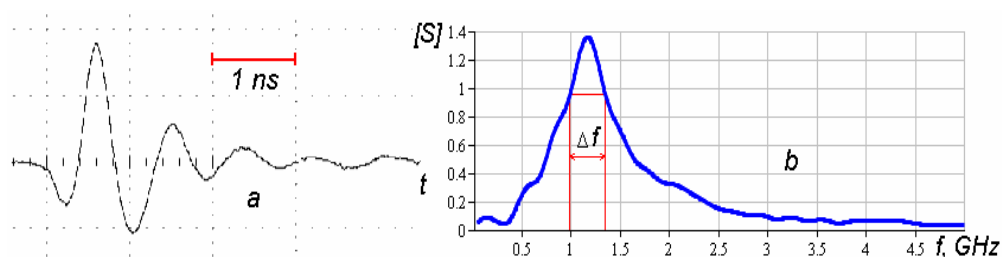


Figure 8. Согласующее устройство – широкополосный трансформатор. а – форма принимаемого сигнала; б – модуль спектральной плотности принимаемого сигнала.

Из анализа сигнала и его спектра следует :

- центральная частота равна 1,2 GHz;
- количество периодов в сигнале – 3;
- наличие переотражений в рабочем окне (20ns) – 20% от максимума
- ширина полосы спектра сигнала на уровне 0,7 – 0,36 GHz
- коэффициент широкополосности сигнала – 0,154

Из приведённых данных следует, что СУ на широкополосном трансформаторе значительно уступает по своим характеристикам дифференциальному усилителю, а именно :

- в рабочем окне сигнала появились переотражения;
- полоса сигнала сузилась в 3 раза;
- по критерию сверхширокополосности сигнал не относится к таковому (0,154 против 0,25)

#### 4. СУ – полуволновое колено длинной линии.

Изначально из определения вытекает, что такое согласование не будет сверхширокополосным так как длина колена выбирается из расчёта длины волны на центральной частоте диапазона. Такое согласование идеально подходит для перехода симметричной 200 омной антенны на несимметричный 50 – омный кабель.

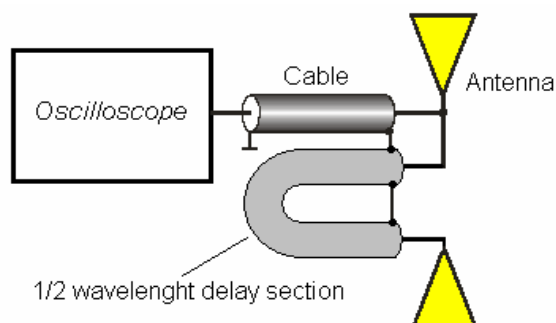


Figure 9. Схема подключения СУ на основе полуволнового колена ( $\lambda / 2$  elbow)

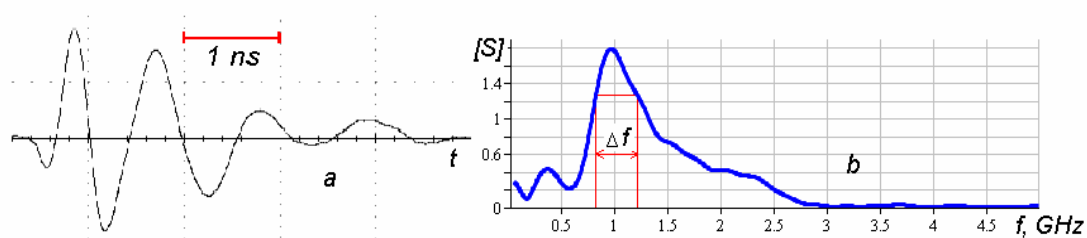


Figure 10. Согласующее устройство –полуволновое колено. а – форма принимаемого сигнала; b – модуль спектральной плотности принимаемого сигнала.

Из анализа сигнала и его спектра следует (Figure10) :

- центральная частота равна 0.95 GHz;
- количество периодов в сигнале – 4;
- наличие переотражений в рабочем окне (20ns) – 30% от максимума
- ширина полосы спектра сигнала на уровне 0,7 – 0,39 GHz
- коэффициент широкополосности сигнала – 0,19

Из приведённых данных следует, что данное СУ значительно уступает по своим характеристикам дифференциальному усилителю, а именно :

- в рабочем окне сигнала значительное количество переотражений;
- полоса сигнала сузилась в : 3 раза;
- по критерию сверхширокополосности сигнал не относится к таковому (0,19 против 0,25)

Из анализа вышеизложенных исследований вытекает простой вывод : наилучшее согласование для симметричной антенны достигается при использовании дифференциального высокоомного усилителя, подключенного непосредственно к клеммам антенны. Однако изготовление такого усилителя с полосой не хуже 4 GHz с идеальными согласующими цепями внутри самого усилителя является трудоёмкой и дорогой задачей. Следующим по качеству согласования является СУ на основе ТДЛ. Хотя трудоёмкость его изготовления и дороговизна значительно ниже, чем для СУ на основе усилителя, тем не менее для хорошего согласования требуется : а) «подгонять» входное сопротивление антенны под значение, равное  $R_0 K_{tr}$ , где  $K_{tr}$  - реализуемый коэффициент трансформации ТДЛ, который нельзя сделать произвольной величиной; б) правильно сконструировать длинную линию, представляющую скрутку двух проводников определённого диаметра и с определённым шагом, для получения волнового сопротивления, соответствующего выбранному для согласования.

СУ на основе широкополосного трансформатора и полуволнового колена не пригодны для сверхширокополосного согласования вследствие неработоспособности в столь широкой полосе.

Компромиссным решением является выбор антенны, требующей минимального согласования. Для такой антенны должны удовлетворяться следующие условия: 1) возможен несимметричный съём сигнала; 2) выходное сопротивление антенны должно быть близко к волновому сопротивлению кабеля, по которому сигнал от антенны подаётся на входное устройство приёмника. Согласовывать такие антенны или вообще не требуется, либо необходимы простые СУ, легко реализуемые на практике.

Для примера проводилось исследование согласования антенны типа «biquad». Антенна представляет собой своеобразную антенную решётку из

четырёх вибраторов, конструктивно оформленную в виде последовательно соединённых двух квадратных рамок. Коэффициент перекрытия частот, равный  $f_{\max} / f_{\min}$ , составляет порядка 2..2,5. В диапазоне  $f_{\min} \div f_{\max}$  диаграмма направленности остаётся практически неизменной. С помощью программы симуляции антенн было рассчитано входное сопротивление антенны с длиной плеча 39 mm, с центральной частотой 2GHz.

$Z_a = 50,06 - j100,9$ . Реальная часть равна волновому сопротивлению кабеля. Для компенсации реактивной составляющей использовали простое СУ в виде LC цепочки. Схема подключения представлена на Figure 11.

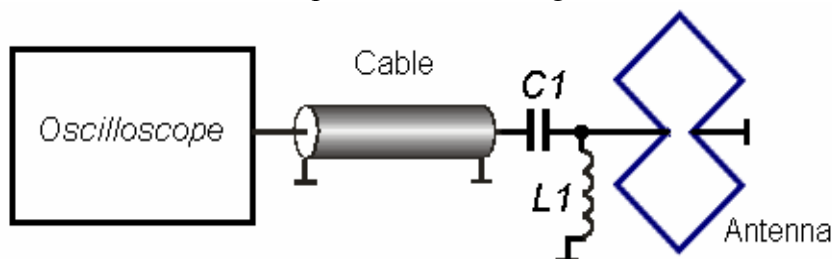


Figure 11. Схема подключения СУ для компенсации реактивной составляющей антенны.

Значения L1 и C1 рассчитаны для центральной частоты 2GHz и составляют соответственно 0,01  $\mu H$  и 0,8 pF

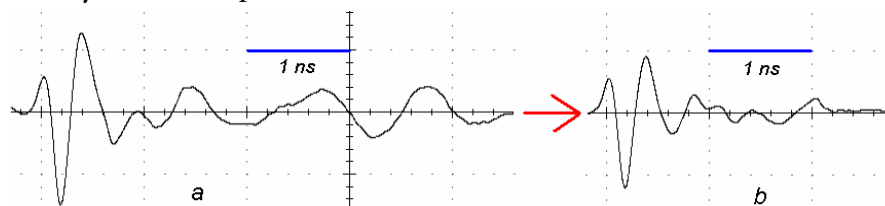


Figure 12. Влияние согласующего устройства (Figure 11) на форму сигнала: a) без СУ; b) СУ-подключено.

Как следует из рисунка, согласование антенны приводит к значительному подавлению переотражений.

Для антенны «biquad» с целью уменьшения КСВ для выбранного рабочего диапазона необходимо использовать проводник большого диаметра. Однако при этом растёт её входное сопротивление. Если оно достигает 75 Ом, то приходится использовать кабель с аналогичным волновым сопротивлением. Тем более, специальные кабели такого стандарта имеют малое затухание, достигающее до 0,1 dB/m на частоте 2GHz. Но, если входное сопротивление приёмника привязано к стандарту в 50 Ом, возникает небольшое рассогласование с коэффициентом отражения  $\Gamma$  равным 0,2 с соответствующим значением Return Loss = 14dB.

Хоть потери незначительны, но переотражения нежелательны. Поэтому для устранения данного рассогласования применяют СУ в виде коаксиального трансформатора. Он представляет собой плавный (оптимальный вариант – экспоненциальный) переход волнового сопротивления кабеля с 75 Ом на 50 Ом. на длине L равной  $\lambda_0 / 4$ , где –  $\lambda_0$  центральная длина волны ( для частоты 2GHz

$\lambda_0 / 4 = 32,4 \text{ mm}$  для кабеля с диэлектриком с диэлектрической проницаемостью 1,337). На Figure 13. показан условный вид трансформатора.

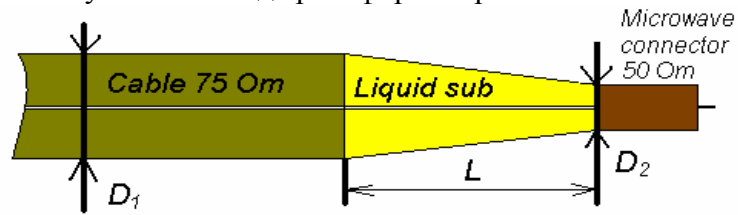


Figure 13. Коаксиальный трансформатор.  $D_1 = 4,8 \text{ mm}$ ,  $L = 32,4 \text{ mm}$ ,  $D_2 = 3,7 \text{ mm}$

Как сказано выше, влияние рассогласования незначительно, но его подключение сказывается на уменьшении уровня переотражений. На Figure 14. видно незначительное уменьшение уровня шумов при наличии СУ в виде коаксиального трансформатора.

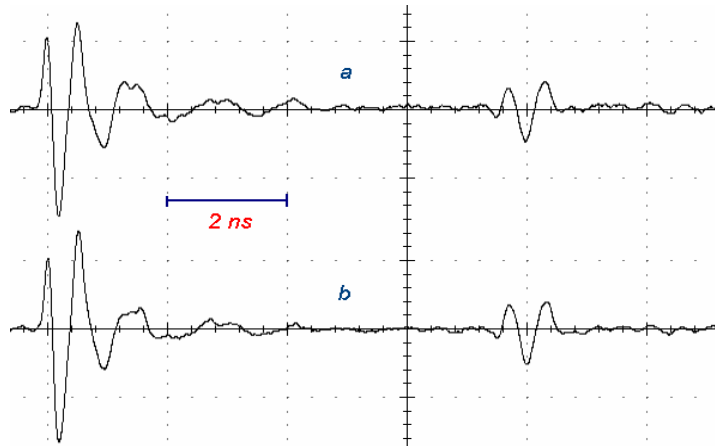


Figure 14. Влияние СУ в виде коаксиального трансформатора проявляется уменьшением шумов. а)- СУ отсутствует; б)- СУ включено

## Выводы

1) Для повышения потенциала радиолокатора, а именно для увеличения излучаемой мощности передатчика и повышения чувствительности приёмника при минимальных искажениях полезного сигнала обязательно применение согласующих устройств, включаемых между антенной и активной выходной (входной) схемой.

2) При использовании в передатчике в качестве активного элемента – SRD возникает сложность согласования в момент переключения диода. Поэтому целесообразно использование временного разнесения фронта возбуждающего антенну импульса и окна полезного сигнала.

3) Среди разнообразия согласующих устройств для симметричной антенны наилучшие результаты могут быть достигнуты при использовании дифференциального высокоомного широкополосного усилителя, включаемого непосредственно к клеммам приёмной антенны.

4) С практической точки зрения для согласования симметричной сверхширокополосной антенны целесообразно использование ТДЛ. Использование последних уступает дифференциальному усилителю на 40% по коэффициенту широкополосности, однако значительно проще в изготовлении и дешевле.